Plasma Physics Reports, Vol. 29, No. 5, 2003, pp. 355–362. Translated from Fizika Plazmy, Vol. 29, No. 5, 2003, pp. 387–394.
Original Russian Text Copyright © 2003 by Pustovitov.

TOKAMAKS

Plasma Equilibrium with Barriers

V. D. Pustovitov

Russian Research Centre Kurchatov Institute, pl. Kurchatova 1, Moscow, 123182 Russia

Received June 26, 2002; in final form, October 24, 2002

Abstract—The recently proposed concept of the transport barrier formation in a tokamak plasma as a bifurcation of the equilibrium state with a change in the toroidal magnetic field over the entire plasma column, including the plasma edge, is analyzed. The analysis is performed in the cylindrical approximation. It is shown that, in the framework of the discussed concept, all of the equilibrium solutions are continuous functions of the parameters involved, bifurcations are absent, and the result is determined by the model assumptions that are necessary in order to make the task self-contained. Removing even part of these restrictive assumptions can substantially change the result. Under typical conditions, the effect of the plasma rotation on the plasma equilibrium is negligibly small. Besides, from the viewpoint of the formal analysis of the force balance, the rotation does not facilitate but, in contrast, hampers the formation of a positive pressure jump. © *2003 MAIK “Nauka/Interperiodica”.*

1. INTRODUCTION

The problem of plasma thermal insulation continues to be among the highest priority problems of fusion research because the critical size of the fusion reactor is determined by the level of the energy loss from the plasma [1–3]. The entire history of tokamaks has been a struggle with losses, which have always been above the level acceptable from the engineering standpoint. The discovery of regimes with improved confinement has become an event essentially strengthening the confidence in the final success of the tokamak program already in the foreseeable future [3]. A distinctive feature of such regimes is the formation of so-called internal transport barriers (ITBs) in the plasma [3–15].

The formation of ITBs is one of the most challenging and interesting problems of tokamak physics. As is the case with many other problems requiring an accurate description of the plasma dynamics on small scales with an account of several competing processes, the problem of ITB formation is very difficult, and complete clarity in this issue has not yet been achieved. However, the present-day theory already allows a quite satisfactory and rather detailed description of ITB formation and the accompanying phenomena (see, e.g., [16–23] and references therein).

The existing theory of ITB formation is a result of serious efforts and an object of close attention and extensive discussions in the fusion community. Very strong arguments would be needed to deny it completely. An example of such denial is the recent paper [24]. It is sufficient to remember only one of its basic conclusions: “The nature of the physical processes that may affect the transport properties of a plasma with an ITB is unimportant.” Further, the logical approaches of [25–27] are announced in [24] not quite adequate for explaining the ITB phenomenon. Finally, the authors of [24] offer a completely new model (called in [24] a “concept”) of ITB formation that differs from the existing models in every respect. Its main feature is that it is based on using only the plasma equilibrium equations; i.e., it takes into account the force balance and nothing more.

In [24], ITB formation in a tokamak plasma is treated as a bifurcation of the equilibrium state. It is stated that “a necessary condition for the buildup of the barrier is the change in the toroidal magnetic field over the entire plasma column (including the plasma edge)” and that “this change may be detected by magnetic measurements.” In the Conclusion of [24], these assertions are ranked as important statements of the paper.

To promptly explain what change is discussed here, let us consider the figure illustrating the cited statement. The figure demonstrates the main properties of solution (28) in [24]. The toroidal field B_z is schematically shown before (dotted line) and after (solid line) a transition into a state with an ITB. According to [24], the ITB formation is accompanied by a reduction in the toroidal field inside the plasma region enclosed by the barrier and an increase in the field outside it. The increase in B_z outside the plasma column is the property of the solution offered in [24] rather than a defect of the figure.

Such behavior of B_z looks rather strange even if we pay no attention to the increase in B_z outside the plasma. A question naturally arises as to whether this solution reflects the real physics of ITB formation or if it is, e.g., only a property of the model used in [24]. The transition from one B_z profile to another is attributed in [24] to some bifurcation. This also creates questions because no mathematical proofs of such a bifurcation are given. It is stated in [24] that, for a transition to a new equilibrium state to occur, the plasma should begin

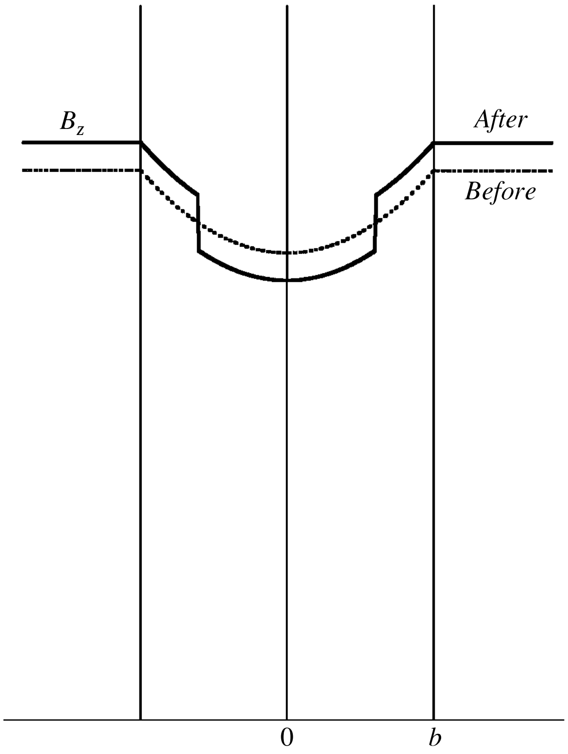

Toroidal magnetic field before and after the formation of an ITB in the concept of [24].

rotating; this also requires explanations because plasma rotation has never been an essential factor in the MHD theory of plasma equilibrium in toroidal systems.

A paper that pretends to the solution of the problem of ITB formation cannot remain unnoticed. This especially concerns a paper with such striking and unexpected conclusions, which at once attract attention and create a lot of questions. Our purpose here is to analyze the proofs given in [24] in support of the above statements and results. Finally, we have to answer whether or not they are correct.

The main results of [24] (in particular, that shown in the figure) are not related to toroidicity; therefore, for simplicity, we will treat the plasma column as a straight cylinder. This is the only difference of our model from that used in [24]. However, this will allow us to essentially simplify all calculations without detriment to the analysis of [24]. Section 2 is devoted to the description of the model. In Section 3, one of the restrictions of the model of [24], namely, the conservation of the magnetic flux, is discussed in more detail. In Section 4, we discuss all of the other restrictions that are necessary to produce the “bifurcation” shown in the figure. In Section 5, we analyze the derivation of the main result of [24] that relates the pressure jump during ITB formation to the velocity of poloidal rotation in ITB zone. In the Conclusion, we summarize the discussion.

2. DESCRIPTION OF THE MODEL

The plasma equilibrium with a stationary flow in a magnetic field is described by the equation [28–32]

$$\rho(\mathbf{v}\cdot\nabla)\mathbf{v} = -\nabla p + \mathbf{j}\times\mathbf{B}. \tag{1}$$

Here, ρ is the plasma mass density, $\mathbf{v}$ is the plasma rotation velocity (usually referred to as the plasma flow velocity), p is the plasma pressure, $\mathbf{B}$ is the magnetic field, and $\mathbf{j} = \nabla\times\mathbf{B}$ is the current density. It is assumed that the plasma flow is stationary; therefore, the term $\rho\partial\mathbf{v}/\partial t$ is absent on the left hand side of Eq. (1).

We consider a cylindrical configuration with all the quantities depending only on the radius r and use cylindrical coordinates r, θ, and z related to the symmetry axis. Following [24], where an equilibrium configuration with purely poloidal rotation was considered, we assume

$$\mathbf{v} = v_\theta(r)\mathbf{e}_\theta. \tag{2}$$

In this case, we have

$$\rho(\mathbf{v}\cdot\nabla)\mathbf{v} = -\frac{\rho v_\theta^2}{r}\mathbf{e}_r, \tag{3}$$

and Eq. (1) in the cylindrical approximation turns into

$$-\frac{d}{dr}\left(p+\frac{\mathbf{B}^2}{2}\right) = \frac{B_\theta^2-\rho v_\theta^2}{r}, \tag{4}$$

where $\mathbf{e}_r$ and $\mathbf{e}_\theta$ are the unit vectors directed along ∇r and $\nabla\theta$, respectively.

Our purpose is to compare two equilibrium states: a state with a barrier, which we will call the final state, and the initial state without a barrier (in the figure, these states are referred to as “after” and “before,” respectively). We assume that, in the initial state, $p = p_i(r)$, and in the final state,

$$p = \begin{cases} p_i(r) + \Delta p, & r < a_B - \Delta_B/2 \\ p_i(r), & r > a_B + \Delta_B/2, \end{cases} \tag{5}$$

where $\Delta p > 0$ is a certain constant, which can be called the pressure jump across the barrier. The zone $a_B - \Delta_B/2 < r < a_B + \Delta_B/2$ will be called the barrier, and the quantity Δ_B will be called the barrier width. The barrier is assumed to be narrow, $\Delta_B/b \ll 1$, where b is the minor radius of the plasma column (in other words, $r = b$ is the plasma boundary). In cases where the barrier width is insignificant, the surface $r = a_B$ will be called the barrier. In what follows, the regions $r < a_B - \Delta_B/2$ and $r > a_B + \Delta_B/2$ will be referred to as the “inside” and “outside” regions with respect to the barrier, respectively.

We assume that the plasma pressure in the final state is described by formula (5) because it is this p profile that was considered in [24]. The choice of profile (5) with Δp = const is just a model assumption, which allows one to describe the difference between two $p(r)$ profiles by a single parameter Δp. There is no other reason to restrict ourselves by profile (5) in considering this problem. Knowledge of $p(r)$ in the barrier zone is not needed here, because we will operate with integral relations.

It was assumed in [24] that the toroidal field B_t in the final state is also described by a relation similar to formula (5), namely, by

$$B_t^2 = \begin{cases} b_t^2(r) - c_{\text{in}} & \text{inside}, \\ b_t^2(r) + c_{\text{out}} & \text{outside}, \end{cases} \qquad (6)$$

where b_t is the toroidal field in the initial state and c_{in} and c_{out} are positive constants. Here, we say "it was assumed," although in [24] the latter relations appeared as a consequence of some other assumptions. These assumptions were formulated not clearly enough in [24]; therefore, we will discuss them later. However, formula (6) is a key relation in [24] on which all calculations are focused. Finally, it is formula (6) that is one of the main results of [24] after the constants c_{in} and c_{out} are expressed through Δp, and it is precisely this result that was discussed in the Introduction and is schematically shown in the figure.

We will not restrict ourselves to profile (6) only. On the contrary, our purpose here is to demonstrate the fact that the transition from the initial state to the final equilibrium state, described by Eq. (5), is also possible with b_t and B_t linked by other relations than formula (6). Formula (6) will be used only when we will need (for comparison with a specific result of [24]) to extract a particular consequence from general relationships.

In addition to relationships (5) and (6), which establish a rather strict link between the initial and final states, it was assumed in [24] that, during a transition from one state to another (called in [24] a bifurcation), the toroidal magnetic flux Φ_{pl} through the plasma cross section $S_\perp$ remains unchanged. This condition can be written as

$$\delta\Phi_{pl} \equiv \delta\int_{S_\perp} \mathbf{B}\,d\mathbf{S}_\perp = 0. \qquad (7)$$

In contrast to the previous restrictions, this condition is not just a simple assumption. Let us discuss it in more detail.

3. CONSERVATION OF THE MAGNETIC FLUX

The conservation of the toroidal magnetic flux during bifurcation is one of the most important elements of the concept of [24], because condition (7) is used in [24] to determine the relation between the quantities c_{in} and c_{out} in formula (6). The result is shown in the figure.

In [24], the use of Eq. (7) is reduced to the integration of the difference $B_t - b_t$ over the plasma cross section. This would be fair if the plasma cross section remain unchanged (e.g., if the plasma were bounded by a rigid wall). Actually, the plasma boundary is always free and can be deformed; this fact must always be taken into account in Eq. (7).

Condition (7) means that

$$S_\perp \delta \bar{B}_z + \bar{B}_z \delta S_\perp = 0, \qquad (8)$$

where the bar stands for the averaging over the entire cross section of the plasma column:

$$\bar{f} \equiv \frac{1}{S_\perp}\int f\,dS_\perp = \frac{2}{b^2}\int_0^b fr\,dr. \qquad (9)$$

If the transverse area of the plasma column remains unchanged ($\delta S_\perp = 0$), the frozenness of the toroidal flux in the plasma would mean $\delta\bar{B}_z = 0$. It is precisely this way in which the relation between c_{in} and c_{out} was established in [24]. For the transition prescribed by Eq. (6), the condition $\delta\bar{B}_z = 0$ can be satisfied only if c_{in} and c_{out} are of the same sign. In [24], both c_{in} and c_{out} are positive.

Under typical conditions, we certainly have $\delta S_\perp \ll S_\perp$. However, the small quantity $\delta S_\perp$ is multiplied in Eq. (8) by the large quantity $\bar{B}_z$; therefore, the term with $\delta S_\perp$ can never be neglected. The reduction of Eq. (8) to $\delta\bar{B}_z = 0$ is a serious mistake. This fact is apparently little known, although it was reported, e.g., in [33, 34]. In particular, it was explained there that condition (8) for the toroidal flux to be frozen in is the equation for $\delta S_\perp$ rather than for $\delta\bar{B}_z$. The value of $\delta\bar{B}_z$ is determined by the equilibrium conditions; in the general case, $\delta\bar{B}_z \neq 0$.

Indeed, multiplying Eq. (4) by r^2/b^2 and integrating over the radius up to the plasma boundary $r = b$, we obtain [35]

$$\bar{p} + \frac{\overline{\mathbf{B}^2}}{2} - \left(p + \frac{\mathbf{B}^2}{2}\right)_{r=b} = \frac{\overline{B_\theta^2} - \overline{\rho v_\theta^2}}{2}. \qquad (10)$$

If $p = 0$ at the plasma boundary, this equality takes the form

$$\bar{p} = \frac{B_e^2 - \overline{B_z^2}}{2} + \frac{B_J^2}{2} - \frac{\overline{\rho v_\theta^2}}{2}. \qquad (11)$$

Here, B_e is the toroidal field at the plasma boundary and $B_J = B_\theta(b)$. It is natural to assume that there are no surface currents on the plasma boundary; in this case, B_e is the external vacuum toroidal field. In systems with a strong toroidal field, the difference between B_z and B_e is small, and exact equality (11) gives approximately

$$\bar{B}_z = B_e\left[1 - \frac{\beta^*}{2} + \frac{B_J^2}{2B_e^2}\right], \qquad (12)$$

where

$$\beta^* \equiv \frac{2\bar{p} + \overline{\rho v_\theta^2}}{B_e^2}. \tag{13}$$

Expression (12) is valid for any equilibrium state, and it is this expression that determines the possible changes in $\bar{B}_z$.

All of the quantities in Eqs. (1), (4), and (10)–(12) characterize a certain equilibrium state at a given instant of time. However, the variations in Eqs. (7) and (8) are calculated as the difference of the values for two states at different times. Therefore, to find the value of

$$\delta\bar{B}_z \equiv \bar{B}_z\Big|_{\text{before}}^{\text{after}} \tag{14}$$

in Eq. (8), one must use formula (11) or (12) twice, applying it to the initial and final states. In these formulas, the external field B_e can differ at different times. This field is determined by the currents in the external conductors. The question as to whether or not B_e will change just as is shown in the figure cannot be answered using only equilibrium equations, even when they are complemented with Eq. (7). Condition (7) applies only to the plasma, and it provides no information about the external circuits determining the vacuum toroidal field B_e.

It follows from Eq. (12) that

$$\delta\bar{B}_z = \delta B_e - B_e\frac{\delta\beta^*}{2} + \frac{\delta B_J^2}{2B_e}. \tag{15}$$

This equality must be complemented with a separate "electrotechnical" equation for the field B_e. It is possible to manage without a description of the magnetic system only in one case, namely, when the plasma is surrounded by a perfectly conducting casing, which prevents the leakage or penetration of the magnetic flux. In this case, the total magnetic flux

$$\Phi_c = \Phi_{pl} + \Phi_{\text{ext}} \tag{16}$$

through the casing cross section S_c is conserved. Here, Φ_{pl} is the magnetic flux through the plasma cross section $S_\perp$ and Φ_{ext} is the flux of the field B_e through the ribbon zone $S_c - S_\perp$, external to the plasma.

When the flux is frozen in the plasma ($\delta\Phi_{pl} = 0$), the conservation of Φ_c means

$$(S_c - S_\perp)\delta B_e - B_e\delta S_\perp = 0, \tag{17}$$

and, consequently, we have

$$\delta B_e = \frac{B_e\delta S_\perp}{S_c - S_\perp} = -\frac{S_\perp}{S_c - S_\perp}\delta\bar{B}_z. \tag{18}$$

In Eq. (18), we have expressed $\delta S_\perp$ using Eq. (8) and have taken into account the fact that the difference between $\bar{B}_z$ and B_e is small [see (12)]. Combining Eqs. (18) and (15), we obtain

$$\delta\bar{B}_z = -\frac{S_c - S_\perp}{S_c}\frac{B_e}{2}\left(\delta\beta^* - \frac{\delta B_J^2}{B_e^2}\right), \tag{19}$$

$$\delta B_e = \frac{S_\perp}{S_c}\frac{B_e}{2}\left(\delta\beta^* - \frac{\delta B_J^2}{B_e^2}\right). \tag{20}$$

Let us recall that these expressions have been derived under two assumptions: the magnetic flux is frozen in the plasma ($\delta\Phi_{pl} = 0$) and Φ_c is conserved. Up to this point, no assumptions have been made on the profiles of the quantities entering equilibrium equation (4).

4. CONCERNING THE SOLUTION OF [24] FOR THE TOROIDAL FIELD

Let us now discuss in more detail the solution of [24], schematically shown in the figure, and the restrictions needed to obtain it.

The jump of B_z in the plasma was determined in [24] from the condition $\delta\bar{B}_z = 0$, which appeared in [24] as a result of the incorrect treatment of condition (7) as equality (8) with $\delta S_\perp = 0$. In the general case, $\delta\bar{B}_z \neq 0$ during the evolution of equilibrium [see (15), (19)]. At the same time, Eq. (15) also permits a particular solution $\delta\bar{B}_z = 0$. To validate this solution (which was used in [24]), we must consider an inverse problem with an initial assumption that $\delta\bar{B}_z = 0$.

General solution (15) shows that the latter condition can only be satisfied at a certain change of B_e, namely, at

$$\delta B_e = B_e\frac{\delta\beta^*}{2} - \frac{\delta B_J^2}{2B_e}. \tag{21}$$

In a real experiment, such a change of the external toroidal field during the evolution (in terms of [24], bifurcation) of the plasma equilibrium can only be specially created. It can arise spontaneously only when Φ_c is conserved and, in addition, $S_\perp = S_c$. Under these two conditions, expressions (20) and (21) coincide and the equality $\delta\bar{B}_z = 0$ is compatible with Eq. (19).

Thus, to reduce the general result to that obtained in [24], at least two conditions are required: the conservation of Φ_c and the equality $S_\perp = S_c$. The latter means that the plasma must be bounded by a perfectly conducting wall. This leads us into unacceptable idealizations. However, the restrictions of the model of [24] are not yet exhausted by these assumptions.

Following [24], in addition to $\delta \bar{B}_z = 0$, we must put $\delta B_J = 0$ in Eq. (21); then, taking into account formulas (5) and (6) and neglecting the effects of rotation and the barrier width, we obtain from Eq. (21)

$$c_{\text{out}} \equiv \delta B_e^2 = 2\frac{a_B^2}{b^2}\Delta p. \qquad (22)$$

Under this condition, the equality $\delta \bar{B}_z = 0$ is satisfied, provided that

$$c_{\text{in}} = 2\Delta p\left(1 - \frac{a_B^2}{b^2}\right). \qquad (23)$$

The relation between c_{in} and c_{out} is determined by directly calculating $\delta \bar{B}_z$ with an account of Eq. (6).

Under the same conditions as those used in [24], we have obtained a different result: formula (32) in [24] gives c_{out} and c_{in} larger by a factor of 3. This quantitative discrepancy is a consequence of the incorrect use of the virial theorem in [24]. We attract the reader's attention to this mistake because it is of a fundamental importance for all of the subsequent calculations in [24], the results and the main conclusions of which will be discussed briefly in the next section. Let us remember that the application of the virial theorem to the plasma equilibrium in a tokamak is described in detail in the famous review [36]; hence, the mistake of [24] can be revealed also in the frame of the formalism of [36], where all of the features of the toroidal equilibrium are taken into account. However, for this purpose, it is sufficient to use a simpler cylindrical model.

Thus, a solution in the form of (6) with c_{in} and c_{out} related to Δp by formulas (22) and (23) (i.e., with c_{in} and c_{out} three times smaller than those in [24]) exists only under rather specific conditions. First, these are the assumptions of [24] that, during the transition into a state with a barrier, the pressure profile changes according to Eq. (6), the poloidal field $B_\theta(r)$ and the toroidal flux in the plasma remain unchanged (and, accordingly, $\delta B_J = 0$), and the role of plasma rotation in the integral force balance is negligible. Second, the plasma must be surrounded with a perfectly conducting casing, and there should be no gap between the plasma and casing.

If the last requirement was even implied in [24], this was done implicitly, without the slightest mentioning of it. We have come to it because this was the only way to make the task self-contained without invoking equations for the external circuit and to justify the use of the rather severe constraint $\delta \bar{B}_z = 0$ in [24]. Certainly, the assumption that the plasma boundary is a perfectly conducting casing is very strong idealization. This condition is inapplicable to real experiments.

Integral relations (19) and (20), which are applicable to describing the evolution of an arbitrary equilibrium state under the flux conservation constraint, allow us to correct the solution for the case $\delta \bar{B}_z \neq 0$ with an account of a vacuum gap between the plasma and the perfectly conducting wall. It follows from equilibrium equation (4) that, in the most general case, we have

$$B_z^2(r) = B_e^2 - 2p(r) + \int_r^b \left[\frac{1}{r^2}\frac{d}{dr}(r^2 B_\theta^2) - \frac{2\rho v_\theta^2}{r}\right]dr. \qquad (24)$$

Applying this formula to the initial and final states, we obtain

$$B_t^2 - b_t^2 = B_e^2 - b_e^2 - 2(p - p_i)$$
$$+ \int_r^b \frac{1}{r^2}\frac{d}{dr}[r^2(B_p^2 - b_p^2)]dr - 2\int_r^b \frac{\rho v_\theta^2}{r}dr. \qquad (25)$$

Here, $B_t(r)$ and $B_p(r)$ are the toroidal (B_z) and poloidal (B_θ) fields in the final state, respectively; b_t and b_p are the same fields in the initial state; and B_e and b_e are the values of B_t and b_t at the plasma boundary. If we now return to the above-discussed restrictions of the model of [24] but without $\delta \bar{B}_z = 0$, we again obtain Eq. (6) for the field B_z in the final state but with another constants (the contribution of the barrier zone is neglected):

$$c_{\text{out}} = 2B_e\delta B_e, \qquad (26)$$

$$c_{\text{in}} = c_{\text{out}}\left(\frac{b^2}{a_B^2} - 1\right) - 2\frac{b^2}{a_B^2}B_e\delta\bar{B}_z. \qquad (27)$$

As can be seen from Eq. (20), the larger the plasma–wall gap, the smaller δB_e. For $S_\perp/S_c \longrightarrow 0$, we have $\delta B_e = 0$. In this case, $c_{\text{out}} = 0$ and we can speak not only about an essential quantitative difference but also about a qualitative difference of the solution obtained from the result of [24], namely, that in the plasma outside the barrier ($r > a_B$), the toroidal field does not change. The smallness of $S_\perp/S_c$ is required here only because we have assumed the wall to be perfectly conducting. In a real experiment, $\delta B_e = 0$ if the currents in the toroidal field coils do not vary and the induced poloidal currents in the vacuum vessel are small.

Formulas (26) and (27), together with Eqs. (19) and (20), cover much wider area than Eqs. (22) and (23). However, even when the mistakes of [24] are corrected and the restriction $\delta \bar{B}_z = 0$ is removed, the result obtained remains a purely model one. The reason is that the two equilibrium states are compared in [24] under the restriction $\delta B_J = 0$. However, the ITB formation means the appearance of large temperature and density gradients in the ITB zone. This should inevitably change the bootstrap current [5–7, 17, 18, 20, 37]. Besides, the conditions of the plasma column equilibrium along the major radius must also change. Under fixed external conditions, the increase in β is accompanied by the outward shift of the plasma column. To keep it in the same position, as is usually needed in tokamaks, it is necessary to increase the external vertical field [36]. Then, an additional e.m.f. appears and the longitudinal current changes.

The restriction $\delta B_J = 0$ contradicts not only logic, but also experimental practice, because an ITB is usually formed in the current ramp-up stage and special measures are taken to control the current [3–15]. However, the restriction $\delta B_J = 0$ is not yet the chief drawback of the model. The model of [24] is based on a much stronger assumption that the poloidal field $B_\theta(r)$ in the initial and final states is identical, so that the first integral on the right hand side of Eq. (25) disappears. This condition can be violated, for instance, due to the change in the bootstrap current during the ITB formation. However, if the profile $B_\theta(r)$ is changed, then, as can be seen from Eq. (25), the behavior of $B_t^2(r)$ becomes different from that prescribed by formula (6).

Thus, formula (6) is only a particular solution obtained under the very strong restriction $\delta B_\theta = 0$ for the p profile given by formula (5). In addition, c_{in} and c_{out} were calculated in [24] under the additional restrictions $\delta \bar{B}_z = 0$ and $\delta B_e = B_e \delta\beta^*/2$ and, moreover, a mistake was made in those calculations. As has been shown above, the result can change essentially if the problem is considered under more realistic assumptions.

In particular, if even one restriction $\delta \bar{B}_z = 0$ is lifted, a solution is possible with $c_{\text{out}} = 0$, which refutes the conclusion of [24] about the obligatory change in B_z at the plasma periphery. Formula (25) also allows other versions of B_z behavior, which differ from those offered in [24].

5. CONCERNING THE MAIN RESULT OF [24]

The main result of [24] is the formula relating the pressure jump Δp in formula (5) to the poloidal rotation velocity in the ITB zone. This formula is obtained by integrating the equilibrium equation over the volume in the barrier zone using the constants c_{in} and c_{out}, which are found by a similar integration of the same equation, but over the entire plasma volume.

The calculations of [24] are very bulky and include the use of a rather complicated technique developed for the description of the toroidal equilibrium [38]. However, the main result, expressed by Eqs. (33) and (36) in [24], is not related to toroidicity. Therefore, one can try to correct these formulas again using a simpler cylindrical approximation.

A correction is necessary at least because the derivation of these formulas in [24] is based on incorrectly calculated values of c_{in} and c_{out}. However, a strict analysis leads to the conclusion that these formulas cannot be corrected at all, because the equality that should serve as a required equation for Δp degenerates into an identity.

Indeed, in the frame of the problem under study, there is only one equilibrium equation (4) at our disposal. Its integral consequence (24) gives an explicit relation of p with the magnetic field and rotation velocity. We consider two states, namely, the initial and final ones. Nothing is known about the initial state (except for, probably, $v_\theta = 0$), and the final state is given as “the initial state + the difference.” In such a problem formulation, from the two equations (24) (for the final and initial states), we obtain a single equation for the quantities that are of interest to us, namely, the difference between the quantities in the final and initial states. This is Eq. (25), in which all the differences appear explicitly.

Equation (25) contains five quantities: $B_t^2 - b_t^2$, $B_e^2 - b_e^2$, $p - p_i$, $B_p^2 - b_p^2$, and ρv_θ^2. To obtain a relation between two quantities, three others must be prescribed somehow. In the problem under consideration, it is supposed that $B_p^2 - b_p^2 = 0$ and $B_e^2 - b_e^2$ is found from the additional constraint $\delta \bar{B}_z = 0$ discussed above. Besides, it is assumed that $v_\theta = 0$ everywhere outside the barrier zone. If p and p_i are related by formula (5), then, with these three assumptions, we obtain from Eq. (25)

$$c_{\text{out}} = B_e^2 - b_e^2, \tag{28}$$

$$c_{\text{in}} + c_{\text{out}} = 2\Delta p + 2\int_{\text{in}}^{\text{out}} \frac{\rho v_\theta^2}{r} dr, \tag{29}$$

where, according to formula (6), $-c_{\text{in}}$ and c_{out} are the result of the subtraction $B_t^2 - b_t^2$.

These are equations for two unknowns, c_{in} and c_{out}. They are an exact consequence of the equilibrium equation under the above model assumptions. There are no additional equations in the problem under consideration (the requirement $\delta \bar{B}_z = 0$ allows us to consider the right hand side of Eq. (28) known). In [24], the virial theorem is considered as an additional equation, which is obtained by integrating the equilibrium equation over the plasma volume [36]. It is clear that the integral consequence of the equation cannot contain any new information compared with that contained in the initial equation. In our case, this statement means that, from the virial theorem, we can only obtain Eq. (29). More precisely, if, following [24], we neglect the rotation effects, then, from the virial theorem, we find again that $c_{\text{in}} + c_{\text{out}} = 2\Delta p$. However, in [24], $6\Delta p$ was obtained instead of $2\Delta p$ in the latter equality. The replacement of the left hand side of Eq. (29) by $6\Delta p$ exactly reproduces the incorrect formula (36) of [24], if toroidicity is neglected there. The correct substitution of $2\Delta p$ turns Eq. (29) into a trivial identity.

Thus, the main result of [24] is a consequence of a mistake in calculating $c_{\text{in}} + c_{\text{out}}$. Accordingly, all the main conclusions of [24] and, on the whole, the offered concept of ITB formation as a bifurcation of an equilibrium are incorrect.

6. CONCLUSION

The change in the toroidal field, whatever its value, cannot be considered as a distinctive feature of ITB formation because it is a natural and inevitable result of any equilibrium evolution. This effect has been known since the very beginning of fusion research and was used to determine β from diamagnetic measurements [39, 40] long before the discovery of regimes with ITB.

According to Eq. (4) or (25), the radial behavior of B_z is determined by three (without rotation, two) functions. One can speak about a specific solution for B_z only when all of these functions are given. The solution shown in the figure is a particular case for two states related by very strong unrealistic restrictions $\delta\bar{B}_z = 0$ and $\delta B_\theta = 0$. If we weaken these restrictions, other solutions are also possible [see Eq. (25)], including those without a change in B_z on the plasma periphery.

In the problem considered in [24] and, in a more general formulation, in the present work, all of the solutions are continuous functions of the parameters involved. There are no selection rules that could force an equilibrium configuration to make a transition of type (5) or any other. The term “bifurcation” is used in [24] incorrectly. Formula (36) in [24], relating the pressure jump Δp to the poloidal rotation velocity and offered as a criterion for the transition into a new state, is incorrect. It is impossible to correct this formula, which is the main result of [24], and thus to save the concept of [24]. This formula is actually obtained by a subtraction like $x - x$, and the correct manipulation with the equations must always give, irrespective of the assumptions, the trivial identity $0 = 0$ instead of this formula.

If we neglect all the terms in Eq. (25) except for the terms with pressure and velocity, then we obtain $\Delta p/p \propto (v_\theta^2/v_T^2)(\Delta_B/a_B)$, where $v_T = \sqrt{T_i/m_i}$ is the ion thermal speed. This estimate shows that the pressure jump produced by the poloidal rotation of the plasma is small. A more careful analysis of Eq. (25) shows that, in addition, this jump is negative. This is natural because the poloidal rotation produces a centrifugal force directed outward. In the concept of [24], plasma rotation is declared a trigger launching the transition from the initial state to the state with an ITB. Actually, the onset of rotation should result in the opposite effect, namely, a reduction in the plasma pressure. We remind that all the above estimates and conclusions are based on the analysis of the plasma equilibrium conditions only.

The equilibrium theory operates with the force balance only [see Eq. (1)] and, at best, allows one to establish a relation of the pressure jump only with the work done by these forces. Heat sources and losses, as well as thermal balance, do not appear in the problem; therefore it is impossible in principle to describe the ITB formation based exclusively on Eq. (1) and Maxwell’s equations.

It is known that the cylindrical model gives a quite reliable result for the diamagnetic signal in tokamaks and stellarators [33, 34, 39, 40]. The integral relations given in the present work can be useful for the interpretation of diamagnetic measurements in the presence of poloidal plasma rotation with allowance for the flux conservation.

ACKNOWLEDGMENTS

I am grateful to my colleagues at the Kurchatov Institute for bringing this problem to my attention and for their keen interest in establishing truth. This work was supported in part by the Russian Foundation for Basic Research, project no. 00-15-96526 (under the program Leading Scientific Schools).

REFERENCES

1. V. S. Mukhovatov, Itogi Nauki Tekh., Ser.: Fiz. Plazmy, Part 1 **1**, 6 (1980).
2. B. B. Kadomtsev, Itogi Nauki Tekh., Ser.: Fiz. Plazmy **6**, 40 (1985).
3. ITER Physics Basis Editors *et al.*, Nucl. Fusion **39**, 2137 (1999).
4. B. W. Rice, E. A. Lazarus, M. E. Austin, *et al.*, Nucl. Fusion **36**, 1271 (1996).
5. ITER Physics Basis (IAEA, Vienna, 1999); Nucl. Fusion **39**, 1883 (1999).
6. V. S. Chan, C. M. Greenfield, L. L. Lao, *et al.*, Nucl. Fusion **40**, 1137 (2000).
7. Y. Kamada and JT-60 Team, Nucl. Fusion **41**, 1311 (2001).
8. JET Team and C. Gormezano, Nucl. Fusion **41**, 1327 (2001).
9. S. L. Allen and DIII-D Team, Nucl. Fusion **41**, 1341 (2001).
10. O. Gruber, R. Arslanbekov, C. Atanasiu, *et al.*, Nucl. Fusion **41**, 1369 (2001).
11. I. H. Hutchinson, R. Boivin, P. T. Bonoli, *et al.*, Nucl. Fusion **41**, 1391 (2001).
12. JET Team and A. C. C. Sips, Nucl. Fusion **41**, 1559 (2001).
13. E. J. Doyle, L. R. Baylor, K. H. Burrel, *et al.*, Plasma Phys. Controlled Fusion **43**, A95 (2001).
14. E. Joffrin, C. D. Challis, T. C. Hender, *et al.*, Nucl. Fusion **42**, 235 (2002).
15. E. J. Doyle, C. M. Greenfield, M. E. Austin, *et al.*, Nucl. Fusion **42**, 333 (2002).
16. Y. Kishimoto, J.-Y. Kim, W. Horton, *et al.*, Nucl. Fusion **40**, 667 (2000).

17. A. Fukuyama, K. Itoh, S.-I. Itoh, and M. Yagi, Nucl. Fusion **40**, 685 (2000).
18. D. López-Bruna, B. A. Carreras, and D. E. Newman, Nucl. Fusion **40**, 1825 (2000).
19. P. Zhu, G. Bateman, A. H. Kritz, and W. Horton, Phys. Plasmas **7**, 2898 (2000).
20. J. W. Connor, P. Helander, A. Thyagaraja, *et al.*, in *Proceedings of 18th International Conference on Fusion Energy 2000, Sorrento, 2000* (IAEA, Vienna, 2001), CD-ROM: IAEA-CN-77/TH4/2, http://www.iaea.org/programmes/ripc/physics/.
21. X. Garbet, Plasma Phys. Controlled Fusion **43**, A251 (2001).
22. A. M. Dimits, B. I. Cohen, W. M. Nevins, and D. E. Shumaker, Nucl. Fusion **41**, 1725 (2001).
23. T. Kurki-Suonio, S. I. Lashkul, and J. A. Heikkinen, Plasma Phys. Controlled Fusion **44**, 301 (2002).
24. V. I. Ilgisonis and Yu. I. Pozdnyakov, Fiz. Plazmy **28**, 99 (2002) [Plasma Phys. Rep. **28**, 83 (2002)].
25. S.-I. Itoh and K. Itoh, Nucl. Fusion **29**, 1031 (1989).
26. K. C. Shaing and E. Crume, Jr., Phys. Rev. Lett. **63**, 2369 (1989).
27. E. L. Hinton, Phys. Fluids B **3**, 696 (1991).
28. H. P. Zehrfeld and B. J. Green, Nucl. Fusion **12**, 569 (1972).
29. E. K. Maschke and H. Perrin, Plasma Phys. **22**, 579 (1980).
30. W. Kerner and O. Jandl, Comput. Phys. Commun. **31**, 269 (1984).
31. S. Semenzato, R. Gruber, and H. P. Zehrfeld, Comput. Phys. Rep. **1**, 389 (1984).
32. T. Takeda and S. Tokuda, J. Comput. Phys. **93**, 1 (1991).
33. V. D. Pustovitov, Itogi Nauki Tekh., Ser.: Fiz. Plazmy **13**, 3 (1993); J. Plasma Fusion Res. **70**, 943 (1994).
34. V. D. Pustovitov, Fusion Eng. Des. **34–35**, 689 (1997).
35. H. P. Zehrfeld and B. J. Green, Nucl. Fusion **13**, 750 (1973).
36. V. D. Shafranov, in *Reviews of Plasma Physics*, Ed. by M. A. Leontovich (Gosatomizdat, Moscow, 1963; Consultants Bureau, New York, 1966), Vol. 2.
37. T. Fujita, T. Oikawa, T. Suzuki, *et al.*, Phys. Rev. Lett. **87**, 245001 (2001).
38. L. E. Zakharov and V. D. Shafranov, in *Reviews of Plasma Physics*, Ed. by M. A. Leontovich (Énergoizdat, Moscow, 1982; Consultants Bureau, New York, 1986), Vol. 11.
39. V. S. Mukhovatov and V. D. Shafranov, Nucl. Fusion **11**, 605 (1971).
40. S. V. Mirnov, *Physical Processes in Tokamak Plasmas* (Énergoatomizdat, Moscow, 1983).

Translated by the author

Plasma Physics Reports, Vol. 29, No. 5, 2003, pp. 363–379. Translated from Fizika Plazmy, Vol. 29, No. 5, 2003, pp. 395–412.
Original Russian Text Copyright © 2003 by Batanov, Kolik, Petrov, Pshenichnikov, Sarksyan, Skvortsova, Kharchev, Khol'nov, Okubo, Shimozuma, Ioshimora, Kubo, Sanchez, Estrada, Milligen.

TURBULENCE AND CHAOS

Studies of Fluctuations in the High-Temperature Plasma of Modern Stellarators by the Microwave Scattering Technique

G. M. Batanov*, L. V. Kolik*, A. E. Petrov*, A. A. Pshenichnikov*, K. A. Sarksyan*, N. N. Skvortsova*, N. K. Kharchev*, Yu. V. Khol'nov*, K. Okubo, T. Shimozuma**, I. Ioshimora**, S. Kubo**, J. Sanchez***, T. Estrada***, and B. van Milligen*****

** Institute of General Physics, Russian Academy of Sciences, ul. Vavilova 38, Moscow, 119991 Russia*
*** National Institute of Fusion Science, Tokyo, Japan*
**** Euroatom–CIEMAT, Madrid, Spain*

Received June 20, 2002; in final form, November 20, 2002

Abstract—Microwave scattering diagnostics are described that allow direct measurements of the turbulent processes in the high-temperature plasma of magnetic confinement systems. The first physical results are presented from fluctuation measurements carried out in 2000–2001 in three stellarators: L-2M (Institute of General Physics, Moscow), LHD (National Institute of Fusion Science, Toki), and TJ-II (CIEMAT, Madrid). Plasma density fluctuations in the axial (heating) regions of the L-2M and LHD stellarators were measured from microwave scattering at the fundamental harmonic of the heating gyrotron radiation. In the TJ-II stellarator, a separate 2-mm microwave source was used to produce a probing beam; the measurements were performed at the middle of the plasma radius. Characteristic features of fluctuations, common for all three devices, are revealed by the methods of statistical and spectral analysis. These features are the wide frequency Fourier and wavelet spectra, autocorrelation functions with slowly decreasing tails, and non-Gaussian probability distributions of the magnitudes and the increments in the magnitude of fluctuations. Observations showed the high level of coherence between turbulent fluctuations in the central region and at the edge of the L-2M plasma. The drift-dissipative instability and the instability driven by trapped electrons are examined as possible sources of turbulence in a high-temperature plasma. *© 2003 MAIK “Nauka/Interperiodica”.*

1. INTRODUCTION

Fluctuations arising due to nonlinear processes in plasma have attracted the attention of physicists for a long time. Interest in these fluctuations has considerably increased in recent years, when it became clear that many global plasma processes (particle diffusion, heat conduction, etc.) in toroidal confinement systems depend on the fluctuations of the plasma density, electric field, and particle temperature [1–4]. In this context, information about the spectral and probabilistic characteristics of the plasma density and temperature fluctuations existing throughout the entire plasma volume (both in the center and at the edge) is very important for solving fundamental and applied problems related to the confinement of high-temperature plasma in toroidal fusion devices.

To date, the spectral and probabilistic characteristics of the fluctuations of the density, floating potential, and particle fluxes in the low-temperature plasma regions in toroidal devices (the edge of the plasma column) have been studied in considerable detail. Methods for studying these fluctuations are well developed and are used in all toroidal devices, both tokamaks and stellarators. Density fluctuations in a low-temperature plasma are described by the strong structural turbulence model [5]. *Strong structural turbulence* means that, against the background of strong turbulence arising due to plasma instabilities, there exists an ensemble of the interacting stochastic plasma structures. Such spatiotemporal structures comprise a substantial fraction of turbulent fluctuations; for this reason, random events in this kind of turbulence can significantly contribute to the variations of the macroscopic plasma parameters. Turbulence in which random events are significant is also called rigid turbulence [6]. Various types of stochastic structures, such as nonlinear solitons, vortices, and MHD structures, have been observed experimentally in low-temperature plasma [5, 7, 8]. It was found that strong structural turbulence in the edge plasma possesses some general properties irrespective of the turbulence source and the type of stochastic plasma structures. Such turbulence in a low-temperature plasma is characterized by slowly decreasing autocorrelation functions (ACFs) with oscillating tails and wide frequency spectra. Its temporal structure is described by an ensemble of damping wavelets [5, 8], and the probability density function (PDF) of the fluctuation magnitudes differs from a Gaussian distribution [9, 10].

The average electron temperature and plasma density in the central region of the plasma column in toroidal devices are two orders of magnitude higher than those at the edge. The study of the fluctuation processes

Table

	L-2M	LHD	TJ-II
Major radius R, cm	100	800	150
Average minor radius $\langle r \rangle$, cm	11.5	80	10–22
Magnetic field B, T	1.3–1.4	≤3	≤1.2
Input microwave power P_0, kW	150–200	600	200–400
Average density $\langle n \rangle$, 10^{13} cm^{-3}	1.0–1.3	~1.0	<1.0
Central electron temperature $T_e(0)$, eV	400–800	~1000	500–800
Relative amplitude of fluctuations in the edge plasma $(\delta n/n)_{\mathrm{edge}}$	0.2–0.25		0.2–0.25
Pulse duration, ms	10–12	>1000	200–300

in a high-temperature plasma is an even more important and challenging problem than the study of fluctuations in the edge plasma. However, these studies are substantially limited by the complexity of the diagnostic techniques. Here, we can note advances in heavy-beam diagnostics [11], reflectometry [12, 13], and enhanced-scattering diagnostics [14], which allow the measurements of density fluctuations in a high-temperature plasma. However, most of the questions that arise in studying fluctuations in the central region of the stellarator plasma, namely, those about the amplitude of the fluctuations, their frequency and wavelet spectra, correlation and probabilistic parameters, etc., are still unanswered. There are also other unresolved problems concerning the high-temperature plasma region: the determination of the types of instabilities giving rise to fluctuations, the degree to which the plasma is nonequilibrium, and the possibility of the formation of stochastic plasma structures.

During the last few years, we have attempted to bridge this gap. Our experiments are based on the method of microwave scattering by density fluctuations in a high-temperature plasma. The parameters of the plasma density fluctuations were studied by the conventional technique of measuring the scattered 2-mm radiation of a separate low-power microwave source [15, 16] and also by measuring the scattered radiation of the heating gyrotron [17, 18]. In 2000–2001, the first experiments on studying the scattered gyrotron radiation were performed in the L-2M (Institute of General Physics, Moscow) and LHD (NIFS, Toki) devices, and the scattering of 2-mm microwaves was studied in the TJ-II device (CIEMAT, Madrid).

In this paper, the microwave-scattering techniques used in the L-2M, LHD, and TJ-II devices are briefly outlined; the first measurements of the plasma density fluctuations in the high-temperature plasmas of these devices are reported; and the first results of the spectral, correlation, and probabilistic analyses of the time samples of the fluctuation magnitudes are demonstrated.

2. DESCRIPTION OF THE DEVICES AND MICROWAVE-SCATTERING TECHNIQUES

2.1. Experimental Devices

Experiments on studying the characteristics of fluctuations in a high-temperature plasma by microwave-scattering techniques were carried out in three toroidal plasma devices: L-2M, LHD, and TJ-II.

The L-2M stellarator has a two-pole winding; a detailed description of it is given in [19]. The main parameters of the device are presented in the first column of the table. In the edge plasma (at a radius of $r/a = 0.9$, where a is the separatrix radius), the density $n \sim 1$–2×10^{12} cm^{-3} and the electron temperature $T_e \sim$ 30–40 eV. The plasma is produced and heated under ECR conditions at the second harmonic of the electron gyrofrequency with the help of a 75-GHz gyrotron.

The LHD device is the largest modern superconducting heliac with a divertor [20]. The LHD plasma parameters are listed in the second column of the table. In this experiment, the plasma was created and heated under ECR conditions at the fundamental and second harmonics of the electron gyrofrequency by several 168-GHz and 84-GHz gyrotrons.

The TJ-II device is a stellarator with four-pole winding [21]. The main parameters are listed in the third column of the table. The plasma has a variable section along the torus; the mean plasma radius varies from 0.1 to 0.22 m. In this experiment, the plasma was produced and heated by a 53.2-GHz gyrotron at the second harmonic of the electron gyrofrequency.

2.2. Use of the Gyrotron Scattering Technique in the L-2M Stellarator

Microwave radiation from the heating gyrotron was launched into the vacuum chamber of the L-2M stellarator as a linearly polarized Gaussian beam. At the plasma boundary, the incident linearly polarized wave splits into an extraordinary and ordinary wave. At densities typical of the existing toroidal devices, the plasma is transparent to ordinary waves, and it is optically thick for extraordinary waves. The fact that the incident radiation excites two waves in the plasma is unfavorable for

ECR plasma heating because the single-pass absorption of the heating wave in the plasma decreases [22]. On the other hand, the ordinary wave can be used as a probing wave in scattering diagnostics. Figure 1 schematically shows the geometry of the gyrotron scattering diagnostics in the poloidal section of the stellarator chamber. A horn antenna placed in the upper port receives gyrotron radiation with a given polarization ($\mathbf{E}_0 \parallel \mathbf{B}$), scattered at an angle of $\pi/2$ by plasma density fluctuations in the central region of the plasma column. The scattered signal is measured in the direct-detection regime. The observation region is marked in the figure by a black quadrangle; this region is located at the intersection of two microwave beams, namely, the incident beam launched by the gyrotron and the beam received by the horn. The size of the observation region is nearly 5 cm. Estimates show that, in the plasma of the L-2M stellarator, up to 10–20% of the gyrotron energy propagates in the form of an ordinary wave, which comprises several tens of kilowatts. For this reason, the receiving line contains diaphragms and a collimator attenuating the scattered signal before it reaches the detector. According to the Bragg condition,[1] the gyrotron radiation (k_0 = 15 cm^{-1}) is scattered by an angle of $\pi/2$ by plasma density fluctuations with a characteristic scale length $\lambda_{sc} \approx$ 3–4 mm ($k \sim$ 20 cm^{-1}). Figure 1 also shows the relative positions of movable Langmuir probes measuring density fluctuations in the edge plasma in the regime of the ion saturation current; the probes were placed in several poloidal sections.

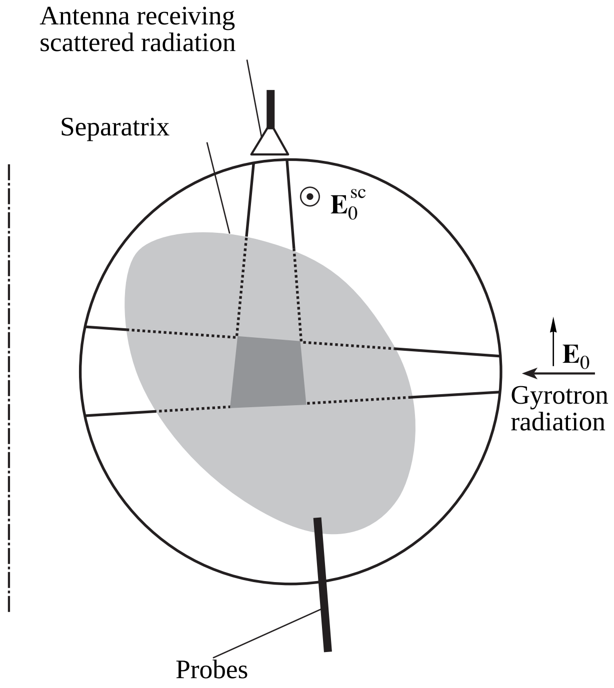

Fig. 1. Gyrotron scattering diagnostics in L-2M.

2.3. Use of the Gyrotron Scattering Technique in the LHD Device

The gyrotron scattering diagnostics were elaborated and mounted in the LHD device to measure fluctuations in the central region of the plasma column. These diagnostics do not differ fundamentally from the scattering diagnostics employed in the L-2M stellarator. In this case, however, the measurement scheme is based on the available system of quasioptical transmission lines of the LHD gyrotron complex. A system for the transmission of microwave radiation from several gyrotrons into the heliac chamber consists of several quasi-optical transmission lines [23]. These lines are designed so that the input power profile in the heating region is sufficiently narrow for the position of this region to be known with certainty when studying local effects related to plasma heating. These transmission lines turned out to be convenient to use in the gyrotron scattering diagnostics. Figure 2a shows the system of quasioptical lines for transmitting radiation from two gyrotrons with frequencies of 168 and 84 GHz. The detector receiving the scattered radiation from the second gyrotron was placed in the transmission line of the first gyrotron. As in L-2M, the radiation from the second gyrotron (84 GHz) was partially converted into the ordinary wave. The power of the ordinary wave was high enough for the scattered signals to be easily detected even through such a long transmission line. Plasma density fluctuations in the central region of the plasma column were measured in the direct-detection regime. The scattered signals were received from a spatial region located at the intersection of the microwave beams launched from two transmission lines. The geometry of the incident and scattered beams is shown in Fig. 2b. In contrast to the L-2M experiment, this geometry of gyrotron scattering is closer to the backward Bragg scattering. In the LHD experiment, the microwave radiation was scattered by plasma density fluctuations with a wavelength of $\lambda_{sc} \sim$ 1.8 mm ($k \sim$ 25–34 cm^{-1}). In this experiment, the heating region could be shifted in the poloidal and toroidal direction, which allowed us to determine the dimensions of the scattering region.

2.4. Use of the 2-mm Scattering Technique in the TJ-II Device

For the TJ-II device, a 2-mm scattering technique was elaborated for studying fluctuations in the high-temperature core plasma. Figure 3 shows the diagnostic arrangement. Microwave radiation from a GDI generator (*T*1) was launched into the plasma, and we received the radiation scattered by angles of 6° and 12° (*R*2, *R*3) and also the radiation passed through the plasma (*R*1) (because of the fairly complicated plasma cross section

---

[1] The relation between the incident and scattered radiation components is given by the Bragg condition: $k = 2k_0\sin(\varphi/2)$, where φ is the scattering angle [15].

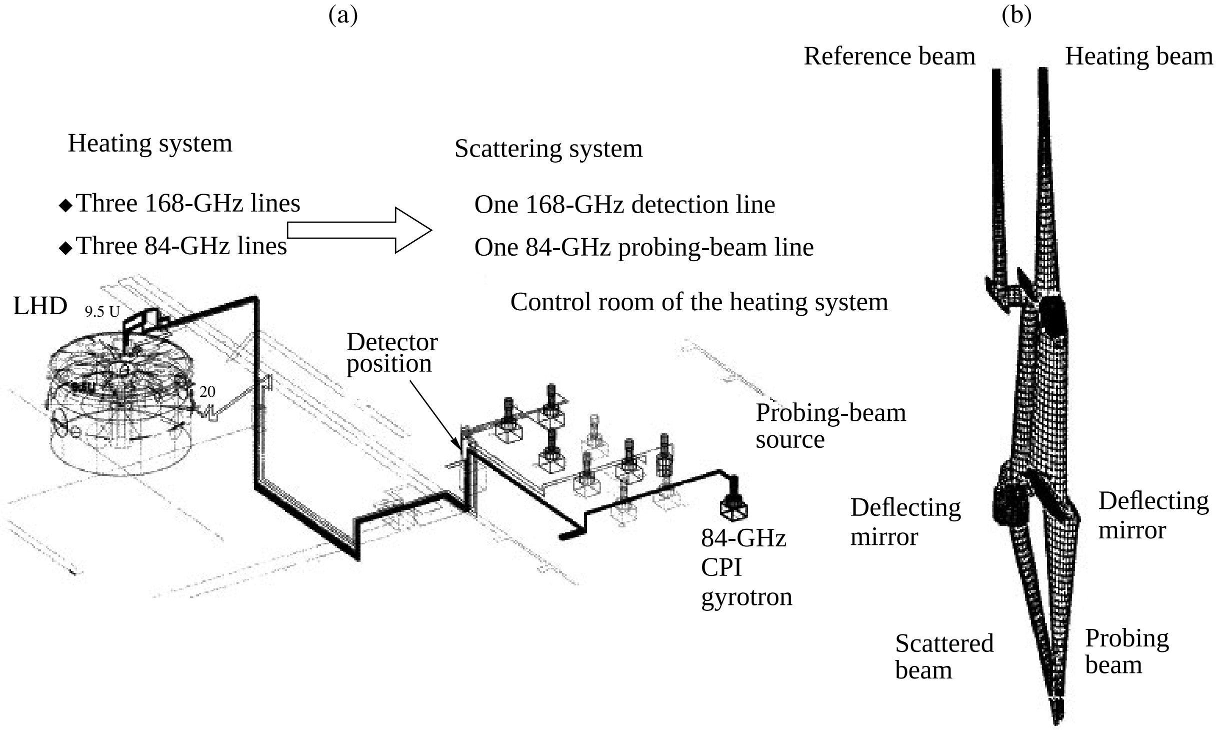

Fig. 2. (a) Gyrotron scattering diagnostics and (b) quasi-optical system for the input of gyrotron radiation in LHD.

in this device, a reference detector was needed to determine the position of the scattering point). Plasma density fluctuations were measured from signals scattered from the inner plasma region lying at the middle of the plasma radius (r/a ~ 0.5); the poloidal and radial dimensions of this region were about 4 cm. We measured plasma density fluctuations with wavenumbers 3 and 6 cm^{-1}. The homodyne detection of the scattered signals was employed. We note that, in this experiment, the 2-mm scattering diagnostic system was located far from the heating-gyrotron port. Previously, several versions of the 2-mm scattering diagnostic systems were created in the Plasma Physics Department of the Institute of General Physics and installed in the L-2 [24] and ATF [25] stellarators and the TJ-IU torsatron [26]. All of these diagnostic systems used GDI microwave oscillators but differed in the reception scheme of the scattered signal; the common disadvantage of these diagnostic systems was the low signal-to-noise ratio. The new 2-mm scattering diagnostics in TJ-II differs from early diagnostics not only in the reception scheme of the scattered signal but also in that some of the receiving transmission lines are made of overmoded waveguides with quasioptical elements [16]. As a result, the loss of the scattered signals in these lines was significantly reduced, which allowed us to substantially enhance the sensitivity of the diagnostics.

2.5. Processing of the Measurement Results

The measurement results in all of the devices were the files of the digitized magnitudes of signals scattered by plasma density fluctuations. The characteristics of the fluctuations were determined by numerically analyzing these time arrays, the number of points in which reached 10^5–10^6. In all three experiments, we used the same program package for numerically processing the time arrays. To study the characteristics of the scattered signals, we used programs for analyzing random time samples; these programs were previously used to study strong structural turbulence in low-temperature plasma [8, 9, 27–31]. The program package includes the spectral Fourier analysis, the correlation analysis, the spectral and coherence wavelet analysis, the construction of sample histograms, the computation of the moment of random quantities, the computation of the Herst parameter, and the analysis of phase trajectories.

3. RESULTS OF FLUCTUATION STUDIES

3.1. Experiments on Gyrotron Scattering in L-2M

Figure 4a shows a typical time realization of the scattered signal from the central region of the L-2M plasma (curve *1*). The signal is proportional to the squared magnitude of the plasma density fluctuations. For comparison, the figure also shows the time realization of the probe signal (curve *2*) measured simultaneously with the scattered signal, namely, the saturation-current fluctuations, which are proportional to plasma density fluctuations. Both signals are stochastic in character. In the L-2M stellarator, all of the experiments on studying the fluctuation characteristics of the high-temperature central plasma were accompanied by simultaneous measurements of the fluctuation characteristics of the low-temperature edge plasma. The subsequent figures illustrating the results obtained in L-2M show the parameters of the fluctuations for both of these regions of the plasma column. We note that the gyrotron scattering signals represent only a narrow region of the k spectrum of fluctuations, whereas the probes measure the entire k spectrum of fluctuations.

The measurements of cross-coherence between the fluctuation spectra in the central region and at the edge of the plasma column allow us to find out whether or not the fluctuations in these regions are correlated. Such an analysis was performed in [18]; however, it seemed to be expedient to repeat a similar study under L-2M conditions somewhat different from those in [18] (the data presented in Fig. 4 were obtained in an experiment with the boronization of the chamber wall). Since both signals are bursty, it is reasonable to analyze this cross-coherence with the help of wavelet spectra. The time behavior of the cross-coherence between the wavelet spectra of the fluctuation signals in the center of the plasma column and in the edge plasma are presented in Figs. 4b and 4c for two stellarator shots. For comparison, Figure 4d also shows the noise wavelet spectrum, demonstrating the low level of the noise wavelet coherence.[2] The value of the cross-coherence coefficient of the wavelet components is shown in shades of gray; the observation time is plotted on the abscissa, and the wavelet frequency is plotted on the ordinate. The time cross-coherence spectrum was compiled by interpolating individual spectra calculated for time intervals of 500 μs. In the low-frequency region[3] (below 100–200 kHz), the cross-coherence coefficient attains 50%.

Figure 5a shows the Fourier spectra of microwave signals scattered by density fluctuations in the high-temperature and low-temperature plasma of the L-2M stellarator. Throughout the entire plasma volume, we observed low-frequency fluctuations with a wide continuous spectrum (up to 300 kHz). Figure 5b shows the phase portraits (delayed magnitude vs. magnitude) of the same signals. The time window in these measurements was 2 ms and included 2000 points. The phase portrait of fluctuations in the edge plasma is more diffuse than in the central region. This difference may be explained by the fact that, for the central region, not all of the k components of fluctuations are present in the spectrum. The comparison of the spectra and the phase portraits clearly illustrates the fact that stochastic processes in the central region and at the edge are similar.

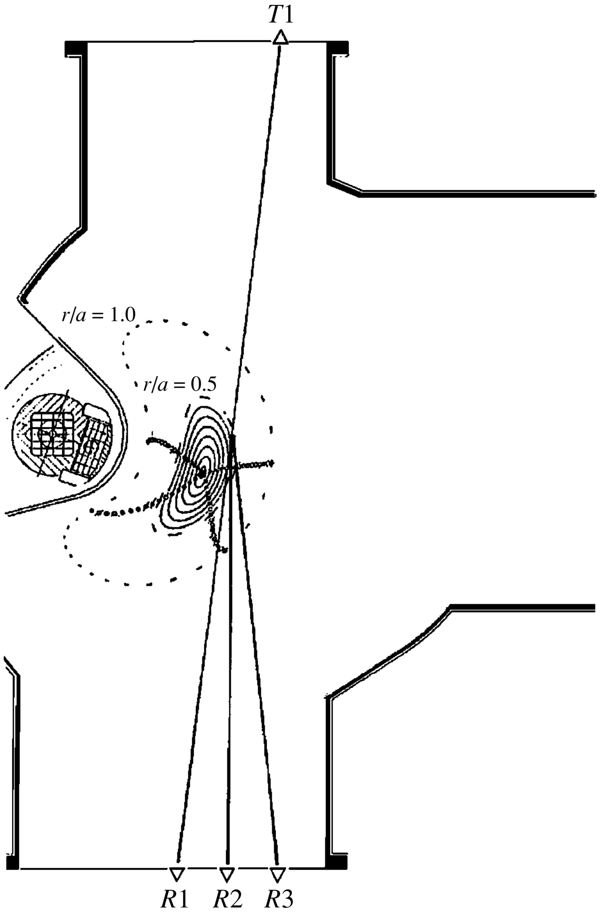

Fig. 3. 2-mm scattering diagnostics in TJ-II.

Now, let us turn to the probabilistic characteristics of the fluctuations. Figures 6a and 6b show the PDFs of the magnitudes of the plasma density fluctuations in the central region and in the edge plasma, respectively. The magnitude of the plasma density fluctuations is plotted on the abscissa, and the number of counts is plotted on the ordinate; the total number of counts in both cases is equal to 2000. The shape of the time-sample histogram of the magnitude of density fluctuations in the edge plasma, as well as the values of the third and fourth moments ($M3 = 0.2$, $M4 = 3.2$), allows us to describe the PDF of the fluctuations by a Gaussian probability distribution.[4] The shape of the time-sample histogram of the magnitude of the plasma density fluctuations in the central region differs substantially from the Gaussian, the third and fourth moments being equal to –1.3 and 4.2, respectively. The turbulent plasma state in the central region differs from equilibrium more strongly

---

[2] The noise wavelet spectrum is calculated from two signals measured in different stellarator shots.

[3] We recall that the wavelet frequency ω is related to the wavelet duration Δ as $\omega = 2\pi/\Delta$.

[4] For such short stationary time samples of the magnitudes of plasma density fluctuations, the self-similar power-law tails of the PDF are usually under the noise level.

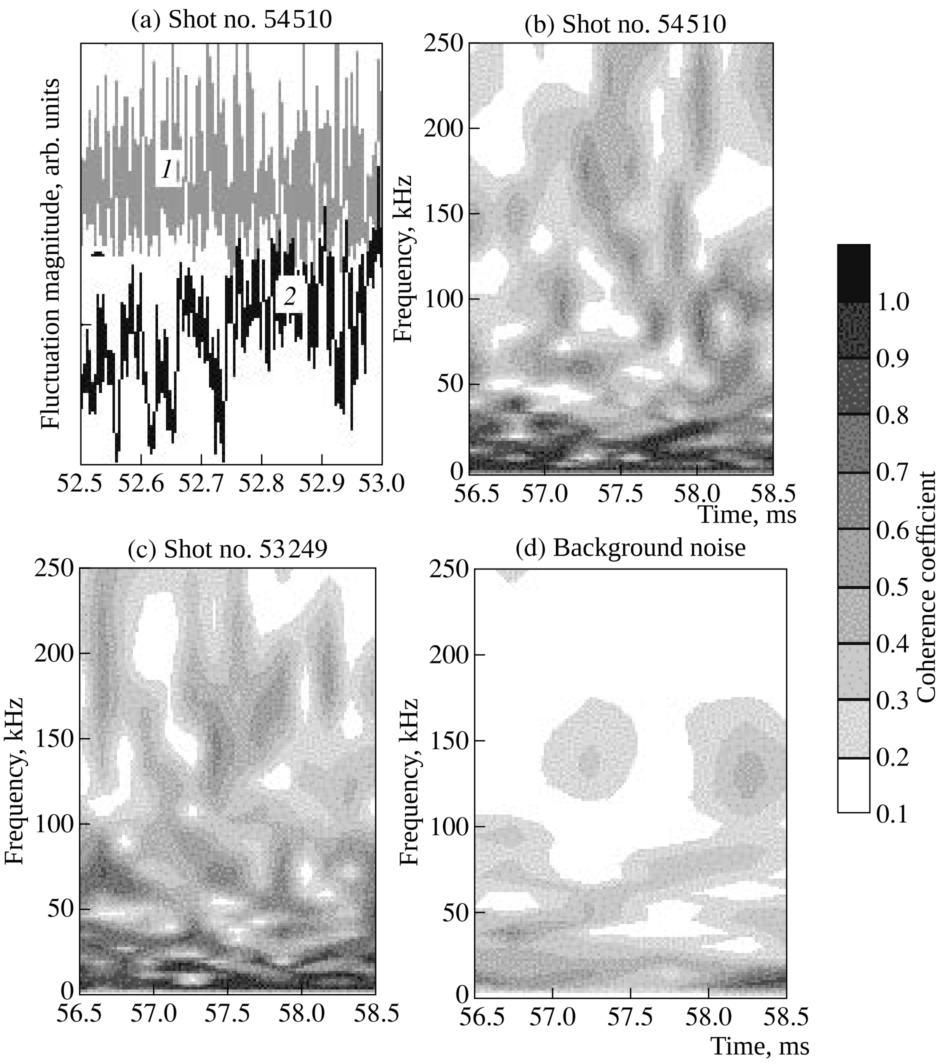

Fig. 4. (a) Density fluctuations (*1*) in the edge plasma and (*2*) in the central region of L-2M; (b, c) cross-coherence wavelet spectra between a signal scattered from the central region of the plasma and fluctuations in the edge plasma; and (d) the noise cross-coherence wavelet spectrum.

than does the edge plasma. The probability of the events with large amplitudes for this turbulence is considerably higher than the probability of similar events for fluctuations obeying a Gaussian distribution. The PDFs of the plasma density fluctuations in the central region turned out to be closer to the PDFs of particle fluxes [10], rather than to the PDFs of density fluctuations in the edge plasma. We note that the high-temperature central plasma is directly affected by the heating gyrotron radiation. It is reasonable to assume that the difference of the PDF of fluctuations from a normal (Gaussian) distribution is due to turbulent processes caused by microwave plasma heating in the central region.

The ACFs of the magnitude of the density fluctuations in the central region and in the edge plasma are shown in Figs. 7a and 7b, respectively. In the ACF of the fluctuation magnitudes in the high-temperature plasma, we can see a broad first maximum and a slowly decreasing tail. The presence of a slowly decreasing tail in the ACF indicates that the time sample of the stochastic process is not homogeneous and independent and that the process is affected by some “influence function.” The correlation time of turbulent fluctuations is longer than the characteristic period of low-frequency oscillations. The autocorrelation function of this kind corresponds to strong structural turbulence in which the influence function is associated with ensembles of interacting stochastic plasma structures [5, 9]. Note that the correlation time of the increments in the magnitude of density fluctuations[5] in the high-temper-

---

[5] The increment in the magnitude of density fluctuations in the time sample is defined as $\Delta X_j = X_j(t_j) - X_{j-1}(t_{j-1})$ [32]. The increments in the random quantity ΔX_j depend on all the linear and nonlinear growth and damping processes giving rise to plasma density fluctuations under given experimental conditions.

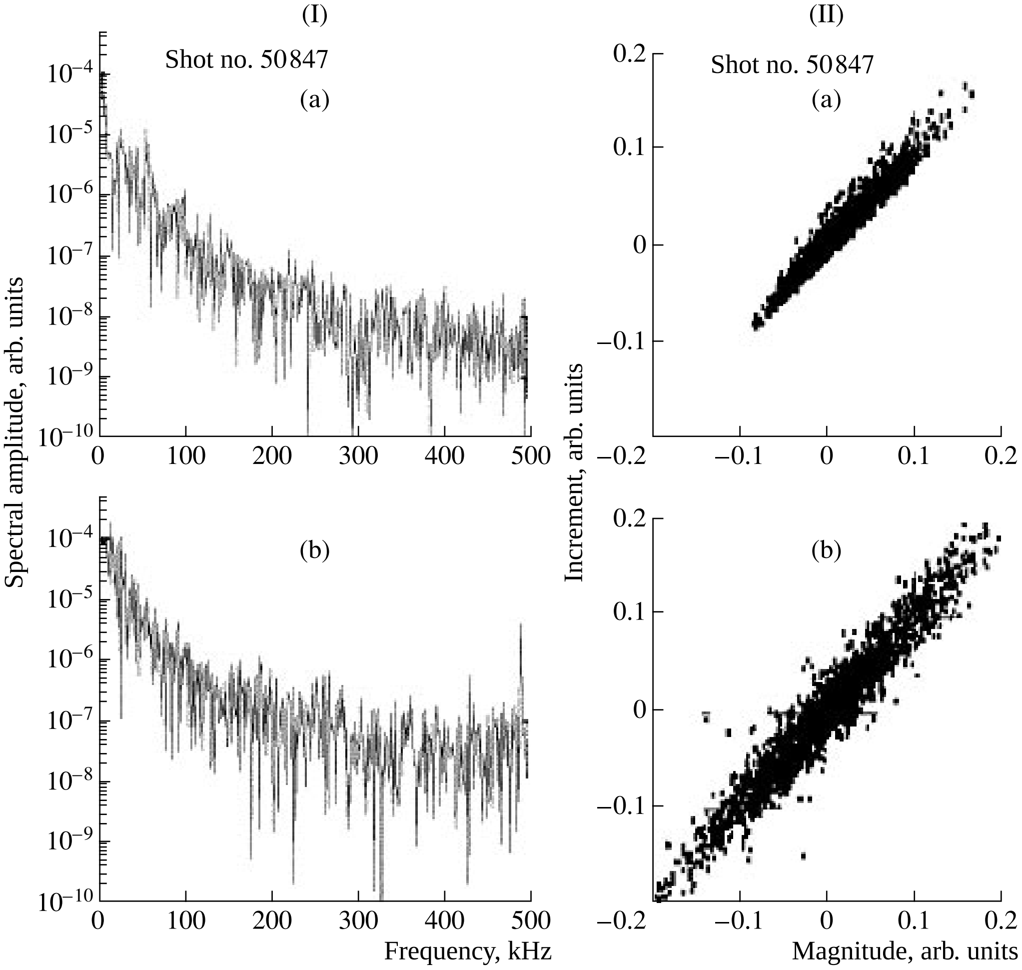

Fig. 5. (I) Fourier spectra and (II) phase portraits (delayed magnitude vs. magnitude; $\Delta t = 1$ μs) of (a) a signal scattered by density fluctuations in the central region of the plasma and (b) fluctuations of the ion saturation current in the edge plasma of L-2M (shot no. 50847).

ature plasma is about 1–2 μs, which is comparable with the characteristic time of the increments in the magnitudes of turbulent fluxes in the edge plasma of the L-2M stellarator [32].

3.2. Experiments on Gyrotron Scattering in LHD

Figures 8a and 8b show how the intensity (mean square deviation) of scattered radiation in LHD varies as the reference microwave beam is displaced in two directions. The scattered signals were received from the central region of length ~10 cm in the poloidal direction and several centimeters in the toroidal direction. For these measurements, it was important to determine the excess of valid signals over the background noise. In the absence of a plasma, the signal fell by a factor of 8–10, and it is this level that was hereinafter taken as the background noise.

Figure 9 shows the following characteristics of the scattered signals measured in the region where the intensity of the signals is maximum: the PDF of the signal magnitude and the ACF and Fourier spectrum of the signal. Figure 9c shows a continuous Fourier spectrum in the frequency range up to 50 kHz (the higher frequencies could not be resolved in this LHD experiment). To construct the PDF and ACF, we only used a valid signal in the frequency band from 1 to 50 kHz (with a signal-to-noise ratio of 8–10). The PDF of the scattered signal (Fig. 9a) differs substantially from a Gaussian distribution: the third and fourth moments are equal to $M3 = -0.15$ and $M4 = 6.29$, respectively. The probability of the observation of large-amplitude scattered signals (rare events that fall beyond the limits of three standard deviations) for this distribution is much higher than for a Gaussian distribution. Figure 9d shows a part of the PDF for large fluctuation magnitudes and the tail of a Gaussian distribution. The ACF in Fig. 9b is similar to the ACF of structural-turbulence fluctuations [5, 6]. The autocorrelation coefficient decreases slowly as the delay time increases, and the oscillating tail of the ACF comprises up to 15% of the

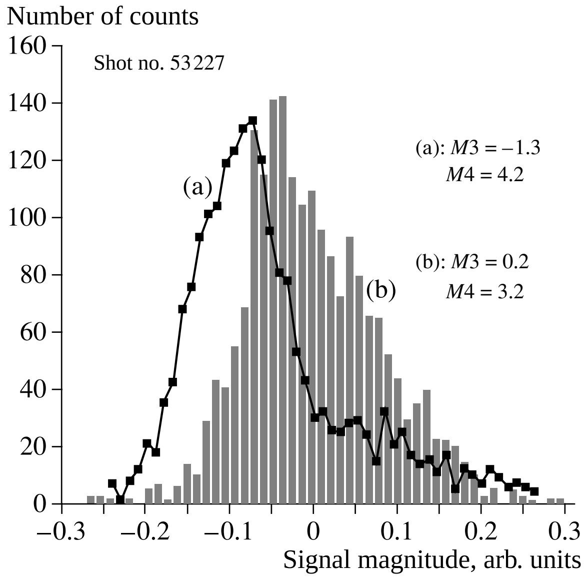

Fig. 6. PDFs of density fluctuations (a) in the central region and (b) in the edge plasma of L-2M.

energy of the scattered signal.[6] It follows from this that the time sample of the magnitudes of plasma fluctuations in the central region of LHD is not homogeneous and independent, as is the case of the L-2M time samples (see Section 3.1). In this case too, we may assume the presence of some influence function in the turbulence of the high-temperature LHD plasma. We note that quasi-harmonics were also observed in a wide wavelet spectrum of the same time samples of scattered-signal magnitudes [23].

It is expedient to determine the characteristics of the increments in the magnitudes of the scattered signals. These characteristics depend on all of the growth and damping rates of the processes resulting in density fluctuations [10]. Figure 10 illustrates the PDF, ACF, and Fourier spectrum of the increments in the magnitudes of the scattered signals. The PDF of the increments (Fig. 10a) is more symmetric ($M3 = 0.07$) than the PDF of the fluctuation magnitudes (Fig. 9a), but, as before, it differs from a Gaussian distribution and has heavy tails ($M4 = 7.1$). The PDF asymmetry points to the absence of equilibrium between the growth and damping of fluctuations. It is seen from the shape of the ACF (Fig. 10b) that the time sample of the increments in the scattered-signal magnitudes is more homogeneous and independent than in the previous case. The Fourier spectrum of the increments (Fig. 10c) is closer to a uniform noise spectrum. Possibly, numerical simulations of homogeneous and independent samples of the increments in the scattered-signal magnitudes (by analogy to the simulations of the samples of the increments in a fluctuating flux [32]) could provide additional information on the type of a random process in the central region of LHD.

3.3. Experiments on 2-mm Scattering in TJ-II

As in the studies of fluctuations in the two above devices, here, we measured the frequency spectra, the PDFs of the magnitudes, and the ACFs of the density fluctuations. The measurements were carried out under different experimental conditions: under standard operating conditions of the device, during the propagation of a cold-nitrogen pulse, and in the different configurations of the magnetic field. In this paper, the results of the measurements in the first two regimes only are presented.

Figure 11 shows the frequency Fourier spectra of plasma density fluctuations with wavenumbers of 3 and 6 cm^{-1}. The wide frequency spectra extend to 130 kHz (for 3 cm^{-1}) and 240 kHz (for 6 cm^{-1}), and the widths of the spectra are close to those of the fluctuation spectra in the central region of L-2M. The fluctuation spectrum with the greater wavenumber is broader than that with the smaller wavenumber; probably, this is related to the dispersion of plasma oscillations.[7] The presence of quasi-harmonics in the wavelet spectra for these regimes complicates the determination of the dispersion and indicates the possible existence of stochastic structures in the plasma. The signal-to-noise ratio for these measurements was lower than for L-2M and LHD and did not exceed 4–5.

In the context of this paper, it seems interesting to describe the results obtained in three experiments in which abrupt changes in the spectral characteristics of plasma fluctuations were observed. Such changes occurred during plasma cooling. The plasma cooling was observed in three cases: in a decaying plasma after the gyrotron was switched off, after a minor disruption occurring during the normal operation of the gyrotron, and after puffing nitrogen at the plasma edge (the cold-pulse propagation experiment [33]). The response of the fluctuations to the local cooling was always the same. Figures 12 and 13 demonstrate the changes in the fluctuation amplitudes when the electron temperature locally decreased in an experiment on the propagation of a cold-nitrogen pulse and after a minor disruption, respectively. For the discharge with a minor disruption, the signals of plasma density, gyrotron radiation, and electron cyclotron emission at the radius $r/a \sim 0.5$ are also shown. When the minor disruption occurred during gyrotron operation, the temperature decreased and the plasma density insignificantly increased in the region where fluctuations were measured. In both cases, as the

---

[6] The ACF of the background noise is usually a δ function and does not contribute to the tails the ACF of the valid signal.

[7] Unfortunately, we failed to determine with certainty to what extent the widths of the spectra depend on the plasma dispersion and to what extent they are affected by the different sensitivities of the measurement channels of the 2-mm scattered diagnostics for fluctuations with wavenumbers of 3 and 6 cm^{-1}.

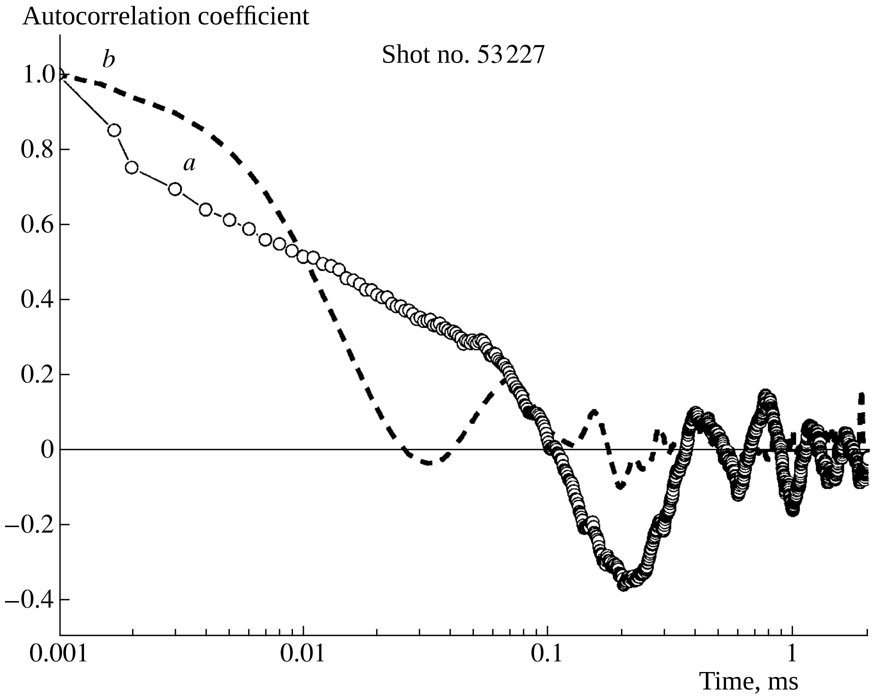

Fig. 7. ACFs of the magnitudes of the plasma density fluctuations in the (*a*) central region and (*b*) edge plasma of L-2M.

temperature decreased, the amplitude of the fluctuations increased by a factor of 2–4. At the same time, the frequency spectrum narrowed and the mean frequency decreased. In Figs. 12 and 13, the time intervals on which the Fourier spectra were determined are marked by shaded rectangles (a) and (b). After the plasma cooling, the half-width of the spectrum in Fig. 12 decreases by a factor of 4 (from 120 to 30 kHz) and in Fig. 13, it decreases by a factor of 5 (from 150 to 30 kHz). Hence, a decrease in the local temperature results in the appearance of intense low-frequency harmonics in the frequency spectrum of plasma fluctuations. For the same regimes, we constructed the PDFs of the fluctuation magnitudes for normal discharge conditions and after cooling. Unlike non-Gaussian distributions of the fluctuation magnitudes in the central regions of L-2M and LHD, the distributions observed at the edge of the hot plasma region in TJ-II appeared to be close to Gaussians. For the same experiments, we calculated the ACFs of the fluctuations, which appeared to be close to δ distributions; no tails were detected in the ACFs. The tails in the ACF and PDF were probably not resolved because of the low signal-to-noise ratio. We note that, in the previous experiments in the L-2 stellarator [2, 5], nonzero tails were observed in the ACFs of the fluctuations, which were also measured by the 2-mm scattering diagnostics at the middle of the plasma radius. For this reason, in order to reveal the difference from a Gaussian distribution, we applied a more sensitive method of numerical *R*/*S* analysis.

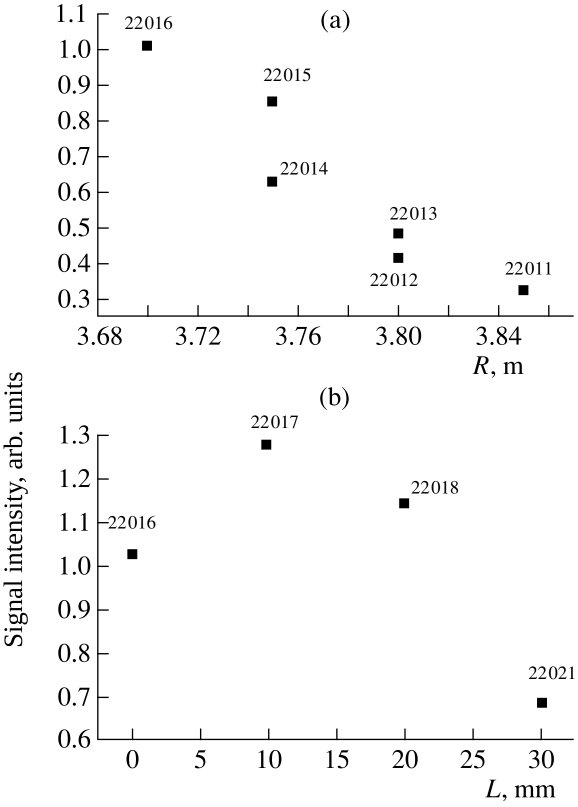

Fig. 8. Intensity of a signal scattered by plasma density fluctuations ($k \sim 30$ cm^{-1}) in LHD vs. (a) poloidal and (b) toroidal positions of the reference microwave beam.

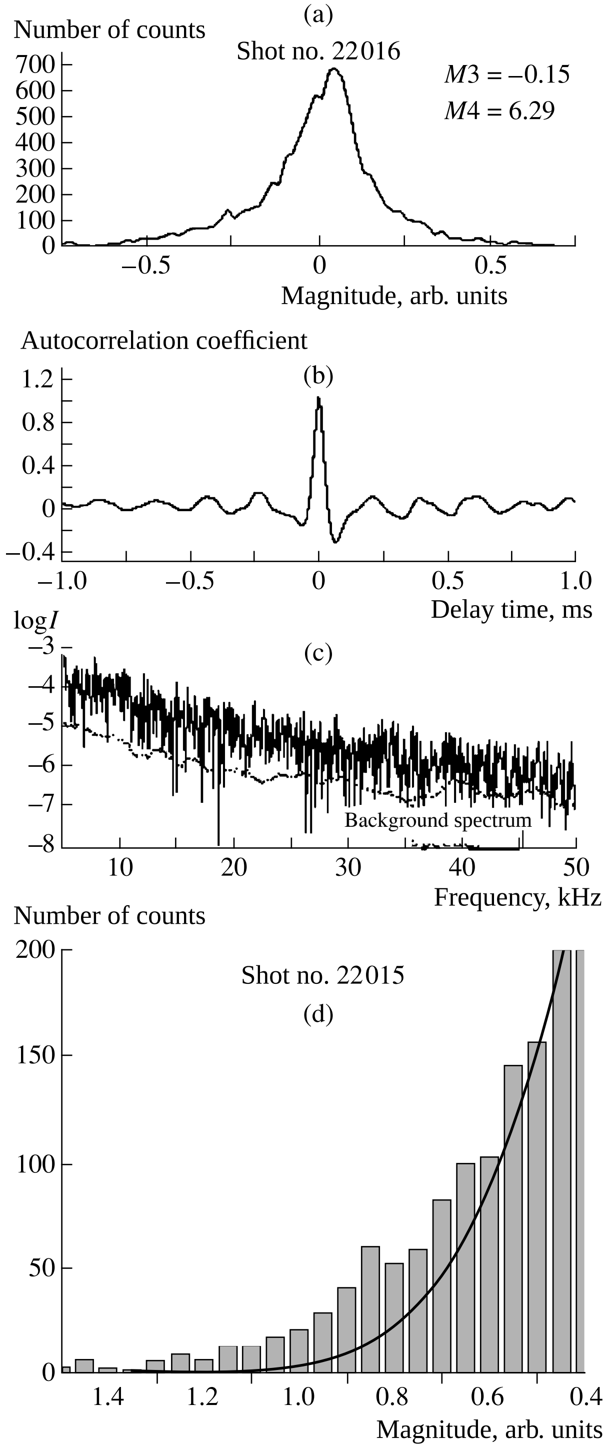

Fig. 9. (a) PDF, (b) ACF, and (c) Fourier spectrum of signals scattered by fluctuations in the high-temperature LHD plasma and (d) the PDF of rare events for the same signals.

The duration of a steady-state discharge in TJ-II attains several hundred milliseconds. Hence, under certain conditions, we could obtain stationary time samples of the fluctuation magnitudes with the total number of points larger than 10^5. Such long samples allowed us to apply R/S analysis,[8] which more definitely shows the presence of a long-living component in the signal than the ACF or the histogram tails. With this method, we estimated the Herst parameter H [31], which characterizes the dependence between distant events. Different processes are characterized by different values of the Herst parameter: $H = 1$ for a regular process, $H = 0.5$ for a Gaussian process, $H > 0.5$ for a self-similar process with a positive correlation, and $H < 0.5$ for a self-similar process with a negative correlation. Previously, we succeeded in distinguishing self-similar (hyperbolic) tails in the PDF of the fluctuation magnitudes for the structural ion-acoustic turbulence [9]. Figure 14 shows the logarithm of the increments in the fluctuation magnitudes versus the logarithm of the delay time (for comparison, the same line is drawn for a Gaussian process). The Herst parameter is equal to $H = 0.76$, which unambiguously indicates that the time samples of the magnitudes of plasma density fluctuations are described by a self-similar process with a positive correlation. Hence, the plasma density fluctuations in TJ-II are described by a non-Gaussian process, as is the case of density fluctuations in the central regions of L-2M and LHD. Consequently, the tails of the PDF and ACF of the fluctuation magnitudes in TJ-II exist but are not resolved in the experiment.

4. DISCUSSION OF RESULTS

When studying the fluctuations in plasma experiments, a question usually arises as to the source of these fluctuations, i.e., the nature of plasma instability. If the initial instability totally determines the fluctuations, then the knowledge of its parameters allows one to adequately describe the plasma process. A different situation occurs when studying the structural strong turbulence in a plasma. In the formation of a steady-state structural strong turbulence, not only one or several initial instabilities but also many additional nonlinear processes are involved. These nonlinear processes form stochastic plasma structures, govern the nonlinear interaction between structures of the same type and the mutual action of structures of different types, govern the processes of the nonlinear decay and aperiodic suppression of fluctuations, etc. Knowledge of the linear

---

[8] For a time sample of a random signal of length n, $X \equiv \{X_i: t = 1, 2, \ldots, n\}$ with the average $\bar{X}(n)$ and the mean square value $S^2(n)$, the ratio R/S is defined as

$$\frac{R(n)}{S(n)} = \frac{\max(0, W_1, W_2, \ldots, W_n) - \min(0, W_1, W_2, \ldots, W_n)}{\sqrt{S^2(n)}},$$

where $W_k = X_1 + X_2 + \ldots + X_k - k\bar{X}(n)$. The ratio R/S is the range of accumulation divided by the standard deviation of the increments for a certain time interval $(s', s' + t)$, where s' is an arbitrary initial instant. To a first approximation, the points in a plot of the logarithm of R/S versus the logarithm of time for various time intervals are concentrated about a straight line with the slope H [31].

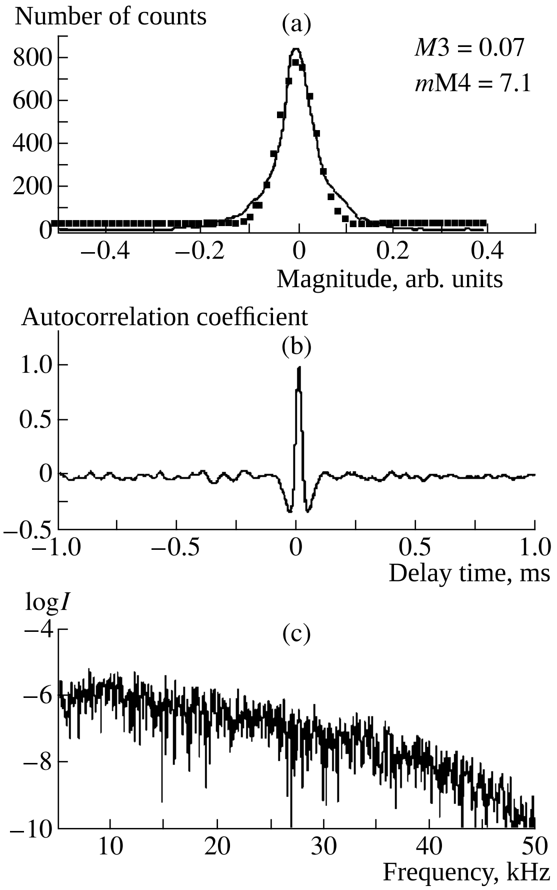

Fig. 10. (a) PDFs, (b) ACFs, and (c) Fourier spectra of the increments in signals scattered by fluctuations in the high-temperature LHD plasma.

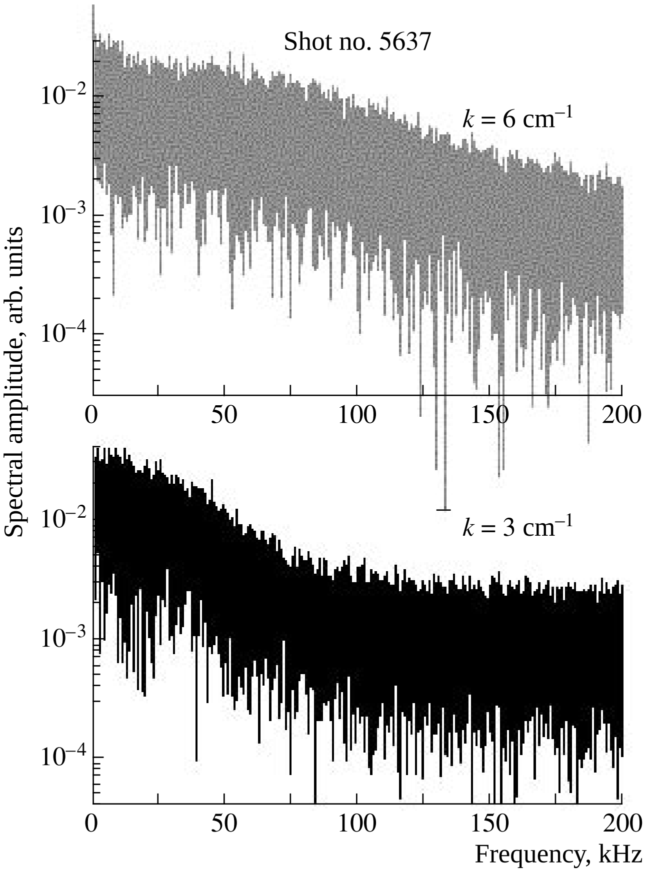

Fig. 11. Fourier spectra of the plasma density fluctuations ($r/a \sim 0.5$) in TJ-II.

mechanisms for the development of plasma oscillations is not enough to adequately describe the final turbulent steady state. The above studies of fluctuations in the central plasma regions in three stellarators by microwave scattering techniques showed that, in these experiments, we observed steady-state low-frequency plasma turbulence. The experiments on studying this steady-state turbulence are still far from being completed. Therefore, only some preliminary conclusions can be made about the linear and nonlinear plasma mechanisms forming turbulence in high-temperature plasma.

When discussing the results of the above experiments, we should first to show that the measured states of the fluctuations in a high-temperature plasma of the three devices are steady states with strong structural turbulence. Second, we should discuss linear plasma instabilities that can initiate fluctuations in the given frequency and wavenumber ranges. Finally, we should propose the possible structural or other nonlinear plasma processes that can be responsible for the formation of a stable steady state.

Let us list the factors indicating that, in the plasmas of all three devices, we observed the low-frequency steady-state plasma turbulence. In all of the experiments, we measured low-frequency fluctuations with nearly fixed wavenumbers: $k \sim 20$ cm^{-1} in L-2M, $k \sim 30$ cm^{-1} in LHD, and $k = 3$ and 6 cm^{-1} in TJ-II. In all these cases, the fluctuations had wide frequency Fourier spectra and wide wavelet spectra containing quasi-harmonics. Such Fourier and wavelet spectra are typical of a turbulent state. The characteristics of the time samples of scattered signals, namely, the ACFs with a narrow first peaks and nonzero tails, non-Gaussian PDFs, and quasi-harmonics in wavelet spectra, indicated the strong structural turbulence. The steady-state character of this turbulence was confirmed by the fact that the first four statistic moments (the average, dispersion, skewness, and kurtosis) of the fluctuation magnitudes were constant in time. Hence, in the high-temperature plasma of all three devices, we observed the steady-state strong structural plasma turbulence. Figure 15 shows the time dependences of the plasma density and the four first moments of the time sample of a signal scattered by density fluctuations with $k = 6$ cm^{-1} in the

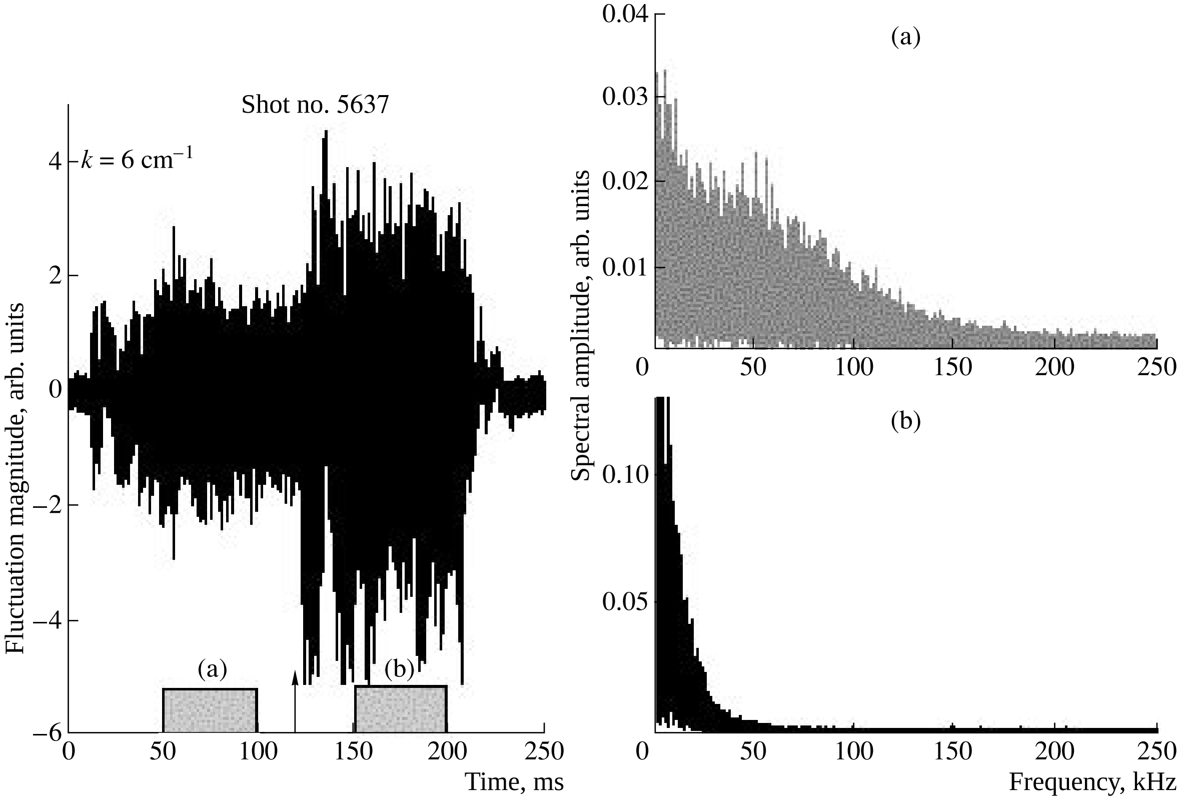

Fig. 12. Waveform and Fourier spectra of plasma density fluctuations with $k = 6$ cm^{-1} in an experiment on the propagation of a cold-nitrogen pulse. The arrow indicates the time at which the cold-nitrogen pulse reaches the measurement region ($r/a \sim 0.5$) of the 2-mm scattering diagnostics in TJ-II. The time intervals on which Fourier spectra (a) and (b) were determined are marked by shaded rectangles.

TJ-II device. It can be seen that the first four statistic moments come to a steady state as the plasma density and temperature reach their steady levels. In all of the other measurements, we also observed steady-state turbulence when the average plasma density and electron temperature reached their steady levels.

Let us now consider the initial plasma instabilities that can give rise to the oscillations in the wavenumber and frequency ranges observed in the experiments in L-2M, LHD, and TJ-II. The generation of low-frequency oscillations with frequencies up to 50 kHz (LHD), 150 kHz (L-2M), and 200 kHz (TJ-II) can be attributed to the onset of drift-dissipative instability [34] and instabilities driven by trapped particles [35]. Here, we do not consider the MHD instabilities that were observed in tokamaks [36], because in our scattering experiments, we did not perform simultaneous measurements of the MHD activity in the L-2M and LHD devices. However, such measurements were performed in the TJ-II device. In TJ-II, the sharp change in the spectra of the scattered signals and their correlation with magnetic-probe signals were only observed at certain specific magnetic field configurations with the 3/2 and 5/4 resonances (narrow spectra of magnetic-probe signals in these magnetic field configurations were also observed in the previous TJ-II experiments [37]). Since we still cannot offer an adequate explanation for these results, we do not present them in this paper. In usual configurations, the wide fluctuation spectra described above were not accompanied by MHD activity and no correlation with magnetic probe signals was observed.

The onset of drift-dissipative instability gives rise to oscillations that are characterized by different dispersion in different frequency ranges [34]:

(i) For frequencies in the interval $k_\parallel v_{Ti} < \omega < k_\parallel v_{Te}$, the dispersion relation is $\omega_1 = k_\perp v_{Te}^2/(1 + \rho_s^2 k^2)\Omega_e r_n$, where $v_s = (T_e/M)^{1/2}$, $\rho_s = v_s/\Omega_e$, and $r_n^{-1} = |d\ln n/dr|$.

(ii) For frequencies in the interval $k_\parallel v_s < \omega < k_\parallel v_{Te}$, the dispersion relation is $\omega_2 = k_\parallel^2 \Omega_e r_n/k_\perp$.

The first interval corresponds to frequencies that are much higher (because of the high temperature in the central region) than the fluctuation frequencies observed in the experiments. For the second frequency interval, the instability condition reads as $d\ln T_e/d\ln n > 2$. Figure 16 shows the plasma density and electron temperature profiles in L-2M, LHD, and TJ-II for shots in which the scattering experiments were conducted. For

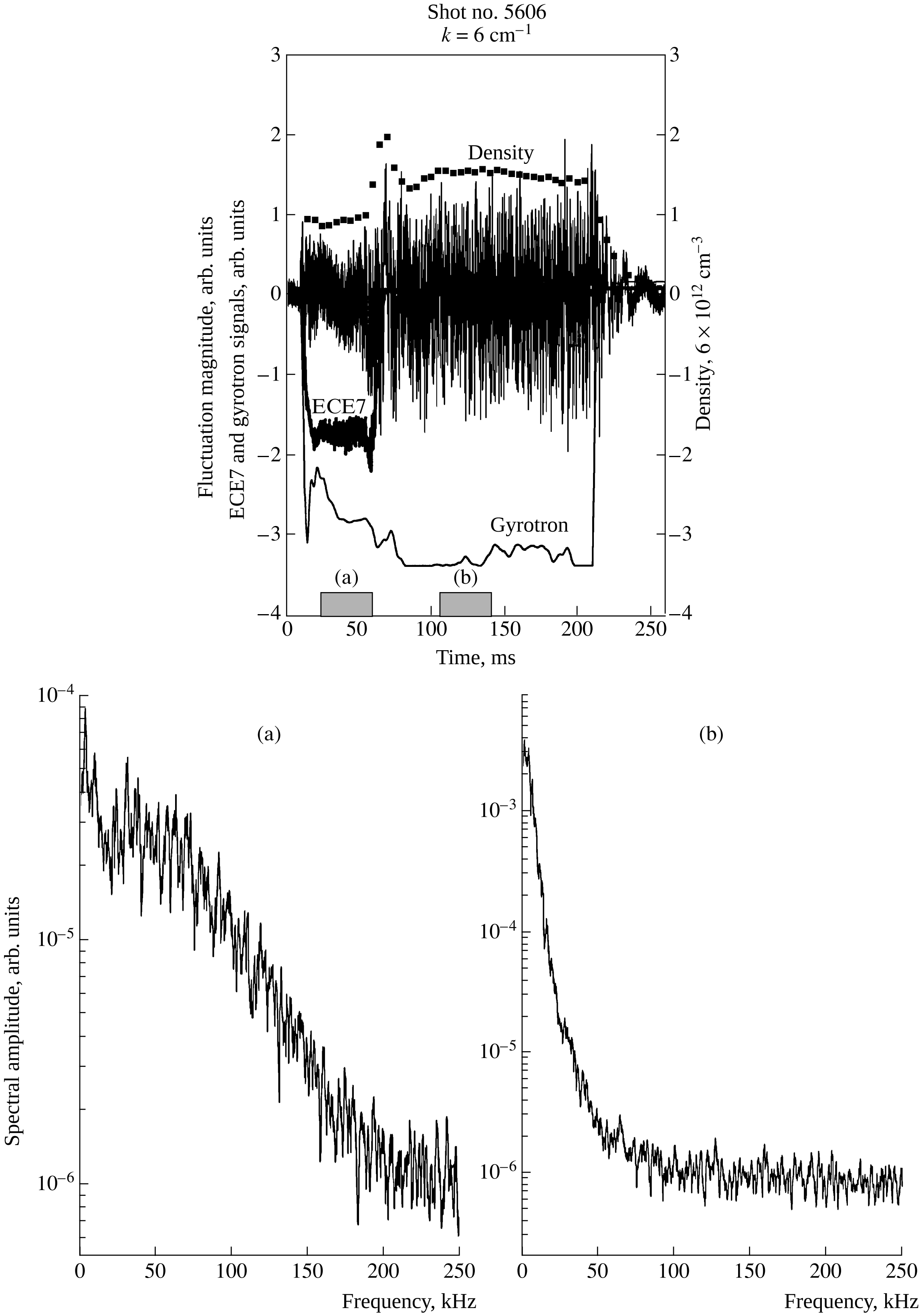

Fig. 13. Variations in the plasma density, fluctuation signal, gyrotron and ECE7 signals, and the spectra of density fluctuations at the middle of the plasma radius after a minor disruption in TJ-II. The time intervals on which Fourier spectra (a) and (b) were determined are marked by shaded rectangles.

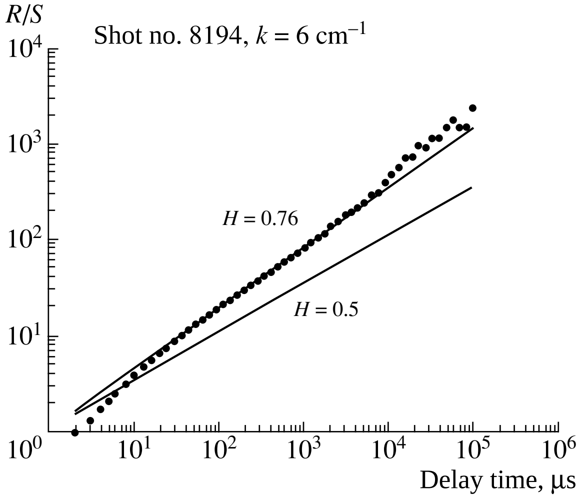

Fig. 14. *R*/*S* coefficient vs. time delay for density fluctuations with $k = 6$ cm^{-1} in TJ-II. The total number of points in the time sample is ~100 000.

all of these shots, the temperature profile is narrower than the density profile and the shapes of the profiles at different devices are similar to each other, which is typical of devices of this kind. Figure 17 illustrates the model profiles of the plasma density and electron temperature and the condition for the onset of drift-dissipative instability. In calculations, the temperature profile was approximated by a second-order parabola and the density profile was approximated by a sixth-order parabola. For the second frequency interval, the condition for the onset of instability is easily satisfied in the plasma core up to $r/a \leq 0.7$. Thus, the drift-dissipative instability can result in low-frequency plasma oscillations in the observation regions in all three of the devices; however, the characteristic frequencies, which are determined by the plasma parameters of each device, will be different.

In the plasma region that was studied using the 2-mm scattering technique in TJ-II ($r/a \approx 0.4$–0.6), one

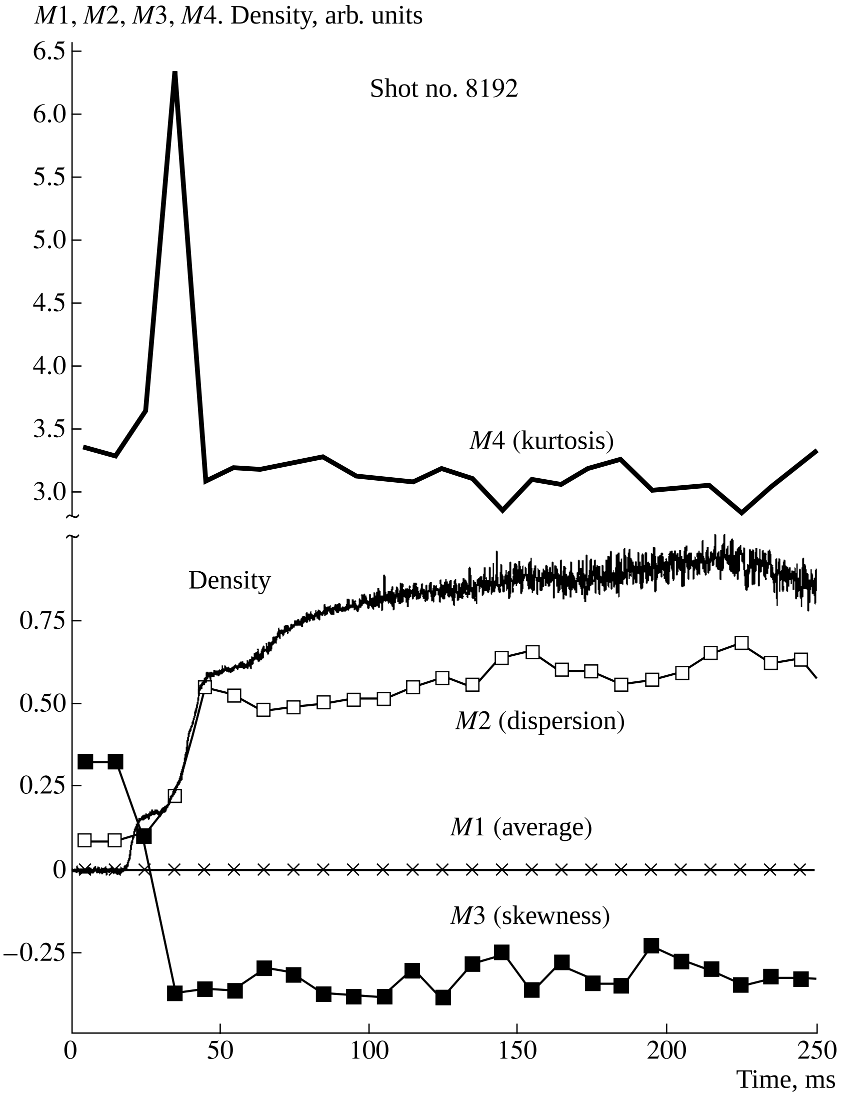

Fig. 15. Time variations in the plasma density and four first statistical moments (the average, dispersion, skewness, and kurtosis) for a time sample of the magnitudes of density fluctuations with $k = 6$ cm^{-1} in TJ-II.

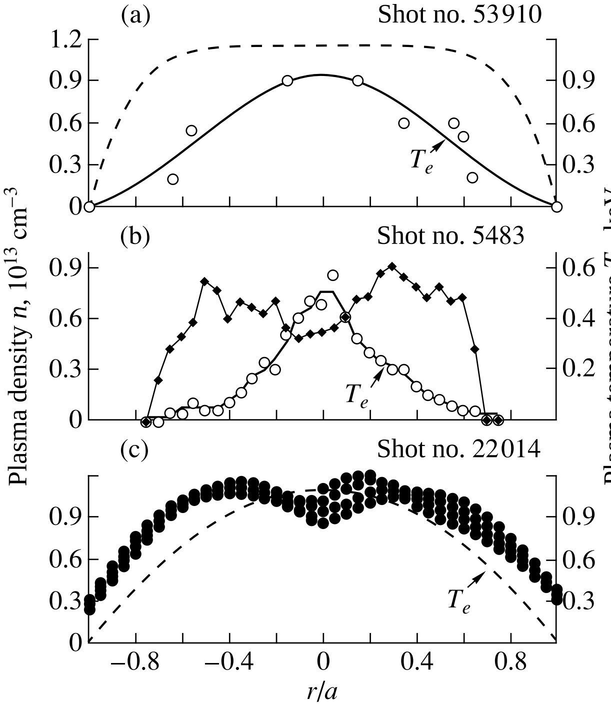

Fig. 16. Density and temperature profiles in (a) L2-M, (b) TJ-II, and (c) LHD in the scattering experiments. The symbols and solid lines show the measurement results and their splines, and the dashed lines correspond to theoretical estimates.

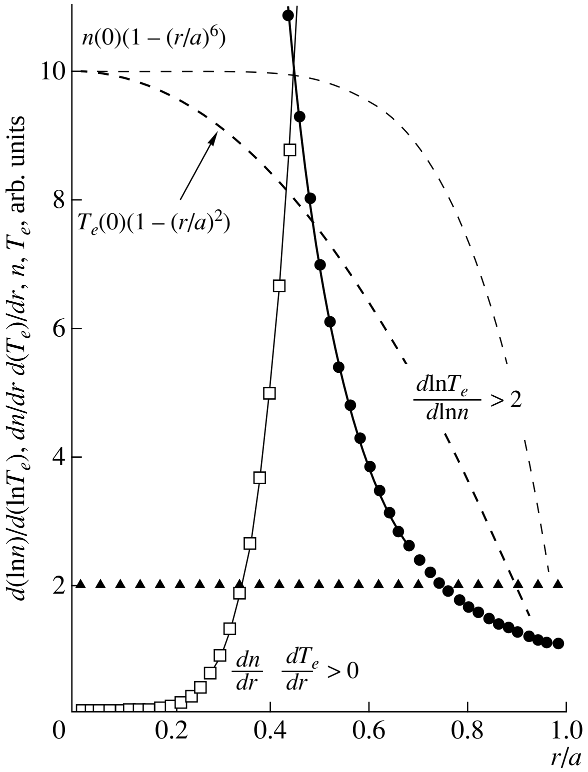

Fig. 17. Regions of the possible development of the drift-dissipative instability and the instability driven by trapped electrons in the L-2M, LHD, and TJ-II devices in the scattering experiments.

could expect the excitation of oscillations in the frequency range 10–100 kHz.[9] The drift-dissipative instability, which is caused by the difference between the density and temperature gradients in the plasma, can give rise to oscillations in TJ-II. In this case, the characteristic oscillation frequency should decrease after plasma cooling, as was actually observed in the experiment. On the other hand, the typical inversely proportional dependence of the frequency on the wavenumber did not take place in the TJ-II experiment.

In the gyrotron-scattering region in the L-2M stellarator ($r/a \approx 0.3$), oscillations may be excited in the frequency range 10–30 kHz. Hence, only very low-frequency oscillations in L-2M can be associated with drift-dissipative instability.

The onset of drift-dissipative instability in the central region of the LHD device ($r/a \approx 0.2$) gives rise to oscillations with frequencies of about 1 kHz. It should be recalled that above we considered the excitation of oscillations immediately in the observation region. However, we may suggest that higher frequency oscillations excited far from the center (for example, in LHD, 10-kHz oscillations caused by this instability arise at $r/a \approx 0.4$) can propagate into the central region.

The instability driven by trapped electrons [35] can appear only in the region where $\frac{dn}{dr}\frac{dT_e}{dr} > 0$. The conditions for the onset of this instability are illustrated in Fig. 17. It can be seen that, for a flat plasma density profile and parabolic temperature profile, plasma oscillations can arise at a distance $r/a \geq 0.25$ from the center. If the plasma density profile has a minimum in the center (Fig. 16), the instability driven by trapped electrons cannot develop. Previously, it was shown that this instability could give rise to oscillations in the L-2M [24] and ATF [25] plasmas. The oscillations are excited in the frequency range $\omega_2 < \nu_e/\varepsilon_h$, where ν_e is the electron–ion collision frequency and ε_h is a small parameter defined as a function of the helical components of the magnetic field (for tokamaks, this parameter is equal to $\varepsilon_h \approx 0.2$, and for stellarators, it depends on the minor radius and varies in the range $\varepsilon_h \approx 0.1$–$0.3$). For all three devices, these frequencies do not exceed 30 kHz. In TJ-II, the instability driven by trapped electrons can give rise to fluctuations at middle radii. In L-2M and LHD, this instability also leads to the excitation of oscillations at middle radii; however, for these oscillations to penetrate into the measurement region (the central

---

[9] The characteristic frequencies were estimated assuming $k_{\parallel} \approx 5 \times 10^{-2}$ cm^{-1} for the L-2M and TJ-II devices and $k_{\parallel} \approx 10^{-2}$ cm^{-1} for LHD.

plasma region), there should exist a certain mechanism for their propagation.

Thus, the experimental results, namely, ACFs with nonzero tails, wavelet spectra with quasi-harmonics, and non-Gaussian PDFs of the fluctuation magnitudes, indicate the possibility of the existence of stochastic plasma structures in a high-temperature plasma. The subject of our further studies will be to find out what these structures are; what their nature is; and how close they are to drift vortices, solitons (plasma density cavities with trapped high-frequency oscillations), or other nonlinear structures.

5. CONCLUSIONS

The results of the first scattering experiments in the L-2M, LHD, and TJ-II stellarators can be formulated as follows:

(i) Steady-state strong structural plasma turbulence was observed in the high-temperature plasma of all three devices.

(ii) At least two plasma instabilities—the drift-dissipative instability and the instability driven by trapped electrons—can give rise to fluctuations.

(iii) Stochastic plasma structures can exist in the high-temperature plasma of these devices.

As one of the possible scenarios of the development of plasma turbulence, we can propose a scenario similar to the formation of the steady-state low-frequency structural turbulence [5, 8]. Plasma oscillations are excited due to linear instabilities; after these oscillations reach a certain threshold amplitude, the processes pass into the nonlinear stage and nonlinear stochastic structures form. Then, nonlinear interaction arises among the structures of the same type (coalescence and decay) or among the structures of different types. The characteristic times of these processes are longer than the inverse linear growth rates. When describing this interaction, it is necessary to take into account all of the accompanying processes: the drift of the structures from the region where they were formed, linear decay, the suppression of instability because of the change in the local parameters (e.g., local heating), etc. With a continuous inflow of energy into an open system,[10] a universal state with strong structural turbulence is established in it, irrespective of the type of linear instability. It was demonstrated more than once that, in a low-temperature plasma, the characteristics of the strong low-frequency structural turbulence are independent of the type of initial instability and even are independent of the type of plasma device. For these steady states to occur, it is necessary and sufficient that the oscillation amplitudes be sufficiently large, nonlinear processes come into play, and stochastic plasma structures arise. In this case, random plasma processes are, as a rule, no longer described by a Gaussian distribution. The probabilities of both rare events with large amplitudes (in comparison with the mean fluctuation amplitude) and rare events with superfast growth or damping (in comparison with the linear growth or damping rates) increase.

ACKNOWLEDGMENTS

This work was supported in part by the Russian Foundation for Basic Research (project nos. 00-02-17507 and 01-02-16527), the LIME Program (Japan), and the Russian Federal Program "Government Support of the Scientific Schools" (project no. 00-15-96676).

REFERENCES

1. N. Ohyabu, K. Narihara, H. Funaba, *et al.*, Phys. Rev. Lett. **84**, 103 (2000).
2. G. M. Batanov, O. I. Fedianin, N. K. Kharchev, *et al.*, Plasma Phys. Controlled Fusion **40**, 1241 (1998).
3. J. W. Connor, P. Burraff, J. Cordey, *et al.*, Plasma Phys. Controlled Fusion **41**, 693 (1999).
4. S. I. Lashkul, V. N. Budnikov, E. O. Vekshina, *et al.*, Fiz. Plazmy **27**, 1059 (2001) [Plasma Phys. Rep. **27**, 1001 (2001)].
5. N. K. Kharchev, K. A. Sarksyan, and N. N. Skvortsova, J. Math. Sci. **106**, 2691 (2001).
6. G. G. Malinetskiĭ and A. B. Potapov, *Contemporary Problems of Nonlinear Dynamics* (Editoral URSS, Moscow, 2000).
7. G. M. Batanov, A. E. Petrov, K. A. Sarksyan, *et al.*, Pis'ma Zh. Éksp. Teor. Fiz. **67**, 634 (1998) [JETP Lett. **67**, 662 (1998)].
8. K. A. Sarksyan, N. N. Skvortsova, N. K. Kharchev, and B. F. Milligen, Fiz. Plazmy **25**, 346 (1999) [Plasma Phys. Rep. **25**, 312 (1999)].
9. N. N. Skvortsova, K. A. Sarksyan, and N. K. Kharchev, Pis'ma Zh. Éksp. Teor. Fiz. **70**, 203 (1999) [JETP Lett. **70**, 201 (1999)].
10. G. M. Batanov, V. E. Bening, V. Yu. Korolev, *et al.*, Pis'ma Zh. Éksp. Teor. Fiz. **73**, 143 (2001) [JETP Lett. **73**, 126 (2001)].
11. V. V. Alikaev, A. A. Borshchegovskiĭ, V. A. Vershkov, *et al.*, Fiz. Plazmy **26**, 979 (2000) [Plasma Phys. Rep. **26**, 917 (2000)].
12. V. V. Bulanin, S. V. Lebedev, L. S. Levin, and V. S. Roĭtershtein, Fiz. Plasmy **26**, 867 (2000) [Plasma Phys. Rep. **26**, 813 (2000)].
13. E. Z. Gusakov and A. Yu. Popov, in *Proceedings of XXIX Conference on Plasma Physics and Controlled Nuclear Fusion, Zvenigorod, 2002*, http://www.fpl.gpi.ru/Zvenigorod/XXIX/Zven_XXIX.html.
14. K. M. Novik and A. D. Pilia, Plasma Phys. Controlled Fusion **35**, 357 (1993).
15. A. G. Zhukovskiĭ, *Fluctuations of Plasma Density* (Énergoatomizdat, Moscow, 1993).
16. K. A. Sarksyan and A. E. Petrov, *Microwave Scattering Technology and Methods for Determining the Parame-*

---

[10] Here, the term "open system" is used in a thermodynamical sense.

ters of Oscillation Processes in Plasma, http://www.plasmaiofan.ru/edu/lec4.htm.

17. D. K. Akulina, G. M. Batanov, M. S. Berezhetskiĭ, *et al.*, Fiz. Plazmy **26**, 3 (2000) [Plasma Phys. Rep. **26**, 1 (2000)].
18. G. M. Batanov, K. A. Sarksyan, N. K. Kharchev, *et al.*, Pis'ma Zh. Éksp. Teor. Fiz. **72**, 250 (2000) [JETP Lett. **72**, 174 (2000)].
19. V. V. Abrakov, D. K. Akulina, E. D. Andryukhina, *et al.*, Nucl. Fusion **37**, 233 (1997).
20. O. Motojima, H. Yamada, A. Komori, *et al.*, Phys. Plasmas **6**, 1843 (1999).
21. C. Alejaldre, J. Alonco, I. Almoguera, *et al.*, Plasma Phys. Controlled Fusion **41**, 109 (1999).
22. E. V. Suvorov and A. A. Fraĭman, Fiz. Plazmy **6**, 1161 (1980) [Sov. J. Plasma Phys. **6**, 639 (1980)].
23. S. Kubo, K. Ohkubo, T. Shimozuma, *et al.*, *Annual Report of Nagoya Institute for Fusion Studies for 1999–2000* (NIFS, Nagoya, 2000), p. 34.
24. G. M. Batanov, K. M. Likin, K. A. Sarksyan, and M. G. Shats, Fiz. Plazmy **19**, 1199 (1993) [Plasma Phys. Rep. **19**, 628 (1993)].
25. M. G. Shats, J. H. Harris, K. M. Likin, *et al.*, Phys. Plasmas **2**, 398 (1995).
26. K. M. Likin, J. Sanchez, B. Branas, and K. A. Sarksian, in *Proceedings of X International Conference on Stellarators, Madrid, 1995*, p. 216.
27. W. H. Press, B. P. Flannery, S. A. Teukolsky, and W. T. Vetterling, *Numerical Recipies in Pascal* (Cambridge Univ. Press, New York, 1989).
28. D. E. Newland, *An Introduction to Random Vibrations: Spectral and Wavelet Analysis* (Longman Scientific & Technical, New York, 1993).
29. N. M. Astaf'eva, Usp. Fiz. Nauk **166** (11), 1145 (1996) [Phys. Usp. **39**, 1085 (1996)].
30. B. Ph. van Milligen, E. Sachez, T. Estrada, *et al.*, Phys. Plasmas **2**, 3017 (1995).
31. F. Hampel, E. Ronchetti, P. Rousseuw, and W. Stahel, *Robust Statistics. The Approach Based on Influence Functions* (Wiley, New York, 1986; Mir, Moscow, 1989).
32. G. M. Batanov, V. E. Bening, V. Yu. Korolev, *et al.*, Fiz. Plazmy **28**, 128 (2002) [Plasma Phys. Rep. **28**, 111 (2002)].
33. B. Ph. van Milligen, E. de la Luna, F. L. Tabares, *et al.*, in *Proceedings of the 13th International Stellarator Workshop, Canberra, 2002*, Paper OIII:2; Nucl. Fusion **42**, 787 (2002).
34. A. F. Alexandrov, L. S. Bogdankevich, and A. A. Rukhadze, *Principles of Plasma Electrodynamics* (Vysshaya Shkola, Moscow, 1978; Springer-Verlag, Berlin, 1984).
35. B. B. Kadomtsev and O. P. Pogutse, Dokl. Akad. Nauk SSSR **186**, 553 (1969) [Sov. Phys. Dokl. **14**, 470 (1969)].
36. Yu. Chanhuan, D. L. Brower, Zhao Shujin, *et al.*, Nucl. Fusion **32**, 15 (1992).
37. I. Garcia-Cortes, E. de la Luna, F. Castejon, *et al.*, Nucl. Fusion **40**, 1867 (2000).

Translated by N.F. Larionova

Plasma Physics Reports, Vol. 29, No. 5, 2003, pp. 380–390. Translated from Fizika Plazmy, Vol. 29, No. 5, 2003, pp. 413–423.
Original Russian Text Copyright © 2003 by Gonchar, A. Chechkin, Sorokovoĭ, V. Chechkin, Grigor'eva, Volkov.

TURBULENCE AND CHAOS

Stable Lévy Distributions of the Density and Potential Fluctuations in the Edge Plasma of the U-3M Torsatron

V. Yu. Gonchar, A. V. Chechkin, E. L. Sorokovoĭ, V. V. Chechkin, L. I. Grigor'eva, and E. D. Volkov

National Science Center Kharkov Institute of Physics and Technology,
ul. Akademicheskaya 1, Kharkov, 61108 Ukraine

Received August 29, 2002; in final form, November 14, 2002

Abstract—A study is presented of the distribution functions of the fluctuations of the ion saturation current and floating potential measured by Langmuir probes in the edge plasma of the U-3M torsatron. It is shown that these distribution functions may be classified as stable Lévy distributions. Using the percentile method, stable-distribution parameters, namely, the Lévy index and the scale factor for different probe positions, are estimated. These parameters are quantitative characteristics of the intensity and intermittency of turbulence in the edge plasma of the torsatron. © *2003 MAIK "Nauka/Interperiodica".*

1. INTRODUCTION

It is well known that edge-plasma turbulence, which is characterized by an anomalously high level of fluctuations of the charged particle density and electrical field, plays a decisive role in the generation of anomalous particle and heat fluxes from the plasma confinement region in various types of closed magnetic confinement systems (see, e.g., [1, 2] and the references cited therein). This was confirmed by experiments carried out in the Uragan-3M (U-3M) stellarator–torsatron [3, 4]. In experimental investigations, much attention is paid to the analysis of the statistical properties of fluctuations. These investigations are important for constructing adequate theoretical models of turbulence and anomalous transport. Thus, in the closing procedures used in the plasma turbulence theory, it is usually assumed that the statistical properties of the fluctuation processes are close to the features of a Gaussian random process. When deriving the turbulence equations, this assumption permits one to express the odd fluctuation moments through the higher order even moments, which then split into binary moments according to the splitting rule for Gaussian random processes (see, e.g., review [5]). In particular, this assumption implies that the probability density functions (PDFs) of the fluctuation magnitudes have asymptotics that decrease rapidly with increasing fluctuation magnitude. Qualitatively, this means that large fluctuation magnitudes (e.g., as large as several standard deviations) are very rare. However, in experiments carried out in different devices, density and potential fluctuations with an "explosive" (i.e., containing sharp spikes) temporal structure were observed in the edge plasma [6–9]. Such a behavior of random signals is a consequence of the plasma turbulence intermittency. Because of the presence of spikes, the PDF of the fluctuations may differ greatly from a Gaussian process. This feature is clearly shown in the realizations of the local radial particle flux [2, 9].

To characterize non-Gaussian properties of the PDF, one traditionally uses the third and fourth moments of the PDF, i.e., the skewness and kurtosis [10]. The kurtosis is often regarded as a measure of the intermittency [5]. More detailed information about the PDF is also of particular interest because it allows the distribution to be assigned to a particular class of the probability laws widely used in various applications. A detailed statistical analysis of the characteristics of turbulent particle fluxes was performed in [2] based on the fluctuation measurements in the plasma of the L-2M stellarator and the TAU-1 model device. The authors of [2] arrived at the conclusion that the PDF of the local flux increments can be described by the scale mixtures of Gaussian laws. In particular, in the case of drift turbulence, the PDF of the increments is described by a Laplacian distribution.

In this paper, we study the PDFs of the fluctuations of the ion saturation current (ISC) and floating potential (FP) measured by Langmuir probes in the edge plasma of the U-3M torsatron. As in studying electrostatic turbulence in the edge plasmas of many other closed magnetic confinement systems (see, e.g., [11]), it was assumed that the contribution of the electron temperature fluctuations to the ISC and FP fluctuations is negligible and these fluctuations were considered to be proportional to the plasma density and potential fluctuations, respectively. In the context of the present paper, this assumption is not of fundamental importance. The analysis performed shows that the recorded fluctuations are distributed according to stable Lévy laws. An important characteristic feature of these distributions is the existence of nonexponential, slowly decreasing power-law asymptotics. In our opinion, these observations are of interest for both experimentally studying the fluctuation processes in other devices and constructing new theoretical models of plasma turbulence and anomalous transport.

2. STABLE DISTRIBUTIONS AND RANDOM LÉVY MOTION. CONCISE INFORMATION

Stable probability distributions, the theory of which was founded by the French mathematician P. Lévy [12], are a remarkable class of the probability laws. The importance of these distributions stems from the limiting theorems formulated and proved in the 1930s in the works by Lévy, A.Ya. Khinchin, B.V. Gnedenko, and W. Doeblin (see, e.g., [13]). According to these theorems, stable distributions (and only they) are limiting for the distributions of the sums of independent, uniformly distributed random variables. This means that these distributions (like Gaussian distributions) take place when the evolution of a physical system and/or the result of a random experiment are determined by the sum of a large number of random factors. That is why stable Lévy distributions serve as mathematical models for a wide class of measured random processes that do not obey Gaussian statistics. An important feature of stable distributions is the existence of power-law asymptotics that decrease as $|x|^{-1-\alpha}$ at $x \longrightarrow \infty$, where α is the Lévy index ($0 < \alpha < 2$). It follows from this that the higher order moments with the order $q \geq \alpha$ (in particular, dispersion) diverge.[1] For this reason, the results from processing experimental data may be sensitive to the sample size. This circumstance means that care should be taken in processing experimental data [15–17]. One of the methods allowing one to estimate the parameters of stable distributions when working with small samples is described in Section 4.

A classical example of a stable distribution, which was known in physics before the works by Lévy, is the Holtzmark distribution [18, 19]. A number of allied examples were given in the monograph [20], which was for a long time the only monograph in the world literature devoted to stable laws. Various examples from physics, financial mathematics, biology, and geology were collected together in the recent monograph [21].

The limiting theorems of the probability theory and the remarkable properties of stable probability distributions form a mathematical basis of the Lévy motion—a type of random walk, which is the natural generalization of the Brownian motion. In physics, interest in the Lévy motion is caused by the problems of anomalous diffusion, in which the mean square displacement increases not as a linear function of time t (as is the case of the usual Brownian motion), but either more slowly (subdiffusion) or more rapidly (superdiffusion) than t. The term "Lévy motion in space" or "Lévy flights in space" is applied to superdiffusion phenomena, and the term "Lévy flights in time" is applied to subdiffusion phenomena. In fact, this terminology is appropriate as a very simple qualitative picture of anomalous diffusion (see [22]). At present, it is clear that anomalous random processes and anomalous diffusion phenomena are often met in nature (see the many examples in [22–26]). The law of subdiffusion particle walk in a random magnetic field was deduced in [27]. Numerical simulations of the anomalous transport of magnetic field lines in a turbulent magnetic field demonstrate sub- or superdiffusion at low levels of the field fluctuations and Gaussian diffusion at high fluctuation levels [28, 29]. Numerical simulations of the diffusion of test charge particles moving in turbulent electrostatic fields that are solutions to the Hasegava–Mima equation demonstrate the anomalous time-dependence of the displacement squared [30]. These problems require constructing models of Lévy motion and developing various efficient methods for estimating the statistical characteristics from the experimental data. Two important types of Lévy motion (usual motion and fractional motion) were studied in detail in [31]. On the other hand, the kinetic description of the Lévy motion requires the application of fractional derivatives, which have now become actively studied (see [26, 32, 33] and the references cited therein). A fractional Fokker–Planck equation containing fractional time and space derivatives was proposed in [34] as a phenomenological equation for the PDF of density fluctuations in the DIII-D tokamak. A fractional Fokker–Planck kinetic equation containing the fractional velocity derivative was proposed in [35] for describing the relaxation, non-Maxwellian steady states, and superdiffusion of plasma in a magnetic field.

3. EXPERIMENTAL CONDITIONS AND PRELIMINARY DATA ANALYSIS

The U-3M device is a three-pole ($l = 3$) torsatron with nine periods ($m = 9$) of the helical magnetic field. The major radius of the torus is $R_0 = 1$ m, the mean plasma radius is $\bar{a} \approx 0.12$ m, and the internal radius of the casings of the helical magnetic field coils is $a_c = 0.19$ m. The entire magnetic system, including the helical coils and the vertical magnetic field coils, is placed into a vacuum chamber 5 m in diameter. Fluctuation studies were performed at a toroidal magnetic field of $B_\phi = 7.2$ kOe. The rotational transform on the boundary of the plasma column was $\iota(\bar{a})/2\pi \approx 0.4$. A hydrogen plasma was produced and heated by an RF field in the regime of the multimode Alfvén resonance [36]. The duration of the heating RF pulse at a frequency of 8.8 MHz was 25 ms. With continuous hydrogen injection into the vacuum chamber, the quasi-steady plasma

---

[1] Note that, even long before Lévy [starting with works by V. Pareto (1897)], distributions with power-law asymptotics (Pareto distributions) had been widely used in the problems of economical statistics (see [14]). In contrast to stable distributions, these distributions are not limiting in terms of the limiting theorems of the probability theory.

density in the confinement volume and near its boundaries was determined by the balance between the ionization of the gas entering this relatively small volume from a much larger surrounding volume and the plasma loss from the confinement volume. In these studies, the initial hydrogen pressure (several units of 10^{-5} torr) and the RF power (~200 kW) were chosen such that the electron density averaged along the central chord was about $\bar{n}_e \simeq 2 \times 10^{18}$ m^{-3} almost throughout the entire RF pulse. The central electron temperature, which was measured by the emission intensity at the second harmonic of the electron gyrofrequency, amounted to $T_e(0) \approx 0.3$ keV. The ion temperature was measured by a mass–energy analyzer of charge-exchange neutrals; the line of sight was tangent to the minor axis of the torus. The measurements showed that the temperature of the bulk (94%) ions was $T_i \approx 0.1$ keV.

Electrostatic fluctuations in the edge plasma were detected with four movable single Langmuir probes. The collecting part of each probe was a molybdenum wire 0.5 mm in diameter and 3 mm in length. The probes were located in the vertices of a 3 × 3 mm square. One pair of the probes with the bias voltage –120 V was oriented in the poloidal direction and measured the ISC and another pair measured the FP fluctuations. Figure 1a shows the top view of helical magnetic field coils I, II, and III and the positions of the RF antenna and the poloidal section of the torus in which the probes were located. This section with coils I, II, and III; the movable Langmuir probes (LP); and the calculated boundary structure of the magnetic field in the form of a Poincaré map of the magnetic field lines are shown in Fig. 1b. The probes could be displaced as a whole along the major radius R of the torus at a distance of 1 cm above the equatorial plane. In this experiment, fluctuations were measured at radii of $110.75 \le R \le 113$ cm in four shots for each probe location.

To measure ISC and FP fluctuations, we used ten-bit analog-to-digital converters (ADC) with a sampling rate of 5 μs per a channel. The ADCs allowed us to record up to 4000 points in one channel. Special measurements showed that, at a fixed probe position near the plasma boundary, the mean values of the ISC and FP fluctuations in the quasi-steady stage of the discharge remained constant within ±2% during the recording of the fluctuation components. The spread in the mean values of the ISC and FP fluctuations from shot to shot did not exceed 10%. The steady-state character of the measured fluctuation signals was verified by the standard criteria of series and inversions [37]. A series is a sequence of points with the same sign of the deviation from the mean value. For the given confidence coefficient equal to 0.05, the confidence range of the number of series for the stationary fluctuations can be found from the tables in [37]. For the inversion criterion, the confidence coefficient was also chosen to be 0.05. The inversion criterion is more appropriate for revealing a monotonic trend than the series criterion, but it is not so efficient in finding oscillation-type trends.

Typical signals of ISC fluctuations at different probe positions R = (a) 111, (b) 112, (c) 112.5, and (d) 113 cm are shown in Fig. 2. On the top, these signals are shown on the same scale. It is seen that the fluctuation intensity decreases with increasing radius R. On the bottom, the same signals are shown on enlarged scales to highlight an essential feature in the fluctuation behavior. It can be seen that the relative magnitude of the fluctuation spikes increase as the probe is displaced outward from the plasma. In other words, the degree of the intermittency of the turbulent plasma increases.

Figure 3 presents the results of estimating the deviation of the measured PDF from a Gaussian distribution. Figures 3a and 3b show the kurtosis

$$K = \frac{\langle x^4 \rangle}{\langle x^2 \rangle^2} - 3 \qquad (1)$$

as a function of the probe position for (a) ISC and (b) FP fluctuations. Here, the angular brackets stand for the average over the sample, namely, the dispersion and the fourth-order moment. The positive values of K correspond to PDFs that have flatter asymptotics than a Gaussian distribution. The dependences presented show that the PDF of the ISC fluctuations is close to Gaussian at distances $R < 112$ cm. It is seen that, at large radii, it deviates from Gaussian, and the deviation increases with R. The PDF of the FP fluctuations deviates from Gaussian in the entire measurement region, except for maybe one point. The normal distribution criterion provides one more quantitative piece of evidence of the non-Gaussian character of fluctuations [37]. In this method, a discrete distribution $f(x_j)$ (where $x_j = -N\Delta x/2 + j\Delta x$; $j = 1, 2, \ldots, N$; and Δx is the cell size) of the experimental data is constructed and the deviation of the distribution from the normal distribution is evaluated using the sampling statistics,

$$\chi^2 = \sum_{j=1}^{N} \frac{[f(x_j) - g(x_j)]^2}{g(x_j)}, \qquad (2)$$

where $g(x_j)$ is the discrete normal (Gaussian) distribution. The region where the hypothesis about a normal (Gaussian) distribution of the experimental data is valid is determined by the fitting criterion $\chi^2 \le \chi^2_{n;\,0.05}$, where the theoretical value of $\chi^2_{n;\,0.05}$ for the given significance level equal to 0.05 is taken from tables (see Table A3 and the details of the applied method in [37]). The results of applying the normal distribution criterion are shown in Figs. 3c and 3d. The symbols show the value of χ^2 as a function of the probe position for (c) ISC and (d) FP fluctuations. It can be seen that the PDF of the ISC fluctuations is close to normal at $R < 112$ cm and deviates from normal as R increases. A characteristic feature of the FP fluctuations is the deviation from a

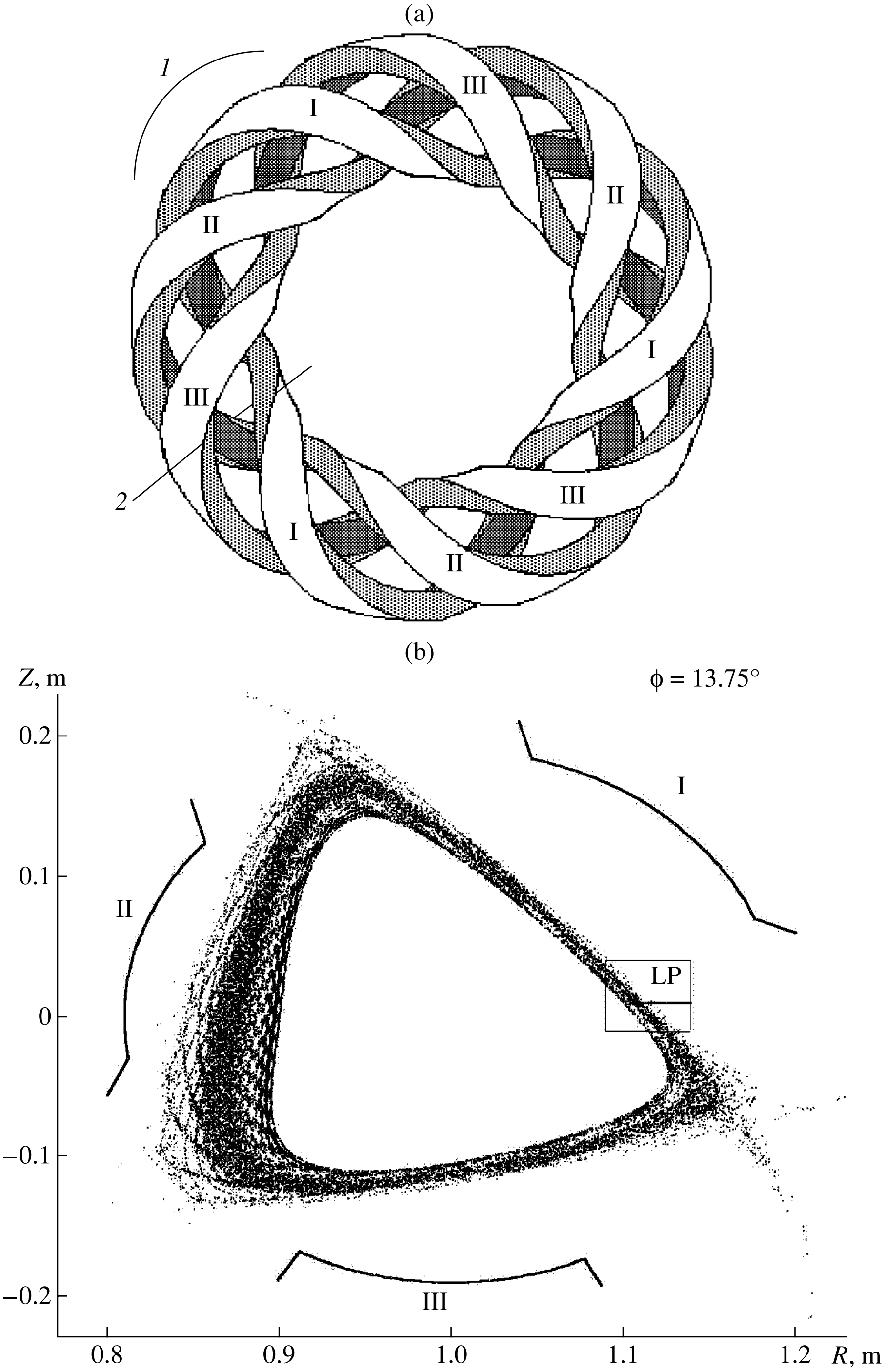

Fig. 1. (a) Top view of helical magnetic field coils I, II, and III of the U-3M torsatron and the positions of (*1*) the RF antenna and (*2*) the poloidal section of the torus in which the probes were located; (b) the calculated Poincaré map of the boundary magnetic field lines and the position of Langmuir probes (LP) in the poloidal cross section in which probe measurements were carried out. The vertical *Z*-axis is directed parallel to the major axis of the torus, and the horizontal axis is directed along the major radius *R*.

normal distribution at all values of *R*. It can easily be seen that the dependences shown in Figs. 3a and 3b are in qualitative agreement with those in Figs. 3c and 3d.

Hence, the estimations of the PDF deviation from a Gaussian distribution show that the measured fluctuations do not obey Gaussian statistics in almost the entire measurement region. Now, we pass over to a more detailed analysis of the properties of the PDFs of ISC and FP fluctuations. For this purpose, we first consider a method for determining the parameters of stable distributions from the experimental data.

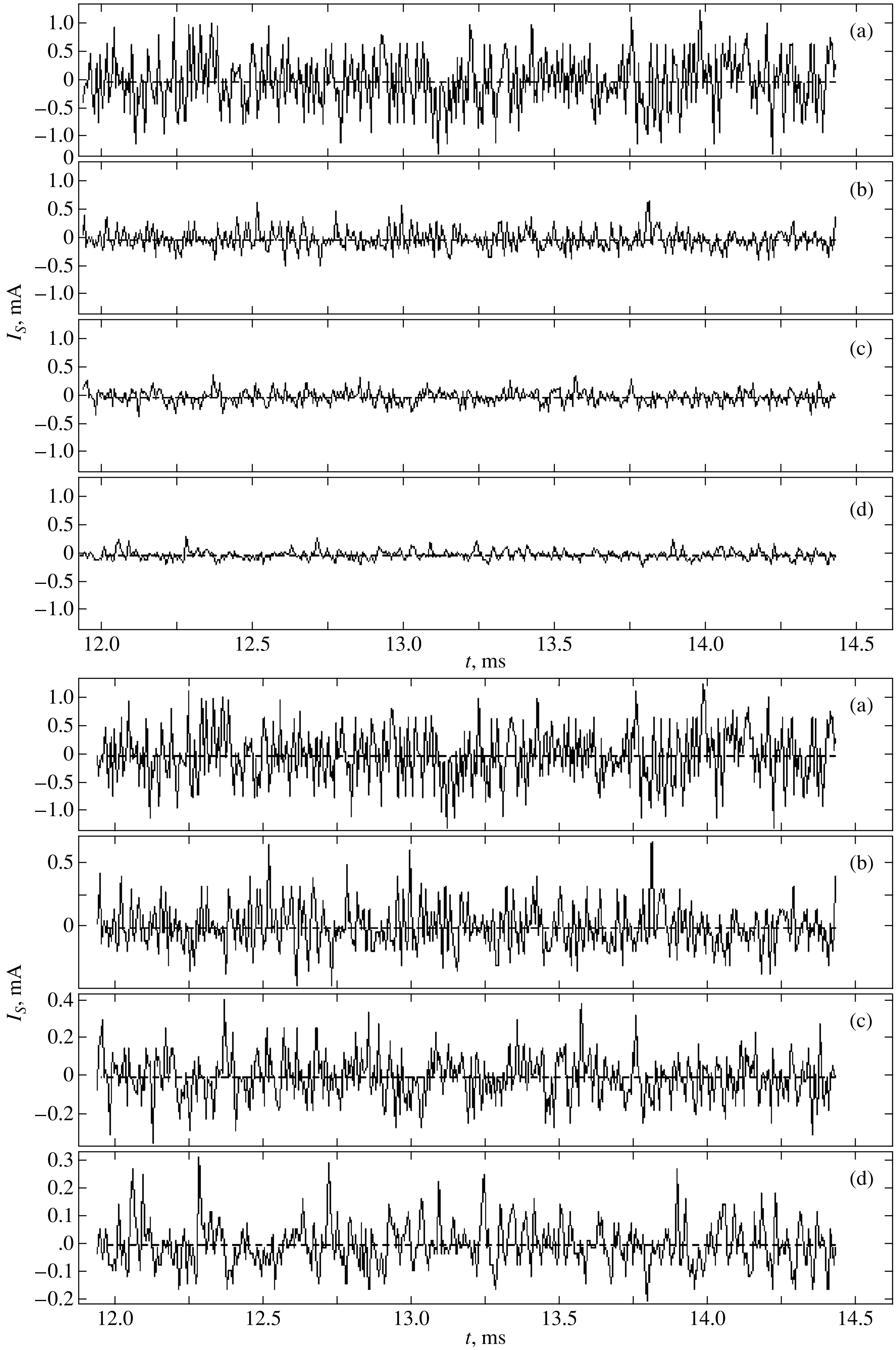

Fig. 2. Waveforms of the ISC fluctuations at R = (a) 111, (b) 112, (c) 112.5, and (d) 113 cm. On the top, the fluctuations are shown on the same scale and, on the bottom, the scale increases with R.

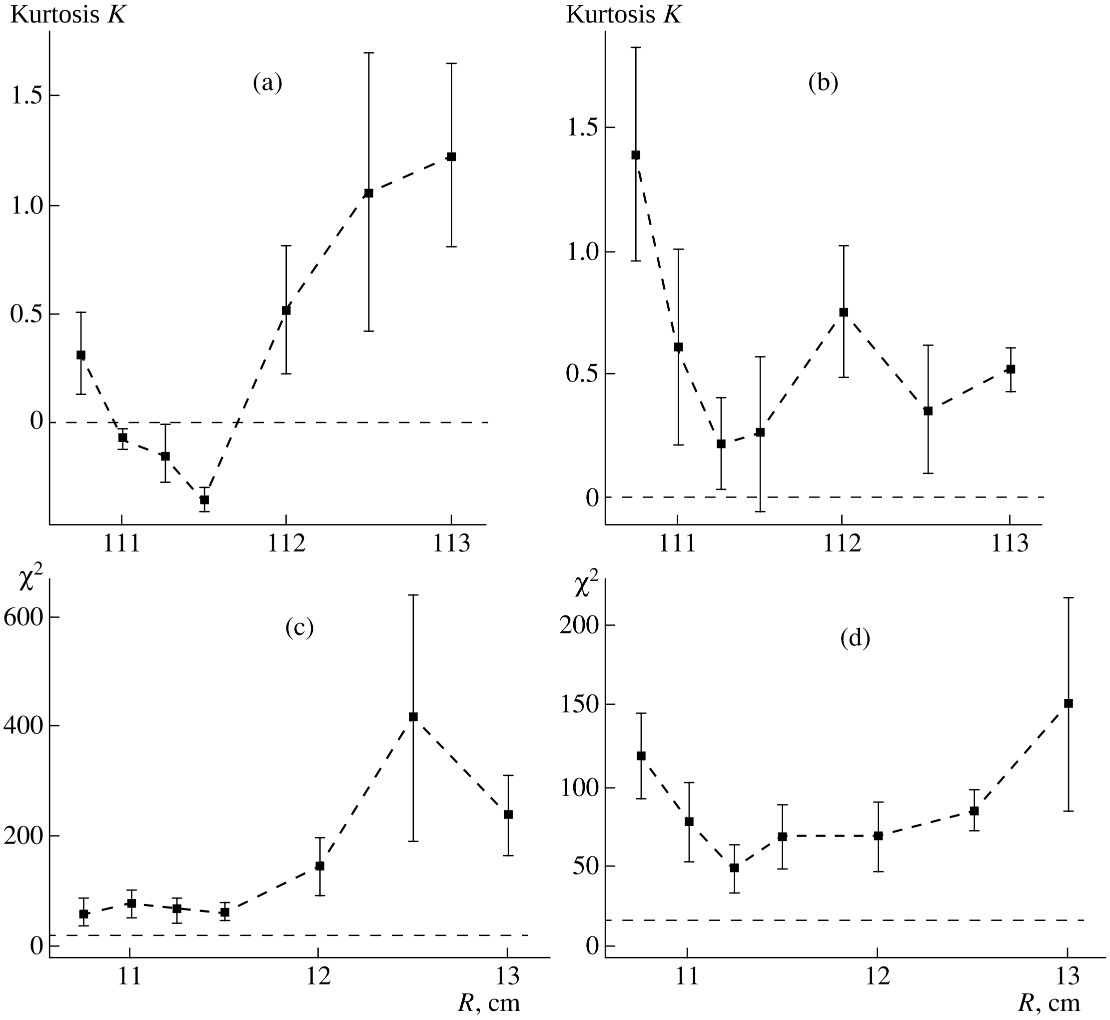

Fig. 3. (a, b) Kurtosis [see Eq. (1)] vs. radius and (c, d) the results of application of the normal-distribution criterion (χ^2 vs. radius) for the (a, c) ISC and (b, d) FP fluctuations. The horizontal dotted line in plots (c) and (d) shows the critical value of $\chi^2_{n;\,0.05}$.

4. METHOD FOR ESTIMATING THE STABLE-DISTRIBUTION PARAMETERS

Let us briefly outline the method used below to estimate the stable-distribution parameters. We restrict ourselves to the case of symmetric stable distributions, because the processes considered in this paper are quite adequately described by these distributions. The characteristic function of the symmetrical stable distribution $p_X(x; \alpha, \sigma)$ of the random variable X has the form [13, 38]

$$\hat{p}_X(k; \alpha, \sigma) = \int_{-\infty}^{\infty} dx \exp(ikx) p_X(x; \alpha, \sigma) = \exp(-\sigma^\alpha |k|^\alpha), \tag{3}$$

where $0 < \alpha \le 2$ and $\sigma > 0$ is the scale factor. The Lévy index $\alpha = 2$ corresponds to a Gaussian distribution that can be derived from Eq. (2) using the inverse Fourier transform: $p_X(x; 2, \sigma) = (4\pi\sigma^2)^{-1}\exp(-x^2/4\sigma^2)$. At $\alpha < 2$, it follows from Eq. (2) that the asymptotics are described by a power-law function: $p_X(x; \alpha, \sigma) \propto \sigma^\alpha |x|^{-1-\alpha}$ as $x \longrightarrow \pm\infty$. The physical sense of the parameters α and σ is different. The Lévy index characterizes the rate at which the PDF decreases at large values of the argument; in other words, α characterizes the magnitude of the spikes observed in the realizations. The presence of these spikes is related to the slowly decreasing power-law asymptotics of the stable distribution. The smaller the α value, the greater the amplitudes of the spikes observed in the realizations against the background noise. As for the scale factor σ, this quantity characterizes the half-width of the distribution, rather than the spike magnitude; therefore, it is a quantitative characteristic of the background against which large spikes occur. In other words, σ is a measure of the background intensity.

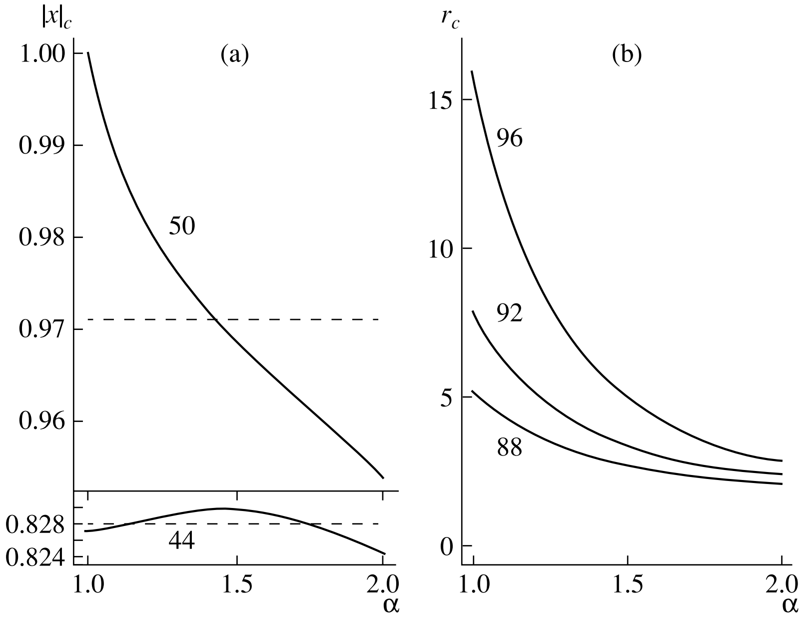

Fig. 4. (a) The $|x|_{50}$ percentile (the mode of the $p_{|X|}(x; \alpha, 1)$ distribution) and the $|x|_{44}$ percentile as functions of the Lévy index α. It is seen that the 44th percentile depends only slightly on α. This allows one to use this percentile for the normalization of data with an unknown index α. In this case, the error does not exceed 0.15%, whereas the error can reach 5% when the mode is used. (b) The function $r_c(\alpha) = |x|_c/|x|_{44}$ (c = 88, 92, 96) used to determine the index α when analyzing the experimental data.

Let us make two notes concerning stable distributions.

(i) The class of stable distributions also includes asymmetric stable distributions characterized, in addition to the parameters α and σ, by the asymmetry parameter β, which takes values from –1 to 1 [20, 21, 38]. For symmetric stable distributions, we have β = 0. For our experimental data, this parameter is close to zero and the limited sample sizes do not allow us to estimate it with a reasonable accuracy. However, numerical simulations with the help of a generator of random-number sequences that obey asymmetrical stable distributions with β in the range from –0.5 to +0.5 (see the generator description in [38, p. 46]) show that this method for determining the Lévy index α is robust even at a small distribution asymmetry.

(ii) Stable distributions that are met in practice have one more parameter, namely, the cutoff parameter $x_{\max}$, above which the power-law character of the asymptotics of a stable distribution gets broken ("truncated" stable distributions by the terminology of [39]). The parameter $x_{\max}$ is determined by the physical nature of the phenomenon under consideration. Its reliable determination from the experimental data requires very large time samples.

The method proposed by us for estimating the parameters α and σ refers to methods based on the tabulated percentiles of stable distributions [15, 40–42].

The cth percentile of a stable distribution with the density $p_X(x; \alpha, \sigma)$, where $c = 1, 2, 3, \ldots, 100$, is the quantity x_c satisfying the relationship [10]

$$\Pr\{X \le x_c\} = \int_{-\infty}^{x_c} du\, p_X(u, \alpha, \sigma) = \frac{c}{100}. \tag{4}$$

For symmetrical distributions, it is convenient to operate with the distributions of the absolute values of a random variable. In this case, the cth percentile of the distribution of the absolute values of a random variable $|x|_c$ is the $(c + 100)/2$th percentile of the symmetrical distribution of the random variable itself. We suggest using a remarkable empirical property of the 44th percentile of the distribution $p_{|X|}(x; \alpha, \sigma)$ of the absolute value of the random variable X obeying a symmetric stable distribution: the value of $|x|_{44}$ with a rather high accuracy is independent of α in the range $0 < \alpha < 2$. Variations of this percentile around a value of 0.828 (for a standard stable distribution with σ = 1) do not exceed 0.15% (Fig. 4a). This allows us to use this percentile for the normalization of data with an unknown index α and, thus, to independently estimate the parameters α and σ. This is important for small samples because it allows us to improve the estimation accuracy. Thus, the estimation method consists in the following:

(i) We determine the percentile $|x|_c$ of the distribution $p_{|X|}(x; \alpha, \sigma)$ for a given sample consisting of N random numbers X_i, where $i = 1, 2, \ldots, N$.

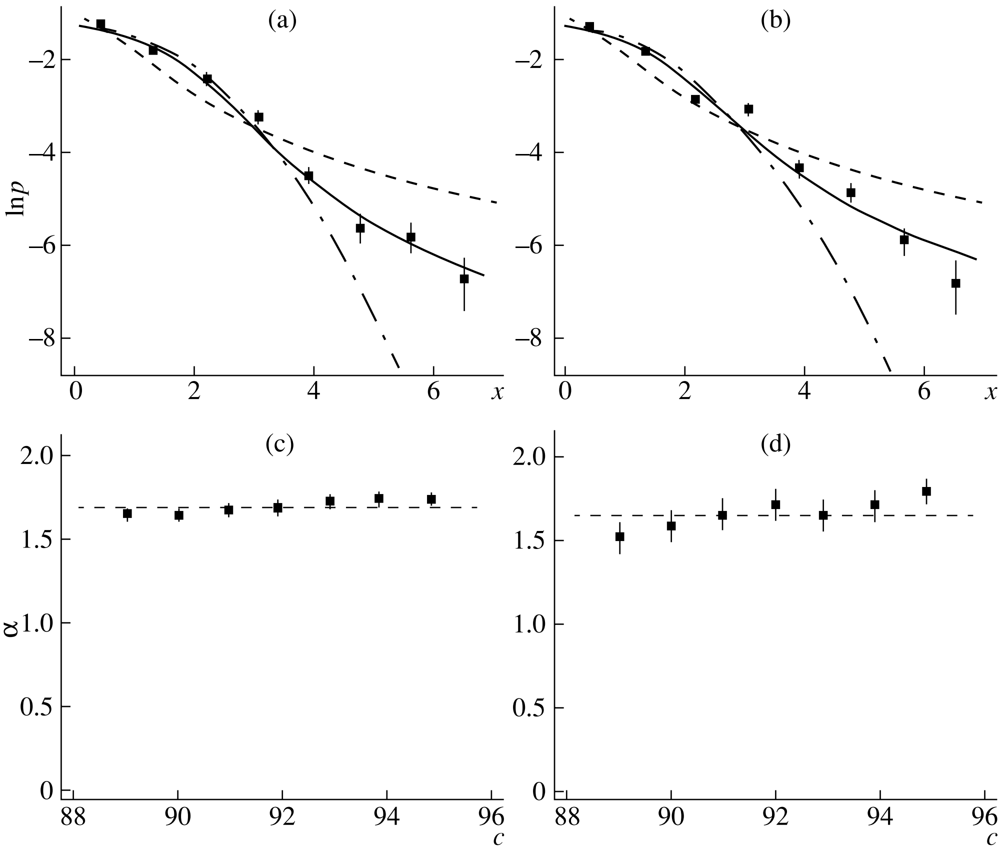

Fig. 5. Determination of the Lévy index by the percentile method: (a, c) the verification of the method with artificial data and (b, d) the results of processing the experimental data for the ISC fluctuations at the radius R = 113 cm (in all of the plots, samples consisting of 1000 points are used). In plots (a) and (b), symbols with error bars show the PDFs for (a) artificial and (b) experimental data ($\sigma = 1$), the solid lines show the calculated PDFs with the Lévy index $\alpha = 1.7$, the slowly decaying dotted line shows the PDF with $\alpha = 1.0$ (Caushy distribution), and the rapidly decaying dotted line shows the PDF with $\alpha = 2.0$ (Gaussian distribution). The symbols in plots (c) and (d) show the α values determined by the percentile method; the horizontal dotted lines show the values α = (c) 1.73 and (d) 1.67 ± 0.07 obtained by averaging over all of the percentile values used.

(ii) We estimate the scale factor

$$\sigma = \frac{|x|_{44}}{0.828}. \quad (5)$$

(iii) To estimate the Lévy index α, we calculate the function

$$r_c(\alpha) = \frac{|x|_c}{|x|_{44}}, \quad (6)$$

where c = 90–95. The $r_c(\alpha)$ values for each value of c are compared with the tabulated dependences for $p_{|X|}(x; \alpha, 1)$. Examples of such dependences for the 88th, 92nd, and 96th percentiles are shown in Fig. 4b. From the comparison, we find α for each value of c. The final value of the Lévy index is calculated by averaging the values determined from the 89th to the 95th percentiles. This percentile range is the most informative from the standpoint of the evaluation of the α parameter. At smaller percentiles, we switch from the asymptotics of stable distributions to the range of the moderate argument values for which the distributions with different α differ not so strongly. On the other hand, at larger percentile values, the accuracy worsens because of the small number of the sample points corresponding to a far asymptotic of a stable distribution.

5. PARAMETERS OF THE STABLE DISTRIBUTIONS OF TURBULENT FLUCTUATIONS

The percentile method described in Section 4 was tested by us with artificial data generated by a generator of independent random numbers that have a stable distribution with given parameters α and σ. The generation method is described in detail in [31]. We used the percentile method to estimate the PDF parameters of the ISC and FP fluctuations. Figures 5a and 5c illustrate the method for determining the parameter α for a sample consisting of 1000 points generated by a random-number generator with $\alpha = 1.7$. The symbols in Fig. 5a show the PDF on a half-logarithmic scale for a distribu-

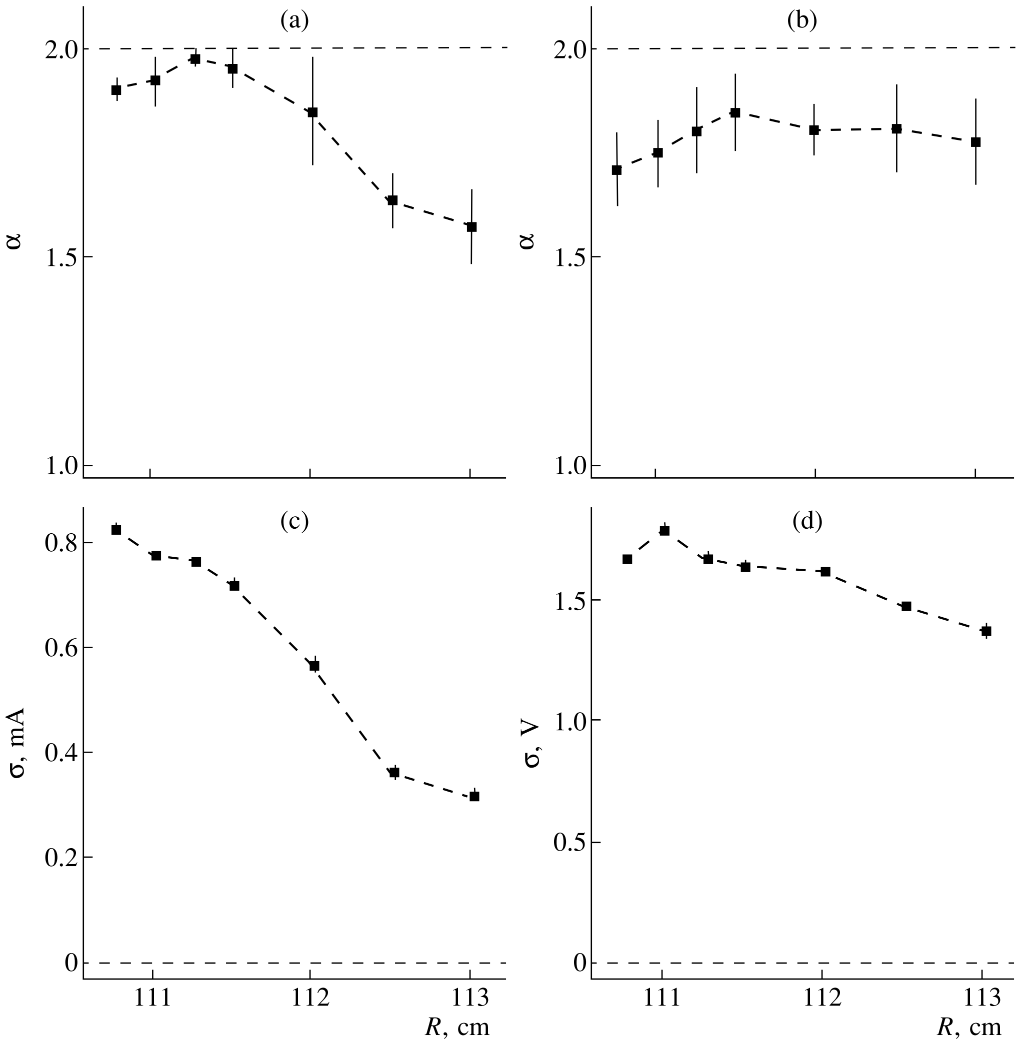

Fig. 6. (a, b) Lévy index and (c, d) the scale factor σ vs. radius for (a, c) ISC and (b, d) FP fluctuations.

tion obtained in the numerical experiment. The solid line corresponds to a stable distribution with the Lévy index determined using the percentile method (α = 1.73). The dashed lines show a Gaussian distribution (α = 2, the rapidly decaying curve) and a Cauchy distribution (α = 1, the slowly decaying curve). The α values determined by the percentile method at c = 89, 90, …, 95 are shown by symbols in Fig. 5c. The value α = 1.73 obtained by averaging over all of the percentile values used is shown by the horizontal dotted line. Similar dependences for the ISC fluctuations measured at the point R = 113 cm are shown in Figs. 5b and 5d. The symbols in Fig. 5b show the distribution characteristics obtained from the experimental data. The solid line corresponds to a stable distribution with the Lévy index equal to 1.67. The α values determined by the percentile method are shown by symbols in Fig. 5d. The value $\alpha = 1.67 \pm 0.07$ obtained by averaging over all the percentile values used is shown by the horizontal dotted line. It follows from Fig. 5 that the percentile method in combination with numerical simulations allows us to determine the Lévy index even for relatively small samples.

Figure 6 shows (a, b) the Lévy indices and (c, d) the scale factors as functions of the plasma radius for the (a, c) ISC and (b, d) FP fluctuations. It can be seen in Fig. 6a that, as the distance from the plasma boundary increases, the Lévy index for the ISC fluctuations decreases, the distribution asymptotics become flatter, and the spikes in the experimental samples become more distinct. We note that the behavior of the kurtosis with increasing R (Fig. 3a) agrees qualitatively with the behavior of the Lévy index α (Fig. 6a): the flatter power-law asymptotics of stable distributions correspond to the larger positive values of the kurtosis. At R = 111, 111.25, and 111.5 cm, where the index α (with allowance for the error bars) is close or equal to 2 (a Gaussian distribution), the kurtosis takes small negative values, which also testifies that the dependences shown in Figs. 3a and 6a are in qualitative agreement.

It can be seen that Figs. 3b and 6b, corresponding to the FP fluctuations, are also in qualitative agreement: the smaller α values correspond to the larger kurtosis. We note that the kurtosis in Fig. 3b is positive over the entire range of R. This is consistent with the fact that the index α shown in Fig. 6b is smaller than 2 over the entire range of R.

Now, let us consider Figs. 6c and 6d. It is seen that the scale factor σ decreases toward the plasma periphery. This means that the intensity of fluctuations decreases. Since in this case, the Lévy index changes only slightly (for the FP fluctuations) or decreases (for the ISC fluctuations), the decrease in the intensity of fluctuations means that the relative contribution of the fluctuation spikes increases. This conclusion agrees with the behavior of the typical signals shown in Fig. 2. Hence, the degree of the intermittency of the turbulence increases toward the plasma periphery, and the quantitative characteristics allowing one to describe this phenomenon are the scale factor σ and the Lévy index α.

6. CONCLUSION

Stable Lévy distributions, which possess unique properties from a probabilistic standpoint, are often met in various applications. In this paper, we have shown that the PDFs of ISC and FP fluctuations measured in the edge plasma of the U-3M torsatron can be classified as stable distributions. The parameters of the stable distributions have been determined by the percentile method. These parameters serve as quantitative characteristics of the intensity and intermittency of the turbulence in the edge plasma.

The experimental investigations of fluctuations in U-3M allow us to have fairly long samples and, hence, increase the accuracy of the estimates. On the other hand, theoretical models of the fluctuation processes in the edge plasma are of great interest because they enable one to demonstrate the appearance of stable distributions analytically or numerically.

ACKNOWLEDGMENTS

We thank K.N. Stepanov and the participants of his seminar for helpful discussions. We also thank the reviewer of this paper for amending the manuscript. This work was supported in part by INTAS, grant no. 00-0847.

REFERENCES

1. H. Y. W. Tsui, A. J. Wootton, J. D. Bell, *et al.*, Phys. Fluids B **5**, 2491 (1990).
2. G. M. Batanov, V. E. Bening, V. Yu. Korolev, *et al.*, Fiz. Plazmy **28**, 128 (2002) [Plasma Phys. Rep. **28**, 111 (2002)].
3. V. V. Chechkin, I. P. Fomin, L. I. Grigor'eva, *et al.*, Nucl. Fusion **36**, 133 (1996).
4. E. L. Sorokovoj, S. P. Bondarenko, A. V. Chechkin, *et al.*, in *Proceedings of the 23rd EPS Conference on Controlled Fusion and Plasma Physics, Kiev, 1996* (EPS, Geneva, 1996), Vol. 20C, Part II, p. 523.
5. J. Krommes, Phys. Rep. **360**, 1 (2002).
6. G. Y. Antar, P. Devinck, X. Garbet, *et al.*, Phys. Plasmas **8**, 1612 (2001).
7. E. Sanchez, C. Hidalgo, D. Lopez-Bruna, *et al.*, Phys. Plasmas **7**, 1408 (2000).
8. G. M. Batanov, O. I. Fedyanin, N. K. Kharchev, *et al.*, Plasma Phys. Controlled Fusion **40**, 1241 (1998).
9. D. L. Rudakov, J. A. Boedo, R. A. Moer, *et al.*, Plasma Phys. Controlled Fusion **44**, 717 (2002).
10. M. G. Kendall and A. Stuart, *The Advanced Theory of Statistics* (Griffin, London, 1977; Nauka, Moscow, 1966).
11. S. J. Levinson, J. M. Beall, E. J. Powers, and R. D. Bengston, Nucl. Fusion **24**, 527 (1984).
12. P. Lévy, *Calcul des Probabilités* (Gauthier-Villiars, Paris, 1937).
13. B. V. Gnedenko and A. N. Kolmogorov, *Limit Distributions for Sums of Independent Random Variables* (Gostekhteorizdat, Moscow, 1949; Addison-Wesley, Reading, 1954).
14. I. M. Vinogradov, *Mathematical Encyclopaedia* (Sov. Étsiklopediya, Moscow, 1984), Vol. 4, p. 222.
15. C. L. Nikias and M. Shao, *Signal Processing with Alpha-Stable Distributions and Applications* (Wiley, New York, 1999).
16. A. V. Chechkin and V. Yu. Gonchar, Chaos, Solitons and Fractals **11** (14), 379 (2000).
17. R. Weron, Int. J. Mod. Phys. C (Amsterdam) **12** (2), 209 (2001).
18. J. von Holtsmark, Ann. der Physik **58**, 577 (1919).
19. S. Chandrasekhar, *Stochastic Problems in Physics and Astronomy* (AIP, New York, 1943; Inostrannaya Literatura, Moscow, 1947); Rev. Mod. Phys. **15**, 1 (1943).
20. V. M. Zolotarev, *One-Dimensional Stable Distributions* (Mir, Moscow, 1983; Am. Math. Soc., Providence, RI, 1986).
21. V. V. Uchaikin and V. M. Zolotarev, *Chance and Stability: Stable Distributions and Their Applications* (VSP, Utrecht, 1999).
22. J.-P. Bouchaud and A. Georges, Phys. Rep. **195**, 127 (1990).
23. *The Wonderful World of Stochastics: A Tribute to E. W. Montroll*, Ed. by M. F. Shlesinger (North-Holland, Amsterdam, 1985).
24. M. F. Shlesinger, G. M. Zaslavsky, and J. Klafter, Nature (London) **363**, 31 (1993).
25. J. Klafter, M. F. Shlesinger, and G. Zumofen, Phys. Today **49** (2), 33 (1996).
26. R. Metzler and J. Klafter, Phys. Rep. **339**, 1 (2000).
27. R. Balescu, H.-D. Wang, and J. H. Misguich, Phys. Plasmas **1**, 3826 (1994).
28. G. Zimbardo, P. Veltri, G. Basile, and S. Principato, Phys. Plasmas **2**, 2653 (1995).

29. P. Pommois, P. Veltri, and G. Zimbardo, Phys. Rev. E **59**, 2244 (1999).
30. S. V. Annibaldi, G. Manfredi, and R. O. Dendy, Phys. Plasmas **9**, 791 (2002).
31. A. V. Chechkin and V. Yu. Gonchar, Physica A (Amsterdam) **277** (3–4), 312 (2000).
32. R. Metzler, E. Barkai, and J. Klafter, Europhys. Lett. **46**, 431 (1999).
33. A. V. Chechkin and V. Yu. Gonchar, Zh. Éksp. Teor. Fiz. **118**, 730 (2000) [JETP **91**, 635 (2000)].
34. G. M. Zaslavsky, M. Edelman, H. Weitzner, *et al.*, Phys. Plasmas **7**, 3691 (2000).
35. A. V. Chechkin, V. Yu. Gonchar, and M. Szydlowski, Phys. Plasmas **9**, 78 (2002).
36. E. D. Volkov, I. Yu. Adamov, N. T. Arsen’ev, *et al.*, in *Proceedings of the 14th International Conference on Plasma Physics and Controlled Nuclear Fusion Research, Wurzburg, 1992* (IAEA, Vienna, 1993), Vol. 2, p. 679.
37. J. S. Bendat and A. Piersol, *Random Data: Analysis and Measurement Procedures* (Wiley, New York, 1986; Mir, Moscow, 1989).
38. G. Samorodnitsky and M. S. Taqqu, *Stable Non-Gaussian Random Processes* (Chapman & Hall, New York, 1994).
39. R. N. Mantegna and H. E. Stanley, Phys. Rev. Lett. **73**, 2946 (1994).
40. B. M. Hill, Ann. Stat. **3**, 1163 (1975).
41. J. P. Nolan, Comm. Stat. Stochastic Models **13**, 759 (1997).
42. M. Meerschaert and H.-P. Scheffler, J. Stat. Plann. Inference **71** (1–2), 19 (1998).

Translated by E.L. Satunina

Plasma Physics Reports, Vol. 29, No. 5, 2003, pp. 391–398. Translated from Fizika Plazmy, Vol. 29, No. 5, 2003, pp. 424–431.
Original Russian Text Copyright © 2003 by Churilov.

PLASMA OSCILLATIONS AND WAVES

Alfvén Wave Spectrum in a Transversely Inhomogeneous Plasma with Dissipation

S. M. Churilov

Institute of Solar–Terrestrial Physics, Siberian Division, Russian Academy of Sciences, Irkutsk, 664033 Russia

Received July 12, 2002; in final form, October 3, 2002

Abstract—The spectrum of Alfvén eigenmodes in a transversely inhomogeneous plasma with Ohmic dissipation is studied in the one-fluid MHD approximation. It is established that, along with a discrete spectrum of the modes confined to the plasma boundaries or the extremes of the Alfvén velocity, there always exists a continuous spectrum of aperiodically damped modes, including those with arbitrarily slow damping rates. It is shown that the set of eigenmodes is complete. © *2003 MAIK “Nauka/Interperiodica”.*

1. INTRODUCTION

In the ideal MHD approximation, Alfvén waves are nondivergent plasma motions (i.e., those retaining the density ρ of each fluid element unchanged) that propagate along the magnetic field $\mathbf{B}$ with the Alfvén velocity $\mathbf{c}_A = \mathbf{B}/(4\pi\rho)^{1/2}$ and are accompanied by oscillations of the magnetic field lines analogous to the vibrations of strings [1].[1] In a homogeneous plasma, Alfvén waves, together with fast and slow magnetosonic waves, constitute a complete set of MHD eigenmodes.

The simplest model for describing a nonuniform plasma assumes that the plasma is in a straight magnetic field $\mathbf{B}_0$ and the equilibrium values of ρ_0 and B_0 depend only on x. The z-axis of the Cartesian coordinate system is chosen to point in the magnetic field direction. The dispersion relation for Alfvén waves, $\omega = \mathbf{c}_A \cdot \mathbf{k}$, is such that they cannot be the eigenmodes of the medium [2, 3], because magnetic field lines that belong to different x values oscillate at different frequencies (for a given $k \equiv k_z$) or the oscillations have different wavelengths (for a given frequency ω). Formally, this indicates that an elementary perturbation should have the form

$$B \sim e^{-i\omega t + ikz}\delta[\omega - \omega(x)], \quad \omega(x) = c_A(x)k, \qquad (1)$$

where $\delta(z)$ is the Dirac delta function; i.e., it should be localized about the surface at which the Alfvén velocity is equal to ω/k. Consequently, Alfvén waves have properties similar to those of Van Kampen–Case waves and it seems natural to consider them as pseudowaves (according to the classification proposed by Timofeev [4, 5]). Among the other phenomena compatible with this line of reasoning are the phenomenon of Alfvén resonance [4, 6] between perturbations propagating in the plasma and modes (1) and also the phase-mixing effect [7]—a shortening of the transverse scale lengths of the initial Alfvén perturbations due to the dephasing of the oscillations of the neighboring magnetic field lines.

Going beyond the limits of ideal MHD theory by taking into account such conservative factors as the electron (ion) inertia and finite ion Larmor radius changes the transverse dispersion of Alfvén waves in such a way that they can again be regarded (at least partially) as the eigenmodes of an inhomogeneous plasma: there arises a discrete spectrum of eigenmodes localized across the magnetic field and propagating along the field lines at which the Alfvén velocity is extreme [8–10]. However, there also remains a continuous spectrum of pseudowaves, which is closely related to the singularity of the equation for eigenmodes at the Alfvén resonance [11].

Incorporating weak dissipation (e.g., Ohmic dissipation) into the ideal MHD equations makes it possible, first of all, to describe the conversion of perturbation energy into heat, in which case the heating is contributed by both of the above effects: Alfvén resonance (in a narrow resonance region) and a reduction in the transverse scale of the initial Alfvén perturbation (over the entire region where the perturbation is localized). For instance, it is because of the latter effect that the wave energy E is dissipated according to the law characteristic of pseudowaves [4, 5, 7],

$$E \sim \exp(-\alpha t^3),$$

where t is time. As for Alfvén eigenmodes, it was proven in [2, 4] that they are absent in a plasma with a monotonic profile $c_A(x)$. Later, it was found [4, 12] that there is an exception: if the plasma has a boundary at $x = x_0$, then, because of dissipation, there arises a discrete spectrum of damped Alfvén eigenmodes, whose eigenfunctions are essentially nonzero only in the vicinity of x_0 (see Section 2.2 for details). Timofeev [4] also supposed that a similar spectrum can arise for a plasma with a nonmonotonic profile $c_A(x)$.

---

[1] In what follows, Alfvén perturbations will be treated as belonging to this class of plasma motions.

The objective of this paper is to further investigate the role of dissipation in the formation of the Alfvén wave spectrum in a plasma with monotonic and nonmonotonic profiles of the Alfvén velocity. It is shown that, along with a discrete spectrum, there always exists a continuous spectrum of aperiodically damped Alfvén eigenmodes. Moreover, under certain conditions, the modes of both the discrete spectrum and the continuum constitute a complete set of eigenmodes.

2. ALFVÉN WAVE SPECTRUM

2.1. Basic Equations and Formulation of the Problem

We consider Alfvén perturbations in which the plasma moves strictly along the surfaces $c_A = \text{const}$. In this case, the Alfvén waves are decoupled from the magnetosonic waves, and Alfvén resonance does not occur. In the model described above, these are perturbations that are independent of y. In such perturbations, the plasma density remains undisturbed and, in the linear approximation, the perturbed velocity and perturbed magnetic field have only y components and are described by the equations

$$\frac{\partial v_y}{\partial t} = \frac{B_0}{4\pi\rho_0}\frac{\partial B_y}{\partial z},$$

$$\frac{\partial B_y}{\partial t} = B_0\frac{\partial v_y}{\partial z} + \eta\left(\frac{\partial^2 B_y}{\partial x^2} + \frac{\partial^2 B_y}{\partial z^2}\right),$$

which take into account the magnetic field diffusion ($\eta = \text{const}$) due to finite conductivity [13]. Evaluating v_y from the first equation and substituting it into the second equation, we arrive at the following evolutionary equation for the structure of Alfvén perturbations in a transversely inhomogeneous plasma:

$$\frac{\partial^2 B_y}{\partial t^2} - c_A^2(x)\frac{\partial^2 B_y}{\partial z^2} = \eta\left(\frac{\partial^2}{\partial x^2} + \frac{\partial^2}{\partial z^2}\right)\frac{\partial B_y}{\partial t},$$
$$c_A^2(x) = \frac{B_0^2(x)}{4\pi\rho_0(x)}. \tag{2}$$

In what follows, we assume that, first, $c_A(x)$ is bounded below, $A = \min c_A(x) > 0$; second, $k > 0$; and third, the dissipation is weak, $\eta \ll aA$, where a is the characteristic scale on which the plasma density varies.

The Alfvén waves will be analyzed by using two models of the plasma: the one in which the profile of the Alfvén velocity is parabolic (quadratic),

$$c_A^2 = A^2\left(1 + \frac{x^2}{a^2}\right), \quad -\infty < x < \infty, \tag{3}$$

and the one in which the profile is linear,

$$c_A^2 = A^2\left(1 + \frac{x}{a}\right), \quad 0 \le x < \infty. \tag{4}$$

For brevity, the models will be referred to as model (3) and model (4) or simply “the parabolic (quadratic) model” and “the linear model.”

These fairly simple and convenient models, which are frequently used in the literature, make it possible to carry out an analysis for both monotonic and nonmonotonic profiles of the Alfvén velocity.

For an elementary perturbation described by one harmonic in the Fourier expansion of the magnetic field in z ($B_y = b(x)\exp(pt + ikz)$), Eq. (2) yields

$$\frac{d^2 b}{dx^2} - \left[\frac{1}{\eta}\left(p + \frac{c_A^2 k^2}{p}\right) + k^2\right]b = 0. \tag{5}$$

The solutions to this equation that are finite over the entire range of variation of x determine the spectrum of the Alfvén eigenmodes and their structure. In model (4), the solutions should satisfy a certain boundary condition at $x = 0$. We choose this condition to be

$$\frac{db}{dx} = 0, \quad x = 0, \tag{6}$$

which indicates that the tangential component of the electric field vanishes at the conducting boundary. We also switch to the dimensionless variables

$$\tilde{x} = \frac{x}{a}, \quad \tilde{k} = ka, \quad \tilde{p} = \frac{pa}{A}, \quad \tilde{\eta} = \frac{\eta}{aA}.$$

Below, the tilde will be omitted.

2.2. Discrete Spectrum

We begin with the model in which the Alfvén velocity is described by parabolic profile (3) and thus has a maximum at the origin of the coordinates, $c_A^2 = 1 + x^2$. In this model, Eq. (5) is the Weber equation

$$\frac{d^2 b}{dx^2} - \left[\frac{p}{\eta} + \left(1 + \frac{1}{\eta p}\right)k^2 + \frac{k^2}{\eta p}x^2\right]b = 0, \tag{7}$$

whose general solution is the superposition of the parabolic-cylinder functions $U(d, \pm\lambda x)$ [14] with

$$d = \frac{1}{2}\left(\frac{p}{\eta}\right)^{1/2}\left(\frac{p}{k} + \frac{k}{p} + \eta k\right),$$
$$\lambda^2 = \frac{2k}{(\eta p)^{1/2}} \left(|\arg\lambda| \le \frac{\pi}{4}\right). \tag{8}$$

For $|\arg p| < \pi$, the functions $U(d, \pm\lambda x)$ approach zero at one of the ends of the x-axis (as $x \longrightarrow \pm\infty$, respectively); at the opposite end, they, as a rule, increase exponentially. By analogy with the problem of the energy levels of a quantum oscillator [15], the solutions to Eq. (7) that are finite everywhere are those with half-integer values of d, $d = -(n + 1/2)$; they are expressed in terms of the Hermite polynomials $H_n(z)$ [14]:

$$b_n(x) \sim f_n(x) = (2^n n!)^{-1/2} \exp\left(-\frac{\lambda_n^2 x^2}{4}\right) H_n\left(\frac{\lambda_n x}{\sqrt{2}}\right), \quad (9)$$
$$\lambda_n = \lambda(p_n), \quad n = 0, 1, 2, \ldots .$$

The eigenvalue equation

$$r^2 + \eta k r + (2n+1)\left(\frac{\eta}{k}\right)^{1/2} r^{1/2} + 1 = 0, \qquad (10)$$

where $r = p/k$, is solvable by radicals as the fourth-order algebraic equation with respect to $r^{1/2}$.[2] However, the solutions to this equations in limiting cases,

$$r_n^{\pm} = \pm i - \left(n + \frac{1}{2}\right)\left(\frac{\eta}{k}\right)^{1/2} e^{\mp i\pi/4} - \frac{\eta k}{2} + O(\eta^{3/2}),$$
$$\eta^{1/2} n \ll 1, \qquad (11)$$
$$r_n^{\pm} \approx -(2n+1)^{2/3}\left(\frac{\eta}{k}\right)^{1/3} \frac{1 \mp i\sqrt{3}}{2} \quad \eta^{1/2} n \gg 1,$$

and also the graphical representation of the solution in Fig. 1 are far more illustrative. At this point, the description of the *discrete* spectrum of parabolic model (3) is completed.

Now, we turn to model (4), in which $c_A^2 = 1 + x$. The substitution

$$\xi = \mu x + \xi_0, \quad \mu = \left(\frac{k^2}{\eta p}\right)^{1/3},$$
$$\xi_0 = \left(\frac{p^2}{\eta k}\right)^{1/3}\left(\frac{p}{k} + \frac{k}{p} + \eta k\right) \qquad (12)$$

reduces Eq. (5) to the Airy equation [14]

$$\frac{d^2 b}{d\xi^2} - \xi b = 0.$$

For $|\arg p| < \pi$, the solutions that are finite at $x \longrightarrow +\infty$ have the form

$$b(x) = C\,\mathrm{Ai}(\xi),$$

where Ai(z) is the Airy function [14]. Boundary condition (6) dictates the rule of quantization (cf. formula (18) in [12])

$$\xi_0 + a_n' = 0,$$

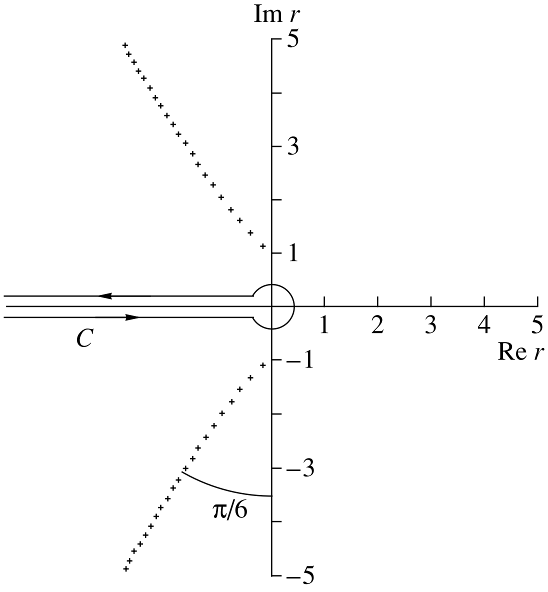

Fig. 1. Eigenvalues r_n in model (3) for $k = 1$ and $\eta = 0.01$.

where $z = -a_n'$ ($n = 1, 2, \ldots$) are the zeros of the derivative of the Airy function, Ai'(z). This rule yields the eigenvalue equation [cf. Eq. (10)]

$$r^2 + \eta k r + a_n'\left(\frac{\eta}{k}\right)^{1/3} r^{1/3} + 1 = 0, \quad r = p/k, \qquad (13)$$

whose physically meaningful solutions are shown in Fig. 2. The solutions in the above two limiting cases are as follows:

$$r_n^{\pm} = \pm i - \frac{a_n'}{2}\left(\frac{\eta}{k}\right)^{1/3} e^{\mp i\pi/3} + \frac{a_n'^2}{24}\left(\frac{\eta}{k}\right)^{2/3} e^{\mp i\pi/6} + O(\eta),$$
$$\eta^{1/2} n \ll 1, \qquad (14)$$
$$r_n^{\pm} \approx \pm i a_n'^{3/5}\left(\frac{\eta}{k}\right)^{1/5} e^{\pm i\pi/10}, \quad \eta^{1/2} n \gg 1.$$

In linear model (4), the eigenfunctions of the discrete spectrum have the form

$$f_n(x) = \frac{\mathrm{Ai}(\mu_n x - a_n')}{\mathrm{Ai}(-a_n')}, \quad \mu_n = \mu(p_n). \qquad (15)$$

Note that the modes of the discrete spectrum in this model correspond to even modes ($n = 0, 2, 4, \ldots$) in parabolic model (3); i.e., their number is two times smaller. If we discard boundary condition (6) and continue linear profile (4) into the region $x < 0$ in a symmetrical manner ($c_A^2 = 1 + |x|$), then we will obtain a discrete spectrum consisting not only of the spectrum just determined but also of the spectrum of odd modes, such that their eigenfunctions vanish at $x = 0$ but their derivatives are nonzero; the corresponding eigenvalues are to be

---

[2] The only physically meaningful solutions to this equation are a pair of complex conjugate solutions $r_n^{\pm}$, because the arguments of the remaining two solutions are $|\arg r| > \pi$.

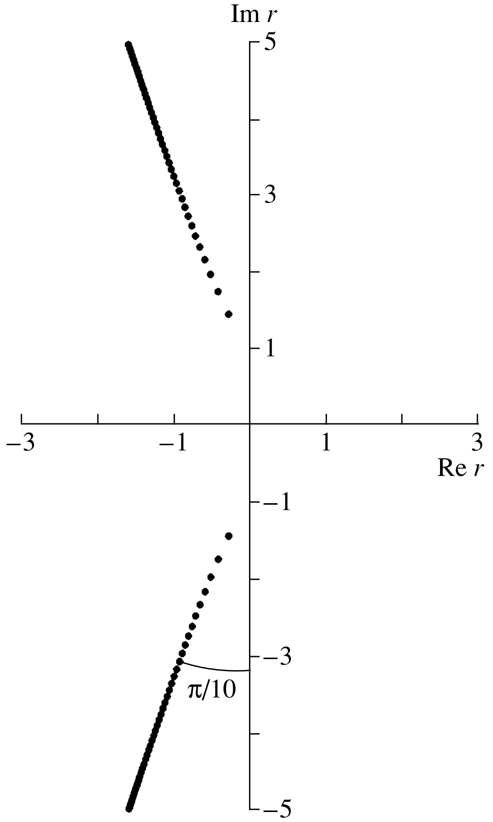

Fig. 2. Eigenvalues r_n in model (4) for $k = 1$ and $\eta = 0.1$.

found by replacing a'_n in Eq. (13) with a_n, where $z = -a_n$ are the zeros of the Airy function Ai(z).[3]

Let us now analyze the properties of the modes of a discrete spectrum. We begin by noting that the modes are small-scale because of their dissipative nature. The fundamental mode varies on the spatial scale

$$L_{0q} \sim \left(\frac{\eta a^2}{\omega}\right)^{1/4} \sim \left(\frac{\eta}{|\omega''|}\right)^{1/4} \text{ or } L_{0l} \sim \left(\frac{\eta a}{\omega}\right)^{1/3} \sim \left(\frac{\eta}{|\omega'|}\right)^{1/3} \quad (16)$$

(where dimensional units are used and the prime denotes the derivative with respect to x) in models (3) and (4), respectively [see relationships (8), (12)]. The mode itself is localized (on the same spatial scales) near the point $x = 0$, at which the Alfvén frequency $\omega(x) = c_A(x)k$ is extreme; i.e., in model (3), it is minimum and, in model (4), it takes on its boundary value. The remaining modes of the discrete spectrum are also localized around the point $x = 0$; moreover, the larger the mode number n, the larger the scale on which the mode is localized,

$$L_{nq} \approx (2n+1)^{1/2} L_{0q}, \; L_{nl} \approx \left(\frac{4n-1}{3}\right)^{2/3} L_{0l} \text{ for } \eta^{1/2} n \ll 1,$$

$$L_{nq} \sim (\eta n^2)^{1/3}, \quad L_{nl} \sim (\eta n^2)^{2/5} \text{ for } \quad \eta^{1/2} n \gg 1,$$

and the smaller the scale on which the mode varies, $l_{ns} \approx L_{ns}/n$ ($s = q, l$).

The modes of the discrete spectrum are damped oscillations whose frequency and damping rate increase with n. The frequency of the fundamental mode is approximately equal to $\omega(0)$; in other words, as is expected [4, 12], the discrete spectrum is confined to the plasma boundary (in the linear model) or to the extreme of $\omega(x)$ (in the parabolic model). The damping rates of all the modes are equal to the viscous damping coefficients corresponding to the scales on which the modes vary, $\delta_{ns} \approx \eta/l_{ns}^2$. This explains why the damping rate increases with n and why the modes with moderate numbers n (such that $\eta^{1/2} n \ll 1$) in model (3) are damped slower than those in model (4), whereas the modes with large n are damped faster [cf. solutions (11) versus solutions (14) and Fig. 1 versus Fig. 2].

To conclude this section, we compare the discrete spectrum determined by Eq. (13) with the spectrum obtained in [12] for the boundary condition $b(0) = 0$ instead of boundary condition (6) or, equivalently, for odd rather than even modes. It turns out that, despite somewhat different formulation of the problem, the portions of the spectra with moderate values of n not merely agree qualitatively (as is the case with the parabolic and linear models) but are essentially identical, to within an error resulting from the replacement of a'_n by a_n (cf. the first of solutions (14) versus formula (10) in [12]). Such a close coincidence between the results is explained as being due to the same dissipative nature of the discrete spectra in the problems. Another reason is that the modes are small-scale; this makes them sensitive to the conditions in the medium near the boundary (which are the same in both problems) and insensitive to large-scale effects (which are different in the problems). It should be mentioned parenthetically that, for other conditions at the boundary, the structures of the discrete spectrum in model (4) and in [12] remain the same, except that the old eigenvalues a'_n (a_n) are replaced by the new eigenvalues b_n, corresponding to the new boundary condition.

2.3. The Continuum

Now, we are left with the problem of analyzing the case of aperiodically damped solutions, $|\arg p| = \pi$. Setting $p = -q$ in Eq. (5), we obtain

$$\frac{d^2 b}{dx^2} + \frac{Q(x)}{\eta} b = 0, \quad Q = q + \frac{c_A^2(x) k^2}{q} - \eta k^2. \quad (17)$$

---

[3] All numbers a_n and a'_n are positive; the table of their values for $n \leq 10$ and the asymptotic formulas for them at $n \gg 1$ can be found in [14].

We can readily see that, in model (3), as well as in model (4), Eq. (17) with $q > 0$ has only finite oscillating solutions. Hence, in our problem, we deal not only with the discrete spectrum of Alfvén eigenmodes but also with their continuous spectrum.

In model (3), the only requirement imposed by the boundary conditions is that the solutions should be finite. Consequently, any solution to Eq. (17) with $q > 0$ describes an Alfvén eigenmode; i.e., each value $q > 0$ corresponds to two eigenmodes of the continuum. In accordance with the features of the problem at hand, these two eigenmodes can be described by any pair of linearly independent solutions to Eq. (17), e.g., by the real functions (see [14], p. 503)

$$f^{\pm}(x;\,q) = (2\pi)^{-1/2}W(\tilde{d}, \pm\tilde{\lambda}x),$$
$$\tilde{d} = -\frac{1}{2}\left(\frac{q}{\eta}\right)^{1/2}\left(\frac{q}{k} + \frac{k}{q} - \eta k\right), \quad \tilde{\lambda}^2 = \frac{2k}{(\eta q)^{1/2}}. \tag{18}$$

In model (4), the restrictions imposed by the boundary conditions are more stringent; as a result, each value $q > 0$ corresponds to only one eigenmode of the continuum,

$$f(x;\,q) = e^{i\Phi}\mathrm{Ai}(se^{-i\pi/3}) + \mathrm{c.c.}; \tag{19}$$

i.e., the number of modes is again one-half that in model (3). In formula (19), the term c.c. is the complex conjugate of the expression indicated and the rest of the notation is as follows:

$$s = \tilde{\mu}x + s_0, \quad \tilde{\mu} = \left(\frac{k^2}{\eta q}\right)^{1/3},$$

$$s_0 = \left(\frac{q^2}{\eta k}\right)^{1/3}\left(\frac{q}{k} + \frac{k}{q} - \eta k\right), \quad \Phi = \arg[\mathrm{Ai}'(s_0e^{i\pi/3})] - \frac{\pi}{6}.$$

The modes of the continuum are not localized and their scales, which are smaller than the scales of the modes of the discrete spectrum, can be estimated from above as [cf. Eq. (16)]

$$L_c \sim \left(\frac{\eta}{\omega}\right)^{1/2}. \tag{20}$$

These are the scales of the modes with $q \sim \omega$; the scales of the modes that are damped at slower and faster rates are smaller. We note that the relationship between the damping rate of the modes of the continuum and their scales differ radically from that for the modes of the discrete spectrum. Thus, the characteristic scale of the most interesting weakly damped ($q \ll k$) modes decreases with decreasing damping rate, $l_c(q) \approx (\eta q)^{1/2}/\omega$.

The properties of Eq. (17), which is typical of the problems of scattering in quantum mechanics and the problems of wave propagation in inhomogeneous conservative media, have been studied quite well [15, 16]. This allows us to take a broader look at the problem and state that aperiodically damped Alfvén eigenmodes exist in a plasma with an arbitrary profile of the Alfvén velocity. In fact, everywhere along the x-axis, the medium is transparent ($Q > 0$) to perturbations whose wavelengths are not too small, $k < k_0 = 2/\eta$,[4] and it is everywhere transparent to perturbations with $k > k_0$ that are damped at sufficiently slow ($0 < q < q^-$) or sufficiently high ($q > q^+$) rates, where

$$q^{\pm} = \frac{\eta k}{2}(k \pm \sqrt{k^2 - k_0^2}).$$

For a transparent medium, all of the solutions to Eq. (17) are finite, which proves the existence of the continuum in the cases at hand.

The existence of Alfvén eigenmodes in the ranges $k > k_0$ and $q^- < q < q^+$ depends on the shape of the profile $c_A(x)$. If the profile is such that the medium is transparent at infinity, as is the case in models (3) and (4), then the modes of the continuum do exist. If, in a certain range of q values, the medium is opaque at infinity ($Q < 0$) and is transparent in some regions along the x-axis, then there exist modes of the discrete spectrum. Finally, if for a given damping rate q, the medium is opaque everywhere, then there can be no Alfvén eigenmodes damped at this rate. Thus, if the Alfvén velocity $c_A(x)$ is bounded both below and above (i.e., $c_A(x) \le A^+$), then, for $k > k_* = 2A^+/\eta$, Alfvén eigenmodes with the damping rates in the range $q_*^- < q < q_*^+$, where

$$q_*^{\pm} = \frac{\eta k}{2}(k \pm \sqrt{k^2 - k_*^2}),$$

do not exist because, in this range, the medium is opaque everywhere along the x-axis.

3. EVOLUTION OF THE INITIAL PERTURBATION

Here, we consider the evolution of the initial (specified at $t = 0$) Alfvén perturbation. We investigate the evolution of one harmonic in the Fourier expansion of the magnetic field in z: $B_y(x, z, t) = b_y(x, t)e^{ikz}$. The function $b_y(x, t)$ is the solution to the initial-value problem

$$\frac{\partial^2 b_y}{\partial t^2} + c_A^2(x)k^2 b_y = \eta\left(\frac{\partial^2}{\partial x^2} - k^2\right)\frac{\partial b_y}{\partial t},$$
$$b_y\big|_{t=0} = b_0(x), \quad \left.\frac{\partial b_y}{\partial t}\right|_{t=0} = b_t(x) \tag{21}$$

and satisfies the same boundary conditions at the x-axis as Alfvén eigenmodes, i.e., the finiteness condition and also, in model (4), condition (6). The arbitrary functions $b_0(x)$ and $b_t(x)$ are assumed to be real and finite.

---

[4] Here, in dimensional variables, $k_0 = 2A/\eta$.

3.1. Solution by the Laplace-Transform Method

Setting

$$b_p(x) = \int_0^\infty dt b_y(x, t)e^{-pt},$$

we arrive at the equation [cf. Eq. (5)]

$$\frac{d^2 b_p}{dx^2} - \left[\frac{p}{\eta} + \frac{c_A^2(x)k^2}{\eta p} + k^2\right]b_p = R(x; p),$$

$$R(x; p) = \left(\frac{d^2}{dx^2} - k^2 - \frac{p}{\eta}\right)\frac{b_0(x)}{p} - \frac{b_t(x)}{\eta p}.$$

We construct the solution using Green's function $G(x, x'; p)$:

$$b_p(x) = \int dx' G(x, x'; p)R(x'; p).$$

Then, we take the inverse Laplace transform to obtain the sought-for solutions to initial-value problem (21):

$$b_y(x, t) = \frac{1}{2\pi i}\int_{\sigma - i\infty}^{\sigma + i\infty} dpe^{pt}\int dx' G(x, x'; p)R(x'; p). \quad (22)$$

In parabolic model (3), we have [see relationships (8)][5]

$$G(x, x'; p)$$

$$= -\frac{\Gamma(d + 1/2)}{\sqrt{2\pi}\lambda}\begin{cases} U(d, \lambda x)U(d, -\lambda x'), & x > x' \\ U(d, -\lambda x)U(d, \lambda x'), & x < x'. \end{cases} \quad (23)$$

The integration over x' is carried out from $-\infty$ to $+\infty$. In linear model (4), we have

$$G(x, x'; p) = \frac{\pi}{\mu \operatorname{Ai}'(\xi_0)}$$

$$\times \begin{cases} \operatorname{Ai}(\xi)[\operatorname{Ai}(\xi')\operatorname{Bi}'(\xi_0) - \operatorname{Ai}'(\xi_0)\operatorname{Bi}(\xi')], & x > x' \\ \operatorname{Ai}(\xi')[\operatorname{Ai}(\xi)\operatorname{Bi}'(\xi_0) - \operatorname{Ai}'(\xi_0)\operatorname{Bi}(\xi)], & x < x', \end{cases} \quad (24)$$

where $\xi' = \mu x' + \xi_0$ [see also relationships (12)], and the integration is carried out from 0 to $+\infty$. Green's functions (23) and (24) are written in terms of the Euler gamma function $\Gamma(z)$, the pair of linearly independent solutions $\operatorname{Ai}(z)$ and $\operatorname{Bi}(z)$ to the Airy equation [14], and their derivatives $\operatorname{Ai}'(z)$ and $\operatorname{Bi}'(z)$ with respect to z.

From formulas (23) and (24) we can see that, in the complex plane p cut along the half-line $|\arg p| = \pi$, Green's function is single-valued and has simple poles at the points $p = kr_n^\pm$ of the discrete spectrum. Transforming the path for integrating over p in Eq. (22) into the contour C shown in Fig. 1, we arrive at the following representation of the solution in the form of a superposition of Alfvén eigenmodes of the discrete spectrum and of the continuum:

$$b_y(x, t) = \sum_n [c_n f_n(x)e^{p_n t} + \text{c.c.}] + b(x, t),$$
$$b(x, t) = \frac{1}{2\pi i}\int_C dpe^{pt}\int dx' G(x, x'; p)R(x', p), \quad (25)$$

where the eigenfunctions $f_n(x)$ of the problem are determined by expressions (9) and (15); the eigenvalues $p_n = kr_n^+$ are determined by Eqs. (10) and (13); and

$$c_n = -\frac{1}{D_n}\int dx' f_n(x')R(x'; p_n),$$

$$D_n = \begin{cases} \sqrt{2\pi}\lambda_n\left(\dfrac{\partial d}{\partial p}\right)_{p = p_n} \\ \mu_n a_n'\left(\dfrac{\partial \xi_0}{\partial p}\right)_{p = p_n} \end{cases}$$

(here, the upper formula refers to model (3), and the lower formula, to model (4)).

The integral along contour C is the sum of the integrals along the contours along both sides of the cut $|\arg p| = \pi$ and the integral along a small circle around the point $p = 0$. Using the familiar asymptotic expansions of Green's function $G(x, x'; p)$, we can readily show that the integral over the circle is negligibly small. Setting $p = -q$ and performing simple but rather laborious manipulations, we expand the part $b(x, t)$ of solution (25) in modes (18) of the continuum in parabolic model (3),

$$b(x, t) = \int_0^\infty \frac{dqe^{-qt}}{\tilde{\lambda}(1 + e^{2\pi\tilde{d}})^{1/2}}$$
$$\times \int_{-\infty}^{\infty} dx'[f^+(x; q)f^+(x'; q) + f^-(x; q)f^-(x'; q)]R(x'; -q), \quad (26)$$

and in modes (19) of the continuum in linear model (4),

$$b(x, t) = \int_0^\infty \frac{dqe^{-qt}}{\tilde{\mu}} f(x; q)\int_0^\infty dx' f(x'; q)R(x'; -q). \quad (27)$$

Hence, we have shown that an arbitrary initial perturbation evolves as a superposition of Alfvén eigenmodes; consequently, Alfvén eigenmodes of both the discrete spectrum and the continuum constitute a complete set of eigenmodes.

---

[5] It is well known that Green's function is constructed from the solutions to Eq. (5) that satisfy only one of the boundary conditions, at the right or left boundary of the range of variation of x; these are solutions $b^+(x)$ and $b^-(x)$, respectively.

3.2. Qualitative Scenario of Evolution

First, we consider the evolution of perturbations in model (4), in which the profile $c_A(x)$ is linear. For $\eta t^3 \ll 1$, we easily obtain from solution (22) the approximate expression

$$b_y(x, t) \approx \left[b_0(x)\cos\omega t + \frac{b_t(x)}{\omega}\sin\omega t\right]\exp\left(-\frac{1}{6}\eta\omega'^2 t^3\right), \tag{28}$$

which describes the initial evolutionary stage of the perturbation. Here, the factor in front of the exponential function is the exact solution to initial-value problem (21) with $\eta = 0$. In turn, the exact solution[6] implies that different plasma layers oscillate at different frequencies $\omega(x) = c_A(x)k$ in such a way that the phase difference of oscillations of the neighboring (separated by a distance Δx) magnetic field lines increases with time, $\Delta\varphi = \omega'\Delta x t$, thereby giving rise to a modulation of the perturbation on a progressively smaller local scale $l \sim |\omega' t|^{-1}$. It is generally agreed [7] that, over time scales t on the order of that of the dissipation, $t \sim \tau_D = l^2/\eta$ or, equivalently, $t \sim \eta^{-1/3}$, the evolving perturbation becomes subject to the viscous damping described by the exponential function in expression (28).

However, the above results imply a somewhat different scenario of evolution. This is because, on time scales $t \sim \eta^{-1/3}$, the modulation period l becomes on the order of the scale L_{0l} of the fundamental mode of the discrete spectrum [see formulas (16)]; as a result Alfvén eigenmodes become decoupled and, then, are damped independently of each other. Since, in the discrete spectrum, modes with larger numbers n are damped faster, the only observable modes will be modes with moderate numbers n, which are damped at a rate of about $\delta_{nl} \sim \eta^{1/3}$ [see expression (15)], and weakly damped modes of the continuum.

In parabolic model (3), the local scale on which the perturbation is modulated around the point at which the Alfvén velocity $c_A(x)$ is minimum decreases according to a different law, $l \sim |\omega'' t|^{-1/2}$. Hence, Alfvén eigenmodes become decoupled on a spatial scale of $l \sim L_{0q}$, or, equivalently, on a time scale of $t \sim \eta^{-1/2}$ [see formulas (16)]. In other respects, the scenario of evolution is the same as that in model (4).

4. CONCLUSION

The above analysis has shown that, in a transversely inhomogeneous plasma with dissipation, Alfvén eigenmodes always exist; generally, these are the modes of the discrete spectrum and continuum. Because of their dissipative nature, such modes are small-scale in the direction in which the plasma is inhomogeneous; therefore, their properties are relatively insensitive to the plasma conditions. These properties have been investigated with two models: the model of a semi-infinite plasma with a monotonic profile of $c_A(x)$ and the model of an unbounded plasma in which the Alfvén velocity $c_A(x)$ has an extreme value (a minimum).

The modes of the discrete spectrum are damped at relatively slow rates. The ratio of the frequency of the modes to their damping rate is always larger than unity, and for modes with moderate numbers ($n \ll \eta^{-1/2}$), it is much larger than unity. The modes are confined to the plasma boundary or to the extreme of the Alfvén frequency $\omega(x) = c_A(x)k$ in the following sense: first, the frequency of the fundamental mode is approximately equal to the boundary value of $\omega(x)$ or, correspondingly, to its extreme value; second, the frequencies of the remaining modes are so weakly dependent on their numbers n that they begin differ appreciably from the boundary frequency only for $n \sim \eta^{-1/2}$; and third, the eigenfunctions are essentially nonzero near the plasma boundary or, correspondingly, near the extreme point. The damping rate δ_n of all of the modes of the discrete spectrum is related to their scale l_n in the direction in which the plasma is inhomogeneous by the dissipation relationship $\delta_n \approx \eta/l_n^2$; however, the order of magnitude of the scale l_n and its dependence on n are different for modes confined to the plasma boundary and those confined to the extreme of the Alfvén frequency.

The above analysis has also revealed the existence of an Alfvén continuum under any plasma conditions, in particular, in a plasma with an arbitrary profile $c_A(x)$. The continuum consists of the modes that are aperiodically damped at rate q and are not associated with Alfvén resonance. The problem of determining the continuum is analogous to the quantum-mechanical problem of scattering in a one-dimensional potential field. A plasma with an arbitrary profile $c_A(x)$ is shown to be transparent at infinity to the modes that are damped at sufficiently fast or (even more interestingly) sufficiently slow rates q. In other words, the continuum should include the ranges $0 < q \le q_1$ and $q_2 \le q < \infty$ (in the above two models, $q_1 = q_2$).

Finally, by solving the problem of the evolution of the initial perturbation, it has been shown that the modes of both the discrete spectrum and the continuum constitute a complete set of eigenmodes.

ACKNOWLEDGMENTS

I am grateful to the reviewer of this paper for valuable remarks.

REFERENCES

1. B. B. Kadomtsev, *Collective Phenomena in Plasma* (Nauka, Moscow, 1976), p. 44.

---

[6] It is a superposition of pseudowaves (1).

2. A. V. Timofeev, in *Reviews of Plasma Physics*, Ed. by M. A. Leontovich (Atomizdat, Moscow, 1979; Consultants Bureau, 1986), Vol. 9.
3. V. A. Mazur, A. B. Mikhaĭlovskiĭ, A. L. Frenkel', and I. G. Shukhman, in *Reviews of Plasma Physics*, Ed. by M. A. Leontovich (Atomizdat, Moscow, 1979; Consultants Bureau, 1986), Vol. 9.
4. A. V. Timofeev, *Resonance Phenomena in Plasma Oscillations* (Fizmatlit, Moscow, 2000).
5. A. V. Timofeev, Fiz. Plazmy **23**, 1069 (1997) [Plasma Phys. Rep. **23**, 989 (1997)].
6. T. Stiks and D. Svanson, in *Basic Plasma Physics*, Ed. by A. A. Galeev and R. N. Sudan (Énergoatomizdat, Moscow, 1983; North-Holland, Amsterdam, 1984), Vol. 1.
7. J. Heyvaerts and E. R. Priest, Astron. Astrophys. **117**, 220 (1983).
8. A. S. Leonovich, V. A. Mazur, and V. N. Senatorov, Zh. Éksp. Teor. Fiz. **85**, 141 (1983) [Sov. Phys. JETP **58**, 83 (1983)].
9. A. V. Gul'el'mi and A. R. Polyakov, Geomagn. Aeron. **23**, 341 (1983).
10. A. S. Leonovich, V. A. Mazur, and V. N. Senatorov, Fiz. Plazmy **11**, 1106 (1985) [Sov. J. Plasma Phys. **11**, 632 (1985)].
11. I. S. Dmitrienko and V. A. Mazur, Issled. Geomagn. Aeron. Fiz. Solntsa, No. 78, 3 (1987).
12. P. M. Blekher, Fiz. Plazmy **11**, 439 (1985) [Sov. J. Plasma Phys. **11**, 254 (1985)].
13. L. D. Landau and E. M. Lifshitz, *Electrodynamics of Continuous Media* (Nauka, Moscow, 1982; Pergamon, New York, 1984).
14. *Handbook of Mathematical Functions*, Ed. by M. Abramovitz and I. Stegun (Nauka, Moscow, 1979; Pergamon Press, New York, 1989).
15. L. D. Landau and E. M. Lifshitz, *Quantum Mechanics: Nonrelativistic Theory* (Nauka, Moscow, 1974; Pergamon Press, New York, 1977).
16. G. M. Zaslavskiĭ, V. P. Meĭtlis, and N. N. Filonenko, *Wave Interactions in Inhomogeneous Media* (Nauka, Novosibirsk, 1982).

Translated by O.E. Khadin

Plasma Physics Reports, Vol. 29, No. 5, 2003, pp. 399–406. Translated from Fizika Plazmy, Vol. 29, No. 5, 2003, pp. 432–439.
Original Russian Text Copyright © 2003 by Belyaev, Girka, Gritsyna.

PLASMA OSCILLATIONS AND WAVES

Effect of the Periodic Ripple in an Axial Confining Magnetic Field on the Alfvén Heating of a Cylindrical Plasma

N. R. Belyaev, I. O. Girka, and V. T. Gritsyna
Karazin National University, pl. Svobody 4, Kharkov, 61077 Ukraine

Received June 25, 2002; in final form, September 25, 2002

Abstract—In a uniform axial magnetic field, the structure of local Alfvén resonance and the resonant absorption of RF power are governed by collisions, finite ion Larmor radius effects, and electron inertia. It is shown that, in a cylindrical plasma in a constant, periodically rippled, axial magnetic field, the structure of Alfvén resonance and the absorption of RF power can strongly depend on the ripple amplitude. The conditions under which the effect in question is dominant are intrinsic, e.g., to the modular Wendelstein stellarators. *© 2003 MAIK “Nauka/Interperiodica”.*

1. INTRODUCTION

Beginning with the paper by Dolgopolov and Stepanov [1], the narrow layer approximation has been widely used to study the conversion and absorption of Alfvén waves (AWs) in the local Alfvén resonance (AR) region in plasmas in a uniform magnetic field. In the AR region, even such weak effects as collisions between plasma particles, the finite ion Larmor radius, electron inertia, and striction nonlinearity become important.

The confining magnetic field $\mathbf{B}_0 = B_{0r}\mathbf{e}_r + B_{0\vartheta}\mathbf{e}_\vartheta + B_{0z}\mathbf{e}_z$ is often weakly rippled; in this case, its components in cylindrical coordinates can be written as

$$B_{0r} = B_0(\varepsilon'/k_b)\sin(k_b z), \quad B_{0\vartheta}(r) \ll B_0, \qquad B_{0z} = B_0[1+\varepsilon(r)\cos(k_b z)], \tag{1}$$

where $|\varepsilon| \ll 1$, $\varepsilon' \equiv d\varepsilon/dr$, $k_b = 2\pi/L$, and L is the ripple period. Such a structure of the field $\mathbf{B}_0$ is characteristic of adiabatic devices with a rippled magnetic field, tokamaks (due to the discreteness of the toroidal magnetic field coils), and toroidal devices with a rippled magnetic field (such as the ELMO bumpy torus) [2–5]. Ripple in the confining axial magnetic field is intrinsic to modular stellarators [6]. The poloidal component $B_{0\vartheta}$ of the confining magnetic field describes the rotational transform produced by the axial current in a tokamak plasma or by the stellarator windings.

In rippled magnetic field (1), an electromagnetic perturbation propagates as a wave envelope composed of the fundamental harmonic and an infinite number of satellite harmonics. The possibility of additional plasma heating in the satellite AR region in a rippled magnetic field was demonstrated in [7]. In the present paper, we investigate the effect of weak ripples in a confining magnetic field on the conversion and absorption of the fundamental mode of AWs in a local AR region. We show that the effect of the magnetic field ripple on the AR structure can be of the same order of magnitude as the effects of collisions between plasma particles, the finite ion Larmor radius, and electron inertia.

2. FORMULATION OF THE PROBLEM

We consider the conversion and absorption of MHD waves with frequencies $\omega \ll |\omega_{ce}|, \omega_{pe}$ (where $\omega_{c\alpha}$ and $\omega_{p\alpha}$ are the cyclotron and plasma frequencies of the particles of species α with $\alpha = i$ for ions and $\alpha = e$ for electrons) in a plasma column placed in constant rippled magnetic field (1). The plasma pressure is assumed to be low in comparison with the magnetic field pressure. In investigating Alfvén and fast magnetosonic (FMS) branches of MHD waves in such a plasma, electron inertia can be neglected everywhere except for a narrow local AR region. The equilibrium density $n(r, z)$ of such a plasma is a function of the magnetic surface, $n(r, z) = n(r_0)$, where

$$r_0 = r + \frac{\cos(k_b z)}{r}\int_0^r r\varepsilon dr + O(\varepsilon^2). \tag{2}$$

We introduce the orthonormal coordinate vectors $(\mathbf{e}_1, \mathbf{e}_2, \mathbf{e}_3)$ associated with the lines of the magnetic field $\mathbf{B}_0$: $\mathbf{e}_1 = \nabla r_0/|\nabla r_0|$, $\mathbf{e}_2 = \mathbf{e}_3 \times \mathbf{e}_1$, and $\mathbf{e}_3 = \mathbf{B}_0/|\mathbf{B}_0|$. In these coordinates, the electric induction vector $\mathbf{D}$ and the components of the electric field $\mathbf{E}$ of the wave are related by

$$\mathbf{D} = \varepsilon_1(E_1\mathbf{e}_1 + E_2\mathbf{e}_2) + \varepsilon_3 E_3\mathbf{e}_3 - i\varepsilon_2\mathbf{e}_3 \times \mathbf{E}. \tag{3}$$

The components of the permittivity tensor of a cold, weakly collisional plasma have the form

$$\begin{aligned}\varepsilon_1 &= 1-\sum_i \omega_{pi}^2(r_0)/(\omega^2-\omega_{ci}^2),\\ \varepsilon_2 &= -\sum_i \omega_{pi}^2(r_0)\omega/[(\omega^2-\omega_{ci}^2)\omega_{ci}]\end{aligned} \tag{4}$$

and the integral operator ε_3 in Eq. (3) determines the absolute value of the longitudinal current density (the longitudinal component of the vector **D**).

Solving Maxwell's equations in the weak ripple approximation and in the limit of small electron inertia ($|\varepsilon_3| \longrightarrow \infty$), we find that the longitudinal component of the wave electric field vanishes over the entire plasma column, $E_3 = (B_{0r}E_r + B_{0\vartheta}E_\vartheta + B_{0z}E_z)/|\mathbf{B}_0| \longrightarrow 0$. With this relationship between the components of the wave electric field, we can neglect the effects of collisions, electron inertia, and the finite ion Larmor radius in order to obtain the following simplified set of Maxwell's equations in cylindrical coordinates:

$$\begin{aligned}&B_{0z}\left[imB_z - r\frac{\partial B_\vartheta}{\partial z}\right] - B_{0r}\left[\frac{\partial(rB_\vartheta)}{\partial r} - imB_r\right]\\ &\quad = \frac{\omega r}{ic}\{\varepsilon_1 B_{0z}E_r + i\varepsilon_2|\mathbf{B}_0|E_\vartheta\},\\ &\left[\frac{\partial B_r}{\partial z} - \frac{\partial B_z}{\partial r}\right] = \frac{\omega}{ic}\left(\varepsilon_1 E_\vartheta - i\varepsilon_2\frac{B_{0z}}{|\mathbf{B}_0|}E_r\right),\\ &B_r = -N_\vartheta\frac{B_{0r}}{B_{0z}}E_r + \frac{ic}{\omega}\frac{\partial E_\vartheta}{\partial z},\\ &B_\vartheta = \frac{c}{i\omega}\frac{\partial E_r}{\partial z} + \frac{c}{i\omega}\frac{\partial}{\partial r}\left[\frac{B_{0r}}{B_{0z}}E_r\right],\\ &B_z = \frac{c}{i\omega r}\frac{\partial}{\partial r}(rE_\vartheta) - N_\vartheta E_r,\end{aligned} \tag{5}$$

where $N_\vartheta = cm/\omega r$ is the poloidal refractive index.

In order to solve Eqs. (5), we need to know the explicit expressions for ε_1 and ε_2 to first order in ε:

$$\varepsilon_{1,2}(r,z) = \varepsilon_{1,2}^{(0)}(r) + \varepsilon_{1,2}^{(1)}(r)\cos(k_b z) + O(\varepsilon^2), \tag{6}$$

where $\left|\varepsilon_{1,2}^{(1)}\right| \sim \left|\varepsilon\varepsilon_{1,2}^{(0)}\right|$,

$$\varepsilon_1^{(0)}(r) \equiv \varepsilon_1(r,z)|_{\varepsilon=0} = 1-\sum_i \omega_{pi}^2(r)/(\omega^2-\omega_{ci}^{(0)^2}), \tag{7}$$

$$\begin{aligned}\varepsilon_2^{(0)}(r) &\equiv \varepsilon_2(r,z)|_{\varepsilon=0}\\ &= -\sum_i \omega_{pi}^2(r)\omega/[(\omega^2-\omega_{ci}^{(0)^2})\omega_{ci}^{(0)}],\end{aligned} \tag{8}$$

$$\begin{aligned}\varepsilon_1^{(1)}(r) &= \left.\frac{\partial\omega_{pi}^2}{\partial r}\right|_{\varepsilon=0}\frac{1}{r}\int_0^r r\varepsilon dr\sum_i\frac{1}{\omega^2-\omega_{ci}^{(0)^2}}\\ &\quad - 2\varepsilon\sum_i\frac{\omega_{pi}^2(r)\omega_{ci}^{(0)^2}}{(\omega^2-\omega_{ci}^{(0)^2})^2},\end{aligned} \tag{9}$$

$$\begin{aligned}\varepsilon_2^{(1)}(r) &= \left.\frac{\partial\ln(\omega_{pi}^2)}{\partial r}\right|_{\varepsilon=0}\frac{1}{r}\int_0^r r\varepsilon dr\varepsilon_2^{(0)}\\ &\quad - \varepsilon\sum_i\frac{\omega_{pi}^2(r)\omega(3\omega_{ci}^{(0)^2}-\omega^2)}{\omega_{ci}^{(0)}(\omega^2-\omega_{ci}^{(0)^2})^2}.\end{aligned} \tag{10}$$

In expressions (7)–(10), the cyclotron frequency is defined in terms of the unrippled magnetic field, $\omega_{ci}^{(0)} = eB_0/(m_i c)$.

The spatial dependence of permittivity tensor components (6) allows us to seek a solution to Eqs. (5) for the radial electric field of an MHD wave in the form

$$\begin{aligned}E_r^{\sim} &= [E_z^{(0)}(r) + E_r^{(+1)}(r)e^{ik_b z} + E_r^{(-1)}(r)e^{-ik_b z}]\\ &\quad\times\exp i(k_z z + m\vartheta - \omega t),\end{aligned} \tag{11}$$

where m is the azimuthal mode number and k_z is the axial wavenumber of the fundamental mode of the wave. In representation (11), we take into account the fundamental harmonic, which is proportional to $\propto\exp(ik_z z)$, and the two nearest satellite harmonics, which are proportional to $\propto\exp[i(k_z \pm k_b)z)]$. The expressions for the remaining components of the magnetic and electric fields of an MHD wave are analogous to representation (11).

3. DERIVATION OF THE BASIC EQUATION

Using expressions (6)–(10) for the permittivity tensor components and the condition that the longitudinal component E_3 of the electric field of an MHD wave is zero, we reduce Maxwell's equations to the following set of equations for the amplitudes of the fundamental ($E_r^{(0)}$) and satellite ($E_r^{(\pm 1)}$) harmonics of the radial electric field of the wave:

$$\begin{aligned}&[(\varepsilon_1^{(0)} - N_z^2 - 2N_zN_\vartheta B_{0\vartheta}/B_0)E_r^{(0)} - A]\\ &\quad + \frac{c^2\delta^2}{2\omega^2}\frac{d^2E_r^{(0)}}{dr^2} + \frac{1}{2}\varepsilon_1^{(1)}E_r^{(+1)} + \frac{c^2k_b\delta}{2\omega^2}\frac{dE_r^{(+1)}}{dr}\\ &+ \frac{c^2}{\omega^2}\delta(k_z-k_b)\frac{dE_r^{(+1)}}{dr} + \frac{c^2k_b\delta}{2\omega^2}\frac{dE_r^{(-1)}}{dr} + \frac{1}{2}\varepsilon_1^{(1)}E_r^{(-1)}\end{aligned} \tag{12}$$

$$-\frac{c^2}{\omega^2}\delta(k_z+k_b)\frac{dE_r^{(-1)}}{dr} = 0,$$

$$\begin{gathered}-\frac{c^2}{2\omega^2}\delta(\pm 2k_z+k_b)\frac{dE_r^{(0)}}{dr}+(N_z\pm N_b)^2E_r^{(\pm1)}\\ -\frac{c^2\delta^2}{2\omega^2}\frac{d^2E_r^{(\pm1)}}{dr^2}-N_z^2E_r^{(\pm1)}+\frac{c^2\delta^2}{4\omega^2}\frac{dE_r^{(\mp1)}}{dr} = 0.\end{gathered} \tag{13}$$

Here, $N_z = ck_z/\omega$ is the axial refractive index and the parameter $\delta = \varepsilon'/k_b$ accounts for the small radial component of the confining magnetic field [see definition (1)]. Let us discuss the dependence of the small parameter δ on the ripple period L. At first glance, this dependence seems to be linear, because δ contains the factor $1/k_b \sim L$. However, the parameter δ is proportional to the radial derivative $d\varepsilon/dr$ of the ripple amplitude of the axial component of the constant magnetic field and the ripple amplitude ε is, in turn, proportional to the zero-order Bessel function. Consequently, as a function of the ripple amplitude, the small parameter is proportional to the first-order modified Bessel function $I_1(k_br_A)$.

Equations (12) and (13) were derived in the narrow layer approximation [1], which indicates that, in the AR region, the wave fields vary gradually in the axial and poloidal directions:

$$\begin{gathered}\left|dB_z^{(0)}/dr\right| \gg \left|k_{\max}B_z^{(0)}\right|,\\ k_{\max} = \max(m/r, k_z, k_b, \omega/c).\end{gathered} \tag{14}$$

The approximation also assumes a gradual variation of the plasma density in the radial direction.

Recall that, in the vicinity of AR, the radial variation in the poloidal component of the wave magnetic field is as sharp as that in E_r [see the fourth of Eqs. (5)]. The radial dependence of the remaining components of the wave electromagnetic field near AR is weaker,

$$\begin{gathered}B_r, B_z, E_\vartheta \propto \ln(\varepsilon_1^{(0)}-N_z-2N_zN_\vartheta B_{0\vartheta}/B_0),\\ E_r, B_\vartheta \propto (\varepsilon_1^{(0)}-N_z^2-2N_zN_\vartheta B_{0\vartheta}/B_0)^{-1}.\end{gathered} \tag{15}$$

Note that, although the components $B_z^{(0)}$ and $E_\vartheta^{(0)}$ have logarithmic singularities at the point r_A in the cold plasma approximation, the expression $A = (-i\varepsilon_2^{(0)}E_\vartheta^{(0)} - N_\vartheta B_z^{(0)})\big|_{r=r_A}$ in the square brackets in Eq. (12) varies gradually in the vicinity of AR [1, 8, 9].

3.1. Propagation of MHD Waves outside the Local Alfvén Resonance Region

Outside the region of AR, at which

$$\varepsilon_1^{(0)} = N_z^2+2N_zN_\vartheta B_{0\vartheta}/B_0, \tag{16}$$

Maxwell's equations can be solved using the perturbation theory [10, 11]. In an unrippled ($\varepsilon = 0$) confining magnetic field, the modes of an MHD wave with different axial numbers and different azimuthal numbers propagate independently of each other; consequently, we can assume that, in the zeroth approximation, it is only the amplitude $E_r^{(0)}$ of the fundamental mode of an MHD wave that is nonzero. Since the distribution of the fields for this case has been investigated in detail (see, e.g., [12] and the references therein), the distributions of the RF fields outside the AR region can be assumed to be known. The poloidal component of the constant magnetic field changes the amplitude of the fundamental harmonic by a small amount proportional to $B_{0\vartheta}/B_0$ [10]. The contribution of the ripples in a confining magnetic field to the amplitude of the fundamental harmonic is second-order in the ripple parameter ε. In this case, the amplitudes of the satellite harmonics are much smaller than the amplitude of the fundamental harmonic [11],

$$E_r^{(\pm1)} \sim \varepsilon E_r^{(0)}. \tag{17}$$

3.2. Conversion and Absorption of MHD Waves near a Local Resonance

Since the amplitude of the fundamental harmonic and, consequently, the amplitudes of the satellite harmonics grow resonantly in the vicinity of AR, we cannot use condition (17) to analyze Eqs. (12) and (13) near a local AR, at which condition (16) is satisfied. Further analysis shows that condition (17) actually fails to hold in the AR region.

The set of three second-order differential equations (12) and (13) reduces to the following sixth-order equation for the amplitude $E_r^{(0)}$ of the fundamental harmonic:

$$\begin{gathered}\frac{3}{16}\frac{c^4}{\omega^4}\delta^4\frac{d^4}{dr^4}[(\varepsilon_1^{(0)}-N_z^2-2N_zN_\vartheta B_{0\vartheta}/B_0)E_r^{(0)}+A]\\ -\frac{c^2}{\omega^2}\delta^2N_b^2\frac{d^2}{dr^2}[(\varepsilon_1^{(0)}-N_z^2-2N_zN_\vartheta B_{0\vartheta}/B_0)E_r^{(0)}+A]\\ +N_b^2(N_b^2-4N_z^2)[(\varepsilon_1^{(0)}-N_z^2-2N_zN_\vartheta B_{0\vartheta}/B_0)E_r^{(0)}+A]\\ +\frac{3}{32}\frac{c^6}{\omega^6}\delta^6\frac{d^6}{dr^6}E_r^{(0)}\bigg|_{(6,6)}\\ -\frac{1}{8}\frac{c^4}{\omega^4}\delta^4(N_b^2+4N_z^2)\frac{d^4}{dr^4}E_r^{(0)}\bigg|_{(4,4)}\\ -\frac{3}{8}\frac{c^3}{\omega^3}\delta^3N_b\varepsilon_1^{(1)}\frac{d^3}{dr^3}E_r^{(0)}\bigg|_{(4,3)}\end{gathered} \tag{18}$$

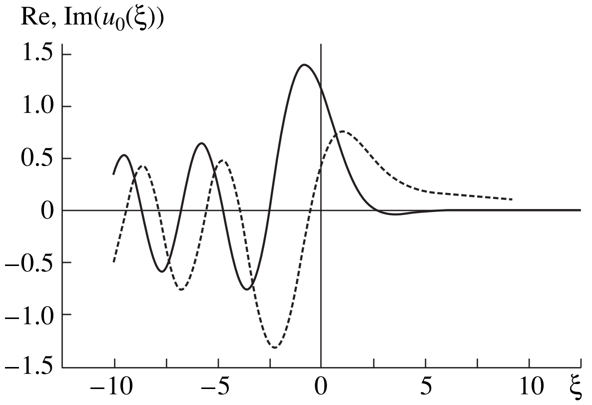

Axial profiles of the real (solid curve) and imaginary (dashed curve) parts of the function $u_0(\xi)$.

$$+\frac{1}{2}\frac{c}{\omega}\delta N_b\varepsilon_1^{(1)}(N_b^2-4N_z^2)\frac{d}{dr}E_r^{(0)}\Big|_{(2,\,1)} = 0.$$

Here, we have assigned a pair of subscripts to the last four terms. Their meaning may be illustrated by taking, e.g., the last of these terms: the pair (2, 1) indicates that the coefficient by the *first* derivative is *second-order* in the small parameter. Analyzing the relationships between the orders of magnitude of the derivatives and of their coefficients, we can further simplify Eq. (18) to

$$-\frac{1}{8}\frac{c^4}{\omega^4}\delta^4(N_b^2+4N_z^2)\frac{d^4}{dr^4}E_r^{(0)} + N_b^2(N_b^2-4N_z^2) \times[(\varepsilon_1^{(0)} - N_z^2 - 2N_zN_\vartheta B_{0\vartheta}/B_0)E_r^{(0)} + A] = 0. \tag{19}$$

Now, we will solve Eq. (19) and, then, examine to what extent this equation is less accurate than Eq. (18).

The solution to Eq. (19) can be found by the Laplace-transform method:

$$E_r^{(0)} = (a^*k_1/N_z^2)Au_0[k_1(r-r_A)], \tag{20}$$

where

$$u_0(\xi) = \int_0^\infty \exp[i(t\xi + t^5/5)]dt,$$

$$k_1 = \left(\frac{c^4\delta^4 a^*}{8\omega^4 N_b^2 N_z^2}\frac{N_b^2+4N_z^2}{N_b^2-4N_z^2}\right)^{-1/5} \sim [k_z^2k_b^2/(\delta^4 a)]^{1/5} \propto \delta^{-4/5}, \tag{21}$$

and $a^* = |d\ln|\varepsilon_1^{(0)}|/dr|^{-1}|_{r_A}$ is the characteristic scale on which the plasma density varies. This solution satisfies the following boundary conditions: (i) it is finite both at and away from the resonant point, (ii) it describes the conversion of an electromagnetic wave into a small-scale wave that carries energy away from the resonance point, and (iii) it describes a damped field when weak dissipation is taken into account in the expression for $\varepsilon_1^{(0)}$.

The figure shows the plot of the function $u_0(\xi)$, whose real and imaginary parts are represented by the solid and dashed curves, respectively. The absolute value $|u_0(\xi)|$ is maximum ($\max\{|u_0(\xi)|\} = 1.459$) at $\xi = -1.325$ rather than at zero. This position of the maximum of $|u_0(\xi)|$ is analogous to that in the case in which the AR structure is governed by the effect of a finite ion Larmor radius or finite electron inertia [13].

In the resonant case in which the coefficient of the second term in Eq. (19) vanishes, the solution describing waves with an axial wavelength equal to half the ripple period, $k_z = 2k_b$, becomes meaningless. For this resonant case, the effect of ripples in a constant magnetic field on the AR structure was investigated in [14].

The width of the AR region $\Delta r = |k_1|^{-1}$ is equal in order of magnitude to that in the resonant case and is $\delta^{-2/15}$ times smaller than the width of the region of the satellite AR, which was studied in [15] under the assumption that its structure is governed by the ripples in a constant magnetic field. Accordingly, Eqs. (20) and (21) yield the following order-of-magnitude estimate of the amplitude $E_r^{(0)}$ of the fundamental harmonic of the radial electric field of the wave at a local AR:

$$E_r^{(0)} \sim ak_1A/N_z^2 \sim \left(\frac{\omega^4a^4N_b^2}{\delta^4N_z^8c^4}\right)^{\frac{1}{5}}A. \tag{22}$$

For the wave field amplitude $E_r^{(0)}(r_A)$ to be comparable to the ambipolar electric field, which is on the order of $\sim T/ea$, the amplitude of the pump wave field should be equal in order of magnitude to

$$E_\vartheta \sim \frac{m_i\rho_{Li}^2\omega_{ci}^3}{e\omega a^2}\left(\frac{a\delta^4}{k_b^2k_z^2}\right)^{\frac{1}{5}}, \tag{23}$$

in which case nonlinear effects occurring in the AR region can be neglected.

In analyzing Eqs. (12) and (13) in the vicinity of AR, we did not use condition (17). To within terms on the order of $\delta^{2/5}$, Eq. (13) yields the following simplified expression for the amplitudes of the satellite harmonics:

$$\begin{aligned} E_r^{(\pm1)} &= -(\varepsilon'/2k_b^2)dE_r^{(0)}/dr, \\ E_r^{(\pm2)} &= -(\varepsilon'/4k_b^2)dE_r^{(\pm1)}/dr\ldots. \end{aligned} \tag{24}$$

We see that, in order of magnitude, the amplitude of the nth satellite harmonic is $\delta^{-n/5}$ times smaller than that of the fundamental harmonic,

$$E_r^{(\pm 1)} \sim \frac{k_1\delta}{k_b}E_r^{(0)} \sim \left(\frac{\omega^3 a^3}{\delta^3 c^3 N_b N_z^6}\right)^{\frac{1}{5}} A. \qquad (25)$$

In the vicinity of AR, the amplitudes of the satellite harmonics grow more sharply than the amplitude of the fundamental harmonic but remain smaller than the latter. However, in the vicinity of AR, this difference is not so pronounced as it is far from it.

Now, we can estimate the degree to which simplified equation (19) is less accurate than Eq. (18). The largest of the terms that we have neglected,

$$-\frac{c^2}{\omega^2}\delta^2 N_b^2 \frac{d^2}{dr^2}[(\varepsilon_1^{(0)} - N_z^2 - 2N_z N_\vartheta B_{0\vartheta}/B_0)E_r^{(0)} + A]$$

is as small as $\sim\delta^{2/5}$ in comparison with the retained third term in Eq. (18). The first term in Eq. (18) is as small as $\delta^{4/5}$. As compared to the retained term with the subscript (4, 4), the omitted terms with subscripts (i, j) are estimated to be as small as $\delta^{(i-4-0.8(j-4))}$.

Among the amplitudes of the fundamental harmonics, it is the amplitude of the axial component of the wave electric field that grows near the AR to the largest amount relative to its values far from the AR region:

$$E_z \approx \frac{ic}{\omega\varepsilon_3}\frac{\partial B_\vartheta}{\partial r} = \frac{ic}{\omega\varepsilon_3}N_z\frac{\partial E_r}{\partial r} \sim \frac{k_z a}{N_z^2}\rho_{Li}^2\left(\frac{k_z^2 k_b^2}{\delta^4 a}\right)^{\frac{2}{5}} A. \quad (26)$$

Nevertheless, the amplitude of this component remains much smaller than the amplitude $E_r^{(0)}$ of the radial component; hence, to first order in the wave amplitude, the effect of E_z on the detrapping of ripple-trapped plasma particles can be neglected.

3.3. Conditions under which the AR Structure is Governed by Ripple Effects

Here, we determine what the conditions are under which the AR structure is governed by the ripples in a constant magnetic field rather than by the effects of electron inertia, the finite ion Larmor radius $\rho_{Li} = v_{Ti}/\omega_{ci}$ (where $v_{T\alpha} = \sqrt{T_\alpha/m_\alpha}$ is the thermal velocity of the particles of species α and T_α is their temperature), and collisions between plasma particles. In Eq. (19), all of these weak effects can be taken into account by the replacement

$$\varepsilon_1^{(0)} \longrightarrow \varepsilon_1^{(0)} + i\varepsilon_1^{(c)} + (\varepsilon_T + N_z^2/\varepsilon_3)c^2/\omega^2\partial^2/\partial r^2; \quad (27)$$

i.e., in much the same way as in the case of a uniform axial magnetic field (see, e.g., [1, 8, 9]). Under the assumption that the plasma parameters in the AR region vary insignificantly, we can use the values of ε_T, ε_3, $\varepsilon_1^{(c)}$, $\varepsilon_{1,2}^{(0,1)}$, and $\varepsilon_1^{(2)}$ at the point $r = r_A$.

In formula (27), the term $\varepsilon_1^{(c)}$ accounts for collisions between plasma particles [16]:

$$\varepsilon_1^{(c)} = \sum_{a,b}\frac{\omega_{pa}^2\nu_{ab}}{\omega(\omega^2 - \omega_{ca}^{(0)^2})} \times\left(\frac{\omega^2 + \omega_{ca}^{(0)^2}}{\omega^2 - \omega_{ca}^{(0)^2}} - \frac{e_b m_a}{e_a m_b}\frac{\omega^2 + \omega_{ca}^{(0)}\omega_{cb}^{(0)}}{\omega^2 - \omega_{cb}^{(0)^2}}\right). \qquad (28)$$

Here, e_a is the charge of the particles of species a; $\nu_{a,b}$ is the frequency of collisions between the particles of species a and those of species b,

$$\nu_{ab} = (4/3)\sqrt{2\pi}e_a^2 e_b^2 n_b L_C[m_a T^3(1 + m_a/m_b)]^{-1/2}; \qquad (29)$$

and L_C is the Coulomb logarithm. The term ε_T in formula (27) accounts for the finite ion Larmor radius [17]:

$$\varepsilon_T = \sum_i \frac{3\omega_{pi}^2(r)\omega^2 v_{Ti}^2(r)}{(\omega^2 - \omega_{ci}^{(0)^2})(\omega^2 - 4\omega_{ci}^{(0)^2})c^2}. \qquad (30)$$

Electron inertia is taken into account by the permittivity tensor component ε_3. In the weak ripple approximation, we can describe ε_3 by the expression derived in the zeroth approximation:

$$\varepsilon_3 = \frac{\omega_{pe}^2}{k_z^2 v_{Te}^2}[1 + i\sqrt{\pi}z_e W(z_e)], \quad z_e \equiv \frac{\omega}{\sqrt{2}|k_z| v_{Te}}, \quad (31)$$

where the function $W(z_e)$ has the form

$$W(\xi) = \exp(-\xi^2)\left[1 + \frac{2i}{\sqrt{\pi}}\int_0^\xi \exp(t^2)dt\right]. \qquad (32)$$

In the case of weak Landau damping ($z_e \gg 1$), expression (31) for ε_3 simplifies to

$$\varepsilon_3 = -\frac{\omega_{pe}^2}{\omega^2}(1 - 2i\sqrt{\pi}z_e^3 e^{-z_e^2}). \qquad (33)$$

In this case, it is necessary to take into account electron–ion collisions; as a result, we obtain

$$\varepsilon_3 = \frac{-\omega_{pe}^2}{\omega(\omega + i\nu_{ei})}. \qquad (34)$$

The conditions under which the effect of a weak periodic ripple in the axial field $\mathbf{B}_0$ predominates over the remaining three weak effects can readily be determined by analyzing formula (27). In particular, the effect of the ripples in $\mathbf{B}_0$ is stronger than the finite ion Larmor radius effect under the condition

$$\delta^{12/5} \gg (\rho_{Li}/a)^2(k_z k_b a^2)^{6/5}, \tag{35}$$

which can easily be satisfied in the edge regions, where the constant magnetic field is rippled most strongly and the plasma is colder than in the core region. Also, condition (35) can be satisfied at lower temperatures than an analogous condition in the case of a satellite AR [15]. Inequality (35) can be interpreted as follows: the radial deviation $r - r_A$ of cylindrical magnetic surface (2) from a cylinder with the mean radius r_A is larger than the characteristic AR width $(\rho_{Li}^2 a)^{1/3}$ in an axial magnetic field (this width is known in the literature, see, e.g., [1]). Under condition (35), the width Δr of the resonance region is larger than that in an axial magnetic field: $\Delta r \sim k_1^{-1} \gg (\rho_{Li}^2 a)^{1/3}$.

Let us estimate the value of the small ripple parameter at which the ripple effects should be taken into account when investigating the conversion of AWs in a local AR region in devices with the parameters of the Helias [6]. According to condition (35), the ripple effect becomes comparable with the finite ion Larmor radius effect for sufficiently small (and, at the same time, quite realistic) values of the axial wavenumber $k_z^{6/5} \ll 10^{-2}$ (where k_z is expressed in inverse centimeters).

4. RF POWER ABSORPTION AT AR

Here, we calculate the electromagnetic energy absorbed per unit length of the plasma column in the vicinity of AR. The RF power absorbed in the plasma is determined by the work done by the wave electric field on the radial RF currents, $P_r = 0.5\mathrm{Re}\left\{\int j_r^* E_r 2\pi r dr\right\}$, and the axial RF currents, $P_z = 0.5\mathrm{Re}\left\{\int j_z^* E_z 2\pi r dr\right\}$. As a result, we have

$$P_r = \frac{r\omega}{4}\left|\frac{d\varepsilon_1}{dr}\right|^{-1}|A|^2\bigg|_{r = r_A}\int\limits_{-\infty}^{+\infty}\mathrm{Im}(u_0(x))dx, \tag{36}$$

$$P_z = \frac{r\omega k_1^3 a^2}{4|\varepsilon_3|^2 k_b^2}\mathrm{Im}(\varepsilon_3)\bigg|_{r = r_A}|A|^2\int\limits_{-\infty}^{+\infty}|u_0'(x)|^2 dx. \tag{37}$$

Expression (36), in which the function u_0 is replaced with the Airy function, coincides with the expression for the power absorbed in the region of AR, whose structure is governed by the finite Larmor radius or by the finite electron inertia (see, e.g., [1, 9]). The integral of the imaginary part of u_0 in expression (36) is equal to π, as is the case with the integral of the imaginary part of the Airy function. Consequently, the RF power absorbed in the vicinity of AR at the expense of the work done on the radial currents is independent of the type of small-scale wave (a kinetic wave or a wave associated with the ripples) into which a large-scale electromagnetic wave is converted near the resonance.

In [7], it was mentioned that, for $\mathrm{Im}(\varepsilon_3) \geq \mathrm{Re}(\varepsilon_3)$, the absorbed RF power P_z can be large in comparison with P_r. Expression (37), in which the function u_0 is replaced by the Airy function with the argument $[k_T(r - r_A)]$, coincides to within the small factor $(k_1/k_T)^3$ with an analogous expression in the case where the AR structure is governed by the finite Larmor radius or by the finite electron inertia. Here,

$$k_T^3 = -\frac{\omega^2}{c^2}\frac{\partial\varepsilon_1}{\partial r}\frac{\varepsilon_3}{\varepsilon_T\varepsilon_3 + N_z^2}. \tag{38}$$

The asymptotic behavior of the function u_0, $|u_0'(\xi)|^2 \propto (-\xi)^{1/4}$ as $\mathrm{Re}(\xi) \longrightarrow -\infty$, is such that the integral $\int_{-\infty}^{+\infty}|u_0'(x)|^2 dx$ in expression (37) diverges. However, this divergence can be avoided by introducing dissipative effects—collisions between plasma particles or Landau damping, which is accounted for by the imaginary part $\mathrm{Im}(\varepsilon_3)$. For $\mathrm{Im}(\varepsilon_3) \sim \mathrm{Re}(\varepsilon_3)$, the corresponding integral of the squared derivative of the Airy function is estimated to be on the order of unity. In this case, the damping rate of a small-scale wave can readily be estimated from Eq. (19) with allowance for replacement (27):

$$\mathrm{Im}(k_1) \sim k_1^4/(2k_T^3). \tag{39}$$

As a result, the integrand in expression (37) decreases in proportion to $\exp[2\mathrm{Im}(k_1)(r - r_A)]$ along the negative axis of the integration interval; hence, in order of magnitude, the integral is estimated as k_T^3/k_1^3. Therefore, our order-of-magnitude estimates show that the RF power absorbed in the vicinity of AR at the expense of the work done on the axial currents is also independent of the type of small-scale wave into which a large-scale electromagnetic wave is converted near the resonance.

5. DISCUSSION OF THE RESULTS OBTAINED

The main results of our investigations can be summarized as follows.

(i) We have found that the effect of a ripple in a confining magnetic field on the AR structure is the displacement of the AR point a small distance δr ($r_A \longrightarrow r_A + \delta r$) from the axis:

$$\delta r = -\varepsilon_1^{(2)}(\partial\varepsilon_1^{(0)}/\partial r)_{r = r_A}^{-1}, \tag{40}$$

where

$$\begin{aligned}\varepsilon_1^{(2)} &= \frac{\partial\varepsilon_1^{(0)}}{\partial n}\frac{\partial^2 n}{\partial r^2}\bigg|_{\varepsilon=0}\frac{1}{4r^2}\left(\int_0^r(r\varepsilon)dr\right)^2 \\ &\quad-\frac{\partial\varepsilon_1^{(0)}}{\partial n}\frac{\partial n}{\partial r}\bigg|_{\varepsilon=0}\frac{1}{4r^3}\left(\int_0^r(r\varepsilon)dr\right)^2 \\ &\quad+\frac{\partial^2\varepsilon_1^{(0)}}{\partial n\partial B}\frac{\partial n}{\partial r}\bigg|_{\varepsilon=0}\frac{B_0\varepsilon}{2r}\int_0^r(r\varepsilon)dr \\ &\quad+\frac{\partial\varepsilon_1^{(0)}}{\partial B}\bigg|_{\varepsilon=0}\frac{B_0\varepsilon'^2}{4k_b^2}+\frac{\partial^2\varepsilon_1^{(0)}}{\partial B^2}\bigg|_{\varepsilon=0}\left(\frac{B_0\varepsilon}{2}\right)^2.\end{aligned} \tag{41}$$

From the form of expression (41) for $\varepsilon_1^{(2)}$, we cannot draw a definite conclusion about the sign of δr. However, in a particular case in which the AR region lies deep in a plasma cylinder ($r_A \sim 0.5a_p$, where a_p is the plasma radius) with a parabolic density profile, $n(r) = n(0)(1 - r^2/a_p^2)$, and the ripple amplitude changes insignificantly over the plasma volume, $|r\varepsilon'| \ll |\varepsilon|$, the AR region is displaced (under the action of the ripple in $\mathbf{B}_0$) a distance $\delta r \sim \varepsilon^2 a_p$ from the plasma axis.

(ii) We have determined the conditions [see, e.g., estimate (39)] under which the effect of a ripple in a magnetic field on the AR structure is stronger than the other weak effects (such as those of dissipation, the finite ion Larmor radius, and electron inertia). These conditions can be satisfied in the edge regions, where the ripple is especially large and the plasma is colder than in the core region.

(iii) The distribution of the RF wave fields has been determined by solving reduced equation (19), which is valid to within small terms on the order of $\varepsilon^{2/5}$.

(iv) Equation (24) implies that, in the vicinity of AR, the amplitudes of the satellite harmonics grow more sharply than the amplitude of the fundamental harmonic, the growth rates of both satellites being essentially the same, $E_r^{(+1)} \approx E_r^{(-1)}$ and $E_r^{(+2)} \approx E_r^{(-2)}$. Nevertheless, near the resonance, they remain as small as about $\varepsilon^{1/5}$ in comparison with the fundamental harmonic amplitude. Their reverse effect on the behavior of the fundamental harmonic amplitude $E_r^{(0)}(r)$ is to smooth out the discontinuity that arises in a straight confining magnetic field within the AR region in the cold plasma approximation. This is the principal difference between the effect of a periodically inhomogeneous plasma and, e.g., the effect of a toroidally nonuniform confining magnetic field, which only slightly deforms the surface where the wave fields are discontinuous [18, 19].

The results just discussed contradict the conclusions reached in [20] when studying a similar problem of the propagation of Alfvén waves in the field of a single adiabatic trap. According to the analytical estimates and numerical results obtained in that paper, the two-dimensional nonuniformity of the system does not eliminate AR. We think that this contradiction stems from the fact that the dispersion relation used in [20] was obtained in the geometrical-optics approximation, which fails to hold for the AR region.

(v) We have calculated the RF power absorbed in the vicinity of AR due to the conversion of an electromagnetic wave into a small-scale wave associated with the ripples, which is then damped by collisions or via the Landau mechanism. This power is found to coincide with that absorbed in the vicinity of AR both in the case where the absorption occurs through collisions and in the case where it occurs through the conversion of an electromagnetic wave into a small-scale kinetic Alfvén wave.

Note that local resonance condition (16) can exist for AWs and FMS waves with $\omega < \omega_{ci}$ (when $k_z^2 > \omega^2/c^2$) and also for FMS waves with $\omega > \omega_{ci}$ in a low-density plasma (when $k_z^2 < \omega^2/c^2$). The conversion and absorption of FMS waves with $\omega > \omega_{ci}$ and $k_z^2 < \omega^2/c^2$ under local resonance condition (16) at the edge of a plasma cylinder in a purely axial magnetic field were investigated in [9].

ACKNOWLEDGMENTS

This work was supported by the Science and Technology Center in Ukraine, project no. 2313.

REFERENCES

1. V. V. Dolgopolov and K. N. Stepanov, Nucl. Fusion **5**, 276 (1965).
2. D. D. Ryutov, Usp. Fiz. Nauk **154**, 565 (1988) [Sov. Phys. Usp. **31**, 300 (1988)].
3. B. B. Kadomtsev, in *Plasma Physics and the Problem of Controlled Thermonuclear Reactions*, Ed. by M. A. Leontovich (Akad. Nauk SSSR, Moscow, 1958; Pergamon, New York, 1960).
4. F. W. Baity, L. A. Berry, L. Bighel, *et al.*, in *Proceedings of the 9th Conference on Plasma Physics and Controlled Nuclear Fusion Research, Baltimore, 1982*; Nucl. Fusion Suppl. **2**, 185 (1983).
5. M. Fujiwara, R. Kamimura, M. Hosawa, *et al.*, Nucl. Fusion Suppl. **2**, 197 (1983).
6. C. D. Beidler, G. Grieger, E. Harmeyer, *et al.*, Report No. IPP 2/330 (Max Planck Inst. für Plasmaphysik, Garching, 1995).
7. I. A. Girka, V. I. Lapshin, and K. N. Stepanov, Fiz. Plazmy **20**, 1020 (1994) [Plasma Phys. Rep. **20**, 916 (1994)].

8. D. L. Grekov, K. N. Stepanov, and G. A. Tataronis, Fiz. Plasmy **7**, 752 (1981) [Sov. J. Plasma Phys. **7**, 411 (1981)].
9. I. A. Girka and K. N. Stepanov, Ukr. Fiz. Zh. **35**, 1680 (1990).
10. I. A. Girka and K. N. Stepanov, Dokl. Akad. Nauk Ukr. SSR, Ser. A, No. 3, 66 (1990).
11. I. A. Girka and K. N. Stepanov, Ukr. Fiz. Zh. **37**, 69 (1992).
12. A. G. Elfimov, A. G. Kirov, and V. P. Sidorov, in *High-Frequency Plasma Heating*, Ed. by A. G. Litvak (Inst. of Applied Physics, USSR Acad. Sci., Gorki, 1983).
13. V. I. Lapshin, K. N. Stepanov, and V. O. Shtrasser, Fiz. Plazmy **18**, 660 (1992) [Sov. J. Plasma Phys. **18**, 344 (1992)].
14. I. O. Girka, Contrib. Plasma Phys. **41**, 33 (2001).
15. I. O. Girka, Contrib. Plasma Phys. **42**, 456 (2002).
16. A. I. Akhiezer, V. I. Lapshin, and K. N. Stepanov, Zh. Éksp. Teor. Fiz. **70**, 81 (1976) [Sov. Phys. JETP **43**, 42 (1976)].
17. *Plasma Electrodynamics*, Ed. by A. I. Akhiezer (Nauka, Moscow, 1974; Pergamon Press, Oxford, 1975).
18. V. E. Moiseenko, Fiz. Plazmy **12**, 1376 (1986) [Sov. J. Plasma Phys. **12**, 798 (1986)].
19. V. V. Dolgopolov, A. V. Kryukov, and S. S. Romanov, Ukr. Fiz. Zh. **31**, 210 (1986).
20. A. V. Timofeev, Fiz. Plazmy **14**, 1266 (1988) [Sov. J. Plasma Phys. **14**, 741 (1988)].

Translated by I.A. Kalabalyk

Plasma Physics Reports, Vol. 29, No. 5, 2003, pp. 407–424. Translated from Fizika Plazmy, Vol. 29, No. 5, 2003, pp. 440–457.
Original Russian Text Copyright © 2003 by Gorbunov, Frolov.

Generation of Plasma Fields in the Interaction between Two Oppositely Propagating Short Laser Pulses in an Underdense Plasma

L. M. Gorbunov* and A. A. Frolov**

**Lebedev Physical Institute, Russian Academy of Sciences, Leninskiĭ pr. 53, Moscow, 119991 Russia*
***Institute for High Energy Densities, Associated Institute for High Temperatures, Russian Academy of Sciences, Izhorskaya ul. 13/19, Moscow, 127412 Russia*

Received September 11, 2002

Abstract—A study is made of the interaction ("collision") between two identical laser pulses with lengths much shorter than the diffraction length, propagating in a plasma toward one another. It is shown that the plasma response to the pulses depends essentially on the value of the parameter $\omega_p\tau$, where ω_p is the plasma frequency and τ is the pulse duration. Short laser pulses (such that $\omega_p\tau \le \sqrt{2}$) efficiently generate plasma waves on two characteristic scale lengths. Large-scale wake waves with a wavelength of about c/ω_p are generated over the entire path of the pulses and form a two-dimensional standing plasma wave in the region between the pulses after their interaction. In the interaction region, the pulses excite small-scale plasma oscillations with a wavelength equal to half the laser wavelength, which remain in the plasma after the interaction. Long laser pulses (such that $\omega_p\tau > \sqrt{2}$) also generate quasistatic plasma perturbations on two scale lengths. Perturbations generated on large scales of about the pulse length accompany the propagating pulses and are somewhat amplified in the interaction between them. Small-scale plasma fields are generated only during the interaction between the pulses, and they disappear after the interaction. The influence of the generation of plasma fields on the energy of the laser pulses and on their shape, as well as the possible applications of the effects under consideration, is discussed. *© 2003 MAIK "Nauka/Interperiodica".*

INTRODUCTION

Significant recent progress in the generation of short (subpicosecond) high-power (terawatt) laser pulses [1] has made it possible to substantially extend the area of research on the laser acceleration of particles [2], laser inertial confinement fusion [3], and the development of X-ray lasers [4]. Increased attention is being focused on the nonlinear effects that occur in the interaction of ultrashort laser pulses. The effect that has received the most complete theoretical and experimental investigation is the channeling of a high-power laser pulse in a plasma channel created by another pulse with a lower power (see, e.g., [5–7]). The possibility of electron acceleration in electric fields generated in a plasma in the interaction of laser pulses was discussed by Shvets *et al.* [8]. For the purposes of injecting ultrashort electron bunches into a laser accelerator, Schroeder *et al.* [9] developed a method for producing them in the interaction between two oppositely propagating laser pulses. Much attention has recently been paid to the idea of amplifying a short laser pulse in its interaction with an oppositely propagating long pulse of lower intensity (see, e.g., [10, 11]). The problem of the amplification of wake fields in the interaction between two laser pulses was investigated numerically and analytically in [12, 13] in the context of the laser wakefield acceleration of charged particles. The possibility of creating short-lived Bragg mirrors in the interaction (collision) between two identical laser pulses in a plasma was considered in our paper [14]. Another possible application of the effects accompanying a collision of two laser pulses in a plasma is related to the possibility of obtaining information about the structure of the pulses from an analysis of the plasma perturbations generated in such a collision [15].

In the present work, which is a continuation of [14], we develop a theory of the effects that are produced in an underdense plasma by two oppositely propagating identical laser pulses. In contrast to [14], we investigate not only small-scale plasma perturbations generated in the interaction region but also large-scale perturbations excited over the entire path of the pulses.

In Section 1, we formulate two relatively simple sets of equations, mutually coupled to one another. One set of equations describes high-frequency laser fields, and the other describes slow plasma perturbations. The coefficients in the linear equations for rapidly varying quantities contain slowly varying quantities, and the linear equations for slowly varying quantities includes the ponderomotive force produced by high-frequency fields. Each of the high- and low-frequency physical subsystems described by these sets of equations is not closed, and they may exchange energy. We also derive and discuss equations describing changes in the energy densities of the high- and low-frequency subsystems. In Section 2, we apply the general relationships obtained to describe a system of two identical laser pulses propagating toward one another. Large-scale plasma perturbations are considered in Section 3. For Gaussian pulses, the plasma field and the energy density of the plasma perturbations are expressed in a general way in terms of functions that are widely utilized in plasma theory. Using the familiar asymptotic expressions for these functions, we analyze the limiting cases of short ($\omega_p\tau \le \sqrt{2}$) and long ($\omega_p\tau > \sqrt{2}$) pulses. Short laser pulses efficiently generate wake waves [16]; in the region between the pulses after their interaction, these waves form a two-dimensional standing plasma wave whose electric field has a complicated, radially dependent structure. Long laser pulses practically do not generate wake fields but produce internal plasma fields, which accompany them and are amplified in the interaction region at the expense of the energy of the pulses. After the interaction, the energy of the pulses is restored to the energy that they had before the interaction. In Section 4, we examine small-scale plasma perturbations with a period equal to half the laser wavelength. Such perturbations are generated only in the interaction region, and their behavior is also determined by the pulse length. Small-scale perturbations excited in the interaction between two short laser pulses oscillate at the plasma frequency, and they remain in the plasma after the interaction. In the case of long laser pulses, small-scale perturbations are quasistatic, exist only during the interaction, and disappear after the interaction. In the Conclusion, we present some estimates for the effects considered and discuss their possible practical applications. In the Appendix, the influence of plasma perturbations on the shape of the laser pulses and their energy is investigated. The analysis is based on perturbation theory, in which this influence is assumed to be small. However, the use of more intense lasers may increase this influence to a measurable level, thereby providing an additional method for diagnosing the effects that occur in a plasma.

1. GENERAL RELATIONSHIPS

In order to describe the propagation of laser pulses in an underdense plasma, we use Maxwell's equations for electromagnetic fields and the hydrodynamic equations for a cold electron fluid. We separately consider the quantities that vary rapidly on a time scale on the order of the laser field period and the quantities that vary slowly on time scales of about the laser pulse duration or plasma oscillation period. As a result, the general set of equations splits into two subsets. The subset describing high-frequency processes is linear in the high-frequency electric ($\mathbf{E}_L$) and magnetic ($\mathbf{B}_L$) laser fields, and its coefficients depend on the parameters characterizing slow plasma processes:

$$\frac{\partial \mathbf{V}_L}{\partial t} = \frac{e}{m}\mathbf{E}_L - \boldsymbol{\nabla}(\mathbf{V}_L \cdot \mathbf{V}_e), \tag{1.1}$$

$$\nabla \times \mathbf{E}_L = -\frac{1}{c}\frac{\partial \mathbf{B}_L}{\partial t}, \tag{1.2}$$

$$\nabla \times \mathbf{B}_L = \frac{1}{c}\frac{\partial \mathbf{E}_L}{\partial t} + \frac{4\pi e}{c}(N_{0e} + \delta N_e)\mathbf{V}_L. \tag{1.3}$$

Here, N_{0e} is the constant electron density in the absence of a laser pulse, $\mathbf{V}_L$ is the high-frequency electron velocity, δN_e and $\mathbf{V}_e$ are the low-frequency electron density perturbations and the electron velocity in them, e and m are the charge and mass of an electron, and c is the speed of light.

The slowly varying quantities are described by the other subset of equations, which is also linear and includes the ponderomotive force as an external source:

$$m\frac{\partial \mathbf{V}_e}{\partial t} = e\mathbf{E} - \boldsymbol{\nabla}\phi, \tag{1.4}$$

$$\frac{\partial}{\partial t}\left(\frac{\delta N_e}{N_{0e}}\right) + \nabla \cdot \mathbf{V}_e = 0, \tag{1.5}$$

$$\frac{\partial \mathbf{E}}{\partial t} + 4\pi e N_{0e}\mathbf{V}_e = 0. \tag{1.6}$$

Here, $\mathbf{E}$ is the low-frequency charge-separation potential electric field and $\phi = \frac{1}{2}m\langle \mathbf{V}_L^2\rangle$ is the high-frequency potential, averaged over the period of high-frequency processes.

The set of quasilinear equations (1.1)–(1.6) assumes that the electron density perturbations are small ($|\delta N_e| \ll N_{0e}$) and that the velocities satisfy the inequalities $|\mathbf{V}_e| \ll |\mathbf{V}_L| \ll c$. In the linear approximation, low-frequency magnetic fields are not excited because of the potential nature of the ponderomotive force [17].

Equations (1.1)–(1.6) take into account only quadratic nonlinearities. With allowance for a significant difference in the frequencies of the interacting fields, the nonlinear current density given by these equations agrees completely with that following from the general expression for the nonlinear (quadratic) dielectric function of a cold dissipationless electron plasma [18].

Although all of the electromagnetic fields in the plasma are produced by a laser pulse, the fact that the general set of equations is split into two subsets allows us to talk about the interaction between the high-frequency fields of the pulse and the low-frequency plasma fields. In particular, we can speak of the energy exchange between the laser pulse and the low-frequency plasma perturbations. In fact, Eqs. (1.4)–(1.6) yield the following equation for the energy of these perturbations:

$$\frac{\partial w_p}{\partial t} + \nabla \cdot (N_{0e}\mathbf{V}_e\phi) = -\phi\frac{\partial \delta N_e}{\partial t}, \tag{1.7}$$

where their energy density w_p has the form

$$w_p = \frac{E^2}{8\pi} + \frac{1}{2}mN_{0e}V_e^2. \tag{1.8}$$

From Eqs. (1.1)–(1.3), we obtain the equation for the energy of the high-frequency laser field:

$$\frac{\partial w_L}{\partial t} + \nabla \cdot \mathbf{S}_L = \phi\frac{\partial \delta N_e}{\partial t}, \tag{1.9}$$

where the energy density w_L and the energy flux density $\mathbf{S}_L$ of the laser pulse are equal, respectively, to

$$w_L = \frac{\langle \mathbf{E}_L^2 + \mathbf{B}_L^2 \rangle}{8\pi} + (N_{0e} + \delta N_e)\phi, \tag{1.10}$$

$$\mathbf{S}_L = \frac{c}{4\pi}\langle \mathbf{E}_L \times \mathbf{B}_L \rangle + mN_{0e}\langle \mathbf{V}_L(\mathbf{V}_L \cdot \mathbf{V}_e)\rangle. \tag{1.11}$$

Note that definition (1.10) of the energy density of the high-frequency laser field differs from that used in [14] in having the last term $\phi\delta N_e$, which coincides with the interaction energy density introduced in [14]. It is convenient to define the pulse energy density in form (1.10) because, in this case, the expressions on the right-hand sides of Eqs. (1.7) and (1.9), which describe the energy exchange between subsystems, are the same but have opposite signs; hence, in the sum of the equations, they cancel one another. This result is a consequence of the conservation of the total energy of the laser pulse and of the low-frequency plasma perturbations.

In investigating laser pulses, we specify the high-frequency electric field as the field of a wave with a slowly varying amplitude:

$$\begin{aligned} \mathbf{E}_L(\mathbf{r}, t) &= \frac{1}{2}\{\mathbf{E}^0(\mathbf{r}, t)\exp(-i\omega_0 t + ik_0 z) \\ &\quad + \mathbf{E}^{0*}(\mathbf{r}, t)\exp(i\omega_0 t - ik_0 z)\}, \end{aligned} \tag{1.12}$$

where ω_0 is the frequency, k_0 is the longitudinal wavenumber, and the complex amplitude (envelope) $\mathbf{E}^0$ is varyies slowly on the time and spatial scales ω_0^{-1} and k_0^{-1}. The equation for the field envelope follows from Eqs. (1.1)–(1.3) and, for waves satisfying the dispersion relation $\omega_0^2 = \omega_p^2 + c^2k_0^2$, has the form

$$\begin{aligned} &\left\{2i\omega_0\frac{\partial}{\partial t} - \frac{\partial^2}{\partial t^2} + c^2\left(2ik_0\frac{\partial}{\partial z} + \frac{\partial^2}{\partial z^2} + \Delta_\perp\right)\right\}\mathbf{E}^0 \\ &\qquad = \omega_p^2\mathbf{E}^0\left(1 + \frac{i}{\omega_0}\frac{\partial}{\partial t}\right)\frac{\delta N_e}{N_{0e}}, \end{aligned} \tag{1.13}$$

where $\Delta_\perp$ is the transverse Laplace operator and $\omega_p = \sqrt{4\pi e^2 N_{0e}/m}$ is the plasma frequency. In Eq. (1.13), we retain small terms containing the second derivatives of the slowly varying field amplitude and a small term with the time derivative on the right-hand side because, as was shown in [19], it is precisely these terms that describe how the pulse energy changes.

To first order, the energy density (1.10) of the high-frequency laser field (1.12) has the form

$$\begin{aligned} w_L = \frac{1}{8\pi}\Bigg\{&|\mathbf{E}^0|^2 + \frac{i}{2\omega_0}\left(\mathbf{E}^0 \cdot \frac{\partial \mathbf{E}^{0*}}{\partial t} - \mathbf{E}^{0*} \cdot \frac{\partial \mathbf{E}^0}{\partial t}\right) \\ &+ \frac{ik_0c^2}{2\omega_0^2}\left(\mathbf{E}^0 \cdot \frac{\partial \mathbf{E}^{0*}}{\partial z} - \mathbf{E}^{0*} \cdot \frac{\partial \mathbf{E}^0}{\partial z}\right)\Bigg\} + \delta N_e\phi. \end{aligned}$$

In the last term, which is proportional to the small perturbation of the electron density, it is sufficient to use the lowest order expression for the high-frequency potential, $\phi = \frac{e^2|\mathbf{E}^0|^2}{4m\omega_0^2}$. This circumstance and Eq. (1.13) allow us to see that the first-order terms in the expression for w_L exactly cancel each other out; as a result, we obtain $w_L = \frac{1}{8\pi}|\mathbf{E}^0|^2$. We emphasize that this simple expression for the energy density is valid in the first-order approximation.

According to formula (1.11), the energy density $\mathbf{S}_L$ of the laser pulse is the sum of two terms. The first term is a conventional Poynting vector, and the second term describes the transport of the energy of high-frequency oscillations due to the slow plasma motion. To first order in the derivatives of the slowly varying quantities, the mean energy flux density $\mathbf{S}_L$ of the high-frequency laser field (1.12) reduces to

$$\begin{aligned} \mathbf{S}_L = \frac{c^2k_0}{8\pi\omega_0}\Bigg\{&\mathbf{e}_z\left[|\mathbf{E}^0|^2 + \frac{i}{2\omega_0}\left(\mathbf{E}^0 \cdot \frac{\partial \mathbf{E}^{0*}}{\partial t} - \text{c.c.}\right)\right] \\ &+ \frac{i}{2k_0}(\nabla \times [\mathbf{E}^0 \times \mathbf{E}^{0*}] + (E_k^0\nabla E_k^{0*} - \text{c.c.}))\Bigg\}. \end{aligned} \tag{1.14}$$

From Eqs. (1.4)–(1.6) for the low-frequency plasma perturbations, we can readily obtain an equation for each of the perturbed quantities:

$$\begin{aligned} \left(\frac{\partial^2}{\partial t^2} + \omega_p^2\right)\mathbf{E} &= \frac{\omega_p^2}{e}\nabla\phi, \\ \left(\frac{\partial^2}{\partial t^2} + \omega_p^2\right)\delta N_e &= \frac{N_{0e}}{m}\Delta\phi, \end{aligned} \tag{1.15}$$

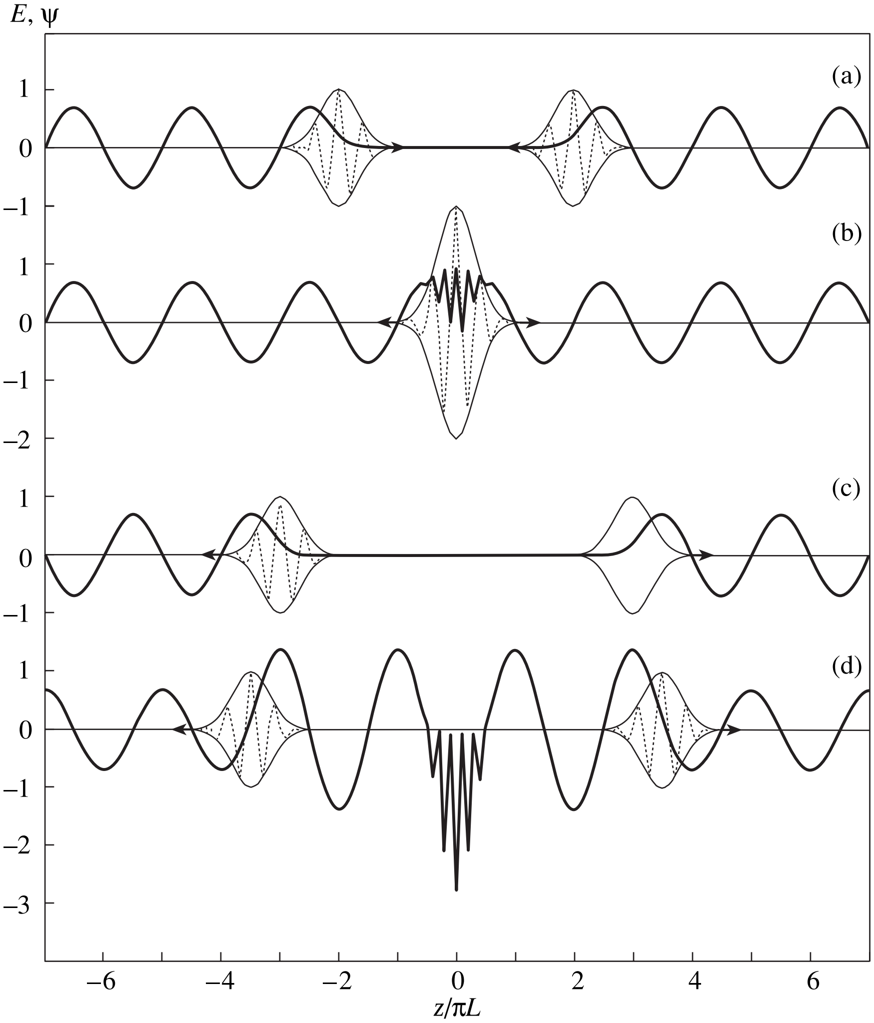

Fig. 1. Scheme illustrating the processes of the interaction between two short laser pulses and the generation of plasma perturbations at different instants of time. The envelopes of the laser pulses and the high-frequency oscillations of the laser field (normalized to the pulse amplitude) are represented by light solid curves and dotted curves, respectively. The heavy solid curves show the potential of the plasma perturbations, $\psi = \frac{1}{2}\left[\Phi\left(-\frac{\xi}{L}, \omega_p\tau\right) + \Phi\left(\frac{\eta}{L}, \omega_p\tau\right)\right] + \exp\left(-\frac{z^2}{L^2}\right)\Phi\left(\frac{t}{\tau}, \omega_p\tau\right)\cos(2k_0z)$ for pulses with the duration $\tau = \omega_p^{-1}$ and a carrier frequency such that $\omega_p/\omega_0 = 0.2$. Plots (a), (b), (c), and (d) refer to the times $t/\pi\tau = -2, 0, 3$, and 3.5. In plot (c), referring to the time $t/\pi\tau = 3$, the potential ψ vanishes in the region between the pulses after their interaction.

$$\left(\frac{\partial^2}{\partial t^2} + \omega_p^2\right)\mathbf{V}_e = -\frac{1}{m}\frac{\partial}{\partial t}\nabla\phi.$$

Note that, using Eq. (1.6), expression (1.8) can be represented the form

$$w_p = \frac{1}{8\pi}\left\{\mathbf{E}^2 + \frac{1}{\omega_p^2}\left(\frac{\partial\mathbf{E}}{\partial t}\right)^2\right\}, \tag{1.16}$$

which will be used below. As a result, to the lowest order in the derivatives of the slowly varying quantities, Eq. (1.7) describing the evolution of the energy density w_p of the low-frequency plasma perturbations takes the form

$$\begin{aligned}\frac{\partial w_p}{\partial t} + \nabla\cdot\left(\frac{\omega_p^2}{16\pi\omega_0^2}\mathbf{V}_e|\mathbf{E}^0|^2\right)\\ = -\frac{\omega_p^2}{16\pi\omega_0^2}|\mathbf{E}^0|^2\frac{\partial}{\partial t}\left(\frac{\delta N_e}{N_{0e}}\right).\end{aligned} \tag{1.17}$$

2. COLLISION BETWEEN TWO LASER PULSES

Below, we will be interested in the interaction between two identical laser pulses propagating toward one another along the *z*-axis (Fig. 1). We assume that the plasma is tenuous and only slightly affects the propagation of laser pulses. Consequently, when considering perturbations produced in a plasma by laser pulses, we can assume in the zeroth approximation that the fields of the pulses are given function of coordinates and time. We specify these fields in the form

$$\mathbf{E}_L(\mathbf{r}, t) = \frac{1}{2}\{\exp(-i\omega_0 t)[\mathbf{E}_+(\mathbf{r}, t)\exp(ik_0 z) + \mathbf{E}_-(\mathbf{r}, t)\exp(-ik_0 z)] + \text{c.c.}\}, \tag{2.1}$$

where $k_0 = \frac{1}{c}\sqrt{\omega_0^2 - \omega_p^2}$. The amplitudes $\mathbf{E}_\pm$ of the electric fields of laser pulses propagating from left to right (the plus sign) and from right to left (the minus sign) vary slowly on the time and spatial scales ω_0^{-1} and k_0^{-1}. The averaged potential ϕ of the high-frequency field is determined by the high-frequency electron velocity $\mathbf{V}_L$, which can be expressed in terms of electric fields (2.1) with the help of Eq. (1.1). To first order in the derivatives of the slowly varying amplitudes, we obtain

$$\begin{aligned}\phi = \frac{e^2}{4m\omega_0^2}\bigg\{&\left[|\mathbf{E}_+|^2 + \frac{i}{\omega_0}\left(\mathbf{E}_+\cdot\frac{\partial\mathbf{E}_+^*}{\partial t} - \text{c.c.}\right)\right] \\ &+ \left[|\mathbf{E}_-|^2 + \frac{i}{\omega_0}\left(\mathbf{E}_-\cdot\frac{\partial\mathbf{E}_-^*}{\partial t} - \text{c.c.}\right)\right] \\ &+ \left[\mathbf{E}_+\cdot\mathbf{E}_-^* + \frac{i}{\omega_0}\left(\mathbf{E}_+\cdot\frac{\partial\mathbf{E}_-^*}{\partial t} - \mathbf{E}_-^*\cdot\frac{\partial\mathbf{E}_+}{\partial t}\right)\right]\exp(2ik_0 z) \\ &+ \left[\mathbf{E}_+^*\cdot\mathbf{E}_- + \frac{i}{\omega_0}\left(\mathbf{E}_-\cdot\frac{\partial\mathbf{E}_+^*}{\partial t} - \mathbf{E}_+^*\cdot\frac{\partial\mathbf{E}_-}{\partial t}\right)\right]\exp(-2ik_0 z)\bigg\}.\end{aligned} \tag{2.2}$$

This formula implies that each of the two pulses produces ponderomotive forces along its path and, in the interaction region, they also generate small-scale high-frequency ponderomotive forces. Accordingly, all of the quantities that vary slowly with time (δN_e, $\mathbf{V}_e$, $\mathbf{E}$) contain terms varying slowly in space and those varying rapidly on a spatial scale of $(2k_0)^{-1}$ and thus can be represented as

$$\mathbf{V}_e = \mathbf{V}_0 + \mathbf{V}_2\exp(2ik_0 z) + \mathbf{V}_2^*\exp(-2ik_0 z), \tag{2.3}$$

$$\delta N_e = n_0 + n_2\exp(2ik_0 z) + n_2^*\exp(-2ik_0 z), \tag{2.4}$$

$$\mathbf{E} = \mathbf{E}_0 + \mathbf{E}_2\exp(2ik_0 z) + \mathbf{E}_2^*\exp(-2ik_0 z), \tag{2.5}$$

where the subscript 0 refers to the large-scale components and the subscript 2 denotes the amplitudes of the small-scale quantities. By means of Eqs. (1.15), it is possible to express all of the slowly varying quantities in terms of high-frequency potential (2.2).

Using formula (2.5), we average expression (1.16) for the energy density of the plasma perturbations over rapid variations in space. As a result, we see that the averaged energy density $\bar{w}_p$ is the sum of two terms, $\bar{w}_p = w_{p0} + w_{p2}$, where

$$w_{p0} = \frac{1}{8\pi}\left\{\mathbf{E}_0^2 + \frac{1}{\omega_p^2}\left(\frac{\partial\mathbf{E}_0}{\partial t}\right)^2\right\}, \tag{2.6}$$

$$w_{p2} = \frac{1}{4\pi}\left\{|\mathbf{E}_2|^2 + \frac{1}{\omega_p^2}\left(\frac{\partial\mathbf{E}_2}{\partial t}\right)^2\right\}. \tag{2.7}$$

The equations describing the temporal evolution of the energy densities of the large- and small-scale plasma perturbations can be obtained from Eq. (1.7). Using Eqs. (2.2), (2.4), and (2.5), to the lowest order in the derivatives of the slowly varying quantities, we obtain

$$\frac{\partial w_{p0}}{\partial t} + \nabla\cdot\mathbf{q}_0 = -\frac{\omega_p^2}{16\pi\omega_0^2}(|\mathbf{E}_+|^2 + |\mathbf{E}_-|^2)\frac{\partial}{\partial t}\left(\frac{n_0}{N_{0e}}\right), \tag{2.8}$$

$$\frac{\partial w_{p2}}{\partial t} + \nabla\cdot\mathbf{q}_0 = -\frac{\omega_p^2}{16\pi\omega_0^2}\left[\mathbf{E}_+\cdot\mathbf{E}_-^*\frac{\partial}{\partial t}\left(\frac{n_2}{N_{0e}}\right)^* + \text{c.c.}\right], \tag{2.9}$$

where

$$\mathbf{q}_0 = \frac{\omega_p^2}{16\pi\omega_0^2}\mathbf{V}_0(|\mathbf{E}_+|^2 + |\mathbf{E}_-^2|), \tag{2.10}$$

$$\mathbf{q}_2 = \frac{\omega_p^2}{16\pi\omega_0^2}[\mathbf{V}_2^*(\mathbf{E}_+\cdot\mathbf{E}_-^*) + \text{c.c.}]. \tag{2.11}$$

The right-hand sides of Eqs. (2.8) and (2.9) describe the energy fractions that the laser pulses lose by generating large- and small-scale plasma perturbations, respectively.

According to the above definition, the energy density of each of the pulses is equal to

$$w_\pm = \frac{|\mathbf{E}_\pm|^2}{8\pi}. \tag{2.12}$$

The equations describing how the energy density of each pulse evolves in time follow from Eq. (1.9) and expressions (2.1), (2.2), and (2.4):

$$\begin{aligned}\frac{\partial w_\pm}{\partial t} + \nabla\cdot\mathbf{S}_\pm = \pm\frac{\omega_p^2}{32\pi\omega_0 i}&\left\{\frac{n_2}{N_{0e}}\left[\mathbf{E}_+^*\cdot\left(1 - \frac{i}{\omega_0}\frac{\partial}{\partial t}\right)\mathbf{E}_- + \mathbf{E}_-\cdot\left(1 + \frac{i}{\omega_0}\frac{\partial}{\partial t}\right)\mathbf{E}_+^*\right] - \text{c.c.}\right\} \\ &+ \frac{\omega_p^2}{16\pi\omega_0^2}\left\{|\mathbf{E}_\pm|^2\frac{\partial}{\partial t}\left(\frac{n_0}{N_{0e}}\right) + \frac{1}{2}\left[\mathbf{E}_+\cdot\mathbf{E}_-^*\frac{\partial}{\partial t}\left(\frac{n_2^*}{N_{0e}}\right) + \text{c.c.}\right]\right\},\end{aligned} \tag{2.13}$$

where

$$\mathbf{S}_\pm = \pm\frac{c^2k_0}{8\pi\omega_0}\left\{\mathbf{e}_Z\left[|\mathbf{E}_\pm|^2 + \frac{i}{2\omega_0}\left(\mathbf{E}_\pm\cdot\frac{\partial\mathbf{E}_\pm^*}{\partial t} - \text{c.c.}\right)\right]\right. \qquad (2.14)$$
$$\left.\pm\frac{i}{2k_0}(\nabla\times[\mathbf{E}_\pm\times\mathbf{E}_\pm^*] + (E_{\pm k}\boldsymbol{\nabla}E_{\pm k}^* - \text{c.c.}))\right\},$$

with $\mathbf{e}_Z$ the unit vector directed along the z-axis.

The first terms on the right-hand side of Eqs. (2.13) describe the interaction between the pulses. In the equation for the total energy of the pulses, $w_L = w_+ + w_-$, which is obtained by summing Eqs. (2.13) for w_+ and w_-, these first terms cancel one another. Therefore, the right-hand side of the equation for the total energy of the pulses coincides in absolute value with the right-hand side of the sum of Eqs. (2.8) and (2.9) but has the opposite sign. As a result, the conservation laws for the total energy of the laser pulses and the plasma perturbations generated by them reduces to the form

$$\frac{\partial}{\partial t}(w_+ + w_- + w_{p0} + w_{p2}) \qquad (2.15)$$
$$+\nabla\cdot(\mathbf{S}_+ + \mathbf{S}_- + \mathbf{q}_0 + \mathbf{q}_2) = 0.$$

It is obvious that, if there is no energy flux through the boundaries of the volume under consideration, then the volume-averaged total energy of the pulses and the plasma perturbations is time-independent and is equal to the initial energy of the pulses injected into the plasma.

3. LARGE-SCALE PLASMA PERTURBATIONS

To the lowest order in the derivatives of the slowly varying amplitudes, the equation that describes the time evolution of the envelope $\mathbf{E}_0$ can be obtained by substituting into the first of Eqs. (1.15) the part of high-frequency potential (2.2) that is associated with large-scale plasma perturbations:

$$\left(\frac{\partial^2}{\partial t^2} + \omega_p^2\right)\mathbf{E}_0 = \frac{e\omega_p^2}{4m\omega_0^2}\boldsymbol{\nabla}(|\mathbf{E}_+|^2 + |\mathbf{E}_-|^2). \qquad (3.1)$$

In the vicinity of the interaction region, the longitudinal profiles of the pulses are assumed to be Gaussian:

$$\mathbf{E}_{+0}(\mathbf{r}, t) = \mathbf{E}_\perp(\rho)\exp\left(-\frac{\xi^2}{2L^2}\right),$$
$$\mathbf{E}_{-0}(\mathbf{r}, t) = \mathbf{E}_\perp(\rho)\exp\left(-\frac{\eta^2}{2L^2}\right), \qquad (3.2)$$

where $\xi = z - V_g t$, $\eta = z + V_g t$, $V_g = c^2k_0/\omega_0$ is the group velocity of the pulses, L is their length, and the vector $\mathbf{E}_\perp(\rho)$ determines their polarization and their radial ($\rho = \sqrt{x^2 + y^2}$) shape. We assume that the polarization of laser pulses is linear (the polarization vector being $\mathbf{e}_L$) and that the spatial distribution of their energy density is axisymmetric. The coordinate system and the initial instant of time are chosen in such a way that, at $t = 0$, the pulses exactly overlap one another and the functions $\mathbf{E}_+$ and $\mathbf{E}_-$ are maximum at the point $z = 0$ (Fig. 1b).

It follows from Eq. (3.1) that, in the given approximation, large-scale plasma fields are generated by the pulses independently of one another and the total field is their superposition:

$$\mathbf{E}_0(\mathbf{r}, t) \qquad (3.3)$$
$$= \frac{e}{4m\omega_0^2}\boldsymbol{\nabla}\left\{|\mathbf{E}_\perp(\rho)|^2\left[\Phi\left(-\frac{\xi}{L}, \omega_p\tau\right) + \Phi\left(\frac{\eta}{L}, \omega_p\tau\right)\right]\right\},$$

where $\tau = (L/V_g)$ is the pulse duration and

$$\Phi(x, a) = a\int_{-\infty}^{x} dy\sin[a(x-y)]\exp(-y^2). \qquad (3.4)$$

In what follows, we assume that the radial profiles of the pulses are also Gaussian:

$$\mathbf{E}_\perp(\rho) = \mathbf{e}_L E_{0L}\exp\left(-\frac{\rho^2}{2R^2}\right), \qquad (3.5)$$

where E_{0L} is the maximum electric field amplitude and R is the characteristic transverse size (radius) of the pulse.

In this case, expression (3.3) becomes

$$\mathbf{E}_0(\mathbf{r}, t) = \frac{\omega_p}{\omega_0}\frac{V_E}{4c}E_{0L}\exp\left(-\frac{\rho^2}{R^2}\right)$$
$$\times\left\{\mathbf{e}_Z\left[F\left(\frac{\eta}{L}, \omega_p\tau\right) - F\left(-\frac{\xi}{L}, \omega_p\tau\right)\right]\right. \qquad (3.6)$$
$$\left.-\mathbf{e}_\rho\frac{2\rho}{k_pR^2}\left[\Phi\left(\frac{\eta}{L}, \omega_p\tau\right) + \Phi\left(-\frac{\xi}{L}, \omega_p\tau\right)\right]\right\},$$

where $V_E = eE_{0L}/m\omega_0$ is the maximum electron oscillatory velocity in the laser field, $k_p = \omega_p/V_g$, $\mathbf{e}_Z$ and $\mathbf{e}_\rho$ are the unit vectors in the axial and radial directions, and

$$F(x, a) = a\int_{-\infty}^{x} dy\cos[a(x-y)]\exp(-y^2) \qquad (3.7)$$
$$= \frac{1}{a}\frac{\partial\Phi(x, a)}{\partial x}.$$

The functions $\Phi(x, a)$ and $F(x, a)$ describe, respectively, the dependence of the axial and radial components of the plasma electric field on the longitudinal coordinates both inside and outside the pulses.

Total large-scale plasma field (3.6) is a superposition of the fields generated by each of the pulses and thus does not provide information about the interaction between them. In the general case, however, the principle of superposition does not apply to energy density (2.6), which is quadratic in the fields. Substituting expression (3.6) into formula (2.6), we obtain

$$
\begin{aligned}
w_{p0} &= \frac{\omega_p^2}{\omega_0^2}\left(\frac{V_E}{4c}\right)^2\frac{E_{0L}^2}{8\pi}\exp\left(-\frac{2\rho^2}{R^2}\right)\\
&\times\left\{\left[F\left(\frac{\eta}{L},\omega_p\tau\right)-F\left(-\frac{\xi}{L},\omega_p\tau\right)\right]^2+\left[\exp\left(-\frac{\eta^2}{L^2}\right)\right.\right.\\
&\left.-\exp\left(-\frac{\xi^2}{L^2}\right)+\Phi\left(-\frac{\xi}{L},\omega_p\tau\right)-\Phi\left(\frac{\eta}{L},\omega_p\tau\right)\right]^2 \qquad (3.8)\\
&+\frac{4\rho^2}{k_p^2R^4}\left(\left[\Phi\left(\frac{\eta}{L},\omega_p\tau\right)+\Phi\left(-\frac{\xi}{L},\omega_p\tau\right)\right]^2\right.\\
&\left.\left.+\left[F\left(\frac{\eta}{L},\omega_p\tau\right)+F\left(-\frac{\xi}{L},\omega_p\tau\right)\right]^2\right)\right\}.
\end{aligned}
$$

The squared expressions in the square brackets in formula (3.8) contain the terms involving the products of the functions that refer to both of the pulses and characterize their interaction.

In order to analyze formulas (3.6) and (3.8), we rewrite the function $\Phi(x, a)$ in terms of the function $J_+(\beta)$ [20], which is widely used in plasma theory:

$$
\Phi(x,a) = \frac{a}{2\sqrt{2}}\exp(-x^2)\left[\frac{1}{\beta}J_+(\beta)+\text{c.c.}\right], \qquad (3.9)
$$

where $\beta = \frac{a}{\sqrt{2}} - i\sqrt{2}x$,

$$
J_+(\beta) = \beta\exp\left(-\frac{\beta^2}{2}\right)\int_{i\infty}^{\beta}dx\exp\left(\frac{x^2}{2}\right), \qquad (3.10)
$$

$a = \omega_p\tau$, and $x = \eta/L$ or $-\xi/L$. The real part of β is equal to the ratio of the pulse duration to the period of plasma oscillations, and the imaginary part of β determines the coordinate normalized to the pulse length in the frames of reference of the propagating pulses. Figure 2 shows how function (3.9) depends on the variable x for different values of the parameter a, characterizing the pulse length. It can be seen that the shape of the function is very sensitive to a. For a values smaller than 3, the function oscillates behind the pulses, whereas, for $a = 5$ (curve *4*), it is essentially nonzero only within the pulses.

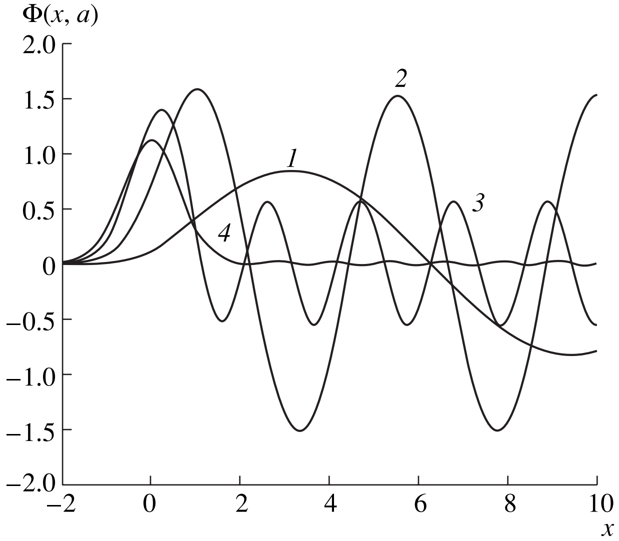

Fig. 2. Function $\Phi(x, a)$ vs. variable x for different values of the parameter a: a = (*1*) 0.5, (*2*) $\sqrt{2}$, (*3*) 3, and (*4*) 5.

For short ($a < 1$) and long ($a > 1$) laser pulses, expression (3.9) and, accordingly, formulas (3.8) and (3.6) can be substantially simplified.

For short pulses, we can utilize the following asymptotic expansion of the function $\Phi(x, a)$ at sufficiently long distances from the centers of the pulses ($|x| > 1, a$):

$$
\Phi(x,a) = \begin{cases}\dfrac{a^2}{a^2+4x^2}\exp(-x^2), & x<0\\ \sqrt{\pi}a\exp(-a^2/4)\sin(ax), & x>0.\end{cases} \qquad (3.11)
$$

Using expansion (3.11), we can see from expression (3.6) that, behind the pulse propagating from left to right, the electric field of the wake wave has the form

$$
\begin{aligned}
\mathbf{E}_0^+(\mathbf{r},t) &= -\sqrt{\pi}\omega_p\tau\frac{\omega_p}{\omega_0}\frac{V_E}{4c}E_{0L} \qquad (3.12)\\
&\times\exp\left(-\frac{\omega_p^2\tau^2}{4}-\frac{\rho^2}{R^2}\right)\left\{\mathbf{e}_Z\cos(k_p\xi)-\mathbf{e}_\rho\frac{2\rho}{k_pR^2}\sin(k_p\xi)\right\}.
\end{aligned}
$$

The wake electric field of the pulse traveling in the opposite direction is represented in an analogous manner.

According to formula (3.12), the electric field at each point in space (except at the axis $\rho = 0$) has both axial and radial components. The phases of these components are shifted by $\pi/2$ with respect to each other. This indicates that the field vector rotates in the (z, ρ) plane in such a way that its end describes an ellipse, whose eccentricity depends on the radial coordinate. For $\rho < k_pR^2/2$, the ellipse is elongated in the z direction. For $\rho = k_pR^2/2$, the end of the electric vector describes a circle, and, for $\rho > k_pR^2/2$, the ellipse is elongated in the radial direction.

The electric field of the standing wake wave that arises between the short pulses after their interaction ($t > 0$) has the form

$$\mathbf{E}_0(\mathbf{r}, t) = -2\sqrt{\pi}\omega_p\tau\frac{\omega_p}{\omega_0}\frac{V_E}{4c}E_{0L}\exp\left(-\frac{\rho^2}{R^2}-\frac{\omega_p^2\tau^2}{4}\right)$$
$$\times\sin(\omega_p t)\left\{\mathbf{e}_Z\sin(k_pz)+\mathbf{e}_\rho\frac{2\rho}{k_pR^2}\cos(k_pz)\right\}. \qquad (3.13)$$

Now, we turn to an analysis of the energy density. According to formula (3.8), the energy density $w_{p0}^{\pm}$ of the wake plasma waves behind each of the short laser pulses ($\omega_p\tau < \sqrt{2}$) before their interaction is equal to

$$w_{p0}^{\pm} = \frac{\pi}{4}\omega_p^2\tau^2\frac{\omega_p^2}{\omega_0^2}\frac{V_E^2}{4c^2}\frac{E_{0L}^2}{8\pi}$$
$$\times\exp\left(-\frac{\omega_p^2\tau^2}{2}-\frac{2\rho^2}{R^2}\right)\left(1+\frac{4\rho^2}{k_p^2R^4}\right). \qquad (3.14)$$

We integrate expression (3.14) over the radius to obtain the energy $W_{p0}^{\pm}$ of the wake waves that is contained in a narrow layer of thickness dz and characterizes the energy lost by a pulse per unit length during its propagation:

$$\frac{dW_{p0}^{\pm}}{dz}$$
$$= \frac{\sqrt{\pi}}{8}\omega_p^2\tau^2\frac{\omega_p^2}{\omega_0^2}\frac{V_E^2}{4c^2}\frac{W_L}{L}\exp\left(-\frac{\omega_p^2\tau^2}{2}\right)\left(1+\frac{2}{k_p^2R^2}\right), \qquad (3.15)$$

where W_L is the total energy of the pulse,

$$W_L = \frac{E_{0L}^2}{8\pi}\pi^{3/2}R^2L. \qquad (3.16)$$

Recall that, in the region between short laser pulses after their interaction, their wake waves form a two-dimensional standing wake wave. According to formula (3.8), the energy density in this standing wave is

$$w_{p0} = \pi\omega_p^2\tau^2\frac{\omega_p^2}{\omega_0^2}\frac{V_E^2}{4c^2}\frac{E_{0L}^2}{8\pi}$$
$$\times\exp\left(-\frac{\omega_p^2\tau^2}{2}-\frac{2\rho^2}{R^2}\right)\left\{\sin^2(k_pz)+\frac{4\rho^2}{k_p^2R^4}\cos^2(k_pz)\right\}. \qquad (3.17)$$

The nodes of the standing wave (the zeros of its electric field) lie only on the axis ($\rho = 0$) at the points $k_pz_0 = \pi n$ ($n = 0, \pm1, \pm2, \ldots$). In the axial region ($\rho < k_pR^2/2$), the energy density is maximum at $k_pz_{\max} = (1 + 2n)(\pi/2)$ and is minimum at $k_pz_{\min} = \pi n$ ($n = 0, \pm1, \pm2, \ldots$). At the distance $\rho = k_pR^2/2$ from the axis, the energy density is independent of the longitudinal coordinate, and, at larger distances ($\rho > k_pR^2/2$), the maxima become the minima and vice versa.

Integrating function (3.17) over the period of its variations along the z-axis yields an energy density two times that in expression (3.14). This means that, in the wake field region, where the laser pulses are already absent, the energy of the plasma waves is conserved and the energy density in the standing wave is distributed in a specific manner.

The structure of the standing wake wave depends essentially on the pulse radius. Figure 3 shows the distribution of the energy density in a two-dimensional standing wake plasma wave for two pulses with different radii.

The total energy of the plasma waves generated by short laser pulses can be estimated by integrating expression (3.17) over a volume limited in the longitudinal direction by a distance equal to two Rayleigh lengths, $2Z_R = k_0R^2$, along which the pulse shapes change relatively insignificantly:

$$W_{p0} \simeq \frac{\sqrt{\pi}}{2}\omega_p\tau\frac{\omega_p}{\omega_0}\frac{V_E^2}{4c^2}\left(1+\frac{k_p^2R^2}{2}\right)W_L\exp\left(-\frac{\omega_p^2\tau^2}{2}\right). \qquad (3.18)$$

Under the restrictions stated above, this energy is much lower than the energy of the laser pulse.

In the opposite limit of long laser pulses ($a > 1$), the function $\Phi(x, a)$ at $a > x$, 1 can be described by the asymptotic formula

$$\Phi(x, a) = \frac{a^2}{a^2+4x^2}\left[1+2\frac{a^2-12x^2}{(a^2+4x^2)^2}\right]\exp(-x^2)$$
$$+\frac{\sqrt{\pi}}{2}a\exp(-a^2/4)\sin(ax). \qquad (3.19)$$

According to formula (3.6), the wake fields behind the pulses are exponentially small, but, inside each of the pulses, there is a large-scale electric field

$$\mathbf{E}_0^{+}(\mathbf{r}, t) = -\frac{\omega_p}{\omega_0}\frac{V_E}{4c}E_{0L}\exp\left(-\frac{\rho^2}{R^2}\right)$$
$$\times\left(\frac{2\xi}{k_pL^2}\mathbf{e}_Z+\frac{2\rho}{k_pR^2}\mathbf{e}_\rho\right)\frac{1}{1+4\xi^2/k_p^2L^4}\exp\left(-\frac{\xi^2}{L^2}\right). \qquad (3.20)$$

The field of the counterpropagating pulse is described by an analogous formula.

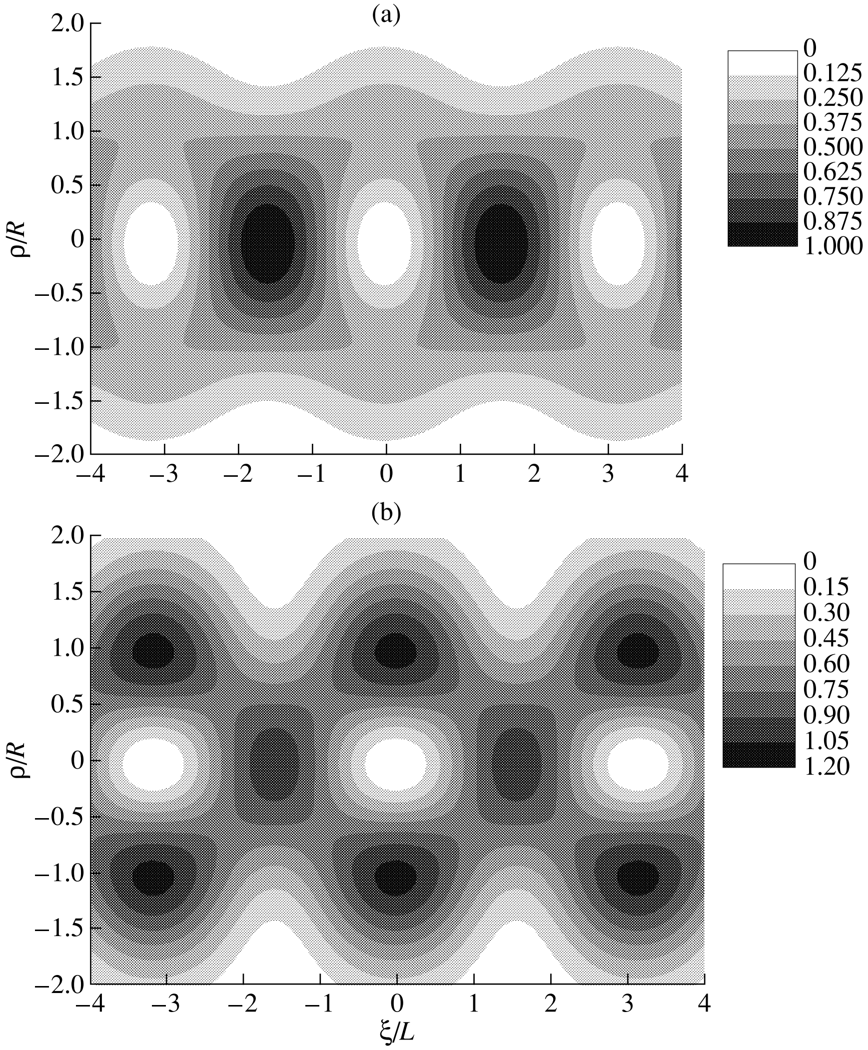

Fig. 3. Distributions of the dimensionless energy density of the standing wake wave in the plane of the variables ρ/R and ξ/L for laser pulses with the radii $R =$ (a) $\sqrt{2}k_p^{-1}$ and (b) $\sqrt{2/3}k_p^{-1}$.

The energy density of the large-scale plasma perturbations generated in the interaction between long pulses ($\omega_p\tau > \sqrt{2}$) can be determined from formula (3.8) by using asymptotic expression (3.19):

$$w_{p0} = \frac{1}{k_0^2R^2}\frac{V_E^2}{4c^2}\frac{E_{0L}^2}{8\pi}\exp\left(-\frac{2\rho^2}{R^2}\right) \times\left[\left(\frac{\rho^2}{R^2}+\frac{\eta^2}{L^2}\frac{R^2}{L^2}\right)\exp\left(-\frac{2\eta^2}{L^2}\right) + \left(\frac{\rho^2}{R^2}+\frac{\xi^2}{L^2}\frac{R^2}{L^2}\right)\exp\left(-\frac{2\xi^2}{L^2}\right) + 2\left(\frac{\rho^2}{R^2}+\frac{\xi\eta}{L^2}\frac{R^2}{L^2}\right)\exp\left(-\frac{2z^2}{L^2}-\frac{2t^2}{\tau^2}\right)\right]. \tag{3.21}$$

The first two terms on the right-hand side of this formula describe the energy density of the plasma perturbations within each of the pulses far from the interaction region. The last (third) term refers only to the collision between the pulses and describes additional energy that is transferred from the pulses to the plasma perturbations in the interaction process.

The energy density of the plasma perturbations inside a long pulse depends on the shape of the pulse. Figure 4 shows the distributions of the energy density within one of the pulses outside the interaction region [the first term in the square brackets in formula (3.21)],

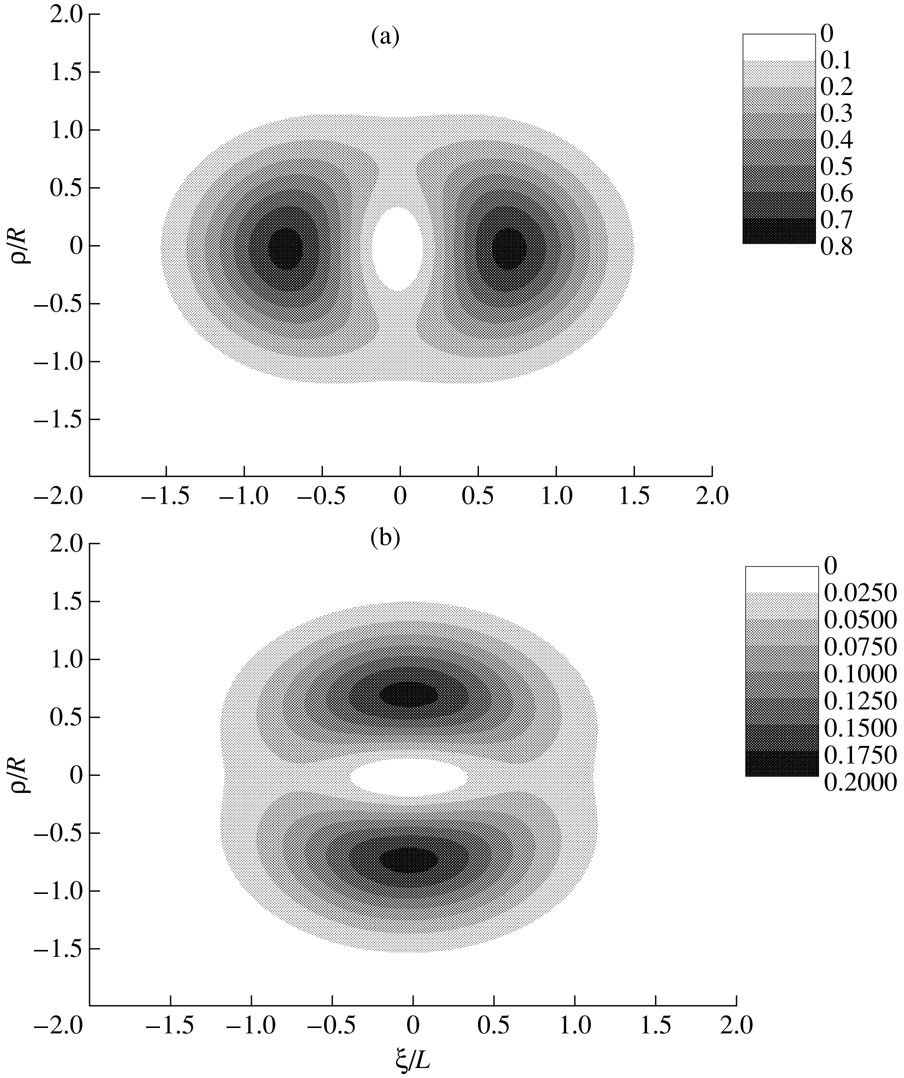

Fig. 4. Distributions of the dimensionless energy density of the plasma perturbations inside long laser pulses with radius-to-length ratios R/L = (a) 2 and (b) 1/2 in the plane of the variables ρ/R and ξ/L.

obtained for two different values of the length-to-radius ratio of the pulse.

We integrate expression (3.21) over the coordinates to obtain the time-dependent total energy of the plasma perturbations:

$$W_{p0} = \frac{1}{k_0^2R^2}\frac{V_E^2}{4c^2}\frac{W_L}{2\sqrt{2}} \times\left\{1+\frac{R^2}{2L^2}+\left[1+\frac{R^2}{2L^2}\left(1-4\frac{t^2}{\tau^2}\right)\right]\exp\left(-\frac{2t^2}{\tau^2}\right)\right\}. \tag{3.22}$$

Before ($t < -\tau$) and after ($t > \tau$) the collision, energy (3.22) is the sum of the energies of the large-scale plasma perturbations accompanying each of the laser pulses. At the beginning of the interaction process $\left(\frac{t}{\tau} < -\sqrt{\frac{3}{4}+\frac{L^2}{2R^2}}\right)$, the energy of the plasma fields is partially converted into the energy of the pulses. During the time interval $-\sqrt{\frac{3}{4}+\frac{L^2}{2R^2}} < \frac{t}{\tau} < 0$, the energy of the plasma perturbations increases and at $t = 0$ reaches its maximum value, which is twice that before the interaction. Then, the energy decreases and, at $\frac{t}{\tau} > \sqrt{\frac{3}{4}+\frac{L^2}{2R^2}}$, becomes equal to the energy before the interaction.

Note that the time evolution of the space-averaged total energy of large-scale plasma perturbations can be obtained from Eq. (2.8) for pulses of arbitrary duration. We determine n_0 from Eqs. (1.15) and formula (2.2) and carry out the necessary manipulations to arrive at the equation

$$\frac{\partial}{\partial t}W_{p0} = \frac{\sqrt{\pi}}{4}\omega_p^2\tau^2\frac{\omega_p^2}{\omega_0^2}\frac{V_E^2}{4c^2}\frac{W_L}{\tau}\left(1+\frac{2}{k_p^2R^2}\right)\exp\left(-\frac{\omega_p^2\tau^2}{2}\right) - \frac{\omega_p^2}{\omega_0^2}\frac{V_E^2}{4c^2}\frac{W_L}{4\sqrt{2}} \times\frac{\partial}{\partial t}\left\{\exp\left(-\frac{2t^2}{\tau^2}\right)-\left(1+\frac{2}{k_p^2R^2}\right)\Phi\left(\sqrt{2}\frac{t}{\tau},\sqrt{2}\omega_p\tau\right)\right\}. \tag{3.23}$$

The first term on the right-hand side describes the energy of the wake waves, which increases linearly with time and is not small only in the case of sufficiently short pulses. The second term becomes nonzero only after the interaction ($t > 0$).

For sufficiently long distances between the pulses after their interaction (on time scales $t \gg \tau$, $\omega_p\tau^2$), Eq. (3.23) transforms into the equation

$$\frac{\partial}{\partial t}W_{p0} = \frac{\sqrt{\pi}}{4}\omega_p^2\tau^2\frac{\omega_p^2}{\omega_0^2}\frac{V_E^2}{4c^2}\frac{W_L}{\tau}\left(1+\frac{2}{k_p^2R^2}\right) \times\exp\left(-\frac{\omega_p^2\tau^2}{2}\right)[1+2\cos(2\omega_p t)]. \tag{3.24}$$

The term oscillating at a frequency twice the plasma frequency is related to the interaction of each of the pulses with the wake field produced by the other pulse. This term is also not exponentially small only for short laser pulses ($\omega_p\tau < \sqrt{2}$).

Note that each of the pulses interacts with the wake field of the other pulse only in the region in which the structure of the wake wave remains unchanged. The length of this region can be estimated as the Rayleigh length Z_R only under the condition $Z_R < c/\omega_{pi}$, where $\omega_{pi} = \omega_p\sqrt{Zm_e/m_i}$ is the plasma frequency of the ions with charge Z and mass m_i. For larger values of Z_R, the effects associated with the perturbations of the ion plasma density can influence the shape of the wake waves.

4. SMALL-SCALE PLASMA PERTURBATIONS

In the interaction region, laser pulses not only perturb the plasma on large scales but also generate small-scale perturbations with a period equal to half the laser wavelength. Such small-scale perturbations were investigated in our recent paper [14], so we present below only the most important of the results obtained there.

Since the period of small-scale perturbations is small in comparison with the pulse radius, they can be treated as quasi-planar. The longitudinal component E_{2z} of the electric field of the perturbations is much stronger than their radial component and is related to the electron density perturbations n_2 in a simple way:

$$E_{2z} \approx \frac{4\pi e N_{0e}}{2ik_0}\frac{n_2}{N_{0e}}. \tag{4.1}$$

In turn, the electron density perturbations are described by the equation that follows from Eqs. (1.15), (2.2), and (2.4):

$$\left(\frac{\partial^2}{\partial t^2}+\omega_p^2\right)\frac{n_2}{N_{0e}} = -\frac{e^2}{m^2\omega_0^2}\left(k_0^2 - ik_0\frac{\partial}{\partial z}\right) \times\left\{\mathbf{E}_+\cdot\mathbf{E}_-^* + \frac{i}{\omega_0}\left(\mathbf{E}_+\cdot\frac{\partial\mathbf{E}_-^*}{\partial t} - \mathbf{E}_-^*\cdot\frac{\partial\mathbf{E}_+}{\partial t}\right)\right\}. \tag{4.2}$$

On the right-hand side of Eq. (4.2), we retain small terms proportional to the derivatives of the slowly varying amplitudes because these terms play an important role in calculating the time evolution of the energy of the laser pulses.

The solution to Eq. (4.2) that satisfies the condition that there be no small-scale electron density perturbations before the interaction has the form

$$\frac{n_2}{N_{0e}} = -\left(k_0^2 + 2ik_0\frac{z}{L^2}\frac{\omega_p^2}{\omega_0^2}\right)\frac{e^2|\mathbf{E}_\perp(\rho)|^2}{m^2\omega_0^2\omega_p^2} \times\exp\left(-\frac{z^2}{L^2}\right)\Phi\left(\frac{t}{\tau},\omega_p\tau\right). \tag{4.3}$$

The time dependence enters solution (4.3) through function (3.9).

According to formula (2.7), the energy density of the small-scale plasma perturbations is also expressed in terms of the function Φ:

$$w_{p2} = \frac{e^2k_0^2|\mathbf{E}_\perp(\rho)|^2}{16\pi m^2\omega_0^4} \times\exp\left(-\frac{2z^2}{L^2}\right)\left\{\Phi^2\left(\frac{t}{\tau},\omega_p\tau\right)+\frac{1}{\omega_p^2}\left[\frac{\partial}{\partial t}\Phi\left(\frac{t}{\tau},\omega_p\tau\right)\right]^2\right\}. \tag{4.4}$$

For laser pulses with a Gaussian radial profile [see formula (3.5)], we integrate the total energy of the small-scale plasma perturbations over the interaction region to obtain, using formula (4.4),

$$W_{p2} = \frac{k_0^2V_E^2}{4\omega_0^2}\frac{W_L}{\sqrt{2}}\left\{\Phi^2\left(\frac{t}{\tau},\omega_p\tau\right)+\frac{1}{\omega_p^2}\left[\frac{\partial}{\partial t}\Phi\left(\frac{t}{\tau},\omega_p\tau\right)\right]^2\right\}, \tag{4.5}$$

where the total energy of the pulse, W_L, is given by expression (3.16). In order of magnitude, the energy of the plasma perturbations is lower than the pulse energy by a factor of $(V_E/c)^2$.

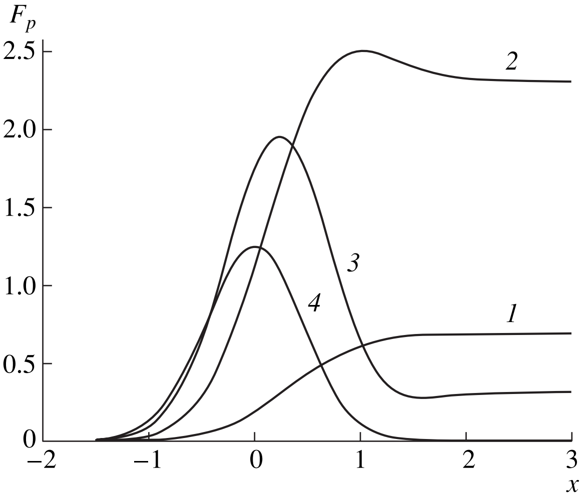

Fig. 5. Dimensionless energy of plasma perturbations $F_p = \frac{W_p}{W_L}\frac{4\sqrt{2}\omega_0^2}{k_0^2V_E^2}$ vs. dimensionless time $x = t/\tau$ for pulses with the same durations as in Fig. 2.

The time evolution of the small-scale perturbations can be examined by using the familiar asymptotic expressions of the function $\Phi(x, a)$. For sufficiently long distances between the pulses after their collision (on time scales such that $t > 0$, $t \gg \tau$, $t \gg \omega_p\tau^2/2$), asymptotic expansion (3.11) puts density perturbations (4.3) in the form

$$\frac{n_2}{N_{0e}} = -\sqrt{\pi}\omega_p\tau\left(k_0^2 + 2ik_0\frac{z}{L^2}\frac{\omega_p^2}{\omega_0^2}\right)\frac{e^2|\mathbf{E}_\perp(\rho)|^2}{m^2\omega_0^2\omega_p^2} \times \exp\left(-\frac{z^2}{L^2} - \frac{\omega_p^2\tau^2}{4}\right)\sin\omega_p t. \tag{4.6}$$

From this formula, we can see that the density perturbations are plasma oscillations localized in space. Under otherwise equal conditions, such oscillations are most efficiently generated by laser pulses with the duration $\tau = \sqrt{2}/\omega_p$. The amplitude of the plasma oscillations excited by long pulses ($\omega_p\tau \gg 1$) is exponentially small.

In accordance with formula (4.5), the total energy of the small-scale plasma oscillations is equal to

$$W_{p2} = \frac{\pi}{\sqrt{2}}\omega_p^2\tau^2\frac{k_0^2V_E^2}{4\omega_0^2}W_L\exp\left(-\frac{\omega_p^2\tau^2}{2}\right). \tag{4.7}$$

The generation of plasma waves and the time evolution of their energy during a collision between the pulses can be investigated separately for long and short laser pulses.

During the collision ($\omega_p\tau < \sqrt{2}$) between short ($t < \tau$) pulses, the function can be described by the asymptotic expression

$$\Phi(x, a) = \frac{1}{2}a^2\exp(-x^2)\left\{1 + \sqrt{\pi}x - \frac{1}{6}(a^2 - 12x^2)\right\}$$

and, in accordance with solution (4.3), the amplitude of the small-scale electron density perturbations has the form

$$\frac{n_2}{N_{0e}} = -\left(k_0^2 + 2ik_0\frac{z}{L^2}\frac{\omega_p^2}{\omega_0^2}\right)\frac{e^2\tau^2|\mathbf{E}_\perp(\rho)|^2}{2m^2\omega_0^2} \times \exp\left(-\frac{z^2}{L^2} - \frac{t^2}{\tau^2}\right)\left\{1 + \sqrt{\pi}\frac{t}{\tau} - \frac{1}{6}\left(\omega_p^2\tau^2 - 12\frac{t^2}{\tau^2}\right)\right\}. \tag{4.8}$$

The energy of the plasma oscillations increases according to the law

$$W_{p2}(t) = \frac{\pi}{4\sqrt{2}}\omega_p^2\tau^2\frac{k_0^2V_E^2}{4\omega_0^2}W_L\exp\left(-\frac{2t^2}{\tau^2}\right)\left(1 + \frac{4}{\sqrt{\pi}}\frac{t}{\tau}\right). \tag{4.9}$$

For long ($\omega_p\tau > \sqrt{2}$) laser pulses, the time evolution of the plasma perturbations on time scales $t < \omega_p\tau^2/2$ during ($t < \tau$) and after ($t > \tau$) the collision is described by the formula

$$\frac{n_2}{N_{0e}} = -\left(k_0^2 + 2ik_0\frac{z}{L^2}\frac{\omega_p^2}{\omega_0^2}\right)\frac{e^2|\mathbf{E}_\perp(\rho)|^2}{m^2\omega_0^2\omega_p^2} \times \exp\left(-\frac{z^2}{L^2}\right)\left\{\frac{\omega_p^2\tau^2}{\omega_p^2\tau^2 + 4\frac{t^2}{\tau^2}}\exp\left(-\frac{t^2}{\tau^2}\right) + \frac{\sqrt{\pi}}{2}\omega_p\tau\exp\left(-\frac{\omega_p^2\tau^2}{4}\right)\sin(\omega_p t)\right\}. \tag{4.10}$$

The first term in parentheses in formula (4.10) describes the quasistatic plasma density perturbations, which are generated only during the interaction between the pulses; on time scales $t > \tau$, these perturbations are exponentially small. The second term describes the generation of plasma oscillations, which are exponentially small in the case of a long pulses.

The time evolutions of the energy of small-scale plasma oscillations generated by laser pulses of different lengths are shown in Fig. 5. One can see that the energy of the plasma perturbations generated by long pulses ($\omega_p\tau > \sqrt{2}$) increases to its maximum during the collision and then decreases. This effect stems from the fact that, at the beginning of the interaction, the pulses lose part of their energy by generating quasistatic electron density perturbations. Then, the phase difference between the driving force and the perturbations changes, and almost the same amount of energy is transferred back to the pulses. In contrast to the case of long pulses, part of the energy of short pulses [see formula (4.7)] is irreversibly converted in the interaction region into the energy of small-scale plasma oscillations, which remain in the plasma after the interaction.

Note that, for short-wavelength plasma oscillations, the cold plasma approximation is valid only under the condition $\delta = 2\sqrt{3}\frac{V_T}{c}\frac{\omega_0}{\omega_p} \ll 1$, where V_T is the electron thermal velocity. In this case, the duration of the pulses and the time scales on which the effects of the electron thermal motion are unimportant are restricted by the inequalities $\omega_p\tau$, $\omega_p t < \frac{2}{\delta^2}, \frac{\delta^3}{2}\exp\left(\frac{3}{2\delta^2}\right)$.

CONCLUSION

The question about the effects that occur in a plasma in the interaction between two laser pulses differing in carrier frequency or duration was discussed in [5–13]. Unlike in those papers, we have discussed the interaction between two identical pulses—the case that seems to be the simplest to realize experimentally. We have shown that the effects produced in such an interaction are sensitive to the ratio of the pulse duration to the period of the plasma waves. This ratio can be changed by changing the pulse duration and/or the plasma density. Short laser pulses ($\omega_p\tau \le \sqrt{2}$) excite plasma oscillations on two spatial scales. Wake plasma waves with the wavelength $\lambda_p = 2\pi/k_p$ are generated over the entire path of the pulses and form a standing wake wave in the region between the pulses after their interaction. In the interaction region, the pulses produce small-scale plasma oscillations with a wavelength equal to half the laser wavelength $\lambda_0 = 2\pi/k_0$, which remain in the plasma after the interaction. In the case of long laser pulses ($\omega_p\tau > \sqrt{2}$), the plasma perturbations are quasistatic and are also generated on two essentially different spatial scales. Plasma fields generated within the pulses on scales of about the pulse length grow in the interaction process. The fields that are generated only in the interaction region are small-scale and disappear after the interaction.

As an example, we consider the interaction between two identical 1-J short laser pulses with duration $\tau = 400$ fs ($L = 120$ μm), frequency $\omega_0 = 2.4 \times 10^{15}$ s^{-1} ($\lambda_0 = 0.8$ μm), and radius $R = 100$ μm in a fully ionized helium plasma with the electron density $N_{0e} = 1.3 \times 10^{19}$ cm^{-3}. For these parameter values, the radiation intensity is equal to 4.5×10^{15} W/cm^2 and the amplitude of the small-scale electron density perturbations is about $n_2/N_{0e} \approx 0.3$. We also have $\omega_p\tau \approx 80 \gg 1$, which corresponds to the generation of quasistatic electron density perturbations in the interaction region in such a plasma. The cold plasma approximation is valid for electron temperatures below 300 eV.

In [14], it was shown that such a stratified plasma can be used as a short-lived Bragg mirror, which may reflect about 25% of the energy of a probing wave.

Another example is provided by small-scale plasma oscillations. For laser pulses with the wavelength $\lambda_0 = 0.8$ μm and the duration $\tau = 30$ fs ($L = 9$ μm), the condition $\omega_p\tau = \sqrt{2}$ is satisfied for the electron density $N_{0e} = 7 \times 10^{17}$ cm^{-3}. Plasma oscillations in which the amplitude of the electron density perturbations amounts to about $n_2/N_{0e} \approx 0.3$ are generated in a collision between two moderate-power laser pulses with an intensity of 2×10^{14} W/cm^2, which, for a pulse with the radius $R = 9$ μm, corresponds to an energy of 1.6×10^{-5} J. For the above plasma parameters, the plasma ions on the Rayleigh length can be treated as immobile and the cold plasma approximation is satisfied for electron temperatures below 20 eV. Such localized coherent plasma oscillations may serve as a convenient object to study the destruction of coherence and the development of Langmuir turbulence under the conditions of laser experiments.

In our analysis, it was assumed that the density perturbations are small and can be described in the linear approximation. This condition restricts the radiation intensity to a level of 10^{15}–10^{17} W/cm^2 at a laser wavelength of about $\lambda_0 \approx 1$ μm. In present-day devices, the radiation intensity can be substantially higher when the density perturbations are nonlinear. By investigating the parameters of the plasma perturbations as functions of the radiation intensity, it is possible to study how the linear perturbations become nonlinear and trace their further evolution.

When propagating through a plasma toward one another and interacting with one another, short laser pulses ($\omega_p\tau < \sqrt{2}$) lose their energy by exciting large-scale plasma waves and small-scale plasma perturbations. The ratio of the fractions of energy lost by these two mechanisms can be estimated using formulas (A.19) and (A.13) (see the Appendix):

$$\frac{\delta W_{+0}}{\delta W_{+2}} = \frac{2 + k_p^2 R^2}{4\sqrt{2\pi}\omega_0\tau}.$$

This estimate shows that, under the condition $\omega_0\tau > (k_pR)^2$, which is easy to satisfy, the additional energy loss resulting from the interaction between two short pulses exceeds the loss by the generation of wake waves. It should be stressed, however, that laser pulses also lose their energy in other processes (Coulomb collisions, stimulated scattering, etc.). That is why energy loss caused by the excitation of plasma oscillations should be considered merely as an additional effect. Nevertheless, it seems quite possible to measure the fraction of energy additionally lost by short laser pulses in their interaction.

The nonlinear interaction between two wake waves propagating toward one another can be accompanied by the emission of radiation from the plasma at a frequency twice the plasma frequency (see, e.g., [21]). Such radiation may be used as a new diagnostic tool providing data on the interaction of high-power laser pulses with plasmas. The results of the investigation of this radiation will be published in a separate paper.

APPENDIX

Effect of the Interaction Process on Laser Pulses

Here, we consider how the energy and shape of the laser pulses change in their interaction. In the approach developed here, these changes are assumed to be small. Nevertheless, an analysis of the effect is helpful in revealing the tendencies that may become important under the conditions in which these changes will turn out to be measurable and thus will serve as a basis for additional diagnostics of the plasma processes accompanying the interaction.

In discussing the question about the pulse shape, we represent the energy density of the pulse in the form $w^{\pm} = w_0^{\pm} + \delta w^{\pm}$, where $w_0^{\pm}$ is the energy density before the interaction and $\delta w^{\pm}$ is the small correction caused by the interaction. As in the preceding discussion, we describe the pulses before the interaction by the Gaussian profiles $w_0^{+} = (E_{0L}^2/8\pi)\exp[-(\rho/R)^2 - (\xi/L)^2]$ and $w_0^{-} = (E_{0L}^2/8\pi)\exp[-(\rho/R)^2 - (\eta/L)^2]$, which satisfy Eqs. (2.13) in the zeroth approximation and depend only on the absolute value of complex amplitude (2.12). However, the first-order terms in Eqs. (2.13) contain the complex amplitude of the field envelope. That is why, in order to determine $\delta w^{\pm}$, it is necessary to know not only the amplitude of the envelope but also its phase, which is determined by field equation (1.13). Hence, the correction $\delta w^{\pm}$ can be found by substituting fields (2.1) into Eq. (1.13) and by using the following expressions for the amplitude of the field envelope:

$$\mathbf{E}_{\pm} = \mathbf{e}_L E_{\pm} = \mathbf{e}_L |E_{\pm}| \exp(i\varphi_{\pm}), \tag{A.1}$$

where $|E_{\pm}|$ is the absolute value of the complex amplitude and $\varphi_{\pm}$ is its phase.

In what follows, we restrict ourselves to considering only the pulse that propagates from left to right, because the results are also valid for the pulse propagating in the opposite direction. Substituting expression (A.1) into Eq. (1.13) and separating the real and imaginary parts, we obtain

$$\left(\frac{\partial}{\partial t} + V_g\frac{\partial}{\partial z}\right)w_+ - \frac{1}{\omega_0}\frac{\partial}{\partial t}\left(w_+\frac{\partial\varphi_+}{\partial t}\right) + \frac{c^2}{\omega_0}\nabla\cdot(w_+\boldsymbol{\nabla}\varphi_+)$$
$$= \frac{\omega_p^2}{16\pi\omega_0 i}\left(\frac{n_2}{N_{0e}}E_+^*E_- - \text{c.c.}\right) + \frac{\omega_p^2}{\omega_0^2}w_+\frac{\partial}{\partial t}\left(\frac{n_0}{N_{0e}}\right) \tag{A.2}$$
$$+ \frac{\omega_p^2}{16\pi\omega_0^2}\left[E_+E_-^*\frac{\partial}{\partial t}\left(\frac{n_2^*}{N_{0e}}\right) + \text{c.c.}\right],$$

$$\left(\frac{\partial}{\partial t} + V_g\frac{\partial}{\partial z}\right)\varphi_+ + \frac{c^2}{2\omega_0}(\boldsymbol{\nabla}\varphi_+)^2 - \frac{1}{2\omega_0}\left(\frac{\partial\varphi_+}{\partial t}\right)^2$$
$$= -\frac{\omega_p^2}{2\omega_0}\left(\frac{n_0}{N_{0e}} + \frac{n_2}{N_{0e}}\frac{E_-}{E_+}\right) + \frac{c^2}{4\omega_0}\left[\frac{\Delta w_+}{w_+} - \frac{(\boldsymbol{\nabla}w_+)^2}{2w_+^2}\right] \tag{A.3}$$
$$- \frac{1}{4\omega_0}\left[\frac{1}{w_+}\frac{\partial^2 w_+}{\partial t^2} - \frac{1}{2w_+^2}\left(\frac{\partial w_+}{\partial t}\right)^2\right].$$

Note that the correction δw_+ to the pulse energy density depends on the coordinate ρ; time t; and variable ξ, which characterizes the position of a point inside the moving pulse with respect to its center. Along with the correction δw_+, it is conventional to introduce the quantity $\delta I_+ = 2\pi\int_0^{\infty} d\rho\rho\delta w_+$, which determines the pulse shape in the longitudinal direction. The time evolution of the total pulse energy will be characterized by the expression $\delta W_+ = \int_{-\infty}^{+\infty} d\xi\delta I_+$.

We solve Eqs. (A.2) and (A.3) by means of the perturbation theory. In this way, Eq. (A.2) takes the form

$$\left(\frac{\partial}{\partial t} + V_g\frac{\partial}{\partial z}\right)\delta w_+ = \frac{1}{\omega_0}\frac{\partial}{\partial t}\left(w_0^+\frac{\partial\varphi_+}{\partial t}\right)$$
$$- \frac{c^2}{\omega_0}\nabla\cdot(w_0^+\boldsymbol{\nabla}\varphi_+) + \frac{\omega_p^2}{16\pi\omega_0 i}\left(\frac{n_2}{N_{0e}}E_+^*E_- - \text{c.c.}\right) \tag{A.4}$$
$$+ \frac{\omega_p^2}{\omega_0^2}w_0^+\frac{\partial}{\partial t}\left(\frac{n_0}{N_{0e}}\right) + \frac{\omega_p^2}{16\pi\omega_0^2}\left[E_+E_-^*\frac{\partial}{\partial t}\left(\frac{n_2^*}{N_{0e}}\right) + \text{c.c.}\right].$$

In the expression for the phase φ_+, we take into account only the effects that are associated with the plasma density perturbations. We also neglect linear dispersion, linear diffraction, and nonlinear effects that are proportional to the second derivatives of the slowly varying quantities. As a result, we arrive at the following solution to Eq. (A.3):

$$\varphi_{+} = \frac{V_E^2}{4c^2}\exp\left(-\frac{\rho^2}{R^2}\right)\left\{\frac{2k_0^2c^2}{\omega_0}\int_{-\infty}^{t} dt'\Phi\left(\frac{t'}{\tau}, \omega_p\tau\right)\right.$$
$$\times \exp\left[-\frac{\xi^2(t) + 4\xi(t)V_gt' + 3V_g^2t'^2}{L^2}\right]$$
$$-\frac{\omega_p^2}{2\omega_0}\left[t\exp\left(-\frac{\xi^2}{L^2}\right) + \int_{-\infty}^{\eta}\frac{d\eta'}{2V_g}\exp\left(-\frac{\eta'^2}{L^2}\right)\right. \tag{A.5}$$
$$+\left(\frac{4}{k_p^2R^2}\left(\frac{\rho^2}{R^2} - 1\right) - 1\right)$$
$$\left.\left.\times\left(t\Phi\left(-\frac{\xi}{L}, \omega_p\tau\right) + \int_{-\infty}^{\eta}\frac{d\eta'}{2V_g}\Phi\left(\frac{\eta'}{L}, \omega_p\tau\right)\right)\right]\right\},$$

where the first term in parentheses, which will be denoted by φ_{+2}, accounts for the effect of the small-scale plasma perturbations on the phase of the envelope and the second term, which will be denoted by φ_{+0}, describes the effect of the large-scale perturbations. According to Eq. (A.4) and solution (A.5), the large- and small-scale perturbations of the electron plasma density contribute additively to the correction to the pulse energy density: $\delta w_{+} = \delta w_{+0} + \delta w_{+2}$. The equations for each of the contributions follow from Eq. (A.4):

$$\left(\frac{\partial}{\partial t} + V_g\frac{\partial}{\partial z}\right)\delta w_{+0} = \frac{1}{\omega_0}\frac{\partial}{\partial t}\left(w_{+0}\frac{\partial\varphi_{+0}}{\partial t}\right)$$
$$-\frac{c^2}{\omega_0}\nabla\cdot(w_{+0}\boldsymbol{\nabla}\varphi_{+0}) + \frac{\omega_p^2}{\omega_0^2}w_{+0}\frac{\partial}{\partial t}\left(\frac{n_0}{N_{0e}}\right), \tag{A.6}$$

$$\left(\frac{\partial}{\partial t} + V_g\frac{\partial}{\partial z}\right)\delta w_{+2} = \frac{1}{\omega_0}\frac{\partial}{\partial t}\left(w_{+0}\frac{\partial\varphi_{+2}}{\partial t}\right)$$
$$-\frac{c^2}{\omega_0}\nabla\cdot(w_{+0}\boldsymbol{\nabla}\varphi_{+2}) + \frac{\omega_p^2}{16\pi\omega_0 i}\left(\frac{n_2}{N_{0e}}E_+^*E_- - \text{c.c.}\right) \tag{A.7}$$
$$+\frac{\omega_p^2}{16\pi\omega_0^2}\left[E_+E_-^*\frac{\partial}{\partial t}\left(\frac{n_2^*}{N_{0e}}\right) + \text{c.c.}\right].$$

First, we consider the change in the energy density of a laser pulse under the action of small-scale plasma perturbations. With allowance for expression (4.3) for the electron density perturbations n_2 and the expression for the phase φ_{+2}, Eq. (A.7) becomes

$$\left(\frac{\partial}{\partial t} + V_g\frac{\partial}{\partial z}\right)\delta w_{+2} = \frac{k_0^2V_E^2}{2\omega_0^2}\frac{E_{0L}^2}{8\pi}\exp\left(-\frac{2\rho^2}{R^2} - \frac{2z^2}{L^2} - \frac{t^2}{\tau^2}\right)$$
$$\times\left\{\frac{2z}{L\tau}\left(1 - 2\frac{\omega_p^2}{c^2k_0^2}\right)\Phi\left(\frac{t}{\tau}, \omega_p\tau\right) - \frac{\partial}{\partial t}\Phi\left(\frac{t}{\tau}, \omega_p\tau\right)\right\}$$
$$-\frac{\omega_p^2}{\omega_0^2}\frac{V_E^2}{c^2}\frac{E_{0L}^2}{8\pi}\frac{1}{\tau^2}\exp\left(-\frac{2\rho^2}{R^2} - \frac{\xi^2}{L^2}\right) \tag{A.8}$$
$$\times\int_{-\infty}^{t} dt'\Phi\left(\frac{t'}{\tau}, \omega_p\tau\right)\exp\left(-\frac{\xi^2 + 4\xi V_gt' + 3V_g^2t'^2}{L^2}\right)$$
$$\times\left\{\frac{4}{L^2}(\xi + 2V_gt')(\xi + V_gt') - 1 + \frac{c^2k_0^2}{\omega_p^2}\frac{2L^2}{R^2}\left(2\frac{\rho^2}{R^2} - 1\right)\right\}.$$

After the interaction ($t > \tau$), but at times that are much shorter than the Rayleigh time ($t \ll t_R = k_0R^2/2c$), Eq. (A.8) has the solution

$$\delta w_{+2} = \sqrt{\pi}\frac{k_0^2V_E^2}{4\omega_0^2}\frac{E_{0L}^2}{8\pi}$$
$$\times\left[\frac{2\xi}{L} + \frac{\omega_0^2}{c^2k_0^2}L\frac{\partial}{\partial\xi} - \frac{4L^2}{R^2}\frac{t}{\tau}\left(\frac{2\rho^2}{R^2} - 1\right)\right] \tag{A.9}$$
$$\times\exp\left(-\frac{2\rho^2}{R^2} - \frac{2\xi^2}{3L^2}\right)\Phi\left(-\frac{\xi}{\sqrt{3}L}, \frac{2\omega_p\tau}{\sqrt{3}}\right),$$

which yields the following expression for the pulse shape:

$$\delta I_{+2} = \frac{k_0^2V_E^2}{8\omega_0^2}\frac{W_L}{L}\left(\frac{2\xi}{L} + \frac{\omega_0^2}{c^2k_0^2}L\frac{\partial}{\partial\xi}\right) \tag{A.10}$$
$$\times\exp\left(-\frac{2\xi^2}{3L^2}\right)\Phi\left(-\frac{\xi}{\sqrt{3}L}, \frac{2\omega_p\tau}{\sqrt{3}}\right).$$

Figure 6 shows function (A.10) calculated for different values of the parameter $\omega_p\tau$, which characterizes the pulse duration in units of the plasma period. We can see that short laser pulses ($\omega_p\tau \le \sqrt{2}$) lose their energy by generating short-wavelength plasma oscillations (which remain in the plasma after the interaction) over the entire interaction region. It can also be seen that the generation is more efficient in the second half of this region (curves *1*, *2*). For longer pulses ($\omega_p\tau > \sqrt{2}$) or a denser plasma, quasistatic density perturbations are excited only during the first half-period of the interaction process. During the second half-period, the energy

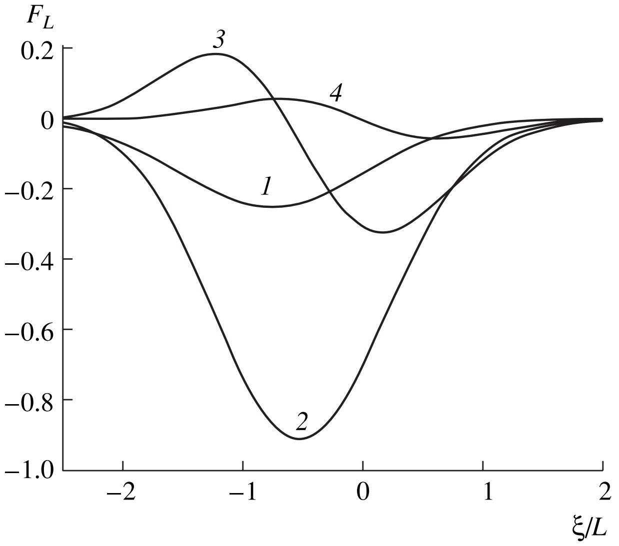

Fig. 6. Change in the dimensionless energy density $F_L = \frac{8\omega_0^2}{k_0^2V_E^2}\frac{L}{W_L}\delta I_{+2}$ vs. dimensionless variable ξ/L in the frame of reference of the propagating pulse after the interaction. The pulse propagates from left to right. Curves *1–4* refer to the same values of the parameter $\omega_p\tau$ as in Figs. 2 and 5.

of the plasma perturbations is transferred back to the pulses (curves *3*, *4*). As a result, the energy of the pulses is restored to the energy that they had before the interaction, but their shape becomes distorted. In this approximation, formula (A.10) reduces to

$$\delta I_{+2} = \frac{k_0^2V_E^2}{8\omega_0^2}\frac{W_L}{L}\left(\frac{2\xi}{L}+\frac{\omega_0^2}{c^2k_0^2}L\frac{\partial}{\partial\xi}\right) \times \frac{\omega_p^2\tau^2}{\omega_p^2\tau^2+(\xi^2/L^2)}\exp\left(-\frac{\xi^2}{L^2}\right). \tag{A.11}$$

The change in the total energy of the pulse in its collision with an identical pulse propagating in the opposite direction can be found by integrating Eq. (A.8) over the spatial variables:

$$\delta W_{+2} = -\frac{k_0^2V_E^2}{4\omega_0^2}\frac{W_L}{\sqrt{2}}\int_{-\infty}^{t}dt\exp\left(-\frac{t^2}{\tau^2}\right)\frac{\partial}{\partial t}\Phi\left(\frac{t}{\tau},\omega_p\tau\right).$$

To evaluate the integral in this expression, we use the following equation for the function Φ:

$$\frac{\partial^2}{\partial t^2}\Phi\left(\frac{t}{\tau},\omega_p\tau\right)+\omega_p^2\Phi\left(\frac{t}{\tau},\omega_p\tau\right) = \omega_p^2\exp\left(-\frac{t^2}{\tau^2}\right).$$

As a result, we obtain

$$\delta W_{+2} = -\frac{k_0^2V_E^2}{4\omega_0^2}\frac{W_L}{2\sqrt{2}} \times\left\{\Phi^2\left(\frac{t}{\tau},\omega_p\tau\right)+\frac{1}{\omega_p^2}\left[\frac{\partial}{\partial t}\Phi\left(\frac{t}{\tau},\omega_p\tau\right)\right]^2\right\}. \tag{A.12}$$

Comparing expression (A.12) with formula (4.5), we see that half of the energy of the generated small-scale plasma oscillations is transferred from one laser pulse, and the remaining half is that lost by the other pulse.

For times $t > \tau$ after the interaction, the total energy lost by the pulse can be determined using asymptotic expansion (3.11):

$$\delta W_{+2} = -\frac{\pi}{2\sqrt{2}}\omega_p^2\tau^2\frac{k_0^2V_E^2}{4\omega_0^2}W_L\exp\left(-\frac{\omega_p^2\tau^2}{2}\right). \tag{A.13}$$

A comparison with formula (4.7) shows that the energy δW_{+2} is equal to half the energy W_{p2}, which is in complete agreement with the energy conservation law.

The change in the energy of a laser pulse (and, accordingly, in its shape) under the action of large-scale electron density perturbations, δw_{+0}, can be represented as the sum of two parts: δw_{++}, which is associated with the perturbations excited by the pulse itself, and δw_{+-}, associated with the perturbations generated in the interaction with an identical pulse propagating in the opposite direction. Using the expression for n_0 that follows from Eqs. (1.15) and formula (2.2), taking into account formula (A.5) for the phase, and performing routine calculations, we find

$$\begin{aligned}\delta w_{++} = &-\frac{\omega_p^2}{\omega_0^2}\frac{V_E^2}{4c^2}\frac{E_{0L}^2}{8\pi}\frac{t'}{\tau}\frac{\xi}{L}\exp\left(-\frac{2\rho^2}{R^2}-\frac{\xi^2}{L^2}\right)\\ &\times\left\{\exp\left(-\frac{\xi^2}{L^2}\right)+\left[\frac{4}{k_p^2R^2}\left(\frac{\rho^2}{R^2}-1\right)-1\right]\Phi\left(-\frac{\xi}{L},\omega_p\tau\right)\right\}\\ &+\frac{\omega_p^2}{\omega_0^2}\frac{V_E^2}{4c^2}\frac{L^2}{R^2}\frac{E_{0L}^2}{8\pi}\frac{t'^2}{\tau^2}\exp\left(-\frac{2\rho^2}{R^2}-\frac{\xi^2}{L^2}\right)\\ &\times\left\{\left(2\frac{\rho^2}{R^2}-1\right)\exp\left(-\frac{\xi^2}{L^2}\right)\right.\\ &\left.+\left[\frac{8}{k_p^2R^2}\left(\frac{\rho^4}{R^4}-3\frac{\rho^2}{R^2}+1\right)+\left(1-\frac{2\rho^2}{R^2}\right)\right]\Phi\left(-\frac{\xi}{L},\omega_p\tau\right)\right\},\end{aligned} \tag{A.14}$$

$$\delta w_{+-} = -\frac{\omega_p^2}{2\omega_0^2}\frac{V_E^2}{4c^2}\frac{E_{0L}^2}{8\pi}\exp\left(-\frac{2\rho^2}{R^2}-\frac{\xi^2}{L^2}\right)$$

$$\times\left\{-\left[1+\frac{4}{k_p^2R^2}\frac{L^2}{R^2}\left(\frac{\rho^4}{R^4}-3\frac{\rho^2}{R^2}+1\right)\right]\exp\left(-\frac{\eta^2}{L^2}\right)\right.$$
$$+\frac{4\sqrt{\pi}}{k_p^2R^2}\left[\left(\frac{\rho^2}{R^2}-1\right)\frac{\xi}{2L}-\frac{L^2}{R^2}\left(\frac{\rho^4}{R^4}-3\frac{\rho^2}{R^2}+1\right)\frac{\eta}{L}\right]$$
$$\times\left[1+\operatorname{erf}\left(\frac{\eta}{L}\right)\right]+\frac{\xi}{k_pL^2}\left[1+\frac{4}{k_p^2R^2}\left(1-\frac{\rho^2}{R^2}\right)\right]F\left(\frac{\eta}{L},\omega_p\tau\right)\tag{A.15}$$
$$+\left[1+\frac{1}{k_p^2R^2}\left(5-6\frac{\rho^2}{R^2}\right)+\frac{8}{k_p^4R^4}\left(\frac{\rho^4}{R^4}-3\frac{\rho^2}{R^2}+1\right)\right]$$
$$\left.\times\Phi\left(\frac{\eta}{L},\omega_p\tau\right)\right\},$$

where $t' = t + t_0$ is the time measured from the instant t_0 of the pulse injection and erf(x) is the probability integral. These expressions are valid under the conditions $|t_0| > \tau$ and $|t| < t_R = k_0R^2/2c$.

Integrating expressions (A.14) and (A.15) over the radial variable ρ and the longitudinal variable ξ, we obtain the change in the energy of the pulse due to the generation of wake plasma waves,

$$\delta W_{++}$$
$$= -\frac{\sqrt{\pi}}{8}\omega_p^2\tau^2\frac{\omega_p^2}{\omega_0^2}\frac{V_E^2}{4c^2}\frac{t'}{\tau}\left(1+\frac{2}{k_p^2R^2}\right)W_L\exp\left(-\frac{\omega_p^2\tau^2}{2}\right),\tag{A.16}$$

and the change associated with its interaction with the wake waves of the other pulse,

$$\delta W_{+-} = \frac{\omega_p^2}{4\omega_0^2}\frac{V_E^2}{4c^2}\frac{W_L}{2\sqrt{2}}$$
$$\times\left\{\exp\left(-\frac{2t^2}{\tau^2}\right)-\left(1+\frac{2}{k_p^2R^2}\right)\Phi\left(\sqrt{2}\frac{t}{\tau},\sqrt{2}\omega_p\tau\right)\right\}.\tag{A.17}$$

From formula (A.17) we can, in particular, see that, on time scales $t > \tau$, $\omega_p\tau^2$ after the collision between short pulses ($\omega_p\tau \le \sqrt{2}$), their energy includes a correction oscillating at a frequency twice the plasma frequency:

$$\delta W_{+-} = -\frac{\sqrt{\pi}}{8}\omega_p\tau\frac{\omega_p^2}{\omega_0^2}\frac{V_E^2}{4c^2}\left(1+\frac{2}{k_p^2R^2}\right)W_L$$
$$\times\exp\left(-\frac{\omega_p^2\tau^2}{2}\right)\sin(2\omega_pt).\tag{A.18}$$

Comparing formula (A.18) with Eq. (3.24), we can readily see that the energy conservation law is satisfied.

During the time required for a laser pulse to propagate over two Rayleigh lengths, $2t_R$, the total energy losses (A.16) due to the generation of wake plasma waves are

$$\delta W_{+0} = -\frac{\sqrt{\pi}}{4}\omega_p\tau\frac{\omega_p}{\omega_0}\frac{V_E^2}{4c^2}\left(1+\frac{1}{2}k_p^2R^2\right)W_L$$
$$\times\exp\left(-\frac{\omega_p^2\tau^2}{2}\right).\tag{A.19}$$

This expression and formula (3.18), which determines the total energy of the wake waves generated by two pulses, differ by the coefficient 1/2 and in that they have opposite signs.

The amplitude of the wake waves excited by long laser pulses is exponentially small. However, as was shown above, the energy of such pulses should decrease during their interaction because of the increase in the energy of the plasma perturbations. In this case, formula (A.17) becomes

$$\delta W_{+-} = -\frac{1}{k_0^2R^2}\frac{V_E^2}{4c^2}\frac{W_L}{4\sqrt{2}}$$
$$\times\left\{1+\frac{R^2}{2L^2}\left(1-\frac{4t^2}{\tau^2}\right)\right\}\exp\left(-\frac{2t^2}{\tau^2}\right).\tag{A.20}$$

Comparing formula (A.20) with formula (3.22), we can conclude that, in the interaction process, a fraction of energy of the long laser pulses is converted into the energy of the plasma perturbations generated on a spatial scale on the order of the pulse length and, then, this fraction of energy is transferred from the perturbations back to the pulses.

ACKNOWLEDGMENTS

This work was supported in part by the Russian Foundation for Basic Research, project nos. 02-02-16110 and 01-02-16723.

REFERENCES

1. M. D. Perry and G. Mourou, Science **264**, 917 (1994).
2. E. Esarey, P. Sprangle, J. Krall, and A. Ting, IEEE Trans. Plasma Sci. **24**, 252 (1996).
3. M. Tabak, J. Hammer, M. E. Glinsky, *et al.*, Phys. Plasmas **1**, 1626 (1994).
4. J. J. Rocca, V. Shlyaptsev, F. G. Tomasel, *et al.*, Phys. Rev. Lett. **73**, 2192 (1994).
5. G. G. Durfee, III and H. M. Milchberg, Phys. Rev. Lett. **71**, 2409 (1993).
6. K. Krushelnick, A. Ting, C. I. Moore, *et al.*, Phys. Rev. Lett. **78**, 4047 (1997).
7. G. Shvets and A. Pukhov, Phys. Rev. E **59**, 1033 (1999).
8. G. Shvets, N. J. Fisch, A. Pukhov, and J. Meyer-ter-Vehn, Phys. Rev. E **60**, 2218 (1999).
9. C. B. Schroeder, P. B. Lee, and J. S. Wurtele, Phys. Rev. E **59**, 6037 (1999).

10. V. M. Malkin, G. Shvets, and N. J. Fisch, Phys. Plasmas **7**, 2232 (2000); Phys. Rev. Lett. **84**, 1208 (2000).
11. Y. Ping, I. Geltner, N. J. Fisch, *et al.*, Phys. Rev. E **62**, 4532 (2000).
12. K. Nagashima, J. Koga, and M. Kando, Phys. Rev. E **64**, 066403 (2001).
13. Z.-M. Sheng, K. Mima, Y. Sentoku, *et al.*, Phys. Plasmas **9**, 3147 (2002).
14. L. M. Gorbunov and A. A. Frolov, Zh. Éksp. Teor. Fiz. **120**, 583 (2001) [JETP **93**, 510 (2001)].
15. I. Y. Dodin and N. J. Fisch, Phys. Rev. Lett. **88**, 165001 (2002).
16. L. M. Gorbunov and V. I. Kirsanov, Zh. Éksp. Teor. Fiz. **93**, 509 (1987) [Sov. Phys. JETP **66**, 290 (1987)].
17. L. M. Gorbunov, P. Mora, and T. M. Antonsen, Jr., Phys. Rev. Lett. **76**, 2495 (1996).
18. V. V. Pustovalov and V. P. Silin, Tr. Fiz. Inst. im. P.N. Lebedeva, Akad. Nauk SSSR **61**, 42 (1972).
19. N. E. Andreev, L. M. Gorbunov, V. I. Kirsanov, *et al.*, Phys. Scripta **49**, 101 (1994).
20. V. P. Silin and A. A. Rukhadze, *Electromagnetic Properties of Plasma and Plasmalike Media* (Gosatomizdat, Moscow, 1961), p. 90.
21. J. Bekefi, *Radiation Processes in Plasmas* (Wiley, New York, 1966; Mir, Moscow, 1971).

Translated by I.A. Kalabalyk

Plasma Physics Reports, Vol. 29, No. 5, 2003, pp. 425–442. Translated from Fizika Plazmy, Vol. 29, No. 5, 2003, pp. 458–475.
Original Russian Text Copyright © 2003 by Gasparyan, Gorshikhin.

PLASMA KINETICS

Linear Noise Approximation Method for Calculating Nonequilibrium Fluctuations of the Occupation Numbers in Radiative–Collisional Average Ion Models

P. D. Gasparyan and A. A. Gorshikhin

Russian Federal Nuclear Center, All-Russia Research Institute of Experimental Physics, Sarov,
Nizhni Novgorod oblast, 607188 Russia

Received May 30, 2002

Abstract—A novel method is proposed for calculating nonequilibrium fluctuations of the mean occupation numbers of the electron shells in the radiative–collisional average-ion models of multicharged plasma kinetics. For the class of Slater ionic models, equations are derived for the mean occupation numbers of the electron shells and their fluctuations in the Fokker–Planck approximation. To calculate the fluctuations, the Fokker–Planck equation is linearized in the vicinity of the steady-state nonequilibrium solution to the kinetic equations (linear noise approximation). The method proposed allows one to take into account both the nonequilibrium correlations of the occupation-number fluctuations and the thermodynamically equilibrium statistical correlations related to the Coulomb interaction among bound electrons. The relation among the coefficients in the Fokker–Planck equation for the occupation-number fluctuations of the electron shells is discussed based on the fluctuation–dissipative theorem. *© 2003 MAIK "Nauka/Interperiodica".*

1. INTRODUCTION

A wide range of plasma physics problems related to the studies of targets for inertial controlled fusion, X-ray lasers, liner implosion in high-current generators, the interaction of ultrashort laser pulses with solids, etc., are dealt with by numerically solving the equations of the nonequilibrium radiative gas-dynamics of multicharged plasma [1–3]. From the computational standpoint, all of these problems are very difficult to solve because of the variety of the physical processes in nonequilibrium plasma and, accordingly, the complexity of the equations. Hence, one needs both a simplified plasma description and simplified kinetic models that do not require too much computational resources and, at the same time, are sufficiently exact for applications.

The kinetics of both equilibrium plasma [i.e., a plasma that is in local thermodynamic equilibrium (LTE)] and nonequilibrium (non-LTE) hot plasma is based on the two main approaches:

(i) the chemical approach [4], in which the kinetics of the ion populations is considered using the theory of ion collisions with photons and free plasma electrons, and

(ii) the solid-state approach, in which the plasma is described in the cell model of an inhomogeneous electron gas. Under LTE conditions, the latter approach is based on the Thomas–Fermi theory [5], and under non-LTE conditions, it is based on the kinetic model of noninteracting electrons in quasineutral plasma cells [6].

The radiative–collisional (RC) models of ion kinetics in a hot plasma take into account one-electron and one-photon reactions (both forward and reverse ones) of the ion excitation and ionization in collisions with electrons and photons and two-electron Auger processes (autoionization and dielectronic recombination). The reaction cross sections are calculated by the theory of collisions for isolated ions (see, e.g., [7, 8]).

Gas-dynamic equations based on chemical RC kinetic models are usually derived from the generalized Boltzmann equations (sometimes called the Wang Chang–Uhlenbeck equations) for the electron and ion plasma components under the assumption of plasma quasineutrality. It is common to describe the electron and ion plasma components in the two-temperature approximation and neglect ion diffusion. In the local RC kinetic model, the spectral transfer of radiation is described by a collision integral in the approximation of the total frequency redistribution of incoherent photon scattering in lines and continua [1–3, 9]. In this approximation, the set of gas-dynamic equations and equations of radiation transfer and population kinetics should be supplemented by the spectral dependences of the phototransition cross sections calculated with allowance for both the broadening of the discrete levels and the rates of the impact processes. Alternatively, when the approximation of the total redistribution over frequencies is inapplicable, the kinetics of the ion level populations in plasma should be described in terms of the spectral densities for the excited states [10–12]. When describing the dynamics of a weakly nonideal emitting plasma by using the local RC model of the population kinetics and the kinetic model of the spectral transfer of radiation in the approximation of the total frequency redistribution of incoherent photon scattering in lines and continua, we will use the term "nonequilibrium radiation gas-dynamics" (NRGD) for the two-temperature gas-dynamic approximation. In this approximation, the velocity distribution functions of the ions and free electrons are assumed to be Maxwellian.

The NRGD problems are very difficult to solve by using chemical RC kinetic models because of the huge number of ion states. For example, the total number of ion configurations with $N = 13$ bound electrons, which can occupy the ion subshells from the 1*s* to the 5*g* states, is $N_C \sim 1.12 \times 10^7$ (for $N = 7$, we have $N_C \sim 1.01 \times 10^5$). The number of the allowed radiative transitions between the energy levels of these configurations (the number of emission lines) is 10 to 30 times higher. Obviously, a detailed description of all of these states and radiative transitions in the RC kinetic model when numerically solving NRGD problems is very time-consuming. Moreover, such detailed information provided by these calculations is often unnecessary because the main physical parameters of the systems under consideration are determined by a moderate number of average characteristics. For this reason, when solving the problems of the NRGD of a hot plasma, simplified methods for describing the RC kinetics are widely used.

In the chemical approach, the methods for simplifying the RC kinetic model are based on statistical hypotheses about the populations of the excited ion states, combining the ion states with close energies into one common state, and describing the variety of radiative transitions between the common levels as a single radiative transition with an effective line profile. This approach is justified when the profiles of the close lines and the line emission spectra overlap.

In a fairly detailed ion-shell approach, the ion states in the RC kinetic model are described by the complete set of *SLJ* (or *SL*) terms; in this case, only the states with $\{C\gamma J\}$ electron configurations that are degenerated in the projections of the moments are assumed to have equal populations. In a less detailed approach, the splitting of the $\Delta\{C\gamma J\}$ terms is ignored and all the energy states of a given configuration are assumed to have equal populations. In complex multicharged ions, the total energies of a large number of configurations are often close to each other. In this case, the so-called superconfigurations that combine a variety of different configurations with close energies are usually used as common states. Finally, in the least detailed RC kinetic approach, the difference in the energies of configurations with different moments of the electrons belonging to the same *nl* shell is completely ignored. This roughest description is used in the hydrogen-like RC kinetic models without allowance for *L* splitting; in this case, the ion states are determined by a set of the integer occupation numbers of the electron shells over the principal quantum numbers. The above approaches to describing both a variety of discrete–discrete (*dd*) transitions between the common levels and the effective line shapes are called the detailed term accounting (DTA), unresolved transition array (UTA), and supertransition array (STA) approximations, respectively (see, e.g., [3, 13–16]). In the UTA and STA approximations, the effective cross sections for *dd* transitions (the envelopes of an array of lines) are described by Gaussian profiles. The parameters of these profiles (namely, the widths and the center positions) are calculated by averaging the positions of the individual lines with statistical weights equal to the spontaneous decay rates; to determine these positions, special time-saving methods based on recursion formulas and sum theorems [15, 17] were developed. For many NRGD problems, the observed complicated emission spectra of hot multicharged plasmas are satisfactorily described by simplified chemical RC kinetic models. However, despite a significant reduction in the computation time, the above approaches remain very time-consuming when applied to the multidimensional problems of radiation gas-dynamics.

An alternative simplified description of RC plasma kinetics is based on the use of the non-LTE solid-state approach. The corresponding RC kinetic models are called the average ion models (AIMs). In these models, the statistical independence of the populations of discrete ion levels is assumed, which is valid in the strict sense for an ideal gas of noninteracting electrons. In contrast to the chemical RC kinetic models, the plasma kinetics in the AIM approximation is described by the electron shell occupation numbers averaged over the ion configuration ensemble [6, 18] rather than by the exact populations of the electron configurations. The kinetics of the average occupation numbers is determined by the rates of the RC processes averaged over the nonequilibrium ensembles of the ions and radiation; for the photon transfer equation, it is determined by average sources and sinks of radiation in radiative processes.

Under LTE conditions, the AIM approximation can be most easily formulated in terms of the density functional theory by using the extreme properties of an equilibrium ensemble (see, e.g., [16, 19]). Various forms of the density functional and various physical approximations (such as taking into account the quasineutrality condition and exchange–correlation terms, the implementation of the cell approximation, and the use of the quasiclassical approximation) allow one to apply the well-known quantum–statistical models of substance, such as the Thomas–Fermi and Hartree–Fock–Slater models [16, 19–21]. In the density functional theory, the single-particle approach with a self-consistent cell potential can be implemented most efficiently to take into account the interelectron interaction, which is required to describe one of the most important phenomena in a nonideal plasma—pressure ionization [22]. The theory enables one to determine the photoabsorption cross sections in an LTE multicharged plasma by calculating the delayed polarizability. In particular, assuming that the fluctuations of the occupation numbers of the average ion levels are continuous, it is relatively simple to take into account the effect of electron interaction on the correlations of the equilibrium fluctuations of the electron shell occupation numbers, which determine the statistical line shapes from *dd* transitions in the AIM [13, 23]. Unfortunately, the density functional theory does not allow one to apply the AIM approximation to nonequilibrium plasmas.

An alternative approach to deriving the AIM approximation under LTE conditions was proposed in [24, 25]. It is based on explicitly calculating the large thermodynamic potential and average occupation numbers in the plasma chemical model by the saddle-point method. In this approach, the hydrogen-like Slater approximation, which was theoretically justified in [26–28], is used in the initial plasma chemical model to describe the structure of isolated ions. In the Slater models, the energy structure of ions is described by the universal matrices of screening constants, which are weakly dependent on the atomic number Z. For the Slater ion models without and with allowance for L splitting, the matrices of screening constants, optimized using the updated atomic databases, are presented in [28] and [29], respectively. The fluctuations of the occupation numbers and the photoabsorption cross sections are calculated using the quasi-thermodynamic fluctuation theory.

In the Slater ion models, analytic expressions for the energy structure and screened charges of the electron shells allow one to use semiempirical (based on the Coulomb–Born and quasiclassical approximations) formulas for the collision rates and photoabsorption cross sections. These expressions are convenient for both developing time-saving (from the calculation standpoint) automated database generators for the chemical RC kinetic models and calculating the RC kinetics based on the nonequilibrium Slater AIMs. Explicit calculations of the large thermodynamic potential for the LTE Slater AIMs allows one to take into account both the correlations of the occupation-number fluctuations caused by the Coulomb interaction among bound electrons and the influence of correlations on the effective photoabsorption cross sections for *dd* transitions in the AIM approximation [25] (the occupation-number fluctuations in the AIM approximation without allowance for correlations were calculated in [30]).

This study is devoted to deriving the equations for the non-LTE Slater AIMs. The equations are obtained by averaging the equations of the chemical RC plasma kinetics over a nonequilibrium ensemble of ions. To enable explicit averaging, the set of equations of the chemical RC kinetics is approximated by the Fokker–Planck equation for the continuous probability density of the occupation numbers of the ion's electron shells with the help of the diffusion approximation for multidimensional probability processes on meshes [31]. In this approach, macroscopic equations for the average occupation numbers are obtained under the assumption of small fluctuations. The method enables one to calculate the nonequilibrium fluctuations of the average occupation numbers in the linear noise approximation. These occupation numbers are needed to simulate the statistical shapes of the lines and photoabsorption cross sections under non-LTE conditions. In the case of LTE, the accuracy of the results obtained by this method (see [25]) is determined by the choice of the ensemble in which fluctuations are calculated (in [25], it was the grand canonical ensemble).

In Sections 2 and 3, the equations of the chemical RC kinetics for the Slater ion models are presented. In Section 4, the AIM equations for the average occupation numbers of electron shells are derived by the moment method [32, 33] and in the Fokker–Planck approximation.

In Section 5, the equations for the nonequilibrium fluctuations of the occupation numbers are derived and the sources in the radiative transfer equations are averaged in the linear noise approximation. The possibility of generalizing the nonequilibrium Slater AIMs and taking into account plasma nonideality (in particular, when calculating the fluctuations of the average occupation numbers in the cell approximation) is discussed.

The results of calculations of the occupation-number fluctuations in a nonequilibrium multicharged hot plasma under the coronal equilibrium conditions are presented in Section 6.

2. ELECTRON GAS IN THE COULOMB FIELD OF A NUCLEUS

Let us consider a system of bound electrons in the field of a nucleus with a charge Z. We introduce the configuration space $\{C\} = \{n_1^{q_1}, n_2^{q_2}, \ldots, n_i^{q_i}, \ldots, n_j^{q_j}, \ldots\}$, where $\{n_i\}$ are the quantum numbers of the ith shell and q_i is the number of electrons in the ith shell. In the ion models without allowance for the L splitting of the levels, n_i is the principal quantum number of the ith shell, and in those with allowance for L splitting, n_i is a pair of numbers $(nl)_i$, where n and l are the principal and orbital quantum numbers of the ith shell, respectively ($1 \le i \le K$, where K is the maximum number of the shell). The ion state is determined by a sequence of the integer occupation numbers $\{q_1, q_2, \ldots\}$ of the shells from the $\{C\}$ configuration, where q_i is the number of electrons in the ith shell, $0 \le q_i \le g_i$, and g_i is the statistical weight (for the ion model without allowance for L splitting, we have $g_i = 2n_i^2$). Each $\{q_1, q_2, \ldots\}$ sequence can be related to a point in a bounded K-dimensional integer-number mesh in configuration space. The functions determining the chemical RC kinetics (the ion

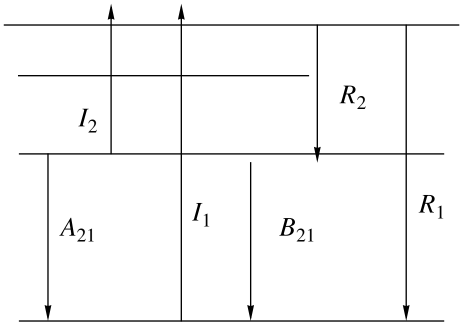

Fig. 1. Energy levels of an [H]-ion.

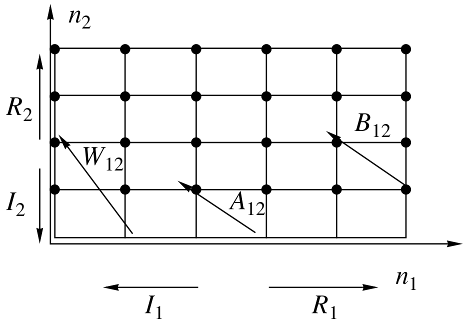

Fig. 2. Configuration space $\{C\}$ of two-shell ions.

energy states, screened shell charges, types of transitions from a given configuration, oscillator strengths, etc.) are defined in configuration space $\{C\}$. We will consider the Slater models of isolated ions in which the total energy of the electron configuration is represented analytically by a cubic polynomial in the occupation numbers [28, 29]

$$U_C = -\sum_k q_k \frac{Q_k^2}{2n_k^2}, \quad Q_k = Z - \sum_n \sigma_{kn}(q_n - \delta_{kn}); \tag{1}$$

where σ_{kn} is the invariable matrix of the screening constants and Q_k is the shielded charge of the kth shell (δ_{nk} is the Kronecker delta function). For $\sigma_{kn} = 0$, we have $Q_k = Z$ and expression (1) describes the simplest ion model, namely, the model of an ideal electron gas in the nucleus Coulomb field, in which case the total energy of the $\{C\}$ configuration is equal to the sum of the energies of the single-electron bound states of hydrogen-like levels: $U_C = -Z^2\sum q_k/2n_k^2 = -Z^2\sum q_k/2k^2$ (here and below, we use the atomic system of units). The system of the energy levels of a hydrogen-like ion ([H]-ion) is shown in Fig. 1.

The arrows in Fig. 1 show the single-electron transitions between the states of the discrete and continuous spectra. The energy levels of a [H]-ion are degenerated. According to the Pauli principle, the number of electrons in any shell of a multielectron ion cannot be higher than the degeneracy order ($2n_k^2$). The configuration space $\{C\}$ for the two-shell ions (a two-dimensional mesh) is shown in Fig. 2. It consists of $(g_i + 1) \times (g_j + 1)$ points.

The arrows in Fig. 2 show the possible types of the processes: ionization (I), photoexcitation (A), electronic excitation (B), autoionization (W), etc., which are also represented in another form in Fig. 1. The ground states of the ions are located at the mesh border, whereas the excited states are inside the mesh. The excited states of ions with a fixed number of bound electrons are located only on the diagonals. Below, the RC kinetic models with allowance for only single-electron and two-electron transitions (for the Auger process only) are considered. The reactions of ionization and ion recombination are shown by the vertical and horizontal transitions between adjacent points in the configuration space. The reactions of the excitation and quenching of the ion levels correspond to the strictly diagonal transitions, which conserve the number of electrons in the configuration. The reactions of autoionization and dielectronic recombination correspond to the diagonal transitions in which the number of electrons in the configuration changes by unity. The parameters of the chemical RC kinetic model without allowance for electron–electron interaction are completely determined by the reaction rates for the [H]- and [He]-ions with one and two electrons, respectively, and by the Pauli principle (in the approximation in which the states of each configuration are described by a single Slater determinant).

3. EQUATIONS OF THE CHEMICAL RC KINETIC MODEL

In the chemical approach, the equations of the RC kinetics are the local equations for the concentrations $N_{\{C\}}$ of the ion components or the normalized probabilities of the configurations $P\{C\} \equiv N_{\{C\}}/N$ ($N = \sum_{\{C\}} N_{\{C\}}$). The kinetic equations for ions (the Pauli equations) describe the change in $P\{C\}$ caused by the radiative and collisional processes. We will describe the reaction rates in the first order of the perturbation theory using the Fermi golden rule. The validity of this approach stems from the Markov approximation [31]. The equations of the RC kinetics for the plasma ion components (electron configurations) are not closed. To close them, the kinetic equations for free electrons and radiation are needed. In the NRGD, the radiation is described by the transfer equation and the subsystem of free electrons is assumed to be in local equilibrium. The electron density is determined from the quasineutrality condition. We assume that the plasma is ideal and one-component and the subsystem of free electrons is an ideal gas with a temperature T and chemical potential μ.

These approximations are valid for a not too dense or not too rarefied hot plasma.

To make the RC kinetic equations more compact, it is suitable to use the step (argument shift) operator E_n, which acts on the integer-number argument of the function $f(n)$ determined by the relations [31]

$$E_n[f(n)] \equiv f(n+1), \quad E_n^2 = E_n \cdot E_n, \quad E_n^1 \cdot E_n^{-1} = E_n^{-1} \cdot E_n^1 = 1. \tag{2}$$

With the help of the E_n operator, the energy ν_{ij} $(i < j)$ of the $i \longrightarrow j$ transition from the configuration $\{C\} = \{\ldots, n_i^{q_i}, \ldots, n_j^{q_j}, \ldots\}$ to the configuration $\{C\}' = E_i^{-1}E_j[C] = \{\ldots, n_i^{q_i-1}, \ldots, n_j^{q_j+1}, \ldots\} \equiv \{C\} - i + j$ is determined by the difference between the total configuration energies and has the form

$$\nu_{ij} = (E_i^{-1}E_j - 1)[U_C]. \tag{3}$$

For an ideal plasma in a state of ionization equilibrium, the Saha equation for $P^*\{C\}$ has the form (here and below, the symbol * stands for the equilibrium probabilities $P^*\{C\}$)

$$\frac{P^*\{C\}e^{U_C/T}}{G\{C\}} = E_i^{-1}\left[\frac{P^*\{C\}e^{U_C/T}}{G\{C\}}\right]e^{\eta}, \qquad P^*\{C\} = E_i^{-1}[P^*\{C\}]\frac{E_i^{-1}[g_i - q_i]}{q_i}e^{\eta}e^{(E_i^{-1}-1)[u_C]/T}, \tag{4}$$

where $\eta = \mu/T$ is the chemical potential of free electrons μ normalized to the temperature T and $G\{C\} = \prod_i \binom{q_i}{g_i} \equiv \prod_i \frac{g_i!}{q_i!(g_i - q_i)!}$ is the total statistical weight of the $\{C\}$ configuration. The general equations of the chemical RC kinetics for the $P\{C\}$ probabilities have the form

$$\begin{aligned}\frac{dP\{C\}}{dt} &= \sum_i (E_i - 1)[I_i q_i P\{C\}] \\ &+ \sum_i (E_i^{-1} - 1)[R_i(g_i - q_i)P\{C\}] \\ &+ \sum_{i<j}(E_i^{-1}E_j - 1)\left[\frac{a_{ji}}{g_i}q_j(g_i - q_i)P\{C\}\right] \\ &+ \sum_{i<j}(E_iE_j^{-1} - 1)\left[\frac{a_{ij}}{g_j}q_i(g_j - q_j)P\{C\}\right] \\ &+ \sum_{i<j\le k}(E_i^{-1}E_jE_k - 1) \\ &\times\left[\frac{W_{jk,i}}{2}q_j(q_k - \delta_{jk})(g_i - q_i)P\{C\}\right] \\ &+ \sum_{i<j\le k}(E_iE_j^{-1}E_k^{-1} - 1) \\ &\times\left[\frac{W_{i,jk}}{2}q_i(g_j - q_j)(g_k - q_k - \delta_{jk})P\{C\}\right].\end{aligned} \tag{5}$$

In Eqs. (5), the summation is performed over the discrete–continuum (*dc*), discrete–discrete (*dd*), and Auger (*ddc*) transitions. In the single-configuration approximation, the rates of the forward (reverse) processes are proportional to the occupation (vacancy) numbers of the electron shells. The rates of collisional ionization and excitation are proportional to the density of free electrons, and the rates of photoionization and photoexcitation are proportional to the radiation intensity. The rates of the Auger transitions [the terms with the $w_{jk,i}$ multiplier in Eqs. (5)] do not depend on the electron density and radiation intensity. The rates of the reverse processes are determined from the rates of the forward processes using the principle of detailed balance. With allowance for the Coulomb interaction among the ion's bound electrons, the kinetic coefficients I_i, R_i, a_{ij}, and $w_{i,jk}$ in Eqs. (5) depend on the occupation numbers of the electron shells. Without this allowance (the ideal gas approximation), the kinetic coefficients are independent of the occupation numbers. To clarify the notation in Eqs. (5), we note that the contribution from a single-electron radiative $i \longrightarrow j$ *dd* transition from the $\{C\}$ configuration to the $\{C\}' = \{C\} - i + j$ configuration [this transition enters into the third and fourth terms of the sum in Eqs. (5)] has the form

$$\left(\frac{dP\{C\}}{dt}\right)_{ij}^{dd} = -\left[\frac{A_{ij}}{g_j}q_i(g_j - q_j)P\{C\}\right] + (E_j^{-1}E_i^1)\left[\frac{A_{ji}}{g_i}q_j(g_i - q_i)P\{C\}\right]. \tag{6}$$

In Eq. (6), the rates of the forward and reverse radiative *dd* transitions (A_{ij} and A_{ji}, respectively) depend on the radiation intensity I_ν, which is determined from the equation for the radiation transfer

$$LI_\nu \equiv \frac{1}{c}\frac{\partial I_\nu}{\partial t} + \mathbf{\Omega}\frac{\partial I_\nu}{\partial \mathbf{r}} = -\chi_\nu I_\nu + \eta_\nu. \tag{7}$$

In this equation, the radiation sources η_ν and sinks $\chi_\nu I_\nu$ include bremsstrahlung, *dd* and *dc* phototransitions, and Compton scattering. For *dd* transitions, these sources can be written in the form [3]

$$\chi_\nu^{dd} = \sum_{i<j}\chi_{\nu,ij}^{dd}, \quad \eta_\nu^{dd} = \sum_{i<j}\eta_{\nu,ij}^{dd}, \tag{8}$$

$$\chi^{dd}_{\nu,ij} = N\sum_{\{C\}}\sigma_{ij}q_i(g_j - q_j)\frac{1}{g_j}P\{C\}, \tag{9}$$

$$\begin{aligned}\eta^{dd}_{\nu,ij} &= N\sum_{\{C\}}\sigma_{ij}q_i(g_j - q_j)\frac{1}{g_i}E_i^{-1}E_j[P\{C\}] \\ &\quad\times\left\{\frac{P^*\{C\}}{E_i^{-1}E_j[P^*\{C\}]}\right\}B_\nu(T) \qquad (10)\\ &= N\sum_{\{C\}}\sigma_{ij}\frac{e^{\nu_{ij}/T}}{g_j}E_i^{-1}E_j\{q_j(g_i - q_i)P\{C\}\}B_\nu(T),\end{aligned}$$

where N is the total ion density, χ^{dd}_ν is the total coefficient of photoabsorption due to *dd* transitions, and σ_{ij} is the absorption cross section for the *dd* transition of an electron from the *i*th shell to the *j*th shell. For the sake of simplicity, Eq. (10) is written in the Wien approximation, in which the equilibrium radiation intensity is $B_\nu \propto \nu^3\exp(-\nu/T)$. The cross section for the radiative $i \longrightarrow j$ *dd* transition can be expressed via the absorption oscillator strength f_{ij} and the normalized line profile $\varphi(x)$:

$$\sigma_{ij} = \sigma_0 f_{ij}\varphi\left(\frac{\nu - \nu_{ij}}{\Delta\nu_{ij}}\right), \quad \int\varphi(x)dx = 1. \tag{11}$$

Then, the rates of the forward and reverse radiative *dd* processes in Eq. (6), A_{ij} and A_{ji}, are determined by the collision integrals that are dependent on the radiation intensity. For narrow lines, they are

$$\begin{gathered}A_{ij} = \int_0^\infty\sigma_0 f_{ij}\frac{I_\nu}{\nu}\varphi\left(\frac{\nu - \nu_{ij}}{\Delta\nu_{ij}}\right)d\nu d\Omega = \sigma_0 f_{ij}\frac{I_{\nu_{ij}}}{\nu_{ij}}, \\ E_j^{-1}E_i[A_{ji}] = A_0\frac{g_i}{g_j}f_{ij}\frac{e^{\nu_{ij}/T}B_{\nu_{ij}}}{\nu_{ij}}.\end{gathered} \tag{12}$$

Without allowance for the interaction among bound electrons, the kinetic coefficients in Eqs. (5) do not depend on the configuration occupation numbers and can thus be factored out from the step operators.

For *dc* transitions, the radiation sources η_ν and sinks $\chi_\nu I_\nu$ in Eq. (7) and the rates of photoionization and photorecombination in Eqs. (5) can be written in a similar way. The additional terms in transfer equation (7) are related to the equilibrium bremsstrahlung processes and Compton scattering by free electrons and do not contribute to kinetic equations (5). On abandoning the Wien approximation, the equations of radiation transfer and RC kinetics will allow for the processes of stimulated emission; in this case, the formulas for the rates of radiation processes change somewhat [3].

4. DERIVATION OF THE NONEQUILIBRIUM AIM EQUATIONS FROM THE CHEMICAL RC KINETIC MODEL

Let us consider the RC ion kinetics in the two-shell model at $\sigma_{kn} = 0$ (ideal gas) for a small ion admixture to the background plasma assuming that the density of free electrons and the plasma density and temperature are constant. In a steady state, Eqs. (5) can be written in the form

$$\begin{aligned}\frac{dP_{q_1q_2}}{dt} &= I_1(E_{q_1} - 1)[q_1P_{q_1q_2}] \\ &\quad + R_1(E_{q_1}^{-1} - 1)[(g_1 - q_1)P_{q_1n_2}] \\ &\quad + I_2(E_{q_2} - 1)[q_2P_{q_1q_2}] + R_2(E_{q_2}^{-1} - 1)[(g_2 - q_2)P_{q_1q_2}] \\ &\quad + \frac{a_{21}}{g_1}(E_{q_1}^{-1}E_{q_2} - 1)[q_2(g_1 - q_1)P_{q_1,q_2}] \\ &\quad + \frac{a_{12}}{g_2}(E_{q_1}E_{q_2}^{-1} - 1)[q_1(g_2 - q_2)P_{q_1q_2}] \\ &\quad + \frac{W_{22,1}}{2}(E_{q_1}^{-1}E_{q_2}^{2} - 1)[(g_1 - q_1)q_2(q_2 - 1)P_{q_1q_2}] \\ &\quad + \frac{W_{1,22}}{2}(E_{q_1}^{1}E_{q_2}^{-2} - 1)[(g_2 - q_2)q_1(g_2 - q_2 - 1)P_{q_1q_2}] = 0,\end{aligned} \tag{13}$$

where $0 \le q_1 \le g_1$ and $0 \le q_2 \le g_2$. In the case at hand, Eqs. (13) are linear with respect to the vector $P_{q_1q_2}$ of dimension $(g_1 + 1) \times (g_2 + 1)$ and the probabilities $P_{q_1q_2}$ satisfy the conservation law $\sum_{q_1,q_2}P_{q_1q_2} = 1$. For large statistical weights g_i, the dimension of set (13) is $K \gg 1$ and its solution is too cumbersome. Under LTE conditions, due to the detailed balance between the forward and reverse transitions, the stationary (equilibrium) solution to Eqs. (13) can be found explicitly and has the form of a factorized binomial distribution:

$$\begin{gathered}P^*_{q_1q_2} = P^*_{q_1}P^*_{q_2}, \quad P^*_{q_i} = C_{g_i}^{q_i}f_i^{q_i}(1 - f_i)^{g_i - q_i}, \\ g_if_i = g_i\frac{1}{\left(e^{-\frac{\nu_i}{T} + \eta} + 1\right)} \equiv \bar{q}_i = \sum_{q_i = 0}^{q_i = g_i}q_iP^*_{q_i},\end{gathered} \tag{14}$$

where f_i are the occupation-number probabilities. Here, due to the statistical independence of the electron distribution over the ion shells, the vector $P_{q_1q_2}$ is entirely determined by the first moments of the solution to the kinetic equations, namely, the average electron shell occupation numbers $\langle q_i\rangle$. The same effect (the statistical independence of the steady-state electron distribution over the ion shells) occurs when the equations of the RC model are solved neglecting the diagonal transitions in Eqs. (13) (Fig. 2).

Let us consider the moment representation of the complete set of Eqs. (13) under non-LTE conditions [32]. We determine the moments of the electron distribution over the shells using the probabilities $P_{q_1q_2}$:

$$\langle q_1^k q_2^l \rangle = \sum q_1^k q_2^l P_{q_1q_2}. \tag{15}$$

The equations for the first moments, $\langle q_1 \rangle$, $\langle q_2 \rangle$, and $\langle q_1q_2 \rangle$, which follow from the set of linear equations (13) of the chemical RC kinetics, are

$$\begin{aligned}
\frac{d\langle q_1\rangle}{dt} &= -I_1\langle q_1\rangle + R_1\langle (g_1-q_1)\rangle + \frac{a_{21}}{g_1}\langle q_2(g_1-q_1)\rangle \\
&- \frac{a_{12}}{g_2}\langle q_1(g_2-q_2)\rangle + \frac{W_{22,1}}{2}\langle q_2(g_1-q_1)(q_2-1)\rangle \\
&- \frac{W_{1,22}}{2}\langle q_1(g_2-q_2)(g_2-q_2-1)\rangle, \\
\frac{d\langle q_2\rangle}{dt} &= -I_2\langle q_2\rangle + R_2\langle (g_2-q_2)\rangle - \frac{a_{21}}{g_1}\langle q_2(g_1-q_1)\rangle \\
&+ \frac{a_{12}}{g_2}\langle q_1(g_2-q_2)\rangle - W_{22,1}\langle q_2(g_1-q_1)(q_2-1)\rangle \\
&+ W_{1,22}\langle q_1(g_2-q_2)(g_2-q_2-1)\rangle,
\end{aligned} \tag{16}$$

$$\begin{aligned}
\frac{d\langle q_1q_2\rangle}{dt} &= -I_1\langle q_1q_2\rangle + R_1\langle q_2(g_1-q_1)\rangle \\
&- I_2\langle q_1q_2\rangle + R_2\langle q_1(g_2-q_2)\rangle \\
&+ \frac{a_{21}}{g_1}\langle (q_2-q_1-1)q_2(g_1-q_1)\rangle \\
&+ \frac{a_{12}}{g_2}\langle (q_1-q_2-1)q_1(g_2-q_2)\rangle \\
&+ \frac{W_{22,1}}{2}\langle (q_2-2q_1-2)q_2(g_1-q_1)(q_2-1)\rangle \\
&+ \frac{W_{1,22}}{2}\langle (2q_1-q_2-2)q_1(g_2-q_2)(g_2-q_2-1)\rangle.
\end{aligned} \tag{16a}$$

The set of all the moment equations (16) is certainly equivalent to Eqs. (13). In the moment representation for the equations of RC kinetics, all the moments are coupled. Equations (16) can be simplified under the assumption of the statistical independence of the electron distribution over the shells with a factorized probability distribution $P_{q_1q_2} = P_{q_1q_2}P_{q_1q_2}$ (14), in which case moments (15) are factorized, $\langle q_1^k q_2^l \rangle = \langle q_1^k \rangle \langle q_2^l \rangle$. In this case, the equations for the first moments are closed but nonlinear and the equations for the highest order moments include only the solutions to the equations for the lowest order moments. If we assume that, in the general case, the solutions to kinetic equations (13) for the vector $P_{q_1q_2}$ are also close to the factorized one, then the equations for the first moments can be expressed in the form

$$\begin{aligned}
\frac{d\langle q_1\rangle}{dt} \equiv g_1\frac{df_1}{dt} &= -I_1g_1f_1 + R_1g_1(1-f_1) \\
&+ a_{21}g_2f_2(1-f_1) - a_{12}g_1f_1(1-f_1) \\
&+ 0.5W_{22,1}g_1g_2(g_2-1)f_2^2(1-f_1) \\
&- 0.5W_{1,22}g_1g_2(g_2-1)f_1(1-f_2)^2, \\
\frac{d\langle q_2\rangle}{dt} \equiv g_2\frac{df_2}{dt} &= -I_2g_2f_2 + R_2g_2(1-f_2) \\
&- a_{21}g_2f_2(1-f_1) + a_{12}g_1f_1(1-f_1) \\
&- W_{22,1}g_1g_2(g_2-1)f_2^2(1-f_1) \\
&+ W_{1,22}g_1g_2(g_2-1)f_1(1-f_2)^2.
\end{aligned} \tag{17}$$

These are the AIM equations for the model of noninteracting electrons. Here, the set of nonlinear low-dimensional equations (17) for the shell occupation probabilities f_i replaces the high-dimensional set of linear equations (13). Under LTE conditions, this approximation is exact. Conditions under which the AIM RC kinetic equations (13) satisfactorily describe a non-LTE plasma were studied in [32]; the common condition is the smallness of the dynamic correlations of the occupation numbers of different shells [these correlations are caused by nondiagonal transitions in kinetic equations (16)] and/or small deviations from LTE conditions.

When deriving the AIM equations from the set of RC equations (16) with allowance for the interaction among bound electrons (e.g., for the Slater ion models), the problem arises of calculating the averaged kinetic coefficients and the averaged spectral sources in transfer equations (7)–(10) because, in this case, the equilibrium solution cannot be reduced to a simple factorized form even under LTE conditions. There are correlations among the average occupation numbers of the shells. Under LTE conditions, the problem of calculating the equilibrium (static) occupation-number correlations, which are related to the influence of the electron Coulomb interaction on the energy structure of an ion, can be solved using the quasi-thermodynamic theory of continuous fluctuations [25]. Under non-LTE conditions, it is necessary to take into account both the static and the dynamic correlations of the occupation numbers.

The separation of the occupation-number correlations into static and dynamic ones is rather arbitrary and is related to the use of the AIM approximation in analyzing the chemical RC kinetic models. Indeed, the dynamic characteristics (reaction rates) and static characteristics (ion energy levels) enter into the matrix elements of the common Coulomb interaction operator. The quantitative difference between them is that the matrix elements are taken between different states of the continuous or line spectra, which makes the kinetic coefficients dependent on the density. The possibility of describing plasma kinetics in the chemical RC model is related to both this density dependence (i.e., the decrease in the dynamic correlations) and the applicability of the Markov approximation when deriving the equations of the chemical RC kinetics (the Pauli equations). For a strongly nonideal plasma, the quantitative difference between the static and dynamic characteristics is smaller, and the description of plasma kinetics by using chemical RC models becomes impossible because the kinetics of highly excited ion states with an electron orbit size on the order of the average distance between the ions cannot be described by the Pauli equations for the states of isolated ions. In this case, the plasma kinetics is to be described using other quasiparticles.

AIM equations (17) for the average occupation numbers can be derived from the kinetic equations of the chemical RC plasma model with the help of an alternative method by using the Fokker–Planck diffusion approximation for the one-step probability processes [31]. We substitute the continuous coordinates of the configuration space $\{C\}$ for the integer-number ones and rewrite Eqs. (13) in the form

$$\begin{aligned}\dot{P} &= (E_x-1)[I_1P]+(E_x^{-1}-1)[R_1P]\\ &+(E_y-1)[I_2P]+(E_y^{-1}-1)[R_2P]\\ &+(E_x^{-1}E_y-1)[a_{21}P]+(E_xE_y^{-1}-1)[a_{12}P]\\ &+(E_x^{-1}E_y^2-1)[d_{22,1}P]+(E_xE_y^{-2}-1)[d_{1,22}P],\end{aligned}\tag{18}$$

where $q_1 = x$, and $q_2 = y$. In Eq. (18), the factors q_i, $(g_i - q_i)$, and others, which are proportional to the occupation and vacancy numbers, are incorporated into the kinetic coefficients. Expanding the step operators E in a Tailor series

$$\begin{aligned}E_x^{\pm 1}-1 &= \pm\partial_x+\frac{1}{2}\partial_{xx}+\ldots,\\ E_y^{\pm 1}-1 &= \pm\partial_y+\frac{1}{2}\partial_{yy}+\ldots,\end{aligned}\tag{19}$$

and omitting all the derivatives of orders higher than two, we obtain the following Fokker–Planck equation for the probability density of the electron configurations $P(x, y, t)$:

$$\begin{aligned}\partial_tP &= \partial_x((I_1-R_1)P)+\partial_y((I_2-R_2)P)\\ &+\frac{1}{2}\partial_{xx}((I_1+R_1)P)+\frac{1}{2}\partial_{yy}((I_2+R_2)P)\\ &+(\partial_x-\partial_y)((a_{12}-a_{21})P)\\ &+\frac{1}{2}(\partial_{xx}^2-2\partial_x\partial_y+\partial_{yy}^2)((a_{12}+a_{21})P)\\ &+(\partial_x-2\partial_y)((d_{1,22}-d_{22,1})P)\\ &+\frac{1}{2}(\partial_{xx}^2-4\partial_x\partial_y+4\partial_{yy}^2)(5(d_{1,22}+d_{22,1})P).\end{aligned}\tag{20}$$

In (20), the kinetic coefficients are functions of x and y. In the general case, in which K electron shells are taken into account, Fokker–Planck equation (5) has the form

$$\begin{gathered}\partial_tP(y_i,t) = -\sum_j\partial_{y_j}(A_jP)+\frac{1}{2}\sum_{ij}\partial_{y_iy_j}^2(B_{ij}P),\\ 1\le i,\quad j\le K.\end{gathered}\tag{21}$$

In this equation, the dependence of the transfer coefficients A_i and diffusion tensor B_{ij} on the coordinates y_i, which are the occupation numbers, is determined by the form of kinetic coefficients in Eqs. (5). From Eq. (21), one can readily obtain the macroscopic equations for the average $\langle y_i\rangle$ values

$$\begin{aligned}\frac{d}{dt}\langle y_i\rangle &= \langle A_i\rangle\approx A_i(\langle y_j\rangle),\\ \langle y_i\rangle &= \int\prod_j dy_jy_iP.\end{aligned}\tag{22}$$

The approximate equality in (22) holds only when the fluctuations of the occupation numbers with respect to their average values are small (the probability density distribution $P(y_i, t)$ is peaked). It is easy to verify that Eqs. (22) for the macrovariables $\langle y_i\rangle \equiv g_if_i$ are completely equivalent to Eqs. (17), which were obtained in the approximation of the uncoupled moments on the integer-number mesh in configuration space.

5. LINEAR NOISE APPROXIMATION FOR CALCULATING THE OCCUPATION NUMBER FLUCTUATIONS IN THE AIM UNDER NON-LTE CONDITIONS

The validity of the small-fluctuation approximation, under which Eqs. (22) were obtained, can be estimated in the linear noise approximation for the multidimensional Fokker–Planck equation [31]. We assume that the stationary solution to Eqs. (22) is $\langle y_i\rangle \equiv y_i^s$. Expanding the coefficients A_i and B_{ij} in a Tailor series in the vicinity of the stationary solution and keeping only the linear terms of the series, we obtain from Eqs. (22) the

Fokker–Planck equation with linear coefficients for the probability density $P(\Delta y_i, t)$

$$\partial_t P = -\sum_{ij} A^s_{ij}\partial_{y_i}(\Delta y_j P) + \frac{1}{2}\sum_{ij} B^s_{ij}\partial^2_{y_i y_j}P, \tag{23}$$

$$A^s_{ij} = (\partial_{y_i}(A_j))_{y_{i,j} = y^s_{i,j}}, \quad B^s_{ij} = (B_{ij})_{y_{i,j} = y^s_{i,j}},$$

where new independent variables, namely, the deviations from the stationary solution, $\Delta y_i \equiv y_i - y^s_i$, are introduced. In Eq. (23), the constant matrix B_{ij} is symmetric, whereas the A_{ij} matrix is generally asymmetric. The solution to linear equation (23) has the form of a Gaussian distribution and is given by the formula

$$P(y, t) = \left(\frac{\operatorname{Det}\Xi^{-1}}{2\pi}\right)^{N/2}\exp\left[-\frac{1}{2}\mathbf{\Delta y}\cdot\Xi^{-1}\mathbf{\Delta y}\right], \tag{24}$$

where the equations for the average values $\langle\Delta y_i\rangle \equiv \int\Delta y_i P(y_j, t)\prod dy_j$ and the correlation matrices Ξ have the form (the steady-state $\langle\Delta y_i\rangle$ values are zero)

$$\frac{d}{dt}\langle\Delta y_i\rangle = \sum_j A^s_{ij}\langle\Delta y_j\rangle,$$

$$\langle\langle y_i y_j\rangle\rangle \equiv \langle y_i y_j\rangle - \langle y_i\rangle\langle y_j\rangle = \Xi_{ij}, \tag{25}$$

$$\frac{d}{dt}\Xi = A^s\Xi + \Xi(A^s)^+ + B^s.$$

Under LTE conditions, there is a relation between the diffusion matrix B^s and the transfer matrix A^s. This relation stems from the principle of detailed balance. First, we consider the diffusion limit for Saha formula (4), which we rewrite in the form

$$q_i P^*\{C\}$$
$$\approx g_i E_i^{-1}[P^*\{C\}]E_i^{-1}[1 - q_i/g_i]e^{(E_i^{-1} - 1)[U_C/T] + \eta}, \tag{26}$$

where $q_i \equiv g_i f_i$. Using expansion (19) of the step operator and integrating Eq. (26) over the continuous configuration space of the occupation numbers, we obtain the equilibrium solution for the occupation-number probabilities f^*_i of the ion's electron shells:

$$f^*_i \equiv \int\frac{q_i}{g_i}P^*\{C\}\prod_j dq_j = (1 - f^*_i)e^{\langle\nu\rangle_i/T + \eta},$$

$$f^*_i = \frac{1}{e^{-\langle\nu\rangle_i/T - \eta} + 1},$$

$$\langle -\nu_i\rangle \equiv \frac{\partial\langle U_C\rangle}{\partial\langle q_i\rangle} \approx \frac{\partial U_C(g_i f_i)}{g_i\partial f_i}, \tag{27}$$

$$g_i f_i \equiv \langle q_i\rangle = \int q_i P\{C\}\prod_j dq_j.$$

Let us now consider an Auger reaction on the right-hand side of RC kinetic equations (5) (the electron transition from the jth and kth shells to the ith shell: $(jk) \longrightarrow (i)$):

$$\left(\frac{dP}{dt}\right)^{Auge}_{jk,\, i} \tag{28}$$
$$= (E_i^{-1}E_j E_k - 1)[d_{jk,\, i}P] + (E_i E_j^{-1}E_k^{-1} - 1)[d_{i,\, jk}P].$$

The principle of detailed balance for this reaction reads as

$$E_i^{-1}E_j E_k[d_{jk,\, i}P^*\{C\}] = d_{i,\, jk}P^*\{C\},$$
$$d_{jk,\, i}P^*\{C\} = E_i E_j^{-1}E_k^{-1}[d_{i,\, jk}P^*\{C\}]. \tag{29}$$

As is the case with the Saha formula, using expansion (19) and the principle of detailed balance, we obtain from Eq. (29) the relation between the rates of the forward and reverse Auger processes,

$$\langle d^*_{jk,\, i}\rangle = \int d_{jk,\, i}P^*\{C\}\prod_i dq_i$$
$$= \int d_{i,\, jk}P^*\{C\}\prod_i dq_i = \langle d^*_{i,\, jk}\rangle. \tag{30}$$

It follows from Eq. (30) that, under LTE conditions, the coefficients $w_{ij,\, k}$ and $d_{ij,\, k}$ [see (5)] are related as

$$\langle d^*_{jk,\, i}\rangle = \left\langle\frac{w^*_{jk,\, i}}{2}q^*_j(q^*_k - \delta_{jk})(g_i - q^*_i)\right\rangle$$

$$\approx\left\langle\frac{w^*_{jk,\, i}}{2}\right\rangle g_j g_k g_i f^*_j f^*_k(1 - f^*_i) \tag{31}$$

$$= \left\langle\frac{w^*_{i,\, jk}}{2}\right\rangle g_j g_k g_i f^*_i(1 - f^*_k)(1 - f^*_j) = \langle d^*_{i,\, jk}\rangle.$$

Here, we took into account that the diffusion approximation is valid at $q_i \gg 1$. Substituting the equilibrium occupation numbers f^*_i into Eq. (31), we rewrite the relation between the probabilities of the forward and reverse Auger processes in the form

$$\left\langle\frac{w^*_{i,\, jk}}{2}\right\rangle = \left\langle\frac{w^*_{jk,\, i}}{2}\right\rangle e^{(-\langle\nu_i\rangle + \langle\nu_j\rangle + \langle\nu_k\rangle)/T + \eta}. \tag{32}$$

For calculation purposes, we introduce the averaged large thermodynamic potential Ω for ions:

$$\begin{aligned}\Omega &= \frac{1}{T}(U - TS)\\ &\equiv \beta U(f_i) + \sum_i g_i[f_i \ln f_i + (1 - f_i)\ln(1 - f_i)].\end{aligned} \tag{33}$$

The extremum of the potential Ω is achieved for the equilibrium shell occupation numbers described by Eq. (27). We also introduce the matrix of equilibrium correlations, which determines the occupation-number fluctuations under LTE conditions:

$$\begin{aligned}(\partial^2\Omega^*)_{ij} &= \Omega''_{ij} \equiv \frac{\partial^2\Omega^*}{\partial\langle q_i^*\rangle\partial\langle q_j^*\rangle}\\ &= \beta\frac{\partial^2 U(f_i^*)}{\partial\langle q_i^*\rangle\partial\langle q_j^*\rangle} + \frac{\delta_{ij}}{g_i f_i^*(1 - f_i^*)}.\end{aligned} \tag{34}$$

Now, we calculate the B_{ij} and A_{ij} matrices under LTE conditions. For the Auger transition $(kk) \longrightarrow (i)$ with $k > i$, calculation gives

$$A^* = 0.5B_{ii}^*\begin{pmatrix} -\Omega''_{ii} + 2\Omega''_{ik} & 2\Omega''_{kk} - \Omega''_{ik} \\ 2(\Omega''_{ii} - 2\Omega''_{ik}) & -2(2\Omega''_{kk} - \Omega''_{ik}) \end{pmatrix},$$

$$B^* = B_{ii}^*\begin{pmatrix} 1 & -2 \\ -2 & 4 \end{pmatrix}, \tag{35}$$

$$B_{ii}^* = \langle d_{kk,\,i}^*\rangle + \langle d_{i,\,kk}^*\rangle = 2\left\langle\frac{w_{kk,\,i}^*}{2}\right\rangle g_k^2 g_i (f_k^*)^2(1 - f_i^*).$$

It can easily be verified that, in the case at hand, the matrix

$$\begin{aligned}\Xi^* &\equiv (\partial^2\Omega^*)^{-1}\\ &\equiv \frac{1}{(\Omega''_{ik}\Omega''_{ik} - \Omega''_{ii}\Omega''_{kk})}\begin{pmatrix} -\Omega''_{kk} & \Omega''_{ik} \\ \Omega''_{ik} & -\Omega''_{ii} \end{pmatrix}\end{aligned} \tag{36}$$

is a solution to Eq. (25):

$$A^*\Xi^* + \Xi^*(A^*)^+ + B^* = 0. \tag{37}$$

Similar calculations for other reactions show that, under LTE conditions, the stationary solution to Eqs. (22) coincides with the equilibrium solution, $f_i^s = f_i^*$; in this case, the matrix B^* of the diffusion coefficients and the matrix A^* of the transfer coefficients are related by expression (37), which is a direct representation of the fluctuation–dissipative theorem for the diffusion approximation to the equations of RC plasma kinetics in the AIM approximation. When the matrices A^s and B^s are commutating, Eq. (35) for the matrix Ξ has a simple stationary solution $\Xi = -0.5(A^s)^{-1}B^s$. This case corresponds to the absence of correlations among the occupation numbers of different electron shells.

Let us determine the macroscopic coefficients of the spectral transfer equation of radiation in the AIM approximation. We consider radiative transfer equation (7) and restrict ourselves to analyzing the contribution from *dd* transitions (8)–(10).

The sources and sinks in Eq. (7) depend on the electron configuration $\{C\}$ (because the energy of *dd* transitions and the oscillator strengths depend on $\{C\}$) and the linewidths of individual transitions $\Delta\nu_{ij}$, which are determined by the collision rates, Stark microfields, the spread in the ion velocities, etc. The above derivation of Eq. (22) for the average occupation numbers in the Fokker–Planck approximation is based on both the continuous approximation of the dependence of the kinetic coefficients on the electron configuration occupation numbers and the assumption of small correlations among the populations of different ions' shells. An analysis of RC kinetic equations (5) and the appearance of coefficient (12) for the rates of the radiative *dd* transitions show that these assumptions are acceptable when the radiation intensity I_ν changes slightly over the linewidth of *dd* transitions. This is the case of a plasma with the optical thickness higher than the mean radiation path lengths in the lines. In fact, this is an additional condition for the applicability of the AIM approximation under non-LTE conditions. On the other hand, in an optically thin plasma, the intensity of line emission is low and the influence of the intrinsic plasma emission (reabsorption) on the kinetic processes is insignificant. Hence, it is reasonable to expect that, in the AIM approximation, the inaccuracy of the RC kinetic equations is maximum in a nonequilibrium plasma with an optical thickness on the order of unity for the most essential *dd* lines.

If we could accurately determine probabilities $P\{C\}$ from the known average populations of the electron shells, then it would be possible to solve transfer equation (7) together with Eqs. (5). However, this approach is inefficient in developing time-saving approximations because it is the solution of the transfer equation that is the most laborious in solving the NRGD equations. An approach based on solving the averaged radiative transfer equation, in which the sources and sinks are determined by a moderate number of the radiation parameters of the electron configuration ensemble, is more efficient.

This approach has long been used in the case of LTE. Under LTE conditions, the main kinetic parameter is the cross section for photon absorption; hence, the problem is to determine the cross sections statistically averaged over the equilibrium electron configuration ensemble, first of all, for *dd* transitions because the calculation of these transitions in a hot multicharged plasma is the most time-consuming. In the AIM approximation and under LTE conditions, the following assumptions are used [13, 16, 25, 30]:

(i) the smallness of the fluctuations of the electron shell occupation numbers,

(ii) the smallness of the correlations among the average electron shell occupation numbers, and

(iii) the assumption of strong overlapping of the line profiles corresponding to single-electron *dd* transitions between the identical electron shells of different ions.

The last assumption is well satisfied for *dc* transitions because the profiles of the photoionization cross sections are very wide. For *dd* transitions, strong overlapping of the line profiles of close lines corresponding to *dd* transitions can be observed in the plasma of high-*Z* elements, in which case the main resonant lines of *dd* transitions are surrounded by a huge number of satellites [16]. We will also use this approximation under non-LTE conditions.

In the Fokker–Planck linear noise approximation for the occupation number density, the sources and sinks in radiation transfer equation (23) can be averaged in a straightforward way. Indeed, substituting integration for the discrete sum over configurations in Eqs. (9) and (10), expanding the smooth functions of continuous occupation numbers q_i in $\chi_{\nu,\,ij}^{dd}$ in Tailor series in the vicinity of the average steady-state populations, and then integrating over q_i, we arrive at an integral representation of the sources and sinks. When the satellite shift caused by the dispersion of the occupation number distribution is much larger than the linewidths of the individual *dd* transitions between electron configurations, the individual line profiles $\varphi(x)$ can be substituted by δ functions. On this substitution, all of the integrals with the Gaussian distribution of the occupation-number fluctuations (24) can be calculated analytically. In the first nonzero approximation, the integral statistical line profile is a Gaussian with the width determined by the matrix of fluctuation correlations Ξ and a dependence of the energy of *dd* transitions on the electron configurations.

Let us thoroughly calculate the averaged absorption coefficient $\langle\chi_{\nu,\,ij}^{dd}\rangle$ in the transfer equation and the statistical line profile of a *dd* transition for the $i \longrightarrow j$ transition between the shells of the average ion. Expanding $\chi_{\nu,\,ij}^{bb}$ in Eq. (9) in Tailor series of smooth functions (oscillator strengths and shell populations) in the vicinity of the average steady-state populations $q_i = q_i^s + \Delta q_i \equiv g_i(f_i^s + \Delta f_i)$, we obtain

$$\langle\chi_{\nu,\,ij}^{dd}\rangle = \chi_{ij}^{dd}(q^s)q_i^s(1-f_j^s)$$

$$\times\int\prod_k dq_k P(C)\left[1+\sum_k a_k\Delta q_k\right]\varphi(\nu-\nu_{ij}(\Delta q_k, q^s)) \quad (38)$$

$$\equiv\chi_{ij}^{dd}(q^s)q_i^s(1-f_j^s)\langle\varphi_{\nu,\,ij}^{dd}\rangle.$$

Here, the distribution $P(C)$ is determined by Eq. (24). The energy shift of *dd* transitions can be determined by expanding the energy of *dd* transitions [see Eqs. (3), (27)] in terms of the occupation-number fluctuations

$$\nu_{ij}(C) \approx \langle\nu_{ij}\rangle + \sum_k \left.\frac{\partial\langle\nu_{ij}\rangle}{\partial q_k}\right|_{q_k^s}\Delta q_k \equiv \langle\nu_{ij}\rangle + \sum_k c_k^{ij}\Delta q_k,$$

$$\langle\nu_{ij}\rangle = \langle\nu_i\rangle - \langle\nu_j\rangle = -\frac{\partial\langle U_C\rangle}{\partial q_i^s} + \frac{\partial\langle U_C\rangle}{\partial q_j^s}, \quad (39)$$

$$c_k^{ij} = \frac{\partial\langle\nu_{ij}\rangle}{\partial q_k^s}.$$

Let us consider the main term in Eq. (38). Let $\tilde{\varphi}(u)$ be the Fourier transform of the line profile of the $i \longrightarrow j$ transition, $\tilde{\varphi}(u) = \frac{1}{\sqrt{2\pi}}\int dx\varphi(x)e^{-iux}$. Then, taking into account Eq. (24), we have

$$\langle\varphi_{\nu,\,ij}^{dd}\rangle = \int\prod_k dq_k P(C)\varphi(\nu-\nu_{ij}(\Delta q_k, q^s))$$

$$= \int\frac{du}{\sqrt{2\pi}}\tilde{\varphi}(u)e^{iu(\nu-\langle\nu_{ij}\rangle)}\int\prod_k dq_k P(C)e^{-iuc_k\Delta q_k}$$

$$= \int\frac{du}{\sqrt{2\pi}}\tilde{\varphi}(u)e^{iu(\nu-\langle\nu_{ij}\rangle)}e^{-\frac{u^2}{2}(\Sigma_{ij}^{dd})^2} \quad (40)$$

$$= \int\frac{dx}{\sqrt{2\pi(\Sigma_{ij}^{dd})^2}}\varphi(\nu-\langle\nu_{ij}\rangle-x)e^{-\frac{x^2}{2(\Sigma_{ij}^{dd})^2}},$$

$$(\Sigma_{ij}^{dd})^2 = \sum_{kl}c_l^{ij}(\Xi)_{lk}c_k^{ij}.$$

For a Gaussian profile $\varphi(\nu)$ with width $\Sigma_{ij,\,0}$ (a particular case is the δ function), statistical profile (40) becomes a Gaussian with the total width equal to the sum of widths:

$$\langle \varphi^{dd}_{\nu,\,ij} \rangle = \frac{1}{\sqrt{2\pi\Sigma^2}} e^{-\frac{(\nu - \langle \nu_{ij} \rangle)^2}{2\Sigma^2}}, \qquad (41)$$

$$\Sigma^2 = (\Sigma^{dd}_{ij})^2 + \Sigma^2_{ij,\,0}.$$

The influence of the correction to profile (40) due to an additional term in square brackets in Eq. (38) results in the profile asymmetry.

The average rates A_{ij} of the radiative *dd* transitions are expressed via the averaged sources in the transfer equation. In the AIM approximation, for the $i \longrightarrow j$ transition in Eq. (9), instead of expression (12), we have

$$A_{ij} = \frac{1}{N}\int_0^{\infty} \frac{\langle \chi^{dd}_{\nu,\,ij} \rangle I_\nu}{\nu} d\nu\, d\Omega$$

$$= \frac{\chi^{dd}_{ij}(q^s) q^s_i (1 - f^s_j)}{N} \int_0^{\infty} \frac{\langle \varphi^{dd}_{\nu,\,ij} \rangle I_\nu}{\nu} d\nu\, d\Omega. \qquad (42)$$

The total absorption coefficient in the transfer equation due to *dd* transitions and the total rates of the *dd* transitions are the corresponding sums over the transitions between the shells of the average ion. The statistical profile of photoabsorption $\langle \chi^{dc}_{\nu,\,i} \rangle$ in the *dc* transitions (with allowance for the fluctuations of the photoionization thresholds), the averaged radiation sources $\langle \eta^{dd}_{\nu,\,ij} \rangle$ and $\langle \eta^{dc}_{\nu,\,i} \rangle$ in the AIM transfer equation, and the remaining reaction rates are calculated in a similar way.

Under LTE conditions, the above derivation of the transfer equation in the Slater AIM approximation gives the statistical AIM photoabsorption coefficients calculated by the quasi-thermodynamic fluctuation theory [25]. Under non-LTE conditions, it generalizes the equilibrium theory and allows one to take into account the influence of both the static and the dynamic correlations of the occupation-number fluctuations on the complete equations of RC kinetics (for populations and radiation) in the linear noise approximation. The explicit form of the nonequilibrium probability density $P(\Delta y_i, t)$ allows one to calculate not only the influence of nonequilibrium kinetics on the effective linewidths, but also some other parameters, in particular, the dispersion of the ion mean charge. Indeed, the normalized fraction of the ions with an integer-number charge $Z' = Z - Z_b$ can be found by integrating over distribution (24):

$$P_{Z'} = \frac{1}{Z}\int \delta\left(\sum_k q_k - Z_b\right) P(C) \prod_k dq_k$$

$$= \frac{1}{Z}\int \delta\left(\sum_k \Delta q_k - \Delta Z'\right) P(C) \prod_k dq_k \equiv \int dP_{Z'},$$

$$\Delta Z' = \langle Z \rangle - Z', \quad Z = \sum_{Z'} \frac{1}{\sqrt{\pi D}} e^{-\left(\frac{\Delta Z'}{D}\right)^2}, \qquad (43)$$

$$D^2 = 2\sum_{ij} (\Xi)_{ij}.$$

It is seen from Eq. (43) that the dispersion of the ion mean charge is determined by the sum of the population correlations of the matrix Ξ.

Radiation transfer in plane geometry was computed by the detailed RC models of a multicharged plasma and by the AIM within a wide range of the plasma thicknesses, densities, and temperatures. The comparison of the results obtained shows that the AIM approximation satisfactorily describes the mean characteristics of a hot multicharged plasma and the large-scale features of the plasma emission spectrum [32, 34], regardless of almost completely ignoring the detailed description of the line emission reabsorption. To a great extent, the successful use of the AIM can be explained by the fact that, in a hot plasma of high-*Z* elements, the main mechanism for the thermalization of the sources of nonequilibrium *dd* and *dc* radiation is the interaction with the bremsstrahlung continuum (whose sources are equilibrium), rather than the collisional thermalization of the sources. Moreover, a favorable factor improving the accuracy of the AIM approximation is the high radiation capacity of a multicharged plasma in continua (*dc* transitions), whose contours are highly overlapped.

The derivation of the Slater AIM equations and the averaged radiative transfer equation from the equations of chemical RC kinetics can easily be generalized, in particular, for

(i) multicomponent plasmas,

(ii) models allowing for the degeneracy of the electron component,

(iii) models allowing for the stimulated radiation processes,

(iv) nonequilibrium distribution functions of free electrons (high-energy electrons in laser plasma), and

(v) combined RC kinetic models (the so-called "ion method" [16]) with incomplete averaging over the configuration ensemble and a description of only a fraction of the configuration occupation numbers by the averaged values.

However, the complicated theoretical problem of correctly describing a strongly nonideal plasma (i.e., the effect of the ambient plasma on the structure of individual ions and the RC kinetics) is still unresolved. The effect of the ambient plasma manifests itself it two ways. First, the excited ion states with electron orbit radii on the order of the average distance between ions are destroyed and reassigned to the continuum. Second, ion collisions also can affect the states with small electron orbit radii, changing the corresponding photoabsorption cross sections (line profiles). The simplest way to take into account plasma nonideality is to use the model of neutral spherical cells that do not interact via the Coulomb field. In this model, the residual interaction with the ambient plasma is described by the boundary conditions on or near the cell surface. In the neutral cell model, the effect of the ambient plasma consists in a decrease in the single-particle density of the electron states near the boundary of the continuum as compared to the density of the isolated ion states. The simplest regular method of taking into account this effect in the chemical RC models and AIMs with the use of the Slater models of an isolated ion is to change the statistical weight of the excited shells [35]. In [35], it was proposed to describe the decrease in the statistical weight of the electron shells by the following function of the ratio of the orbit radius of an isolated ion r_n to the cell radius R_0:

$$g_n = 2n^2\left[1 + a\left(\frac{r_n}{R_0}\right)^b\right]^{-1}, \tag{44}$$

where a and b are the fitting parameters. Besides, the model of a homogeneous ion sphere (with a constant density of free electrons in the cell) [35] is used to take into account the decrease in the ionization potential due to the external shielding of the bound states by the free electrons of the cell. The fitting parameters a and b in Eq. (44) are chosen so as to match the pressure in the Slater AIMs to that in the Thomas–Fermi model. The "chemical bond" effects, which are important for a cold substance, are not taken into account in this model. As in the Thomas–Fermi model, these effects can be taken into account via an additional term in the free energy or the nonequilibrium free energy [36]. The above simplified method for considering the plasma nonideality is presently employed instead of a still absent exact theory of a strongly nonideal plasma. From the standpoint of the problems of radiative gas-dynamics, the favorable circumstance is the relatively weak influence of the highly-excited states and the transitions between them on the radiative transfer. As a result, the average characteristics of radiation are slightly sensitive to the method of truncating the number of the ion levels.

We note another problem related to the calculation of the occupation-number fluctuations in the AIM and their influence on the statistical profiles of the lines corresponding to dd transitions. In deriving Eqs. (22) and (25), the density of free electrons was assumed to be constant. Under LTE conditions, this corresponds to the use of the grand canonical ensemble; in this case, the chemical potential of free electrons is one of the independent variables. On the other hand, the plasma cell models that employ the approximation of strictly neutral cells correspond to a canonical ensemble in which the number of the bound and free electrons in a cell is determined by the nucleus charge. In calculating the average plasma characteristics, the models using different ensembles are equivalent. However, the calculated fluctuations depend on the ensemble type because it determines the characteristics of free electrons. The choice of the ensemble in the nonideal plasma cell model is an independent procedure, in which the separation of electrons into the bound and free ones is not strictly determined.

Let us illustrate this situation by using the kinetic equations. We consider the kinetics of collisional ionization of single-shell ions. In Eqs. (5), the ionization and recombination rates can be written in two versions:

$$\begin{aligned} &\text{(a)}\; I_1 = I_0\left(Z - \sum_{0 \le q \le g} qP(q)\right), \\ &R_1 = R_0\left(Z - \sum_{0 \le q \le g} qP(q)\right)^2, \\ &\text{(b)}\; I_1 = I_0(Z - q), \quad R_1 = R_0(Z - q)^2. \end{aligned} \tag{45}$$

In version (a), the number of free electrons in a cell is determined by the condition of average quasineutrality, and version (b) corresponds to the strictly neutral cell with a constant total number of electrons. These versions are related to the equations of chemical RC kinetics,

$$\begin{aligned} &\text{(a)}\; \frac{dP}{dt} = \left(Z - \sum_q qP(q)\right)(E - 1)[I_0 qP(q)] \\ &+ \left(Z - \sum_q qP(q)\right)^2 (E^{-1} - 1)[R_0(g - q)P(q)], \\ &\text{(b)}\; \frac{dP}{dt} = (E - 1)[I_0 q(Z - q)P(q)] \\ &+ (E^{-1} - 1)[R_0(Z - q)^2(g - q)P(q)] \end{aligned} \tag{46}$$

and to the corresponding Fokker–Planck equations

$$\begin{aligned} &\text{(a)}\; \frac{\partial P}{\partial t} = (Z - \langle q\rangle)\frac{\partial}{\partial q}[I_0 qP] \\ &- (Z - \langle q\rangle)^2\frac{\partial}{\partial q}[R_0(g - q)P] \\ &+ \frac{1}{2}(Z - \langle q\rangle)\frac{\partial^2}{\partial q^2}[I_0 qP] \end{aligned}$$

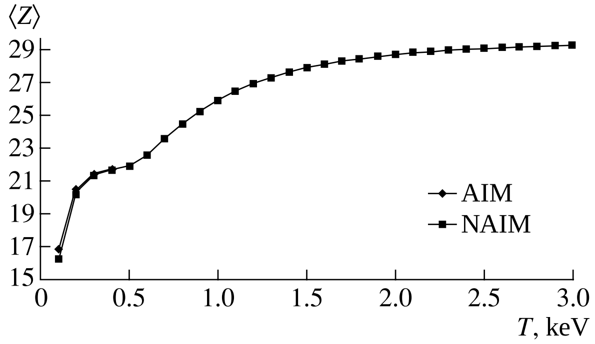

Fig. 3. Mean charge ⟨Z⟩ in a Ge plasma vs. electron temperature in the AIM and NAIM.

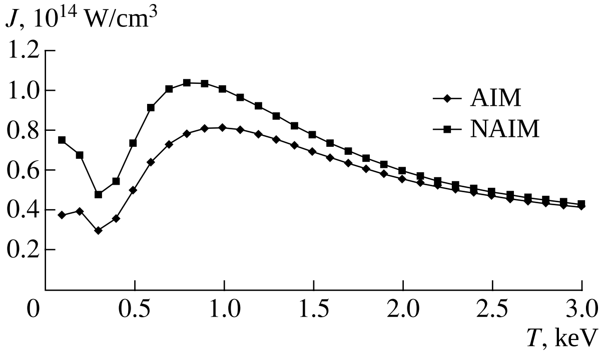

Fig. 4. Radiation capacity J of a Ge plasma vs. electron temperature in the AIM and NAIM.

$$+\frac{1}{2}(Z-\langle q\rangle)^2\frac{\partial^2}{\partial q^2}[R_0(g-q)P], \tag{47}$$

$$\text{(b)}\ \frac{\partial P}{\partial t} = \frac{\partial}{\partial q}[I_0 q(Z-q)P]$$

$$-\frac{\partial}{\partial q}[R_0(Z-q)^2(g-q)P]+\frac{1}{2}\frac{\partial^2}{\partial q^2}[I_0 q(Z-q)P]$$

$$+\frac{1}{2}\frac{\partial^2}{\partial q^2}[R_0(Z-q)^2(g-q)P].$$

Both versions lead to similar equations for the averages, but different equations for the fluctuations. The choice between these approximations should be done based on a more rigorous approach to considering the nonideal plasma kinetics. At present, the grand canonical ensemble [version (a)] is usually used to calculate the radiation path lengths. It is reasonable to expect that this approximation more adequately describes real plasmas with high degrees of ionization, although this issue is not quite clear in the case of weakly bound, highly excited states (this problem is important when the fluctuations of these states significantly contribute to the statistical broadening of the lines).

6. COMPUTATION OF THE OCCUPATION-NUMBER FLUCTUATIONS UNDER CONDITIONS OF CORONAL EQUILIBRIUM

The local nonequilibrium Slater AIMs with and without allowance for the L splitting of the levels (see Sections 4, 5) was realized in the AVI-L numerical code. An implicit first-order difference scheme and the Newton method, which provided rapid convergence of the iterations, were used to solve Eqs. (22) of the nonsteady kinetics of the occupation numbers.

The AVI-L code uses the dependence of the rates of collision processes on the mean occupation numbers and the shielded charges of the electron shells according to the interpolations of calculations by the Coulomb–Born model (the Lotz and Van Regemorter formulas [1, 8, 33]). Either quasiclassical Kramers interpolations [3, 7, 8, 33] or simple quadrature formulas from [16] are used to calculate the photoabsorption cross sections and the oscillator strengths. For the probabilities of the Auger processes, the calculated table data from [37] or their analytical interpolations corrected by introducing the branching factor with the aim of taking into account cascade processes [34, 38] are used.

In the AIM without allowance for the L splitting of the levels, the matrix of the screening constants is taken from [28], whereas the “new” AIM (NAIM), which takes into account L splitting, uses the matrix of the screening constants from [29], extended to take into account the ion’s electron shells with the principal quantum numbers $n \le 10$. In kinetic equations (22), an allowance is made for the stimulated radiative processes and the degeneracy of the plasma electron component in the ideal gas model. The possibility is also realized of phenomenologically taking into account strong plasma nonideality with different dependences of the effective statistical weights of the shells on the density [see (44)] and with allowance for a decrease in the ionization potential in the model of homogeneous ion spheres.

The computations of the equilibrium characteristics of a hot multicharged plasma in a wide range of plasma densities, temperatures, compositions, and degrees of ionization and for various spectral and mean Planck and Rosseland radiation path lengths by the AVI-L code show that these characteristics are in fair agreement with the results of calculations by the more complete quantum–statistical models. Thus, at temperatures higher than 0.3 keV, the mean radiation path lengths calculated by the NAIM differ from the data from [16] by no more than ~20–30%. Note that the calculations by the simpler Slater AIM (without allowance for L splitting) are in noticeably worse agreement with these data: the difference in the mean Rosseland path lengths attained a factor of 2 and higher [32].

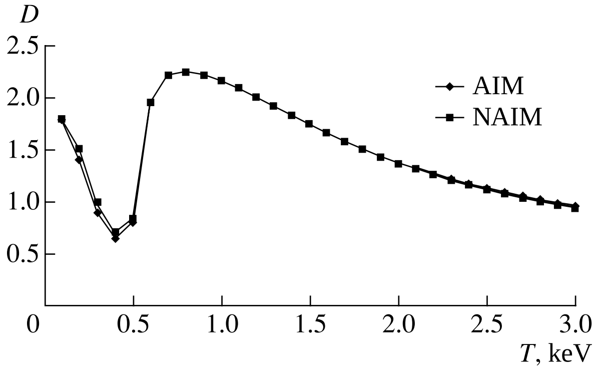

Fig. 5. Dispersion D of the mean charge $\langle Z\rangle$ in a Ge plasma vs. electron temperature in the AIM and NAIM.

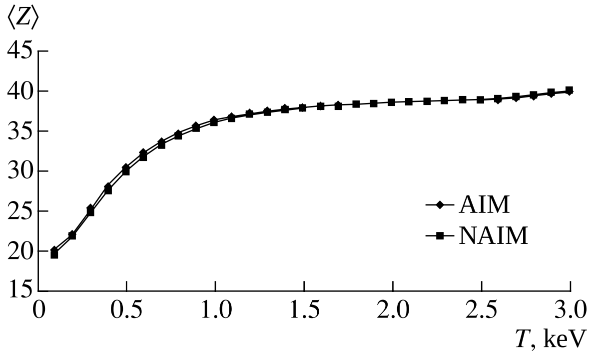

Fig. 6. Mean charge $\langle Z\rangle$ in an In plasma vs. electron temperature in the AIM and NAIM.

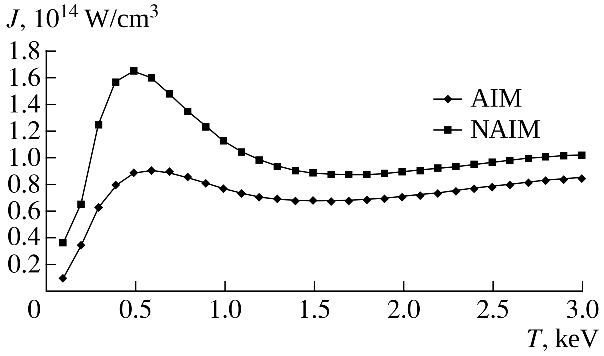

Fig. 7. Radiation capacity J of an In plasma vs. electron temperature in the AIM and NAIM.

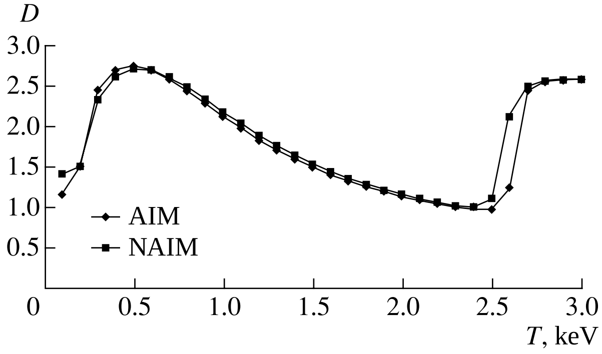

Fig. 8. Dispersion D of the mean charge $\langle Z\rangle$ in an In plasma vs. electron temperature in the AIM and NAIM.

Let us consider the results of calculations of the nonequilibrium characteristics of a hot plasma by the AVI-L code.

6.1. Calculations without Allowance for the Auger Processes

Figures 3–8 show the results of the AIM and NAIM calculations of the ion mean charge $\langle Z\rangle$, the dispersion of the mean charge D [see Eq. (43)], and the plasma volume radiation capacity J versus the electron temperature T for Ge and In plasmas at density $\rho = 0.002$ g/cm^3. The plasma was assumed to be ideal, and the ion's electron shells with the principal quantum numbers $n \le 6$ were taken into account.

The calculations (without allowance for the Auger processes) for Ge ($Z = 32$ and $A = 72.5$) and In ($Z = 49$ and $A = 115$) plasmas show the following:

(i) Within a wide range of Z, the average ion charge $\langle Z\rangle$ and its dispersion D are approximately the same in the AIM and NAIM models.

(ii) The dependence of the integral plasma radiation capacity J on the model type is more pronounced. The difference in J increases with Z; at low electron temperatures, this difference attains a factor of 2 for In plasmas (Fig. 7).

(iii) The radiation capacity J of a hot plasma correlates with the dispersion D of the ion mean charge. The maximum of the radiation capacity J is attained when the ion's shells are half-filled, and the minimum is attained when the ion's shells are filled almost completely. The minimum of the radiation capacity J in the temperature range under consideration is attained when the stripping of the Kth ion shells begins.

(iv) The absolute maximum of the radiation capacity (at a fixed density) increases with Z. The dependence of J on the density is approximately proportional to $\sim\rho^2$.

(v) The effect of the shells on the radiation capacity J is most pronounced for low-lying shells, which is naturally explained by the corresponding behavior of the ionization potentials, $I \sim 1/n^2$.

In the AVI-L code, the nonequilibrium correlations of the occupation-number fluctuations were calculated for the first time. In the linear noise approximation, these fluctuations determine the effective statistical linewidths and the dispersion of the ion distribution. The

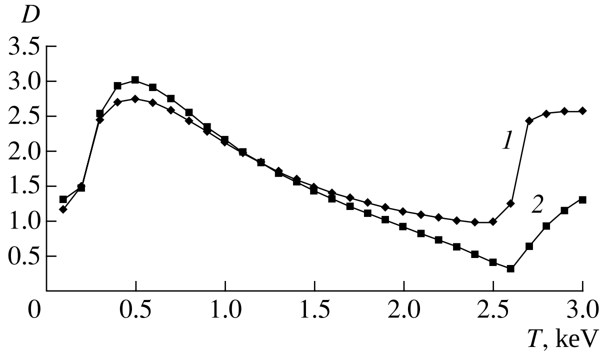

Fig. 9. Dispersion D of the mean charge $\langle Z\rangle$ in an In plasma (ρ = 0.002 g/cm^3) vs. electron temperature in the AIM (*1*) with and (*2*) without allowance for the dynamic correlations.

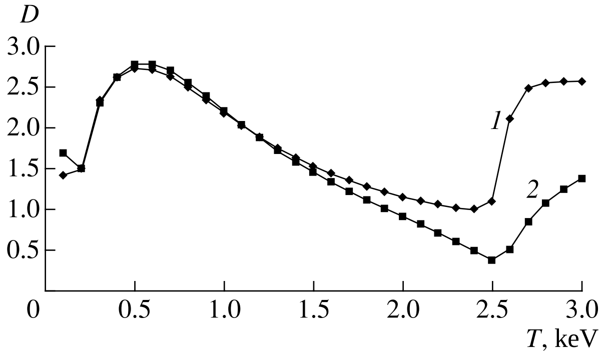

Fig. 10. Dispersion D of the mean charge $\langle Z\rangle$ in an In plasma (ρ = 0.002 g/cm^3) vs. electron temperature in the NAIM (*1*) with and (*2*) without allowance for the dynamic correlations.

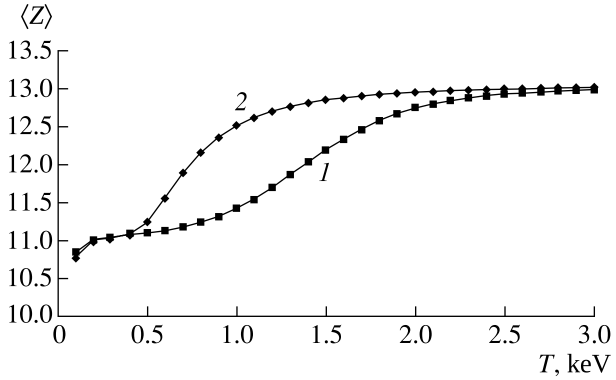

Fig. 11. Mean charge $\langle Z\rangle$ in an Al plasma vs. electron temperature in the AIM (*1*) with and (*2*) without allowance for the Auger processes.

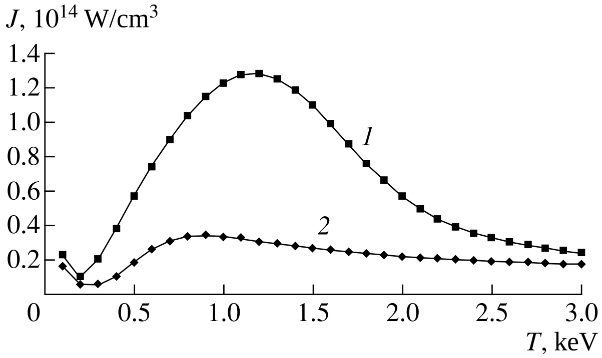

Fig. 12. Radiation capacity J of an Al plasma vs. electron temperature in the AIM (*1*) with and (*2*) without allowance for the Auger processes.

calculations showed that, under non-LTE conditions, these quantities are sensitive to the kinetic constants. In the NAIM, artificially excluding transitions between the subshells with the same principal quantum numbers significantly changes the correlation matrix. Hence, the mixing of the electron subshells with different orbital moments should be taken into account.

In the coronal equilibrium, the effect of dynamic correlations (i.e., nonequilibrium kinetics) on the fluctuations of the mean occupation numbers is also significant. This effect can be illustrated by the example of the ion charge dispersion D. Figures 9 and 10 show the ion charge dispersion computed without allowance for dynamic correlations [in this case, only the diagonal part of equilibrium correlation matrix (34) is used, which, under LTE conditions, corresponds to statistically independent fluctuations] and in the complete formulation of the problem [in this case, the correlation matrix Ξ is determined by solving the equation $A\Xi + \Xi A^+ + B = 0$; see Eq. (25)]. It is seen that, under non-LTE conditions, the dynamic correlations significantly increase the ion distribution width and the statistical linewidths. These results demonstrate the importance of taking into account all of the effects that influence the fluctuation correlations. Indeed, in the average ion approximation, it is these effects that determine both the linewidths and the influence of the line emission reabsorption on the formation of spectra in the nonlocal NRGD problems.

6.2. Calculations with Allowance for the Auger Processes

The first results of the AIM calculations of the ion mean charge $\langle Z\rangle$, the dispersion of the mean charge D, and the plasma volume radiation capacity J versus the electron temperature T by the AVI-L code for the density ρ = 0.002 g/cm^3 are shown in Figs. 11–13. The calculations were performed without allowance for the correlation multiplier (the branching factor) in the effective rate of the Auger process.

It can be seen from Figs. 11–13 that taking into account the Auger processes significantly affects all the

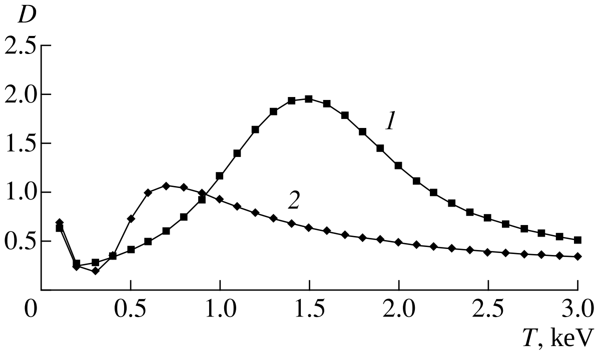

Fig. 13. Dispersion D of the mean charge $\langle Z \rangle$ in an Al plasma vs. electron temperature in the AIM (*1*) with and (*2*) without allowance for the Auger processes.

parameters of a nonequilibrium plasma. The inclusion of the Auger processes (dielectronic recombination) impedes the increase in the degree of ionization with temperature due to the recombination to the lower ion's shells and significantly enlarges the population of the excited ion states, which, in the coronal approximation, results in a sharp increase in the plasma radiation capacity. As in the case without allowance for the Auger processes, the dispersion D of the ion mean charge correlates with the radiation capacity J.

7. CONCLUSION

The theory of fluctuations of the occupation numbers of the electron shells of ions in a nonequilibrium plasma is developed in the AIM approximation. The AIM equations for both the mean occupation numbers of the ion shells and their correlations are deduced in the Fokker–Planck approximation by averaging the equations of the chemical RC kinetics for the hydrogen-like Slater ion models. In the linear noise approximation (as in the quasi-thermodynamic theory of fluctuations in an LTE plasma), the nonequilibrium fluctuations of the occupation numbers are described by a Gaussian distribution function. In a steady state, the correlators of the occupation numbers are explicitly described by analytical formulas via the solution to the AIM equations for the mean occupation numbers of the electron shells.

In the AIM, the occupation-number fluctuations determine the statistical shapes of the photoabsorption cross sections, which enter into the averaged spectral equation of radiative transfer. The calculations of the nonequilibrium fluctuations of the occupation numbers in the AIM approximation allow one to refine some characteristics of a nonequilibrium plasma (such as the radiation capacity and the non-LTE ion composition). The assumptions used in deriving the AIM equations for the nonequilibrium kinetics of a multicharged plasma are best justified for a weakly nonideal plasma and small deviations from the LTE conditions. To quantitatively determine the applicability range and accuracy of the nonequilibrium Slater AIMs, it is necessary to develop a theory of a nonequilibrium nonideal plasma and thoroughly compare the nonequilibrium plasma characteristics with the results of calculations by more exact models.

Currently, the Slater AIMs seem to be the best approximation for simulating the kinetics of a nonequilibrium multicharged plasma. They combine such advantages as simplicity (a significant reduction in the details of plasma description), universality, and acceptable accuracy. These advantages determine a wide use of these models in the in-line calculations of the multidimensional problems of the nonequilibrium radiative plasma gas-dynamics in the physics of high energy densities.

ACKNOWLEDGMENTS

We are grateful to B.A. Voinov, V.I. Roslov, and A.N. Starostin for discussing the problems of the physical kinetics of a nonequilibrium plasma. This study was supported in part by the International Science and Technology Center, project no. 1137.

REFERENCES

1. V. V. Ivanov, *Radiation Transfer and Spectra of Selestial Bodies* (Nauka, Moscow, 1969).
2. L. M. Biberman, V. S. Vorob'ev, and I. T. Yakubov, *Kinetics of Nonequilibrium Low-Temperature Plasmas* (Nauka, Moscow, 1982; Consultans Bureau, New York, 1987).
3. D. Mihalas, *Stellar Atmospheres* (W. H. Freeman and Co., San Francisco, 1978; Mir, Moscow, 1982).
4. D. R. Bates and A. Damgaard, Philos. Trans. **242**, 101 (1949).
5. R. P. Feynman, N. Metropolis, and E. Teller, Phys. Rev. **75**, 1561 (1949).
6. D. E. Post and R. V. Jensen, At. Data Nucl. Data Tables **20**, 397 (1977).
7. I. I. Sobel'man, *Atomic Spectra and Radiation Transitions* (Nauka, Moscow, 1977; Springer-Verlag, Berlin, 1979).
8. L. P. Presnyakov, V. P. Shevel'ko, and R. K. Yanev, *Elementary Processes with the Participation of Multiply Charged Ions* (Énergoatomizdat, Moscow, 1986).
9. L. M. Biberman, Zh. Éksp. Teor. Fiz. **17**, 416 (1947).
10. W. Unno, Publ. Astron. Soc. Jpn. **3**, 158 (1952).
11. D. G. Hammer, Mon. Not. R. Astron. Soc. **125**, 21 (1962).
12. V. A. Makhrov, A. Yu. Sechin, and A. N. Starostin, Zh. Éksp. Teor. Fiz. **97**, 1114 (1990) [Sov. Phys. JETP **70**, 623 (1990)].
13. T. Blenski and S. Morel, Laser Part. Beams **13**, 255 (1995).
14. C. Bauche-Arnoult, J. Bauche, and M. Klapisch, Adv. At. Mol. Phys. **23**, 131 (1988).
15. A. Bar-Shalom, J. Oreg, W. H. Goldstein, *et al.*, Phys. Rev. A **40**, 3183 (1989).

16. A. F. Nikiforov, V. G. Novikov, and V. B. Uvarov, *Quantum-Statistical Models of High-Temperature Plasma. Methods for Calculating Rosseland's Runs and Equations of State* (Fizmatlit, Moscow, 2000).
17. S. A. Moscowski, Prog. Theor. Phys. **28**, 1 (1961).
18. S. Kiyokawa, T. Yabe, and T. Mochizuki, J. Appl. Phys. **22**, 1772 (1983).
19. V. Cohn and P. Vashishta, *Theory of the Inhomogeneous Electron Gas*, Ed. by S. Lundquist and N. March (Plenum Press, New York, 1983; Mir, Moscow, 1987).
20. D. A. Liberman, J. Quant. Spectrosc. Radiat. Transf. **27**, 335 (1982).
21. M. C. Dharma-Wardana and F. Perrot, Phys. Rev. A **26**, 2096 (1982).
22. R. M. More, Adv. At. Mol. Phys. **21**, 305 (1985).
23. T. Blenski and B. Cichocki, Phys. Rev. A **41**, 6973 (1990).
24. G. Faussurier, C. Blancard, and A. Decoster, Phys. Rev. E **56**, 3474 (1997).
25. G. Faussurier, C. Blancard, and A. Decoster, Phys. Rev. E **56**, 3488 (1997).
26. J. C. Slater, Phys. Rev. **36**, 57 (1930).
27. D. Layzer, Ann. Phys. (New York) **8**, 271 (1959).
28. R. M. More, J. Quant. Spectrosc. Radiat. Transf. **27**, 345 (1982).
29. G. Faussurier, C. Blancard, and A. Decoster, J. Quant. Spectrosc. Radiat. Transf. **58**, 233 (1997).
30. J. Stein, D. Shalitin, and A. Ron, Phys. Rev. A **31**, 446 (1985).
31. N. G. van Kampen, *Stochastic Processes in Physics and Chemistry* (North-Holland, Amsterdam, 1984; Vysshaya Shkola, Moscow, 1990).
32. S. A. Bel'kov, P. D. Gasparian, G. V. Dolgolyova, and Yu. K. Kochubey, J. Quant. Spectrosc. Radiat. Transf. **58**, 471 (1997).
33. S. A. Bel'kov, P. D. Gasparyan, Yu. K. Kochubey, and E. I. Mitrofanov, Zh. Éksp. Teor. Fiz. **111**, 496 (1997) [JETP **84**, 272 (1997)].
34. P. D. Gasparian, S. A. Bel'kov, Yu. K. Kochubey, *et al.*, *Strongly Coupled Coulomb Systems*, Ed. by G. J. Kalman, J. M. Rommel, and K. Blagoev (Plenum, New York, 1998).
35. G. B. Zimmerman and R. M. More, J. Quant. Spectrosc. Radiat. Transf. **23**, 517 (1980).
36. R. M. More, K. H. Warren, D. A. Young, and G. B. Zimmerman, Phys. Fluids **31**, 3059 (1988).
37. B. A. Voinov, Vopr. At. Nauki Tekh., Ser.: Mat. Model. Fiz. Protsessov, No. 2, 65 (1986).
38. R. M. More, G. B. Zimmerman, and Z. Zinamon, in *Proceedings of the 6th AIP Conference on Atomic Processes in High-Temperature Plasmas, Santa Fe, 1987*, Ed. by A. Hauer and A. Merts, p. 33.

Translated by N.N. Ustinovskiĭ

Plasma Physics Reports, Vol. 29, No. 5, 2003, pp. 443–446. Translated from Fizika Plazmy, Vol. 29, No. 5, 2003, pp. 476–480.
Original Russian Text Copyright © 2003 by Gavrilenko, Kyrie, Frank.

PLASMA DIAGNOSTICS

Diagnostics of a Current-Sheet Plasma with the Use of Helium Spectral Lines with Forbidden Components

V. P. Gavrilenko[1, 2], N. P. Kyrie[1], and A. G. Frank[1]

[1]Prokhorov Institute of General Physics, Russian Academy of Sciences,
ul. Vavilova 38, Moscow, 119991 Russia

[2]Center for Surface and Vacuum Research, Russian State Committee for Standards,
Andreevskaya nab. 2, Moscow, 117334 Russia

Received October 18, 2002; in final form, December 20, 2002

Abstract—Results are presented from the first measurements of the profiles of the HeI 447.1-nm and HeI 492.2-nm neutral helium spectral lines emitted by the plasma of a current sheet formed in the CS-3D experimental device. A theoretical analysis of these profiles is performed with the model microfield method. A comparison of the theoretical and experimental profiles shows that the electron density in the peripheral regions of the current sheets amounts to (1.0–2.0) × 10^{15} cm^{-3}. *© 2003 MAIK "Nauka/Interperiodica".*

1. INTRODUCTION

The objective of this study is to diagnose the plasma of a current sheet by analyzing the profiles of the HeI 447.1-nm (2^3P–4^3D transition) and HeI 492.2-nm (2^1P–4^1D transition) spectral lines of neutral helium. The Current Sheet 3D (CS-3D) device is intended for studying the evolution of current sheets in various two- and three-dimensional magnetic configurations. The longstanding interest in current sheets [1, 2] is motivated by the fact that they are very suitable objects for studying magnetic reconnection, which is one of the fundamental problems of modern plasma physics. As was demonstrated in our previous studies, spectroscopic methods are very efficient in determining plasma parameters, such as the electron temperature [3–7], ion temperature [3, 5], nonequilibrium electric fields [8, 9], and plasma densities in different spatial regions of the sheet [10–13]. The electron and ion temperatures and the plasma density usually reach their maximum values in the midplane of the sheet and decrease rapidly along the normal to the sheet surface [6, 7, 10–15]. For current sheets produced in high-pressure helium [10–15], the spectral lines of helium ions are emitted predominantly from regions lying near the midplane of the sheet. Thus, analyzing the profiles of the HeII 468.6-nm and HeII 656.0-nm spectral lines, we could determine the maximum values of the electron density [10–13]. In the present paper, we report the first measurements of the profiles of the HeI 447.1-nm and HeI 492.2-nm spectral lines of atomic helium. Analysis of these profiles has allowed us to determine the electron density in the peripheral region of the current sheet.

2. EXPERIMENTAL DEVICE AND THE PROCEDURE OF THE SPECTROSCOPIC MEASUREMENTS

Experimental studies were carried out in the CS-3D device [11, 12, 14]. When electric current is excited along the null line of a two-dimensional (2D) magnetic configuration, a plane current sheet is formed in a plasma [12, 15]. In the experiments described in this paper, the null line of the magnetic field coincided with the axis of the cylindrical vacuum chamber and the radial gradient of the magnetic field was $h = 600$ G/cm. The vacuum chamber was filled with helium at the pressure $p_0 = 300$ mtorr. The initial plasma was produced with the help of an auxiliary theta discharge with intense preionization. Then, the current was excited in the plasma along the null line of the magnetic field. This current initiated 2D plasma flows, which, in turn, resulted in the formation of a current sheet. In these experiments, the current half-period was $T/2 \cong 5$ μs and the current amplitude was $I_{\max} \cong 50$ kA.

The optical scheme of the spectral measurements was similar to that used in [10, 11]. Plasma emission from the central region of the chamber was collected with the help of an achromatic lens. This region was 1.2 cm in diameter and 60 cm long. Then, the radiation was transmitted through quartz fibers to the entrance slit of an MDR-3 monochromator and was recorded with the help of an MORS-3 multichannel optical recording system. This system consisted of an image converter with a microchannel-plate intensifier and a receiving CCD array connected through an adapter to a computer (see [10] for details).

In [5, 10–12], it was shown that, within a layer 1.2–1.5 cm thick, the plasma was strongly nonuniform: the electron temperature and density, which were maximum in the midplane of the sheet, decreased several-

1063-780X/03/2905-0443$24.00 © 2003 MAIK "Nauka/Interperiodica"

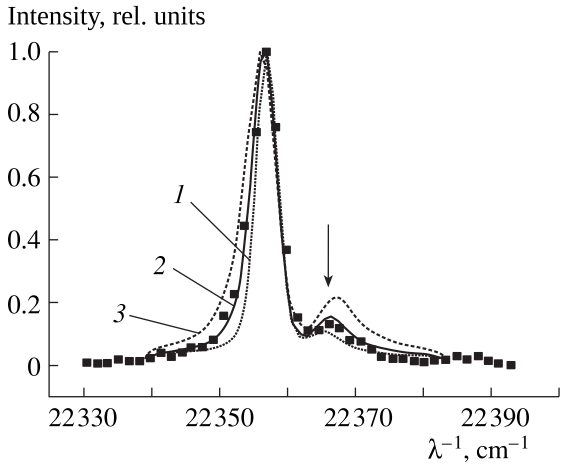

Fig. 1. Experimental and theoretical profiles of the HeI 447.1-nm spectral line. The experimental profile of the HeI 447.1-nm spectral line (squares) corresponds to emission from the peripheral region of the current sheet. The theoretical profiles are calculated with the MMM for different values of the plasma density: N_e = (*1*) 6.0×10^{14}, (*2*) 1.6×10^{15}, and (*3*) 2.8×10^{15} cm^{-3}. The vertical arrow shows the position of the dipole-forbidden spectral line corresponding to the 2^3P–4^3F transition.

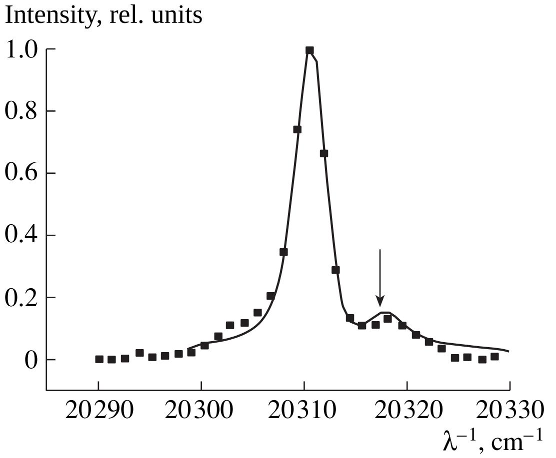

Fig. 2. Experimental and theoretical profiles of the HeI 492.2-nm spectral line. The experimental profile of the HeI 492.2-nm spectral line (squares) corresponds to emission from the peripheral region of the current sheet. The theoretical profile is calculated with the MMM for the plasma density $N_e = 1.02 \times 10^{15}$ cm^{-3}. The vertical arrow shows the position of the dipole-forbidden spectral line corresponding to the 2^1P–4^1F transition.

fold toward the periphery. As a result, the spectral lines of atomic helium were emitted from the peripheral regions of the current sheet and also from the plasma surrounding the sheet. For plasma sheets formed at high initial pressures (p_0 = 300 mtorr), this conclusion was also confirmed by the results of an analysis of 2D distributions of plasma emission in various spectral lines [11, 12, 14]. These distributions were obtained with the help of an image converter in combination with narrowband interference filters ($\Delta\lambda_{1/2}$ = 1.1 nm), which gave a general qualitative picture of the structure of the current-sheet plasma.

Typical experimental profiles of the HeI 447.1-nm and HeI 492.2-nm spectral lines are shown by symbols in Figs. 1 and 2; these profiles contain dipole-forbidden components, which are indicated by vertical arrows. These dipole-forbidden components correspond to the $4^3F \longrightarrow 2^3P$ (for the HeI 447.1-nm line) and $4^1F \longrightarrow 2^1P$ (for the HeI 492.2-nm line) transitions. The appearance of dipole-forbidden components is explained by the fact that, under the action of plasma microfields, the Stark mixing of the states of a pair of closely spaced upper levels $4^{2S+1}D$ and $4^{2S+1}F$ of atomic helium occurs, which enables the radiative transition $4^{2S+1}F \longrightarrow 2^{2S+1}P$ ($S = 0; 1$).

3. ANALYSIS OF HELIUM SPECTRAL LINES AND DISCUSSION

To analyze the experimental profiles of the HeI 447.1-nm and HeI 492.2-nm spectral lines, we numerically calculated the profiles of these lines for different values of the plasma density. It was taken into account that the plasma density was related to the strength of electric microfields produced by charged plasma particles. Under the action of electric microfields, the profiles of the HeI 447.1-nm and HeI 492.2-nm lines are modified (due to the Stark effect), which can be used for diagnostic purposes.

The basic formula for calculating the spectral profile $I(\omega)$ of atomic line radiation emitted in the transition $a \longrightarrow b$ has the form [16, 17]

$$I(\omega) = \frac{1}{2\pi}\int_{-\infty}^{+\infty} \exp(i\omega t)C(t)dt, \tag{1}$$

where the correlation function $C(t)$ in the case of an electric dipole transition is written as

$$C(t) = \mathrm{Tr}\{\mathbf{d} \cdot T^{+}(t)\mathbf{d} \cdot T(t)\}_{av}. \tag{2}$$

In formula (2), **d** is the dipole moment of an atom, $T(t)$ is the operator of the atom evolution, $T^{+}(t)$ is the operator that is Hermitian conjugate to $T(t)$, $\{\ldots\}_{av}$ stands for the averaging over all of the possible types of motions of the perturbing particles, and the symbol Tr denotes the sum of the diagonal matrix elements. Formula (2) assumes that all the Zeeman states of the upper energy level a have equal populations and there are no nonzero nondiagonal matrix elements of the atomic density matrix between the Zeeman states of the upper level a. We use the term “Zeeman state” to indicate a state characterized by a definite value of the magnetic quantum number m. The atom evolution operator $T(t)$ is a solution to the Schrödinger equation

$$i\hbar\frac{dT(t)}{dt} = [H_0 - \mathbf{d}\cdot\mathbf{F}(t)]T(t), \quad T(0) = I, \tag{3}$$

where H_0 is the Hamiltonian of an unperturbed atom, $\mathbf{F}(t)$ is the electric microfield produced by the plasma electrons and ions, and I is the unity matrix.

We studied the profiles of helium spectral lines in the vicinity of the allowed HeI 447.1-nm and HeI 492.2-nm spectral lines. The profiles are formed due to the Stark interaction of the closely spaced upper levels $4^{2S+1}P$, $4^{2S+1}D$, and $4^{2S+1}F$ ($S = 0$; 1). Taking into account that the electric microfields negligibly affect the state of the lower $2^{2S+1}P$ level, formula (2) for the correlation function is significantly simplified:

$$C(t) = \mathrm{Tr}[\mathbf{d}\cdot I_b\mathbf{d}\cdot\{T_a(t)\}_{av}], \tag{4}$$

where I_b is the unity operator acting on the Zeeman states of the lower level $2^{2S+1}P$ and $T_a(t)$ is the evolution operator determining the time evolution of the Zeeman states of the upper levels $4^{2S+1}P$, $4^{2S+1}D$, and $4^{2S+1}F$. In formula (4), the energies of the levels are counted from the energy of the level $2^{2S+1}P$. It follows from formulas (1) and (4) that, in the problem under consideration, the calculation of the profile of the spectral line reduces to the calculation of the operator $\{\tau_a(\omega)\}_{av}$, which is the Fourier transform of the evolution operator for the upper states $\{T_a(t)\}_{av}$, averaged over all of the perturbing particles.

The operator $\{\tau_a(\omega)\}_{av}$ was calculated by the model microfield method (MMM) proposed in [18]. We note that main ideas of the MMM are given in the review [19]. This method implies that the actual electric microfield produced by charged plasma particles is substituted by a simpler stochastic process for which an exact analytic expression can be derived for the operator $\{\tau_a(\omega)\}_{av}$. In this case, the MMM suggests that the electric microfield $\mathbf{F}(t)$ changes by jumps at random instants of time t_j distributed by Poisson's law with the jump probability density depending on the field strength, $\nu = \nu(\mathbf{F})$. In the time interval $t_j < t < t_{j+1}$, the electric field vector $\mathbf{F}$ is constant. The random process $\mathbf{F}(t)$ defined in this fashion is called the "kangaroo" process.

In the MMM, the Fourier transform of the atom-evolution operator averaged over the realizations of the electric microfield is defined by the following expression:

$$\begin{aligned}\tau_{MMM}(\omega) &= \{\tau_S(\omega_1)\}_P \\ &+ \{\nu\tau_S(\omega_1)\}_P\{\nu I - \nu^2\tau_S(\omega_1)\}_P^{-1}\{\nu\tau_S(\omega_1)\}_P.\end{aligned} \tag{5}$$

Here, $\tau_S(\omega_1)$ denotes the Laplace transform (at the frequency $\omega_1 = \omega + i\nu(\mathbf{F})$ of the time-evolution operator $T_S(t)$ calculated for a static (time-independent) electric field $\mathbf{F}$,

$$\tau_S(\omega_1) = (\{\nu(\mathbf{F}) - i\omega\}I + i\hbar\{H_0 - \mathbf{d}\cdot\mathbf{F}\})^{-1}, \tag{6}$$

and $\{A\}_P$ stands for the averaging of the operator A over the distribution function $P(\mathbf{F})$ of the electric field $\mathbf{F}$ in the plasma,

$$\{A(\mathbf{F})\}_P = \int d^3\mathbf{F}A(\mathbf{F})P(\mathbf{F}).$$

Relationship (5) corresponds to the situation in which the electric field $\mathbf{F}$ is produced by one charged particle species (electrons or ions). With the MMM, we can also determine $\tau(\omega)\}_{av}^{(MMM)}$ in the general case where the electric field $\mathbf{F}$ in plasma is a superposition of the electron ($\mathbf{F}_e$) and ion ($\mathbf{F}_i$) microfields: $\mathbf{F} = \mathbf{F}_e + \mathbf{F}_i$. The method for determining $\tau(\omega)\}_{av}^{(MMM)}$ in this case is based on the fact that the correlation time for the electron microfield is much shorter than the correlation time for the ion microfield. With this fact taken into account, the model microfield $\mathbf{F}$ for the general case is determined as follows. First, we construct a kangaroo process $\mathbf{F}_i(t)$ with the jump probability density $\nu_i(\mathbf{F}_i)$ for the ion microfield. Then, in each of the time intervals in which the ion microfield remains constant, we construct a kangaroo process $\mathbf{F}_e(t)$ with the jump probability density $\nu_e(\mathbf{F}_e)$ for the electron microfield. It is this approach that was used in our study, which allowed us to take into account both the ion and the electron microfields in the frame of the MMM.

When calculating the profiles of the helium spectral lines, we assumed that $T_e = T_i = T_a = 2$ eV, where T_e is the electron temperature, T_i is the ion temperature (in our case, the temperature of HeII ions), and T_a is the temperature of the helium atoms. This temperature value was taken from the results of our previous studies [10, 14].

Figure 1 shows three calculated profiles of the HeI 447.1-nm spectral line for three values of the plasma density: $N_e = 6.0\times10^{14}$, 1.6×10^{15}, and 2.8×10^{15} cm^{-3}. It can be seen from the figure that the profile of the HeI 447.1-nm line changes markedly as N_e changes from 6.0×10^{14} to 2.8×10^{15} cm^{-3}. In this case, both the width of the main line (corresponding to the 2^3P–4^3D transition) and the intensity of the dipole-forbidden line (corresponding to the 2^3P–4^3F transition) increase with increasing N_e. It also follows from Fig. 1 that the best fit to the experimental profile of the HeI 447.1-nm line is provided by the theoretical profile calculated for $N_e = 1.6\times10^{15}$ cm^{-3}. For the HeI 492.2-nm line in Fig. 2, the theoretical profile that gives the best fit to the experimental profile is shown by the solid line. This theoretical profile was calculated for a plasma density of $N_e = 1.02\times10^{15}$ cm^{-3}. We note that, in calculations, the resulting profile of each of the helium spectral lines was obtained by convoluting the Stark profile of this line (determined with the MMM) and the Gaussian profile accounting for the Doppler effect and the instrumental width.

Thus, the electron density determined in this study from an analysis of the profiles of the HeI 447.1-nm and HeI 492.2-nm spectral lines of neutral helium amounts to (1–2) × 10^{15} cm^{-3}. This density corresponds to the peripheral region of the current sheet, whereas the electron density in the midplane of the sheet is usually higher than 10^{16} cm^{-3} [15]. We note that, at the periphery of the current sheet, the plasma is spatially nonuniform. Therefore, the measured density $N_e = (1–2) \times 10^{15}$ cm^{-3} is actually the density averaged over the entire peripheral region of the current sheet. Although theoretical calculations of the profiles of helium spectral lines were performed for a uniform equilibrium plasma, the results obtained for the averaged electron density appear to be realistic. This is confirmed by the fact that, when comparing the experimental profiles of the helium spectral lines with the theoretical ones, these profiles agree well in the main spectroscopic parameters, including the shapes of the profiles of the allowed and forbidden components and the intensity ratio between these components.

ACKNOWLEDGMENTS

V.P. Gavrilenko thanks Prof. V.N. Kolokol'tsov (Nottingham Trent University, Nottingham, UK) for fruitful discussions. This work was supported in part by the Russian Foundation for Basic Research (project no. 01- 02-17810) and the Russian Federal Program "Government Support of the Leading Scientific Schools" (project no. 00-15-96676).

REFERENCES

1. S. I. Syrovatskii, Annu. Rev. Astron. Astrophys. **19**, 163 (1981).
2. A. G. Frank, Plasma Phys. Controlled Fusion, Suppl. 3A **41**, 687 (1999).
3. N. P. Kyrie, V. S. Markov, and A. G. Frank, Pis'ma Zh. Éksp. Teor. Fiz. **48**, 419 (1988) [JETP Lett. **48**, 459 (1988)].
4. I. L. Beĭgman, V. P. Gavrilenko, N. P. Kyrie, and A. G. Frank, Zh. Prikl. Spektrosk. **54**, 1021 (1991).
5. N. P. Kyrie, V. S. Markov, and A. G. Frank, Pis'ma Zh. Éksp. Teor. Fiz. **56**, 82 (1992) [JETP Lett. **56**, 82 (1992)].
6. S. Yu. Bogdanov, V. B. Burilina, N. P. Kyrie, *et al.*, Fiz. Plazmy **24**, 467 (1998) [Plasma Phys. Rep. **24**, 427 (1998)].
7. G. S. Voronov, N. P. Kyrie, and A. G. Frank, Fiz. Plazmy **28**, 1004 (2002) [Plasma Phys. Rep. **28**, 925 (2002)].
8. A. G. Frank, V. P. Gavrilenko, Ya. O. Ispolatov, *et al.*, Contrib. Plasma Phys. **36**, 667 (1996).
9. V. P. Gavrilenko, N. P. Kyrie, and A. G. Frank, Opt. Spektrosk. **87**, 916 (1999) [Opt. Spectrosc. **87**, 834 (1999)].
10. S. Büscher, N. P. Kyrie, H.-J. Kunze, and A. G. Frank, Fiz. Plazmy **25**, 185 (1999) [Plasma Phys. Rep. **25**, 164 (1999)].
11. A. G. Frank, S. Yu. Bogdanov, V. B. Burilina, *et al.*, Contrib. Plasma Phys. **40**, 106 (2000).
12. S. Yu. Bogdanov, N. P. Kyrie, V. S. Markov, and A. G. Frank, Pis'ma Zh. Éksp. Teor. Fiz. **71**, 78 (2000) [JETP Lett. **71**, 53 (2000)].
13. A. G. Frank, V. P. Gavrilenko, N. P. Kyrie, and V. S. Markov, Contrib. Plasma Phys. **41**, 85 (2001).
14. S. Yu. Bogdanov, V. B. Burilina, and A. G. Frank, Zh. Éksp. Teor. Fiz. **114**, 1202 (1998) [JETP **87**, 655 (1998)].
15. S. Yu. Bogdanov, V. S. Markov, A. G. Frank, *et al.*, Fiz. Plazmy **28**, 594 (2002) [Plasma Phys. Rep. **28**, 549 (2002)].
16. M. Baranger, in *Atomic and Molecular Processes*, Ed. by D. R. Bates (Academic, New York, 1962; Mir, Moscow, 1964), Chap. 13.
17. H. Griem, *Spectral Line Broadening by Plasmas* (Academic, New York, 1974; Mir, Moscow, 1978).
18. A. Brissaud and U. Frisch, J. Quant. Spectrosc. Radiat. Transf. **11**, 1767 (1971).
19. L. A. Bureeva, V. P. Gavrilenko, and V. S. Lisitsa, in *Encyclopaedia of Low-Temperature Plasma*, Ed. by V. E. Fortov (Nauka, Moscow, 2000), Vol. 1, p. 351.

Translated by N.F. Larionova

Plasma Physics Reports, Vol. 29, No. 5, 2003, p. 447.

ERRATA

Erratum: Laser Probing of the Plasma in the S-300 Facility (Plasma Phys. Rep. 28, 790 (2002))

Yu. G. Kalinin, V. A. Korel'skiĭ, E. V. Kravchenko, and A. Yu. Shashkov

The Editorial board of Plasma Physics Reports apologizes for the misprints in the paper by Yu. G. Kalinin *et al. Laser Probing of the Plasma in the S-300 Facility*, Plasma Phys. Rep. **28** (9), 790 (2002).

On page 790, in the list of authors, V. A. Korel'skiĭ should instead read A. V. Korel'skiĭ.

On page 795, in the 26th line in the left column, the words "no larger than 3…" should instead read "no less than 3…."

On page 795, in the ninth line in the right column, the exponent 8 should be replaced by 7.

1063-780X/03/2905-0447$24.00